UNIVERSITA' DEGLI STUDI DI TRIESTE

XXVII CICLO DI DOTTORATO DI RICERCA IN SCIENZE CHIMICHE E TECNOLOGIE FARMACEUTICHE

STRUCTURAL CHARACTERIZATION OF POLYMERIC MATRICES FOR BIOMEDICAL APPLICATIONS

SSD: **CHIM/05**

PhD Student:
Simona Maria Fiorentino

PhD Program Director
Prof. Mauro Stener

PhD Supervisor
Prof. Mario Grassi

ACADEMIC YEAR 2014/2015

I Sogni non sempre si realizzano, è vero

Ma non perché siano troppo grandi o impossibili,

ma perché si smette di crederci.

Martin Luther King

Table of Contents

Acknowledgements

First of all I would like to express my sincere appreciation to my advisor and mentor Prof. Mario Grassi for his kindness, guidance and encouragement during the entire course of this work. His encouragement, advices, patience helped me going through the difficulties and crisis I met during the path of this work.

I would like to thank everyone who has contributed to this work. I would like to thank my committee members: Prof. Eleonora Marsich, Prof. Gianluca Turco for reviewing my work and making suggestions and critical comments.

I would like to acknowledge and thank Prof. Valerio Brucato, Prof Giulio Ghersi and Prof. Francesco Carfì Pavia for the various opportunities that have helped to make this journey an educational as well as an enjoyable one.

I'm truly grateful to my boyfriend Vincenzo for his support and his love and patience during my stressful day. And finally I would like to express my thank to my family (my mother, my grandparents, my uncles, and my cousins) because even if far I have stood with their love and their support.

To my friends Angela, Martina and Diego, who have always encouraged me to pursue my goals, always succeed, and never admit defeat. To Luigi, Angela, Mary and Manfredo, my second family in Trieste and finally thanks to Fede, Lollo and Gabry for these three years in Via Fabio Severo 47.

List of figures

List of tables

1 Abstract

The main goal of this research work was the determination of some important micro and nano structural characteristics of polymeric matrices intended for biomedical applications. In particular, the attention was focused on the application of the Low-Field Nuclear Magnetic Resonance (LF-NMR), a fast and non destructive technology used in food and polymeric companies to study *homogeneous* (i.e. not porous) and *porous* polymeric *matrices*.

Indeed, in the case of *homogeneous matrices* (typically used as delivery systems), LF-NMR can provide interesting informations about the polymeric network mesh size distribution, this being a key parameter ruling the drug release kinetics. One of the most interesting homogeneous matrix studied was that composed by alginate and pluronic F127. This is a composite polymeric blend proposed for artery endoluminal delivery of an emerging class of molecules called nucleic acid based drugs (NABDs). The physical characterization of this gel was performed according to rheology, low/high field NMR and TEM. In particular, it was observed that Pluronic micelles, organizing in cubic ordered domains, generate, upon alginate crosslinking (due to the addition of divalent cations), meshes (≈ 150 nm) larger than those occurring in a Pluronic-free alginate network (≈ 25 nm). Accordingly, the gel structure is quite inhomogeneous, where big meshes (filled by crystalline Pluronic) co-exist with smaller meshes (hosting water and un-structured PF127 micelles). The presence of big and small meshes indicates that drug release may follow a double kinetics characterized by a fast and a slow release. Notably, this behaviour is considered appropriate for endoluminal drug release to the arterial wall. In this context, it was also explored the possibility of recurring to cryoporosimetry in order to evaluate the mesh size distribution of both alginates and polyvinylpirrolidone gels. Indeed, cryoporosimetry relies on the depression of the ice melting point when nanocrystals are considered (the smaller the nanocrystal size, the smaller the melting temperature and enthalpy). Upon gel freezing, the water contained in the polymeric network cannot give origin to a unique macro-crystals due to the presence of the three-

dimensional polymeric network that obliges water to crystallize in many nanocrystals confined in the polymeric meshes. Thus, the evaluation of the melting temperature depression of the water contained in the hydrogel enables the determination of nanocrystals size distribution and, thus, of the mesh size distribution. This study evidenced that the application of cryoporosimetry to polymeric gels, although not so uncommon in literature, requires extreme care as the water melting point can be influenced not only by the mesh size but also by the presence of unreacted polymer, crosslinker, salts and impurities. Accordingly, it is highly recommended comparing the water melting temperature variation in the polymeric network and the melting temperature occurring in a water – polymer solution of the same concentration.

In the case of *porous matrices*, typically used as scaffolds for tissue engineering and regenerative medicine, low field NMR can provide interesting information about the size distribution of matrix pores, this being a key parameter for cells growth. Indeed, it is well know that cells can grow on condition that pores are sufficiently wide (typically around 100 microns in diameters). By measuring the apparent reduction of the water self-diffusion coefficient inside the scaffold, it was possible estimating the mean pores dimension according to the Mitra theory. Then, the Brownstein and Tarr approach, suitable for mono-dispersed spherical pores, was extended to a micro-porous structure characterized by poly-dispersed spherical pores according to the Chui approach. On the basis of this study, it was finally possible getting the pore size distribution relying on transverse relaxation measurements. In order to verify the robustness and reliability of this approach, different systems were considered:

- Spherical glass beads
- Styrene-butadiene rubber
- Toasted coffee seeds
- Bacterial Cellulose/ Acrylic Acid gels

In the case of glass beads, the correctness of the low field NMR approach was proved by means of a theoretical evaluation of the mean diameter of the voids formed among beads. In the case of the styrene-butadiene rubber (used to produce pillows and mattresses) the estimation of pores diameter according to low field NMR approach completely agreed with the outcomes deriving from SEM images of the same rubber. Interestingly, the low field NMR approach yielded important results also in the evaluation of pores dimension

in swollen toasted coffee seeds. At our knowledge, this aspect of coffee seeds has never been accounted for and it could represent an important parameter for the determination of coffee quality and/or maintenance of coffee seeds properties. Once the reliability of the low field NMR approach was definitively proved, the attention moved on more interesting, from the biomedical point of view, systems. In particular, two different kinds of scaffolds were considered:

- Poly Left lactide Acid (PLLA) scaffolds
- Alginate/Hydroxyapatite (Alg/Hap) scaffolds.

In this framework, the attention was devoted to the production of PLLA scaffolds with and without functionalizing agents such as collagen and glycosaminoglycans (GAGs), polysaccharides devoted to ameliorate the environment for cells growth. Indeed, cells vitality after seeding in the PLLA scaffolds was improved by the GAGs presence. Also in this case the low field approach furnished an estimation of pores size distribution in agreement with what evaluable by means of SEM and micro–CT. Interestingly, this agreement holds also when different operating conditions are considered in the scaffold preparation, this yielding to different mean pores diameter. Undoubtedly, one of the most important results reached in this work was connected to the characterization of alginate - hydroxyapatite scaffold intended for osteocytes growth in the bone regeneration frame. Indeed, it was possible observing the temporal evolution of the pore size distribution of the scaffold without and with seeded cells. Interestingly, it was observed that while the temporal evolution of pores size, for what concerns smaller pores (< 100 μm), is similar for scaffolds hosting or not living cells, a different behaviour was observed for bigger pores. Indeed, in this case, the presence of cells made the time evolution of the pores size different from what occurred in the scaffolds without cells. This sounds reasonable as the effect of cell growth should be evident only in bigger pores while, in smaller pores, where cells access is more difficult, cells effect should be less evident if not negligible.

Finally, it is important to stress that low field NMR proved to be a reliable, not invasive approach for the characterization of scaffolds structure also in the presence of living cells, this being not the case of many other characterization approaches that unavoidably tend to kill the seeded cells. Vitality tests proved that cells are alive up to 20 days after seeding, despite the numerous expositions to the low field NMR for the determination of pore size evolution.

2 Introduction

2.1 Tissue Engineering

Tissue or organ failure is one of the most frequent and devastating problem medicine. Current therapeutics approaches (allografts, xenografts, autografts and implantation of biomedical devices) had largely improved the quality of life but they are associated with clear limitations including donor availability, infection, poor integration and potential rejection of the implant. Regenerative medicine was developed with the aim to overcome such limitations and to find revolutionary and powerful therapies for the treatment of tissues diseases, with the basic idea to repair or re-create tissues or organs in order to restore impaired functions [**1**, **2**]. Since its origin, regenerative medicine has rapidly grown and has attracted the interest of many scientists and surgeons throughout the world. Nowadays regenerative medicine encompasses different strategies for the creation of new tissue including the use of cloning, of isolated cells, of non-cellular structures and of cells constructs.

The latter approach, which is usually referred to as Tissue Engineering (TE), is believed to be highly promising for regenerating tissues. It is pointed out that a clear distinction between TE and regenerative medicine does not exist in the literature and some scientists use these terms as synonyms.

Even if the term "**Tissue Engineering**" was firstly coined in the mid of 1980's, it became part of the scientists common language only in 1993, when Robert Langer and Joseph P. Vacanti defined TE as "an interdisciplinary field that applies the principles of engineering and life science towards the development of biological substitutes that restore, maintain, or improve tissue function or a whole organ" [**3**].

Figure 2.1 sketches TE approach for the preparation of cell constructs: cells are cultured in vitro under precisely controlled culture conditions on a porous three-dimensional (3D) materials that act as a scaffolds for cell growth and proliferation. Those structures are characterized by an interconnected pore network able to guide, after the degradation of the scaffold, the implanted cells to form a new tissue showing a well-integrated structure.

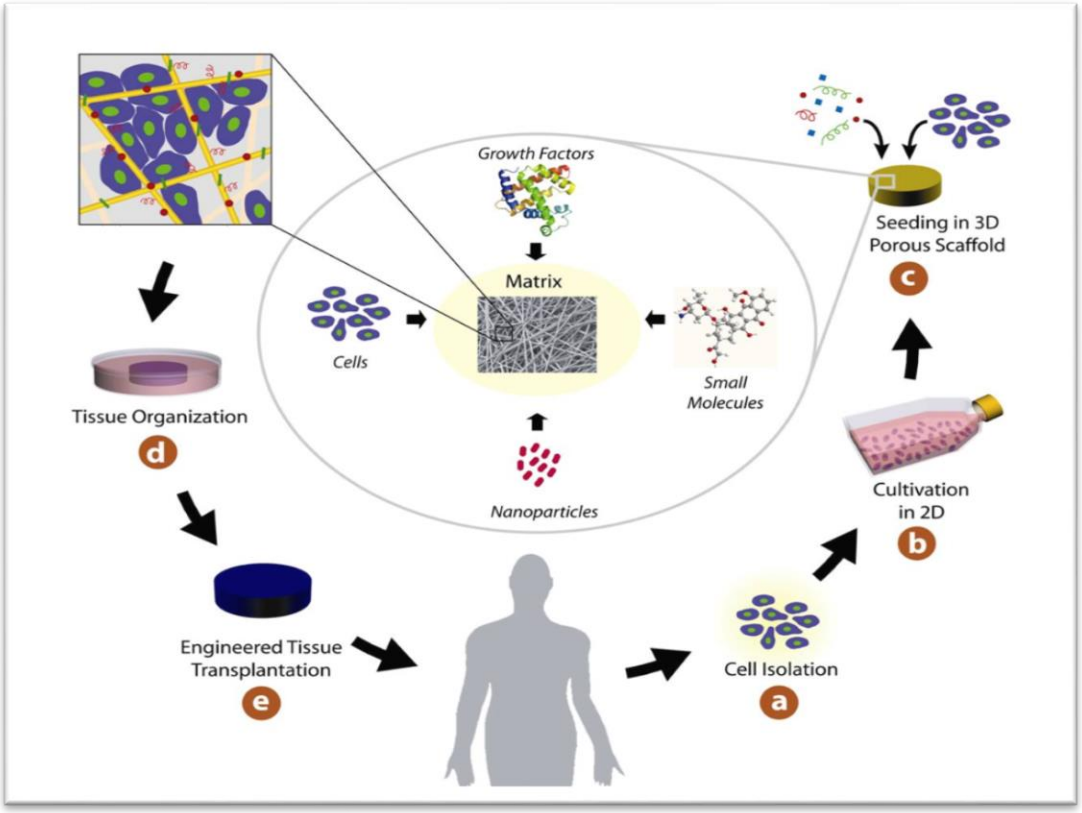

Figure 2.1: TE approach by using cell-scaffolds constructs

Significant progress has been realized in TE since its principles were defined and to date several products, incorporating cells together with scaffold, have gained regulatory approval [**4**]. Commercial devices are mostly dedicated to skin, bone and cartilage engineering whereas products for cardiac, nerve, kidney or pancreas engineering are not widespread yet [**4**].

2.2 Tissue Engineering Products

Based on the concept that each tissue is characterized by different functions and features the tissue engineering products design strongly depends on material properties and on cellular response to the chosen biomaterials. In addition, the ability to shape into the suitable cellular level architecture has to be taken into account and the final architecture must be compatible with the desired tissue response. The proper biomaterial selection is assisted by the development of methods and sophisticated modeling techniques that permit prediction of polymer properties and cellular response to the material. Such techniques allow a wide use of biodegradable polymers for tissue engineering

applications. Tissue engineering products can be designed to conduct, induct or block tissue responses and architectures. Depending on the final purpose barriers (membranes or tubes), gels or matrices can be developed [**5**].

Membranes are required where cell activity is needed on one surface of a device precluding transverse movement of surrounding cells onto that surface. For instance peripheral nerve regeneration needs an axonal growth and, at the same time, preventing fibroblast activity that would produce neural-inhibiting connective tissue [**6**]. Furthermore, collagen membranes used in periodontal repairing provide the right environment for periodontal ligament regrowth and attachment but at the same time they avoid the epithelial ingrowth into the healing site [**7**]. Prevention of post-surgical adhesion obtained by using hyaluronic acid compounds is another example of barrier biomaterials. Hydrogel biomaterials can encapsulate and represent a specialized environment for isolated cells. Collagen gels, for instance, can be used for the preservation and immuneprotection xenograft and homograft cells, such as hepatocytes, chondrocytes, and islets of Langerhans, used for transplantation. Semipermeable gels can be a support for cells in systems where cell-cell communication and interaction with surrounding tissue has to be minimized as well as the movement of peptide factors and nutrients through the implant.

Gels are particularly suitable in applications such as bone and cartilage tissue regeneration where the material has to be injectable and polymerization in situ is needed [**8**].

Tissue engineering **scaffolds** or matrices are an important component for tissue development and their characteristics such as pore size and the structure, ordered and regular or randomly distributed, are fundamental in forming tissues with a proper cell morphology, orientation, arrangement of intercellular material, and the relationship between different cell types. Besides several techniques have been developed to form well defined scaffolds using different kind of biomaterials and physical characteristics of the matrices can be varied to maximize cellular and tissue responses [**5**, **9**, **10**].

2.3 Biological Tissues

Detailed understanding of structure and function of normal biological tissues is central to the design of artificial organs and to the development of tissue engineering strategies. In general biological tissues are composed of cell and of a not cellular part called **Extracellular Matrix** (ECM). Physiological functions in the human body are coordinated by different types of organs composed of a great variety of mammalian cells surrounded by ECM, which displays different chemical compositions and different spatially organized configurations depending on the type of organ.

The ECM is composed of carbohydrates and proteins locally secreted by cells and assembled in an organized network. For the sake of simplicity ECM can be composed of [**11**]:

- A gel like component
- A fibrous component
- Specialized proteins.

The highly viscous and hydrated gel-like part confers lubricant and hit-absorption properties to the ECM. It consist of carbohydrates assembled to form polysaccharides commonly called glycosaminoglycans which, in turn, are covalently attached to a protein backbone to form proteoglycans. The fibrous component of ECM is essentially composed of collagen and elastin that create a complex network of fibers with diameters ranging from few to hundreds of nanometers, imparting rigidity and strength to the entire tissue. Finally, ECM holds proteins such as growth factors (GFs), cytokines, enzymes and multidomain proteins (e.g. fibronectin, laminin, vibronectin, etc.) that play a key function in the communication with the surrounding cells. Besides providing structural support to cells, ECM plays a central role in modulating cell behavior and in maintaining tissue architecture and functions thanks to its dynamic interaction with cells. Indeed, cells continuously interact with the external environment via membrane proteins (receptors, e.g. integrins) that bind external proteins (ligands, e.g. fibronectin) located both on the surface of surrounding cells and in the ECM, by following a lock-and-key mechanism. Through an intracellular cascade of reactions, the ligand-receptor interaction is translated into a specific signal to guide the cell to a specific activity [**12**].

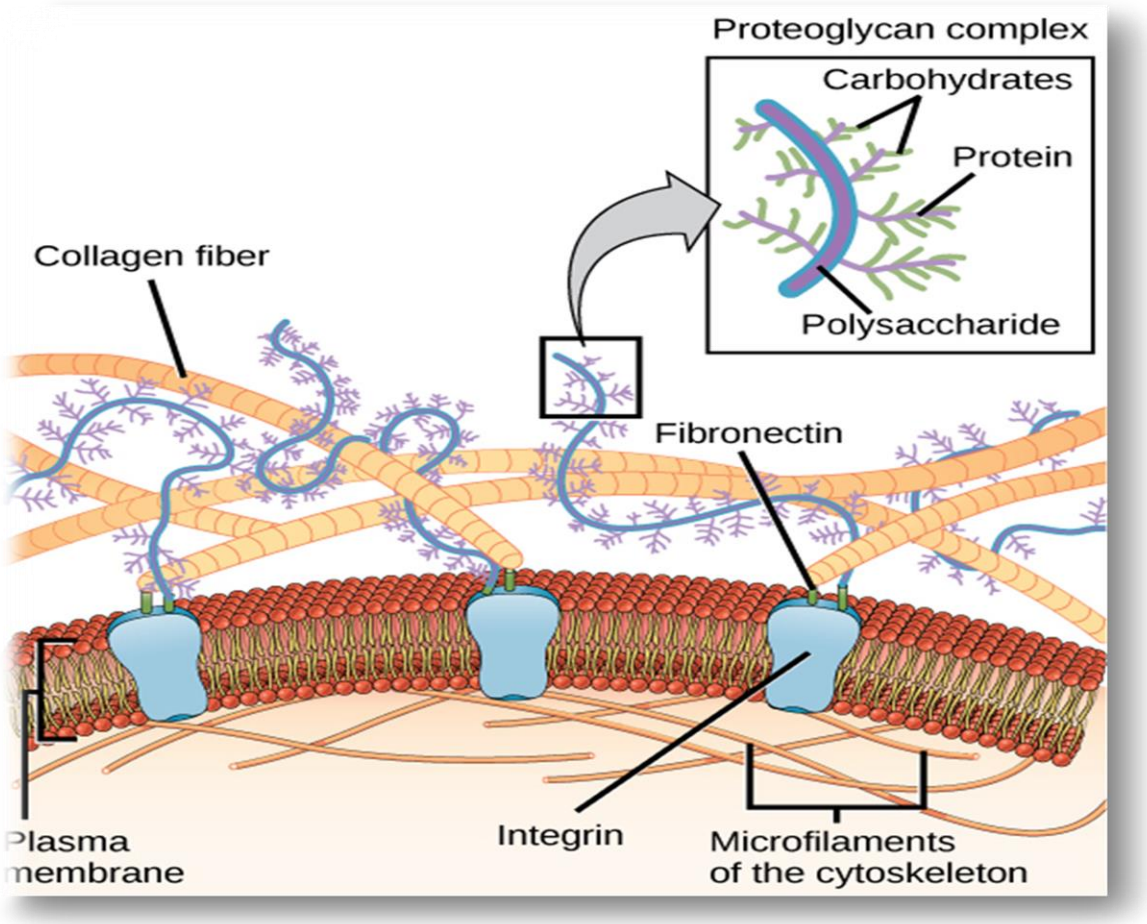

Figure 2.2: The structure of ECM

This dynamic interaction allows to finely control cell fate, shape and behavior in response to even small changes in ECM composition [**13-16**].

Generally, ECM functions can be summarized as follow [**17**]:

- Establishment of a hierarchical patterned micro/nano environment;
- Mechanical and structural support;
- Regulation of cell shape and cell polarity;
- Storage of regulatory molecules (enzymes, GFs, multidomain proteins);
- Regulations of cell function (e.g. proliferation, growth, survival, migration and differentiation).

Given the central role of ECM and of cell environment in determining cell response and behavior, it is quite evident that biologists and biochemists need to deeply understand the biological phenomena that rule cell-ECM and cell-cell interactions. It is also clear that

cells must be provided with a scaffold, having suitable biological and mechanical features to ensure cell attachment, proliferation and spontaneous deposition of ECM by cells. To this aim, materials science play its role in TE field, by fabricating and ECM-substitute scaffold with appropriate physical and chemical properties and with a proper 3D structure and architecture.

2.4 Biomaterials

A **biomaterial** can be considered a synthetic material used to make a device designed to replace a part or a function of the body. The commonly accepted definition of biomaterial was proposed at the Conference of the European Society for Biomaterials (England, 1986): "any substance, other than a drug, or combination of substances, synthetic or natural in origin, which can be used for any period of time, as a whole or as a part of a system which treats, augments, or replaces any tissue, organ, or function of the body" [**18**].

The basic requirement of a biomaterial is to be biocompatible, namely "to perform with an appropriate host response in a specific application" [**18**]. The biomaterial itself, but also additives or degradation products, must not cause harmful reactions in contact with the body. For this reason the design and the fabrication of a biomedical device, in terms of synthesis of the raw materials but also of manufacture technologies, must respect, first to all, the biocompatibility requirement. Biocompatibility must be tested and the device must be approved by appropriate regulatory agencies (such as Food and Drug Administration, USA) before it can marketed. According to the definition of biomaterial reported above, the following devices fall within this category:

- Implantable devices, e.g. dental implants, pacemakers, orthopedic and vascular prostheses, etc.;
- Devices working in contact with biological tissues/fluids for a limited period of time, e.g. surgical instruments, catheters, contact lenses, sutures, etc.;
- Devices for extra-body treatments, e.g. dialysis membranes, blood vessels.

According to their chemical nature, synthetic biomaterials can be classified as:

- Polymers
- Metals

- Ceramics
- Composites.

Table 2.1 reports some examples of application, together with some considerations about advantages and disadvantages related to each class of biomaterial.

Materials	**Uses**	**Advantages**	**Disadvantages**
Polymers Polyammides, silicon rubber, polyesters, polyurethans, polytetrafluoroethylene, polymethylmetharilate, etc.	Sutures, blood vessels, catheters, devices for drug delivery, contact lens, etc.	Resilient Easy to fabricate Wide range of mechanical properties	Biodegradable Not strong Deformation with time
Metals Ti and its alloys, stainless steels, Au, Ag, Co-Cr alloys, etc.	Join replacements, bone plates and screws, dental implants, surgical instruments, etc.	Strong Tough Ductile	May corrode High densities
Ceramics Aluminium oxides, calcium phosphates, hydroxyapatite, bioglasses, etc.	Dental implants, femoral heads, coating of orthopaedic devices	Strong under compression Good trybological properties	Brittle Not resilient
Composites	Joint implants, tendon and hip replacements, Heart valves	Strong Tailor-made	Difficult to fabricate

Table 2.1: Categories of Biomaterials (adopted from [**19**]).

Thanks to the continuous progress in molecular biology and in the comprehension of cell-biomaterial interactions, since its birth, biomaterial science has seen an extraordinary evolution in the development of increasingly biocompatible, bioactive and specifically functional biomedical devices. The improvement of biomaterial features went through three different stages, each concerning different purposes [**20**]. The “first generation” of

biomaterials, development in 1960s as implantable devices, were designed to possess suitable physical properties in view of their function as organ substitutes, and they were intended to be inert, namely to cause minimal tissue reactions. Later in the 1980s, the "second generation" of biomaterials was born with the necessity not only to be tolerated by the organism, but also to elicit desired and controlled response by the biological tissue, again with no harmful effects. The so called bioactive materials were used, for example, in orthopaedic surgery (Bioglass).

Moreover, in this period problems connected with long term tissue-biomaterial interactions were minimized with the development of bioresorbable materials that were used also as drug delivery systems. Subsequently biomaterials have evolved into their "third generation" and nowadays they are intended to stimulate highly precise reactions at the molecular level with biological tissues. With this aim it is clear that precise surface engineering and nanotechnology are needed in order to build tailored architectures for specific applications. Scaffolds for tissue engineering can be considered as "third generation" biomaterials. For this reason it is clear that raw materials suitable to produce bioresorbable scaffolds are exclusively either biodegradable polymers (either natural or synthetic ones) or biodegradable ceramics (calcium phosphates) that must disappear in the human body as a consequence of hydrolytic and/or enzymatic degradation, whereas metals and all the other non-degradable materials are not used in this context.

Biodegradable ceramics, most of all hydroxyapatite (Hap) and β-tricalcium phosphate (β-TCP), are naturally found in bone and they are used in combination with degradable polymers to make composite scaffolds for bone tissue regeneration [**21-23**]. Indeed, these inorganic substances are often difficult to be processed by their own into highly porous structures. Moreover, their inherent brittleness limits their use as plain materials for scaffolds, so that, in order to obtain structural resistant supports, it is necessary to combine them with polymer matrices [**24**]. Natural polymers such as proteins (e.g. gelatin, collagen, fibrin, starch, etc.), polysaccharides (e.g. hyaluronic acid, alginate, chitin, etc.) and bacterial polyesters (e.g. polyhydroxybutyrate, etc.) are widely used to produce scaffolds with different topography, either as pure materials or in combination with synthetic polymers or inorganic substances [**25-28**]. The use of natural polymers ensured excellent bioactivity towards biological environment because of their inherent properties of biological recognition. In particular, if ECM polymers, such as collagen or hyaluronic

acid, are employed, scaffolds that mimic the chemical properties of natural ECM are obtained. Biomimetic features are so relevant that, besides pure natural polymers, decellularized ECM, containing multiple natural macromolecules, is also used as scaffolds for tissue repair. Despite the incredible advantage of biomimicry, some issues, associated with purification, pathogen transmission, processability into porous structure and sustainable production, restrict the use of natural polymers for scaffolds fabrication. Moreover, poor control of mechanical properties and degradation rate limits the possibility to tailor their employment to specific functions. Some problems associated with the use of natural materials can be overcome with the employment of synthetic polymers. Indeed, the latter, besides being less expensive and better processable, can be synthesized ad hoc with a precise control of molecular structure to tune mechanical and degradation properties. Furthermore, polymers can be synthesized with specific functional groups in order to make them bioactive towards biological environment. These characteristics make synthetic polymers extremely attractive raw materials for scaffolds fabrication. The molecular structures of the most common ones are reported in *Figure 2.3* [**29**, **30**].

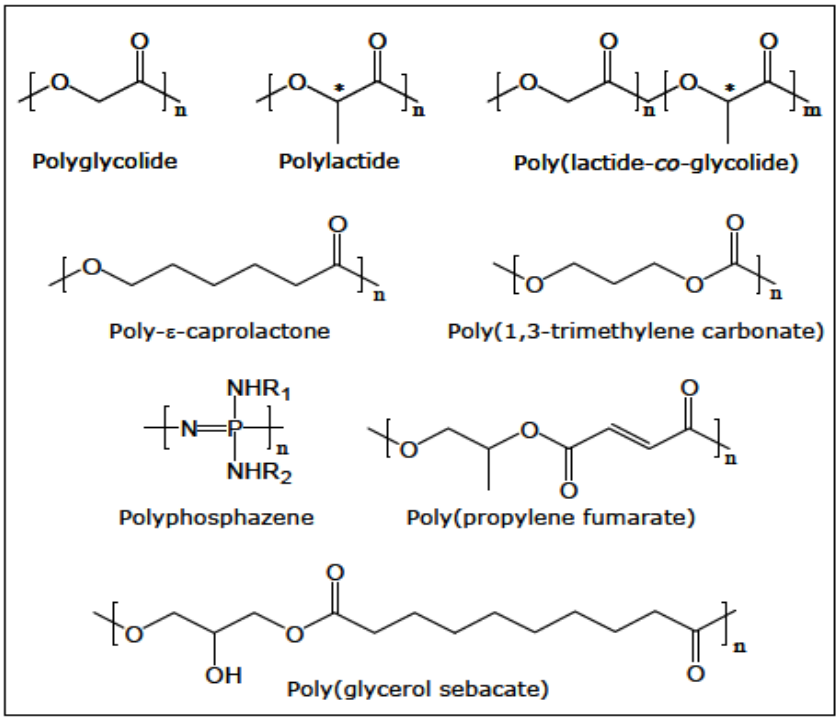

Figure 2.3: Common synthetic biodegradable polymers for scaffolds based TE.

Scientific literature focuses its efforts mainly in the development of scaffolds made of polyesters, which possess the most suitable features to be employed in this context. This class of materials can degrade in water as consequence of ester bond hydrolysis. It is pointed out, however, that hydrolysis occurs depending mainly on material hydrophilicity and for this reason, not all polyesters can be considered as hydrolizable materials. Currently, the most widely investigated and most commonly used biomedical polyesters are polylactide (PLA), polyglicolide (PGA) and their copolymer, usually referred as poly-α-hydroxyacids [**31**, **32**]. These materials degrade upon water exposure into products absorbable by the organism: lactic acid, which is normally produced by muscular contraction, can be metabolized through the citric acid cycle whereas glycolic acid may be eliminated directly in urine or may be converted to enter the citric acid cycle [**33**].

Poly-α-hydroxyacids are usually synthesized by ring-opening polymerization of the cyclic dimers of lactic acid and glycolic acid (lactide and glycolide). Lactic acid is a chiral molecule existing as L or D isomer, thus polylactide can be optically pure, poly(L) lactide or poly (D) lactide, or it can exist in the racemic form, poly (D,L) lactide, depending on the starting monomer. PGA and the stereo regular forms of PLA are semicristalline polymers whereas PLGA copolymers can be amorphous depending on molecular composition because the presence of a co-monomer disturbs the crystallization ability of the chains. It has been reported that PLAGA random copolymers with L-lactic acid units are amorphous when glycolic acid amounts falls within the range 25-75%, whereas PLAGA copolymers with lactic acid in both L and D forms are amorphous in the range 0-75% of glycolic acid content [**34**]. Copolymerization modulates not only the phase morphology (amorphous to crystalline phase ratio) and the thermal properties (glass transition temperature, crystallization and melting temperature) but also the degradation rate. Degradation mechanism and kinetics of this series of polymers have been intensively studied [**35**, **36**]. Hydrolysis rate is primarily correlated with hydrophobicity of the material that changes depending on the copolymer composition, being lactic acid more hydrophobic than glycolic acid because of the presence of an extra CH_3 group. The hydrophobicity of lactic acid limits the water uptake and, accordingly, the homopolymer PGA should be the faster degrading one, with degradation rate that should decrease with the increase of lactic acid content. However, hydrophobicity is not the only parameter affecting degradation rate, which is deeply influenced also by phase morphology. Indeed,

molecular chains packed in the crystalline phase absorb a lower amount of water with respect to the less dense amorphous phase. This fact explains why the amorphous $PLA_{50}GA_{50}$ degrades faster than the semicrystalline PGA, even if the latter is more hydrophilic [**37**, **38**]. Other factors affecting degradation kinetics are polymer molecular weight and shape of the device. The possibility to modulate, within a wide range, degradation rate and mechanical properties by controlling copolymer composition and molecular structure makes these polyesters the most widely employed bioresorbable materials suitable for many and different applications, such as resorbable surgical sutures, drug delivery systems, orthopaedic appliances and scaffolds.

Polyesters with a long carbon backbone chain are identified as ω-polyhydroxyalcanoates among which poly-ε-caprolactone (PCL) is frequently employed to produce scaffolds (*Fig. 2.3*). As these polymers are highly hydrophobic and semicrystalline, their degradation kinetic is extremely slow, thus they are suitable for long-term tissue engineering applications. In particular, ε-caprolactone is largely used also as co-monomer to slow down degradation rate of homopolymers such as PLA (giving rise to PLAxCLy copolymers) [**39-41**]. Aliphatic polycarbonates are also applied in tissue engineering [**42**], in particular poly (1,3-trimethylene carbonate) (PTMC), an elastomeric polymer potentiallycandidate for soft tissue engineering. Trimethylene carbonate is also widely used as co-monomer with lactic acid, glicolic acid or ε-caprolactone in order to obtain scaffolds with elastomeric properties [**43-47**].

Other categories of materials are currently under investigation [**48**]:

- Polyphosphazenes: these polymers with a backbone of alternating phosphorus and nitrogen atoms are at the interface between inorganic and organic polymers. Biodegradable polyphosphazenes can be synthesized by incorporating side groups on phosphorous atoms with the possibility to modulate the degradation rate over hours, days, months, or years by carefully controlling the nature and composition of side substitutes [**49**, **50**]. Thanks to their synthetic flexibility, good biocompatibility, not-toxic degradation products and tailored mechanical properties they are very good candidates for various soft and hard tissue engineering appliations [**51-53**].
- Poly (propylene fumarate): being available as an injectable system that is cross-linked in situ, it is very interesting material for bone tissue engineering in the

treatment of crevices and defects. Its mechanical properties vary according to the cross-linking agents used and they often improved by the addiction of inorganic particles such as β-TCP [**54-56**].

2.5 Polymeric Hydrogels

Polymeric hydrogels are three-dimensional networks of polymer chains that are loosely cross-linked, enabling the system to entrap a high amount of water and causing the matrix to swell [**57**, **58**]. In the last years, these materials have been used in numerous applications, with special emphasis on the biomedical and pharmaceutical fields. In tissue engineering and regenerative medicine, hydrogels have shown to be promising materials for the repair of cartilage [**59**, **60**], bone [**61**, **62**] and soft tissue [**63**, **64**], where they form scaffolds for cell growth and proliferation. The applicability in biomedical devices, such as films, sponges and biosensors is also recognized [**65**]. In drug delivery, hydrogels have been widely used as depot systems, for instance through the oral [**66**], topical and transdermal [**66**, **68**], gastrointestinal [**69**, **70**], ocular [71], nasal [**72**] and vaginal [**73**] administration routes.

2.5.1 Properties of Hydrogels

Hydrogels are water swollen polymer matrices, with a tendency to imbibe water when placed in aqueous environment. This ability to swell, under biological conditions, makes it an ideal material for use in drug delivery and immobilization of proteins, peptides, and other biological compounds. Due to their high water content, these gels resemble natural living tissue more than any other type of synthetic biomaterial [**74**]. These networks, have a three dimensional structure, crosslinked together either physically (entanglements, crystallites), or chemically (tie-points, junctions). This insoluble crosslinked structure allows immobilization of active agents, biomolecules effectively, and allows for its release in well-defined specific manner. Thus the hydrogels‟ biocompatibility and crosslinked structure are responsible for its varied applications.

2.5.2 Mechanical properties

For not biodegradable applications, it is essential that the carrier gel matrix maintain physical and mechanical integrity. Mechanical stability of the gel is, therefore, an important consideration when designing a therapeutic system. For example, drugs and

other biomolecules must be protected from the harmful environments in the body such as, extreme pH environment before it is released at the required site. To this end, the carrier gel must be able to maintain its physical integrity and mechanical strength in order to prove an effective biomaterial. The strength of the material can be increased by incorporating crosslinking agents and increasing degree of crosslinking. There is however an optimum degree of crosslinking, as a higher degree of crosslinking also leads to brittleness and less elasticity. Elasticity of the gel is important to give flexibility to the crosslinked chains, to facilitate movement of incorporated bioactive agent. Thus a compromise between mechanical strength and flexibility is necessary for appropriate use of these materials.

2.5.3 Biological properties

It is important for synthetic materials, such as hydrogels, to be biocompatible and non toxic in order for it to be a useful biomedical polymer. Most polymers used for biomedical application must pass a cytotoxicity and in-vivo toxicity tests. Most toxicity problems associated with hydrogels arise due to unreacted monomers, oligomers and initiators that leach out during application. Thus an assessment of the potential toxicity of all materials used for fabrication of gel is an integral part of determining suitability of the gel for biological applications. To lower chances of toxic effects, the use of initiators is being eliminated, with the advent of γ-irradiation as polymerization technique. Steps are also taken to eliminate contaminants from hydrogels, by repeated washing and treatment.

2.5.4 Classification of hydrogels

Hydrogels can be classified as neutral or ionic, based on the nature of side groups. In neutral hydrogels, the driving force for swelling is due to the water-polymer thermodynamic mixing contribution to the overall free energy, along with elastic polymer contribution [**75**]. The swelling of ionic hydrogels is also affected by the ionic interactions between charged polymers and free ions [**76**]. Ionic hydrogels containing ionic groups, such as carboxylic acid, imbibe larger amount of water, because of its increased hydrophilicity. Hydrogels are also classified as homopolymers or copolymers, based on the method of preparation. Hydrogels can be classified based on the physical structure of the network as amorphous, semicrystalline, hydrogen bonded structures, supermolecular structures and hydrocolloidal aggregates [**75**]. An important class of hydrogels are the

stimuli responsive gels [**77**]. These gels show swelling behavior dependent on their physical environment. These gels can swell, or de-swell in response to changes in pH, temperature, ionic strength, and electromagnetic radiation [**78**]. These properties allow for usage in a number of applications, such as separation membranes, biosensors, artificial muscles, and drug delivery devices [**74**].

2.6 Preparation Methods of Hydrogels

Hydrogels are polymeric networks. This implies that crosslinks have to be present in order to avoid dissolution of the hydrophilic polymer chain in aqueous solution. Hydrogels are most frequently used for controlled release of bioactive agents and for encapsulation of cells and biomolecules. In many of these cases the three dimensional structure of the hydrogels have to disintegrate into harmless non toxic products to ensure biocompatibility of the gel. The nature of the degradation products can be tailored by a proper selection of the hydrogel building blocks. Keeping this consideration in mind, various chemical and physical crosslinking methods are used today for the design of biocompatible hydrogels. Chemically crosslinked gels have ionic or covalent bonds between polymer chains. Even though this leads to more mechanical stability, some of the crosslinking agents used can be toxic, and give unwanted reactions, thus rendering the hydrogel unsuitable for biological use. These adverse effects can be removed with the use of physically crosslinked gels. In physically crosslinked gels, dissolution is prevented by physical interactions between different polymer chains. Both of these methods are used today for preparation of synthetic hydrogels and are discussed in detail.

2.6.1 Chemically Crosslinked Gels

As stated earlier, chemically crosslinked gels are mechanically quite stable due to the ionic and covalent bond which comprises these gels. The various methods for chemical crosslinking are as follows [**79**]:

- Copolymerization/Crosslinking Reactions

Initiators used in these reactions are radical and anionic initiators.

- Crosslinking of polymers

In this method chemically crosslinked gels are formed by radical polymerization of low molecular weight monomers, or branched homopolymers, or copolymers in the presence

of crosslinking agent. This reaction is mostly carried out in solution for biomedical applications.

- Crosslinking by High Energy Radiation

High energy radiation, such as gamma [1.38] and electron beam radiation can be used to polymerize unsaturated compounds.

- Crosslinking Using Enzymes

In this method chemically crosslinked hydrogels are formed by enzymes addition such us transglutaminase into solution.

2.6.2 Physically Crosslinked Gels

Chemically crosslinked gels imply use of a crosslinking agent, which is often toxic. This requires that the crosslinking agent be removed from gel, which can affect the gel integrity. For these reasons, physically crosslinked gels are now coming into prominence. Several methods have been investigated exploring preparation of physically crosslinked gels. Below are mentioned some of the most widely used methods and their areas of application [**79**]:

- Crosslinking by Ionic Interactions

An example of crosslinking via ionic interactions is crosslinking of Alginate. Alginate consists of glucuronic acid residues and mannuronic acid residues and can be crosslinked by calcium ions. Crosslinking can be carried out at normal temperature and pH. These gels are used as matrix for encapsulation of cells and for release of proteins. Also Chitosan based hydrogels, as well as dextran based hydrogels, crosslinked with potassium ions are also other gels synthesized with ionic interactions. In addition to anionic polymers being crosslinked with metallic ions, hydrogels can also be obtained by complexation of polyanions and polycations.

- Crosslinking by Crystallization

An aqueous solution of PVA that undergoes a freeze-thaw process yields a strong highly elastic gel. Gel formation is attributed to the formation of PVA crystallites which act as physical crosslinking sites in the network. The gel properties could be modified by varying polymer concentration, temperature, and freezing and thawing cycle times. These gels have been shown to be useful for drug release

- Crosslinking by Hydrogen Bonds

Poly(acrylic acid) and poly(methacrylic acid) form complexes with poly(ethylene glycol) by hydrogen bonding between the oxygen of the poly(ethylene glycol) and the carboxylic acid group of poly((meth)acrylic acid). The hydrogen bonds are only formed when the carboxylic acid groups are protonated. This also implies that the swelling of gels is pH dependent [**79**].

2.7 The scaffolds

The officially accepted definition considers a scaffold as a "support, delivery vehicle or matrix for facilitating the migration, binding or transport of cells or bioactive molecules used to replace, repair or regenerate tissues" [**80**]. Indeed, recent scaffolds are not intended only to support cell growth but they can also load bioactive molecules having a specific biological function. Moreover, it is worth noting that last generation scaffolds are intended to be as much biomimetic as possible, in terms of mechanical performances, 3D morphology and surface chemistry, and they are designed according to this scope. It is well-accepted that an ideal functional scaffold should meet the following challenging requirements [**81, 84**]:

- To be biocompatible;
- To have mechanical properties consistent with those of the tissue it replaces;
- To be bioresorbable;
- To degrade at a rate matching that of new tissue formation;
- To have proper surface properties to enable cell attachment, growth, proliferation, and differentiation as well as to promote extracellular matrix formation;
- To have the optimum architectural properties in terms of pore size, porosity, pore interconnectivity, and permeability in order to allow efficiently delivery of nutrients and removal of waste.

The imperative requirement for a scaffold is to be biocompatible. Since the scaffold works in contact with leaving cells in vitro and with tissue, once implanted in vivo, it must not elicit harmful response from the biological environment, i.e. it should interact with cells and host tissue without inducing cytotoxicity or adverse immune response.

Scaffolds mechanical properties are another key element that distinguishes a successful implant from a failed one. Indeed, since many tissues undergo mechanical stress and strains, it is extremely important that mechanical properties of the scaffolds match as closely as possible those of the tissue intended to regenerate, so that formation of new ECM is not limited by mechanical failure of the scaffold. Moreover, a good mechanical transfer between the scaffolds and the new forming tissue is required in order to provide sufficient mechanical stimulation for ensuring a proper tissue growth [**85**].

Scaffolds are intended to be a temporary support that is eventually replaced in the organism by new regenerated tissue. Hence, scaffolds must be degradable in the human body through molecular fragmentation mechanisms that results in the formation of degradation by-products and the gradual disappearance of the scaffold. Degradation can occur via hydrolysis or it can be mediated by enzymes, depending on polymer chemical structure. In any case, the long-term success of an engineered tissue will be achieved only if degradation products are completely resorbed by the organism by naturally occurring metabolic pathways, i.e. if the scaffold is bioresorbable [**86**, **87**]. Moreover, scaffold degradation rate should mirror the rate of tissue formation. This criterion is extremely difficult to achieve but it is particularly important as regards the structural supporting role of the scaffold. Indeed, in order not to compromise the integrity of the implant, the scaffold should maintain its structural function until the regenerated tissue can assume its supporting role and, over time, the degrading scaffold should gradually transfer its function of load bearing to the new forming tissue. The control of the scaffold mechanical properties over time and during degradation process remains one of the greatest challenges in tissue engineering [**88**, **89**].

Another significant feature of the scaffold is its surface properties which are directly connected to its capability of creating a chemically suitable environment that promotes cell adhesion, migration and proliferation in order to obtain an entirely colonized 3D cell construct. Cell adhesion is always a receptor–mediated process that occurs via interaction between membrane proteins, called integrins and multidomain protein that act as ligand. In natural tissues, typical ligands dislocated in the ECM are fibronectin, laminin and vitronectin that binds integrins, forcing the cells to attach to the ECM [**90**, **91**]. Cell-scaffold interaction similarly occurs. Therefore cell-scaffold interactions are related to the composition of the protein layer attached to the scaffold surface. It has been largely

demonstrated that polymers can adsorb many proteins [**92**] and it is also possible to adapt a material presenting good bulk properties by improving its surface properties towards cell adhesion through surface modification. Many techniques have been developed to modify material surfaces such as plasma or ion treatment but, more recently, ECM biomolecules, such as proteins, peptides or growth factors, have been immobilized on scaffold surface with the aim to obtain bioactive and biomimetic scaffolds [**93**].

Cell colonization of the scaffold depends not only on scaffold surface properties but also, indirectly, on its 3D architecture.

Porosity (the amount of void space), size, geometry, orientation and interconnectivity of pores and channels directly affect the transport and delivery of nutrients for cells throughout the scaffold [**94**]. In particular high porosity, high surface area to volume ratio and high pore interconnectivity are required in order to ensure uniform tissue ingrowth, efficient delivery of nutrients to the interior of the scaffold and removal of waste towards the exterior [**95**].

The optimum porosity is strictly connected to the tissue type and diverse nature tissue architectures can be associated to a different microenvironment to reproduce. Cell dimension, together with cell activity behavior, phenotypic expression and ECM production has also to be taken into account when designing a scaffold for tissue regeneration. In bone tissue regeneration, for instance, the minimum pore size required is considered to be about 100 μm due to cell size, migration conditions and transport. However, pore sizes bigger than 300 μm are recommended, to improve new bone formation and to develop a net of capillaries [**96**]. In PLLA scaffolds, vascular smooth muscle specifically bind to one range of pore sizes (63 – 150 μm) while fibroblast, for their ability to form bridge connections, to a wider range (38 - 150 μm) [**97**].

The above described scaffold characteristics (i.e. biocompatibility, mechanical properties, bioresorbability, surface properties and architecture) are strictly related to two major factors that interplay in controlling scaffold properties:

1. The type of polymer material
2. The scaffold fabrication technology.

The supply of nutrients and oxygen is realized in vivo by the blood vascular system. The achievement of vascularization of 3D scaffolds is still one of the greatest challenges in TE. For instance, toxic residual substances can be released from the scaffold causing

harmful effects. Such substances can be either monomers or impurities in the starting material or substances deriving from material processing (e.g. degradation products, organic solvents, etc.) Mechanical properties primary depend on the raw material but they can dramatically change according to scaffold architecture which, in turn, is determined by the technique employed to produce the scaffold. Another example is bioresorbability and, in particular, the degradation rate that depends not only on polymer properties (i.e. chemical composition, monomer distribution and microstructure in copolymers and molecular weight) but also on scaffold architecture (i.e. scaffold dimension and pore walls).

It is clear that the correct design of a scaffold for a specific application requires to accurately know which properties it should exhibit in order to successfully achieve its function. Once the necessary scaffold features are clearly defined, material science intervenes in selecting the proper polymer material, the suitable scaffold fabrication technology and the appropriate treatments in order to obtain a scaffold that matches as closely as possible the specific requirements.

The following subchapters outline the principles of biomaterials science and describe the more frequently used biomaterials for tissue engineering applications, with particular attention towards polymeric ones. Common scaffold fabrication approaches are introduced, focusing mainly on freeze drying and thermally induced phase separation.

2.8 Scaffold fabrication technologies

Selection of the raw material for producing the scaffold is complementary to the choice of the proper fabrication technology suitable to achieve the desired aim and even nowadays new methods are invented, though they are mostly modification or smart combination of already existing techniques. This section aims at providing an overview of conventional and well-known processes for scaffold fabrication by illustrating the characteristics of the obtained scaffold.

2.8.1 Solvent casting and particulate leaching

This technique, firstly described by Mikos et al. in 1994 [**98**], uses a water soluble porogen to produce pores within a polymer matrix. In brief, a polymer solution is cast in a mould containing particles of desired dimension. After solvent evaporation, particles

are leached out by immersion in water. Mainly PLA and PLAGA scaffolds were produced with this approach. Salts are the most commonly used porogen [**99**], but also sugar [**98**], paraffin [**100**] and gelatin spheres have been employed. This method enables to tune independently pore size (up to 500 mm in diameter) and porosity (up to 90%) by controlling particle dimensions and porogen/polymer ratio respectively. However, due to gravity, homogeneous pore distribution is only obtained in scaffolds less than a few millimeters thick [**101**] and complete elimination of both organic solvent and porogen is rather difficult to achieve if pores are not completely interconnected. Moreover, biomolecules potentially added to the scaffold can be partially removed during the leaching step in water.

2.8.2 Freeze drying

Freeze drying is a technique based on sublimation, very easily performed and widely used to fabricate porous scaffolds [**102**]. The polymer is dissolved in a solvent (water, acetic acid or benzene), poured into a mould, frozen and finally freeze-dried under high vacuum. Pore size can be modulated depending on pH or freezing rate (a rapid lyophilization produces smaller pores) [**103, 105**]. Forcing unidirectional solidification, homogenous and well-ordered porous structures can be obtained. The choice of freeze drying can be advantageous since it does not require high temperature or a washing step to remove the porogen. Its limits are the small pore size and the long fabrication time [**106**].

2.8.3 Thermally Induced Phase Separation

The phase separation technique is based on thermodynamic demixing of a homogeneous polymer–solvent solution into a polymer-rich phase and a polymer-poor phase, usually by either exposure of the solution to another immiscible solvent or cooling the solution to a point below the binodal solubility curve [**107**]. Particularly, thermally induced phase separation (TIPS) uses thermal energy as the latent solvent to induce phase separation [**108**]. The polymer solution is quenched below the freezing point of the solvent and subsequently freeze dried, producing a porous structure which can be finely tuned byadjusting the variousthermodynamic and kinetic parameters [**109, 110**].

2.8.4 Solid freeform fabrication

Solid freeform fabrication process is a computerized technique involving the design of a scaffold model through a CAD system which elaborates it as a seriesof cross sections

[**111, 116**]. These sections are built by a rapid prototyping machine that lays down layers of material starting from the bottom and moving up a layer at a time to create the scaffold. This method enables to fabricate large and complex 3D objects with a precise control of pore architecture. Unfortunately, this top-down approach does not create nano-scaled structures and requires expensive equipments.

2.8.5 Gas foaming

Gas foaming has been commonly employed to produce microcellular foams of thermoplastic polymers [**116, 119**] such as polymethylmethacrylate and polystyrene, but only in 1994 Mooney et al. applied this method for the production of $PLA_{50}GA_{50}$ scaffolds for TE [**120**]. Since then gas foaming has become an appealing technique for fabricating microporous scaffolds [**121, 122**].

Supercritical carbon dioxide ($scCO_2$) is the most common substance employed, which, once turned into gas phase, acts as a porogen to generate pores within a polymer matrix.The method exploits the unique properties of $scCO_2$ that, combining liquid-like densities (high solvent power) with gas-like viscosities (high diffusion rates) [**123**], is used for a wide range of applications in polymer synthesis, extraction and impregnation processes, particle formation and blending [**124, 125**]. Moreover, CO_2 has a relatively low critical point (Tc = 31 °C, Pc = 7.4 MPa) that can be easily achieved in a high-pressure equipped laboratory.

Briefly, the method consists in dissolving $scCO_2$ in a solid polymer at high pressure, generating a low viscosity mixture. Subsequently, the depressurization decreases $scCO_2$ solubility in the polymer and leads to the phase transition of CO_2 from supercritical to gas. CO_2 bubble nucleation occurs and nuclei growth generates pores within the polymer. Concomitantly, viscosity of the polymer $scCO_2$ mixture increases till all the gas has escaped from the polymer, leavingbehind a solid structure with “locked in” pores [**126**]. Scaffold morphology can be controlled by varying the amount of $scCO_2$ incorporated and its release rate from the polymer.

The main benefit of using $scCO_2$ foaming for the production of scaffolds is the reduction of problems associated with residual solvents that can be toxic to mammalian cells. The capability of producing scaffolds without the use of any toxic solvent makes this technique unique and extremely interesting with respect to all other scaffold fabrication methods known to date. However, it is well documented that foamed scaffolds can exhibit

inadequate pore interconnectivity especially at the scaffold surface, where a non-porous layer forms probably because of the rapid diffusion of the CO_2 from the surface as the pressure is released [**127**]. This issue has been overcome by combining gas foaming with the salt leaching procedure [**98**, **128**] or by trimming off the non-porous skin from the scaffold after its fabrication [**129**, **130**].

2.8.6 Electrospinning

Electrospinning is a technique used widely to fabricate micro and nano-fibrous scaffolds that mimic the native ECM environment to various degrees [**131**].

The electrospinning setup and process mechanism is very simple (*Fig. 2.4*). The polymer solution is supplied through the nozzle connected to a high voltage power supply. Due to electrostatic forces, overcoming solution surface tension forces, Taylor's cone is created at the end of the nozzle [**132**]. The electrostatic field between the nozzle and grounded collector causes polymeric jet to stretch and bend, generating ultrafine polymeric fibres with diameter in the submicron range. Fibres produced this way are collected on a grounded collector as non-woven randomly aligned sheets or arrays. The simplicity of the process, its versatility, and the ability to control generated material properties makes electrospinning technique extremely suitable for production of specifically designed scaffolds for tissue engineering and cell culturing [**133**]. Nature of electrospinning inspires many scientists to find the best conditions to produce desired nano and microfibrous polymeric materials for biomedical applications.

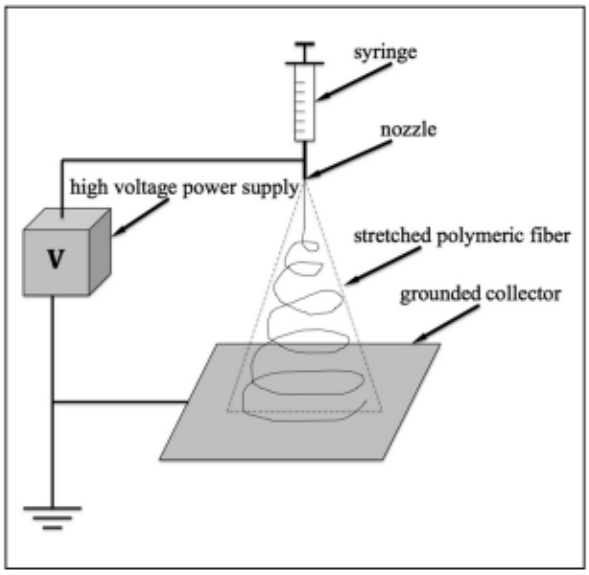

Figure 2.4: Schematic of the electrospinning setup.

References:

1. Mason C, Dunnill P. A brief definition of regenerative medicine. Regenerative Medicine 2008; 3: 1.

2. Vacanti JP and Vacanti CA. The history and scope of tissue engineering. In:Lanza R, Langer R, Vacanti J editors. Principles of Tissue Engineering. Elsevier Academic Press, 2007.pp. 3-6.

3. Langer R, Vacanti JP. Tissue engineering. Science 1993; 260: 920.

4. Place ES, Evans ND, Stevens MM. Complexity in biomaterials for tissue engineering. Nature Materials 2009; 8: 457.

5. Vacanti, J. P. & Langer, R. Synthetic Biodegradable Polymer Scaffolds (ed. Anthony Atala, D. J. M.) (1997).

6. Faweett, J. W. & Keynes, R. J. Peripheral Nerve Regeneration. Annual Review of Neuroscience 13, 43-60 (1990).

7. Pitaru, S., Tal, H., Soldinger, M., Grosskopf, A. & Noff, M. Partialregeneration of periodontal tissues using collagen barriers. Initialobservations in the canine. Periodontol 59, 380-386 (1988).

8. Drury, J. L. & Mooney, D. J. Hydrogels for tissue engineering: scaffold design variables and applications. BiomaterialsSynthesis of Biomimetic Polymers 24, 4337-4351 (2003).

9. Hutmacher, D. W., Sittinger, M.& Risbud, M. V. Scaffold-based tissue engineering: rationale for computer-aided design and solidfree-form fabrication systems. Trends in Biotechnology 22, 354-362 (2004).

10. Vats, A., Tolley, N. S., Polak, J. M. & Gough, J. E. Scaffolds and biomaterials for tissue engineering: a review of clinical applications. Clinical Otolaryngology & Allied Sciences 28, 165-172 (2002).

11. Lutolf MP, Hubbell JA. Synthetic biomaterials as instructive extracellularmicroenvironments for morphogenesis in tissue engineering. Nature Biotechnology 2005; 23: 47.

12. Giancotti FG. Complexity and specificity of integrin signaling. Nature Cell Biology 2000; 2: E13.

13. Bissell MJ, Hall HG, Parry G. How does the extracellular matrix direct gene expression Journal of Theoretical Biology 1982; 99: 31.

14. Streuli CH, Bailey N, Bissell MJ. Control of mammary epithelial differentiation: basement membrane induces tissue-specific gene expression in the absence of cell-cell interaction and morphological polarity. Journal of Cell Biology 1991; 115: 1383.

15. Chen CS, Mrksich M, Huang S, Whitesides GM, Ingber DE. Geometric control of cell live and death. Science 1997; 276:1425.

16. Blaschke RJ, Howlett AR, Desprez P-Y, Peterson OW, Bissell MJ. Cell differentiation by extracellular matrix components. Methods in Enzymology 1994; 245: 535.

17. Veiseh M, Turley EA, Bissell MJ. Top–down analysis of a dynamic environment: extracellular matrix structure and function. In:Laurencin CT and Nair LS editors. Nanotechnology and tissue engineering: the scaffold. CRC Press, Taylor & Frencis Group, 2008.pp. 33-51.

18. Williams DF. Definitions in biomaterials. Proceeding of a consensus conference of the european society for biomaterials. Amsterdam: Elsevier; 1987.

19. Park JB. Biomaterials. In: Bronzino JD editors. The Biomedical Engineering Handbook. CRC Press LLC, 2000.pp.

20. Hench LL, Polak JM. Third-generation biomedical materials. Science 2002; 295: 1014.

21. Kim S-S, Park MS, Jeon O, Choi CY, Kim B-S. Poly(lactide-coglycolide)/ hydroxyapatite composite scaffolds for bone tissue engineering. Biomaterials 2006; 27: 1399.

22. Zhang R, Ma PX. Poly(α-hydroxyl acids)/hydroxyapatite porous composites for bone-tissue engineering. I. Preparation and morphology. Journal of Biomedical Materials Research 1999; 44: 446.

23. Rezwan K, Chen QZ, Blacker JJ, Boccaccini AR. Biodegradable and bioactive porous polymer/inorganic composite scaffolds for bone tissue engineering. Biomaterials 2006; 27: 3413.

24. Ikada Y. Tissue engineering: fundamentals and applications. Elsevier Academic Press; 2006.

25. Caterson EJ, Nesti LJ, Li W-J, Danielson KG, Albert TJ, Vaccaro AR, Tuan RS. Three-dimensional cartilage formation by bone marrow-derived cells seeded in polylactide/alginate amalgam. Journal of Biomedical Materials Research 2001; 57: 394.

25. Zhang Y, Zhang M. Synthesis and characterization of macroporous chitosan/calcium phosphate composite scaffolds for tissue engineering. Journal of Biomedical Materials Research 2001; 55: 304.

26. Kim H-W, Kim H-E, Salih V. Stimulation of osteoblast responses to biomimetic nanocomposites of gelatin-hydroxyapatite for tissue engineering scaffolds. Biomaterials 2005; 26: 5221.

27. Chen G, Sato T, Ushida T, Hirochika R, Shirasaki Y, Ochiai N, Tateishi T. The use of a novel PLGA fiber/collagen composite web as a scaffold for engineering of articular cartilage tissue with adjustable thikness. Journal of Biomedical Materials Research 2003; 67: 1170.

28. Sarasam AR, Samli AI, Hess L, IHnat MA, Madihally SV. Blending chitosan with polycaprolactone: porous scaffolds and toxicity. Macromolecular Bioscience 2007; 7: 1160.

29. Agrawal CM, Ray RB. Biodegradable polymeric scaffolds for musculoskeletal tissue engineering. Journal of Biomedical Materials Research 2001; 55: 141.

30. Seal BL, Otero TC, Panitch A. Polymeric biomaterials for tissue and organ regeneration. Materials Science and Engineering R 2001; 34: 147.

31. Agrawal CM, Athanasiou KA. Technique to control pH in vicinity of biodegrading PLA-PGA implants. Journal of Biomedical Materials Research 1997; 38: 105.

32. Morita S-I and Ikada Y. Lactide copolymers for scaffolds in tissue engineering.In:Tissue engineering and biodegradable equivalents: scientific and clinical applications. 2002.pp. 111-122.

33. Athanasiou KA, Agrawal CM, Barber FA, Burkhart SS. Orthopaedic applications for PLA-PGA biodegradable polymers. Arthroscopy: The Journal of Arthroscopy and Related Surgery 1998; 14: 726.

34. Gilding DK, Reed AM. Biodegradable polymers for use in surgery--polyglycolic/poly(actic acid) homo- and copolymers. Polymer 1979; 20: 1459.

35. Li S. Hydrolytic degradation characteristics of aliphatic polyesters derived from lactic and glycolic acid. Journal of Biomedical Materials Research 1999; 48: 342.

36. Vert M, Garreau H, Maudit J, Boustta M, Schwach G, Engel R, Coudane J. Complexity of the hydrolitic degradation of aliphatic polyesters. Die Angew Makrom Chem 1997; 247: 239.

37. Li S, Garreau H, Vert M. Structure-property relationships in the case of the degradation of massive aliphatic poly-(α-hydroxy acids) in aqueous media, part 2:degradation of lactide-glycolide copolymers: PLA37.5GA25 and PLA75GA25. Journal of Materials Science: Materials in Medicine 1990; 1: 131.

38. Miller RA, Brady JM, Cutright DE. Degradation rate of oral resorbable implants (polylactate and polyglycolate): rate modification with changes in PLA/PGA copolymer ratios. Journal of Biomedical Materials Research 1977; 11: 711.

39. De Groot JH, Zijlstra FM, Kuipers HW, Pennings AJ, Klompmaker J, Veth RPH, Jansen HWB. Meniscal tissue regeneration in porous 50/50 copoly(L-lactide/ε-caprolactone) implants. Biomaterials 1997; 18: 613.

40. Xu CY, Inai R, Kotaki M, Ramakrishna S. Aligned biodegradable nanofibrous structure: a potential scaffold for blood vessel engineering. Biomaterials 2004; 25: 877.

41. Mo XM, Xu CY, Kotaki M, Ramakrishna S. Electrospun P(LLA-CL) nanofiber: a biomimetic extracellular matrix for smooth muscle cell and endothelial cell proliferation. Biomaterials 2004; 25: 1883.

42. Welle A, Kroger M, Doring M, Niederer K, Pindel E, Chronakis IS. Electrospun aliphatic polycarbonates as tailored tissue scaffold materials. Biomaterials 2007; 28: 2211.

43. Mukherjee DP, Smith DF, Rogers SH, Emmanual JE, Jadin KD, Hayes BK. Effect of 3D-microstructure of bioabsorbable PGA:TMC scaffolds on the growth of chondrogenic cell. Journal of Biomedical Materials Research Part B: Applied Biomaterilas 2009; 88B: 92.

44. Vinoy T, Zhang X, Catledge SA, Vohra YK. Functionally graded electrospun scaffolds with tunable mechanical properties for vascular tissue regeneration. Biomedical Materials 2007; 2: 224.

45. Pego AP, Siebum B, Luyn V, Gallego XJ, Seijen YV, Poot AA, Grijpma DW, Feijen J. Preparation of degradable porous structures based on 1,3-trimethylene carbonate and D,L-lactide (co)polymers for heart tissue engineering. Tissue Engineering 2003; 9: 981.

46. Pego AP, Poot AA, Grijpma DW, Feijen J. Biodegradable elastomeric scaffolds for soft tissue engineering. Journal of Controlled Release 2003; 87: 69.

47. Plikk P, Malberg S, Albertsson A-C. Design of resorbable porous tubular copolyester scaffolds for use in nerve regeneration. Biomacromolecules 2009; 10:1259.

48. Martina M, Hutmacher DW. Biodegradable polymers applied in tissue engineering research: a review. Polymer International 2007; 56: 145.

49. Ambrosio AMA, Allcock HR, Katti DS, Laurencin CT. Degradable polyphosphazene/poly(¬-hydroxyester) blends: degradation studies. Biomaterials 2002; 23: 1667.

50. Allcock HR, Fuller TJ, Matsumura K. Hydrolysis pathways for amminophosphazenes. Inorganic Chemistry 1982; 21: 515.

51. Laurencin CT, El-Amin SF, Ibim SE, Willoughby DA, Attawia M, Allcock HR, Ambrosio AMA. A highly porous 3-dimensional polyphosphazene polymer matrix for skeletal tissue regeneration. Journal of Biomedical Materials Research 1996; 30: 133.

52. Conconi MT, Lora S, Baiguera S, Boscolo E, Folin M, Scienza R, Rebuffat P, Parnigotto PP, Nussdorfer GG. In vitro culture of rat neuromicrovascular endothelial cells on polymeric scaffolds. Journal of Biomedical Materials Research 2004; 71A: 669.

53. Ambrosio AMA, Sahota JS, Runge C, Kurtz SM, Lakshmi S, Allcock HR, Laurencin CT. Novel polyphosphazene-hydroxyapatite composites as biomaterials. IEEE Engineering in Medicine and Biology magazine 2003; Sept/Osc: 18.

54. Temenoff JS, Mikos AG. Injectable biodegradable materials for orthopedic tissue engineering. Biomaterials 2000; 21: 2405.

55. Payne RG, McGonigle JS, Yaszemski Mj, Yasko AW, Mikos AG. Development of an injectable, in situ crosslinkable, degradable polymeric carrier for osteogenic cell populations. Part 3. Proliferation and differentiation of encapsulated marrow stromal osteoblasts cultured on crosslinking poly(propylene fumarate). Biomaterials 2002; 23: 4381.

56. Yaszemski Mj, Payne RG, Hayes WC, Langer R, Aufdemorte TB, Mikos AG. The ingrowth of new bone tissue and initial mechanical properties of a degrading polymeric composite scaffold. Tissue Engineering 1995; 1: 41.

57. Appel, E. A.; Del Barrio, J.; Loh, X. J.; Scherman, O. A., Supramolecular polymeric hydrogels. Chemical Society Reviews 2012, 41, 6195-6214.

57. JagurüGrodzinski, J., Polymeric gels and hydrogels for biomedical and pharmaceutical applications. Polymers for Advanced Technologies 2010, 21, (1), 27-47.

58. Tan, H.; Chu, C. R.; Payne, K. A.; Marra, K. G., Injectable in situ forming biodegradable chitosanhyaluronic acid based hydrogels for cartilage tissue engineering. Biomaterials 2009, 30, (13), 2499-2506.

59. Jin, R.; Teixeira, L.; Dijkstra, P.; Karperien, M.; Van Blitterswijk, C.; Zhong, Z.; Feijen, J., Injectable chitosan-based hydrogels for cartilage tissue engineering. Biomaterials 2009, 30, (13), 2544-2551.

60. Ma, G.; Yang, D.; Li, Q.; Wang, K.; Chen, B.; Kennedy, J. F.; Nie, J., Injectable hydrogels based on chitosan derivative/polyethylene glycol dimethacrylate/N, N-dimethylacrylamide as bone tissue engineering matrix. Carbohydrate Polymers 2010, 79, (3), 620-627.

61. Santo, V. E.; Frias, A. M.; Carida, M.; Cancedda, R.; Gomes, M. E.; Mano, J. F.; Reis, R. L., Carrageenan-based hydrogels for the controlled delivery of PDGF-BB in bone tissue engineering applications. Biomacromolecules 2009, 10, (6), 1392-1401.

62. Möller, S.; Weisser, J.; Bischoff, S.; Schnabelrauch, M., Dextran and hyaluronan methacrylate based hydrogels as matrices for soft tissue reconstruction. Biomolecular Engineering 2007, 24, (5), 496-504.

63. Brandl, F. P.; Seitz, A. K.; Teßmar, J. K. V.; Blunk, T.; Göpferich, A. M., Enzymatically degradable poly (ethylene glycol) based hydrogels for adipose tissue engineering. Biomaterials 2010, 31, (14), 3957-3966.

64. Chaterji, S.; Kwon, I. K.; Park, K., Smart polymeric gels: redefining the limits of biomedical devices. Progress in Polymer Science 2007, 32, (8), 1083-1122.

65. Zhang, Z.; Chen, L.; Deng, M.; Bai, Y.; Chen, X.; Jing, X., Biodegradable thermo- and pH-responsive hydrogels for oral drug delivery. Journal of Polymer Science Part A: Polymer Chemistry 2011, 49, (13), 2941- 2951.

66. Don, T. M.; Huang, M. L.; Chiu, A. C.; Kuo, K. H.; Chiu, W. Y.; Chiu, L. H., Preparation of thermoresponsive acrylic hydrogels useful for the application in transdermal drug delivery systems. Materials Chemistry and Physics 2008, 107, (2-3), 266-273.

67. Cassano, R.; Trombino, S.; Muzzalupo, R.; Tavano, L.; Picci, N., A novel dextran hydrogel linking trans-ferulic acid for the stabilization and transdermal delivery of vitamin E. European Journal of Pharmaceutics and Biopharmaceutics 2009, 72, (1), 232-238.

68. Prinderre, P.; Sauzet, C.; Fuxen, C., Advances in gastro retentive drug-delivery systems. Expert Opinion on Drug Delivery 2011, 8, (9), 1189-1203.

69. Park, H.; Park, K.; Kim, D., Preparation and swelling behavior of chitosan-based superporoushydrogels for gastric retention application. Journal of Biomedical Materials Research Part A 2006, 76, (1), 144-150.

70. Anumolu, S. N. S.; Singh, Y.; Gao, D.; Stein, S.; Sinko, P. J., Design and evaluation of novel fast forming pilocarpine-loaded ocular hydrogels for sustained pharmacological response. Journal of Controlled Release 2009, 137, (2), 152-159.

71. Alsarra, I. A.; Hamed, A. Y.; Mahrous, G. M.; El Maghraby, G. M.; Al-Robayan, A. A.; Alanazi, F. K., Mucoadhesive polymeric hydrogels for nasal delivery of acyclovir. Drug Development and Industrial Pharmacy 2009, 35, (3), 352-362.

72. Luppi, B.; Bigucci, F.; Cerchiara, T.; Zecchi, V., Chitosan-based hydrogels for nasal drug delivery: from inserts to nanoparticles. Expert Opinion on Drug Delivery 2010, 7, (7), 811-828.

73. Araújo Pereira, R. R.; Bruschi, M. L., Vaginal mucoadhesive drug delivery systems. Drug Development and Industrial Pharmacy 2011, 38, (6), 643-652.

74. Lin, C.-C. and A.T. Metters, Hydrogels in controlled release formulations: Network design and mathematical modeling. Advanced Drug Delivery Reviews, 2006. 58(12-13): p. 1379-1408.

75. Peppas, N.A., et al., Hydrogels in pharmaceutical formulations. European Journal of Pharmaceutics and Biopharmaceutics, 2000. 50(1): p. 27-46.

76. Peppas, N.A. and A.R. Khare, Preparation, structure and diffusional behavior of hydrogels in controlled release. Advanced Drug Delivery Reviews, 1993. 11(1-2): p. 1-35.

77. Ji, H., et al., Kinetics of thermally induced swelling of hydrogels. International Journal of Solids and Structures, 2006. 43(7-8): p. 1878-1907.

78. Dolbow, J., E. Fried, and H. Ji, A numerical strategy for investigating the kinetic response of stimulus-responsive hydrogels. Computer Methods in Applied Mechanics and Engineering, 2005. 194(42-44): p. 4447-4480.

79. Maitra J.; Shulka V.K., Cross-linking in hydrogels- A review. American Journal of Polymer Science 2014; 4(2)

80. ASTM F2150-07. Standard guide for characterization and testing of biomaterial scaffolds used in tissue-engineered medical products, 2007.

81. Salgado AJ, Coutinho OP, Reis RL. Bone tissue engineering: state of the art and future trends. Macromolecular Bioscience 2004; 4: 743.

82. Ma PX. Scaffolds for tissue fabrication. Materials Today 2004; 7: 30.

83. Yoon DM and Fisher JP. Polymeric scaffolds for tissue engineering applications. In: Fisher JP, Mikos AG, Bronzino JD editors. Tissue engineering. CRC Press: Taylor & Francis Group, 2007.pp. 8-1-8-18.

84. Karande TS and Agrawal CM. Functions and requirments of synthetic scaffolds in tissue engineering. In: Laurencin CT and Nair LS editors. Nanotechnology and tissue engineering: the scaffold. CRC Press, Taylor & Frencis Group, 2008.pp. 53-86.

85. Muschler GF, Nakamoto C, Griffith LG. Engineering principles of clinical cellbased tissue engineering. The Journal of Bone and Joint Surgery 2004; 86-A: 1541.

86. Vert M, Li SM, Spenlehauer G, Guerin P. Bioresorbability and biocompatibility of aliphatic polyesters. Journal of Materials Science: Materials in Medicine 1992; 3: 432.

87. Hutmacher DW. Scaffolds in tissue engineering bone and cartilage. Biomaterials 2000; 21: 2529.

88. MUschler GF, Nakamoto C, Griffith LG. Engineering principles of clinical cell based tissue engineering. The Journal of Bone and Joint Surgery 2004; 86-A:1541.

89. Van der Flier A, Sonnenberg A. Function and interactions of integrins. Cell and Tissue Research 2001; 305: 285.

90. Plow EF, Haas TA, Zhang L, Loftus J, Smith JW. Ligand binding to integrins. The Journal of Biological Chemistry 2000; 275: 21785.

91. Saltzman WM and Kyriakides TR. Cell interactions with polymers. In:Lanza R, Langer R, Vacanti J editors. Principles of Tissue Engineering. Elsevier Academic Press, 2007.pp. 279-296.

92. Jiao Y-P, Cui F-Z. Surface modification of polyester biomaterials for tissue engineering. Biomedical Materials 2007; 2: R24.

93. Karande TS, Ong JL, Agrawal CM. Diffusion in musculoskeletal tissue engineering scaffolds: design issues related to porosity, permeability, architecture, and nutrient mixing. Annals of Biomedical Engineering 2004; 32: 1728.

94. Kim B-S, Mooney DJ. Development of biocompatible synthetic extracellular matrices for tissue engineering. Trends in Biotechnology 1998; 16: 224.

95. Salem, A. K. et al. Interactions of 3T3 fibroblasts and endothelial cells with defined pore features. Journal of Biomedical Materials Research 61, 212-217 (2002).

96. Zeltinger, J., Sherwood, J. K., Graham, D. A., Mueller, R. & Griffith, L. G. Effect of Pore Size and Void Fraction on Cellular Adhesion, Proliferation, and Matrix Deposition. Tissue Engineering 7, 557-572 (2001).

97. Mikos AG, Thorsen AJ, Czerwonka LA, Bao Y, Langer R, Winslow DN, Vacanti JP. Preparation and characterization of poly(-lactic acid) foams. Polymer 1994; 35: 1068.

98. Holy CE, Dang SM, Davies JE, Shoichet MS. In vitro degradation of a novel poly(lactide-co-glycolide) 75/25 foam. Biomaterials 1999; 20: 1177.

99. Suh SW, Shin YJ, Kim J, Min CH, Beak CH, Kim D-I, Kim H, Jeon SS, Choo IW. Effect of different particles on cell proliferation in polymer scaffolds using a solvent-casting and particulate leaching technique. ASAIO Journal 2002; 48: 460.

100. Wake MC, Gupta PK, Mikos AG. Fabrication of pliable biodegradable polymer foams to engineer soft tissues. Cell Transplantation 1996; 5: 465.

101. Whang K, Thomas H, Healy KE, Nuber G. A novel method to fabricate bioabsorbable scaffolds. Polymer 1995; 36: 837.

102. Subia B, Kundu J and Kundu SC, Biomaterial scaffold fabrication techniques for potential tissue engineering applications, in Tissue Engineering, ed. by Eberli D. InTech, Vukovar, pp. 141–158 (2010).

103. Shen F, Cui YL, Yang LF, Yao KD, Dong XH, Jia WY, Shi HD. A study on the fabrication of porous chitosan/gelatin network scaffold for tissue engineering. Polymer International 2000; 49: 1596.

104. Hou Q, Grijpma DW, Feijen J. Preparation of interconnected highly porous polymeric structures by a replication and freeze-drying process. Journal of Biomedical Materials Research Part B: Applied Biomaterilas 2003; 67B: 732.

105. Ho M-H, Kuo P-Y, Hsieh H-J, Hsien T-Y, Hou L-T, Lai J-Y, Wang D-M. Preparation of porous scaffolds by using freeze-extraction and freeze-gelation methods. Biomaterials 2004; 25: 129.

106. Y.S. Nam, T.G. Park, Porous biodegradable polymeric scaffolds prepared by thermally induced phase separation, J. Biomed. Mater. Res. 47 (1999) 8–17.

107. Y.S. Nam, T.G. Park, Biodegradable polymeric microcellular foams by modified thermally induced phase separation method, Biomaterials20 (1999) 1783–1790

108. Schugens C, Maquet V, Grandfils C, Jerome R, Teyssie P. Polylactide macroporous biodegradable implants for cell transplantation. II. Preparation of polylactide foams by liquid-liquid phase separation. Journal of Biomedical Materials Research 1996; 30: 449.

109. Nam YS, Park TG. Porous biodegradable polymeric scaffolds prepared by thermally induced phase separation. Journal of Biomedical Materials Research 1999; 47: 8.

110. Nam YS, Park TG. Biodegradable polymeric microcellular foams by modified thermally induced phase separation method. Biomaterials 1999; 20: 1783.

111. Leong KF, Cheah CM, Chua CK. Solid freeform fabrication of threedimensional scaffolds for engineering replacement tissues and organs. Biomaterials 2003; 24: 2363.

112. Hollister SJ. Porous scaffold design for tissue engineering. Nature Materials2005; 4: 518.

113. Yan Y, Xiong Z, Hu Y, Wang S, Zhang R, Zhang C. Layered manufacturing of tissue engineering scaffolds via multi-nozzle deposition. Materials Letters 2003; 57: 2623.

114. Hutmacher DW, Sittinger M, Risbud MV. Scaffold-based tissue engineering: rationale for computer-aided design and solid free-form fabrication systems. Trends in Biotechnology 2004; 22: 354.

115. Goel SK, Beckman EJ. Generation of microcellular polymeric foams using supercritical carbon dioxide. I: effect of pressure and temperature on nucleation. Polymer Engineering and Science 1994; 34: 1137.

116. Arora KA, Lesser AJ, McCarthy TJ. Preparation and characterization of microcellular polystyrene foams processed in supercritical carbon dioxide. Macromolecules 1998; 31: 4614.

117. Colton JS, Suh NP. The nucleation of microcellular thermoplastic foam with additives part I: theoretical considerations. Polymer Engineering and Science 1987; 27: 485.

118. Kumar V, Suh NP. A process for making microcellular thermoplastic parts. Polymer Engineering and Science 1990; 30: 1323.

119. Mooney DJ, Baldwin DF, Suh NP, Vacanti JP, Langer R. Novel approach to fabricate porous sponges of poly(D,L-lactic-co-glycolic acid) without the use of organic solvents. Biomaterials 1996; 17: 1417.

120. Woods HM, Silva MCG, Nouvel C, Shakesheff KM, Howdle SM. Materials processing in supercritical carbon dioxide: surfactants, polymers and biomaterials. Journal of Materials Chemistry 2004; 14: 1663.

121. Quirk RA, France RM, Shakesheff KM, Howdle SM. Supercritical fluid technologies and tissue engineering scaffolds. Current Opinion in Solid State andMaterials Science 2004; 8: 313.

122. Tomasko DL, Li H, Liu D, Han X, Wingert MJ, Lee LJ, Koelling KW. A review of CO_2 applications in the processing of polymers. Industrial and Engineering Chemical Research 2003; 42: 6431.

123. Kazarian SG. Polymer processing with supercritical fluids. Polymer Science, Ser C 2000; 42: 78.

124. Barry JJA, Silva MMCG, Popov VK, Shakesheff KM, Howdle SM. Supercritical carbon dioxide: putting the fizz into biomaterials. Philosophical Transactions of the Royal Society A 2006; 364: 249.

125. Goel SK, Beckman EJ. Generation of microcellular polymeric foams using supercritical carbon dioxide. II: cell growth and skin formation. Polymer Engineering and Science 1994; 34: 1148.

126. Murphy WL, Dennis RG, Kileny JL, Mooney DJ. Salt fusion: an approach to improve pore interconnectivity within tissue engineering scaffolds. Tissue Engineering 2002; 8: 43.

127. Tai H, Mather ML, Howard D, Wang W, White LJ, Crowe JA, Morgan SP, Williams DJ, Howdle SM, Shakesheff KM. Control of pore size and structure of tissue engineering scaffolds produced by supercritical fluid processing. European Cells and Materials 2007; 14: 64.

128. Barry JJA, Gidda HS, Scotchford CA, Howdle SM. Porous methacrylate scaffolds: supercritical fluid fabrication and in vitro chondrocyte responses. Biomaterials 2004; 25: 3559.

129. Rogers CM, Morris GE, Gould T.W., Bail R., Toumpaniari S., Harrington H., Dixon JE, Shakesheff K.M., A novel technique for the production ofelectrospun scaffolds with tailored three-dimensional micro-patterns employing additive manufacturing. Biofabrication 6 (2014) 035003.

130. Ciach, T., K.B. Geerse, and J.C.M. Marijnissen. Chapter in the book: Nanostructured materials, Application of electrospray in nanoparticle production. Eds P. Knauth, and J. Shoonman.Kluwer Academic Publishers, 2002.

131. Lavik, E., and R. Langer. "Tissue engineering: current state and perspectives." Applied Microbiology and Biotechnology 65 (2004): 1–8.

132. Xu, C.Y., et al. "Aligned biodegradable nanofibrous structure: a potential scaffold for blood vessel engineering." Biomaterials 25 (2004): 877–886.

133. Yang, F., et al. "Electrospinning of nano/micro scale poly(Llactic acid) aligned fibres and their potential in neural tissue engineering." Biomaterials 26 (2005): 2603–2610.

3 Investigation Methods

In this chapter, five main techniques for matrices structure characterization were presented. The first one is the Nuclear Magnetic Resonance (NMR), in particular the *low field NMR analysis*, that allows the investigation of microscopic matrices characteristics. The second one is the *Rheology* that, instead, allows to study the effect of the matrices structure on the macroscopic and mechanical behavior. The third one is called *Cryoporosimetry*, an indirect method for the determination of pore size and shape in matrices. Last, but not least, two other methods were described for the structural characterization of polymeric matrices. They are the *Scanning Electron Microscope* and the *Micro Computed Tomography*. In the following sections it is explained how it is possible to adapt this technique also for the estimation of the matrices mesh size.

3.1 Nuclear Magnetic Resonance (NMR) spectroscopy

The physical principles of the Nuclear Magnetic Resonance (NMR) spectroscopy, are based on the magnetic properties of the atomic nuclei [**1**]. According to the quantum mechanics rules, the interaction of the magnetic moment of an atomic nucleus with an external magnetic field (B_0) separates the nuclear energetic levels. The energetic levels separation happens because, the nuclear magnetic energy is restricted to discrete values E_p called *autovalues*.

The autovalues are associated to the autostates, also called steady states that are the only possible existing states of an elementary particle. Irradiating the nucleolus with an electromagnetic radiation of appropriate frequency, it is possible to induce a transition within steady stated and the energetic abortion could be detected by the instrument and registered as a signal on a spectrum. With this method it is possible to obtain the spectrum of a compound that contains atoms with nuclear magnetic moment different from zero. The most analyzed nuclei are the protons (^{1}H), fluorine (^{19}F), the isotopes ^{14}N and ^{15}N of the nitrogen and the isotope ^{13}C of carbon [**1**].

3.1.1 NMR principles

3.1.1.1 Quantum mechanics model for an isolated nucleus

Many atomic nuclei have an angular moment (*P*) that is responsible for the exhibition of a magnetic moment (μ) [**2**]. The relation within *P* and μ is expressed by the following equation:

$$\mu = \gamma P \tag{3.1}$$

Where γ is the gyromagnetic ratio, a characteristic of the specific nucleus. For the Quantum theory, the angular moment and the magnetic moment are quantized, a fact that is not explained by classical physics. The allowed autovalues of the angular moment maximum component in the z direction in an arbitrary cartesian system, are defined by the relation:

$$P_z = \frac{h}{2\pi} m_I \tag{3.2}$$

Where m_I is the *magnetic quantum number* of the correspondent nucleus steady states and *h* is the *Plank constant*. According to the quantistic condition, the magnetic quantum numbers m_I are related to *nuclear spin quantum number* (*I*) and can assume a integer number within +I and –I.

Therefore, the number of steady states or possible energy levels is:

$$\text{Number of possible energy levels} = 2I + 1 \tag{3.3}$$

For the proton (^{1}H nucleus), the nuclear spin quantum number is $I = {}^1/_2$ and the regular moment z component becomes:

$$P_z = \pm \frac{h}{2\pi} I \tag{3.4}$$

In consequence of I, the proton can exist in only two spin state with a magnetic quantum number respectively of $m_I = +{}^1/_2$ and $m_I = -{}^1/_2$. The magnetic moment in the z direction is:

$$\mu_z = \gamma \frac{h}{2\pi} m_I = \pm \gamma \frac{h}{4\pi} \tag{3.5}$$

The proton therefore, can be represented as a magnetic dipole where μ_z is parallel or anti-parallel to the positive direction of z axes in the cartesian coordinates and the direction of μ vector is quantified (*Fig. 3.1a*). In normal situation, without an orienting system, the two states have the same energy and are so called degenerated. In presence of an external magnetic field B_0, the interaction with μ causes an energetic differentiation of the two

states. If B_0 is parallel to z axes, the energy of a magnetic dipole is $+\mu_0 B_0$ when the dipole is oriented in the same direction of B_0, while it is $-\mu_{0B_0}$, when it is oriented in opposite direction (*Fig. 3.1b*).

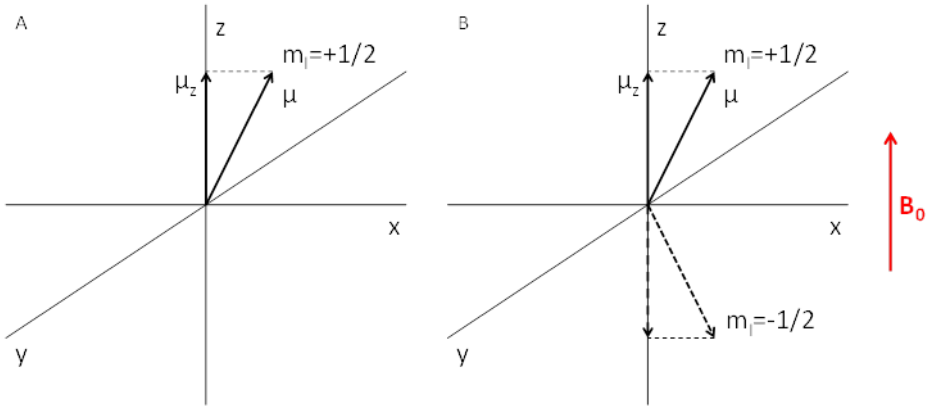

Figure 3.1: The quantified magnetic moment μ vector direction in absence (**a**) or in presence (**b**)of an external magnetic field B_0.

Therefore, the energy difference within the two spin states is proportional to the intensity applied magnetic field B_0 (*Fig. 3.2*) with the relation:

$$\Delta E = 2\mu_z B_0 \qquad (3.6)$$

The lower energy state $m_I = +{}^1/_2$ is more stable and to induce the transition to the higher energy level a quantum of energy corresponding to ΔE is required.

$$\Delta E = h\nu_o = 2\mu_z B_o = \gamma \frac{h}{2\pi} B_o \qquad (3.7)$$

In other terms, the nucleus must be irradiated with a frequency equal to:

$$\nu_0 = \frac{\gamma B_0}{2\pi} \qquad (3.8)$$

Or, considering $\omega_0 = 2\pi\nu_0$, the expression (3.8) can be written as:

$$\omega_0 = \gamma B_0 \qquad (3.9)$$

This equation expresses the resonance condition when the radiations frequency is equal to ΔE within the two states. In the equation (3.8), ν_0 (in Hertz; Hz= cycle sec $^{-1}$) or ω_0 (rad sec $^{-1}$) is the Larmor frequency and depends linearly on the applied B_0 intensity. For example, the proton has a giromagnetic ratio γH= 2,675x108 T $^{-1}$ sec $^{-1}$. In a magnetic fields of 1,41 T, the Larmor frequency is 60 MHz (λ= 5 meters, in the region of radio wave). *Figure 3.3* shows different ν_0 values as function of imposed magnetic field [**3**].

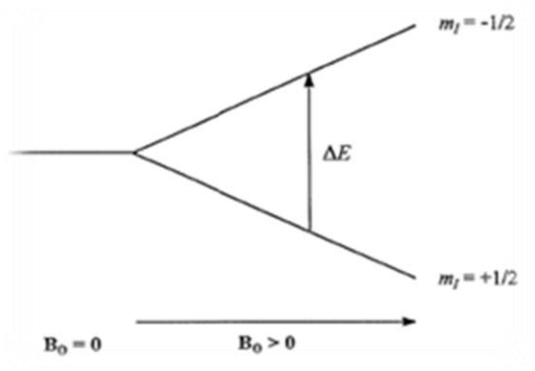

Figure 3.2: energetic separation with ΔE within two state proportional to the applied magnetic field B_0.

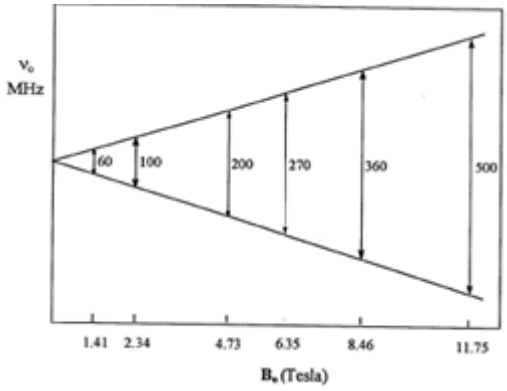

Figure 3.3: nuclear energetic separation levels (expressed as resonance frequency ν_0) in functions of magnetic field B_0 (in Tesla)

For systems with I=1, the quantum mechanics treatment gives a result not expected by the classical physics. The magnetic quantum number mI can be -1, 0, +1 so that, only closer levels transition are allowed. For example, for I=1 three levels are possible with mI equal to -1, 0 and +1 respectively and the possible level transitions are mI= +1 ↔ mI=0 and mI=0 ↔ mI=-1; energy levels transitions within mI=+1 ↔ mI=-1 are not allowed (*Fig. 3.4*).

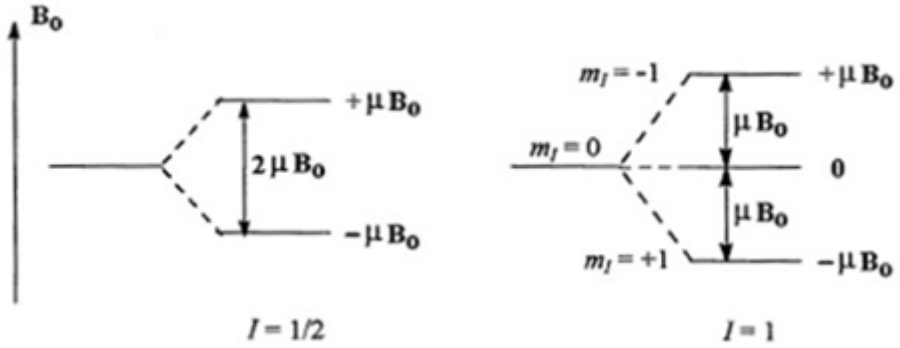

Figure 3.4: on the left, separation in two energetic levels of a nucleus with spin quantum number I=1/2 in a magnetic field B_0, on the right, separation in three energetic levels of a nucleus with I=1.

From above considerations, the nuclear magnetic moment can be expressed as a function of the gyromagnetic ratio:

$$\gamma = \frac{2\pi\mu}{Ih} \tag{3.10}$$

Moreover, it is possible to demonstrate, for a rotating spherical particle of mass *M* and charge *e* uniformly distributed on the surface, the generation of a magnetic moment defined as:

$$\mu = \frac{eh}{4\pi Mc} \tag{3.11}$$

Where *c* is the light speed. For the proton equation (3.11) became:

$$\mu_N = \frac{eh}{4\pi Mc} = 5{,}0505 \text{ x } 10^{-27} (\text{J T}^{-1}) \tag{3.12}$$

In reality, the value of the proton magnetic moment is about 2,79 times higher than the calculated by using this simplified model. Although a simplified model to explain or predict the nuclear magnetic moment does not exist, the calculated values represent a usefully starting point (μ_N is called *magneton*). For these reasons, the general equation for the nuclear magnetic moment reads:

$$\mu = g_N \frac{ehI}{4\pi Mc} \tag{3.13}$$

Equation (3.13) can be simplified by expressing μ in terms of units of magneton becoming

$$\mu = g_N I \tag{3.14}$$

Where g_N is the *g* nuclear factor, an empiric parameter. In *Table 3.1*, some nuclear magnetic moments expressed in magnetons are reported.

Nucleus	***I***	**μ ($\mu_N$units)**	**γ (10^{-8}rad/Ts)**	**ν_0 (MHz) (field 1 T)**	**Relative sensibility to constant field**	**Isotopes naturally abundance (%)**
^{1}H	1/2	2,79277	2,676	42,577	1,000	99,98
^{2}H	1	0,85735	0,411	6,536	0,009	0,0156
^{10}B	3	1,8007	0,288	4,575	0,02	18,83
^{11}B	3/2	2,6880	0,858	13,660	0,165	81,17
^{13}C	1/2	0,70216	0,673	10,705	0,016	1,108
^{14}N	1	0,40369	0,193	3,076	0,001	99,635
^{15}N	1/2	-0,28298	-0,271	4,315	0,001	0,365
^{17}O	5/2	-1,8930	-0,363	5,772	0,029	0,037
^{19}F	1/2	2,6273	2,517	40,055	0,834	100,0
^{29}Si	1/2	-0,55492	-0,531	8,460	0,079	4,70
^{31}P	1/2	1,1316	1,083	17,235	0,066	100,0

Table 3.1: properties of some nuclei interesting for NMR spettroscopy [**3**].

3.1.1.2 Energy absorption mechanism: the resonance

The nuclei with $I=1/2$, as the protons ^1H, are usually represented as magnetic bar but, because of their spin movement, their behavior is different from that of macroscopic magnetic bar. In a magnetic field, the rotating nucleus does not allaying its magnetic moment to the direction of the field. On the contrary, as a spinning top in the gravitational field, their spin axes assume a precession movement around the magnetic field direction (*Fig. 3.5*). The precession frequency corresponds to the Larmor frequency as seen in equation (3.8) and (3.9), and it could be expressed as ω_0 in (radiants sec-1) or v_0 (Hz) [**1-3**].

An increase in the intensity of the magnetic field, results in a faster precession but, it is possible to modify the orientation of magnetic moment μ by application of a rotating magnetic field (B_1) perpendicular to B_0. When B_1 *rotation frequency* (v_{RF}) has the same value of precession frequency v_0, *resonance* condition is established and the system absorbs energy with a variation of the angle θ within vector μ and the static magnetic field B_0 (*Fig. 3.6*). The process occurs without variation of the precession frequency.

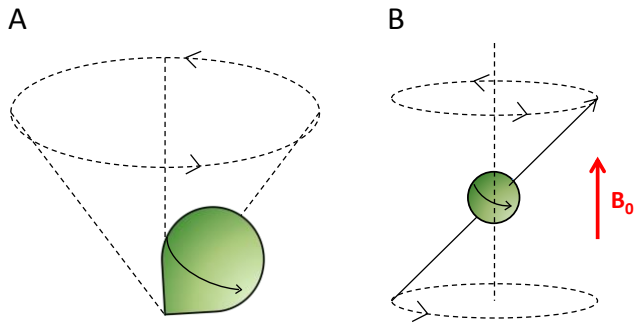

Figure 3.5: as a spinner in the hearth gravitational field **(a),** the nuclear magnetic precess in a magnetic field **(b).**

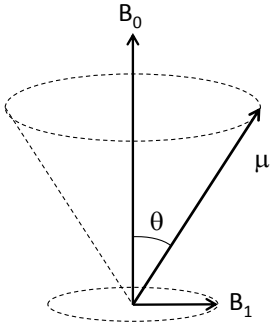

Figure 3.6: the application of arotating magnetic field B_1 perpendicular to B_0 turn the nuclear magnetic moment μ by the angle θ.

3.1.1.3 Macroscopic Magnetization

During an NMR experiment, there is not only one nucleus under examination but a huge amount. Therefore, in order to describe the properties of *nuclear magnetization* (defined as magnetic moment per unit volume), it is possible to apply a simple treatment. The magnetization *M* is a vector that can be divided into three component in the *x*, *y* and z

directions. M_z, is conventionally aligned to the direction of B_0 whereas M_x and M_y, are perpendicular. For a nucleus with I=1/2, all the magnetic moment precess at the same frequency and, because the direction x and y are equivalent, no phase coherence occurs on xy plane and M_{xy}=0. On the contrary, in the z direction, there is a small excess of nuclei parallel to the B_0 direction because the Boltzmann distribution favors the lower energy state. The nuclei populations difference within parallel and antiparallel magnetization, generate a macroscopic net magnetization M_z (*Fig. 3.7a and b*).

$$M_z = \gamma h\,(N_1 - N_2) \qquad (3.15)$$

The application of a radiofrequency (*RF*) field B_1 rotating at the resonance frequency ($\omega_0 = \gamma B_0$; equation 3.9), allows the spin resonance with a modification of the casual orientation in the xy plane and the appearing of a magnetization component $M_{xy} \neq 0$. Spin systems originating net component of the magnetization in the xy plane (M_{xy}) are in phase coherence (*Fig. 3.7c*).

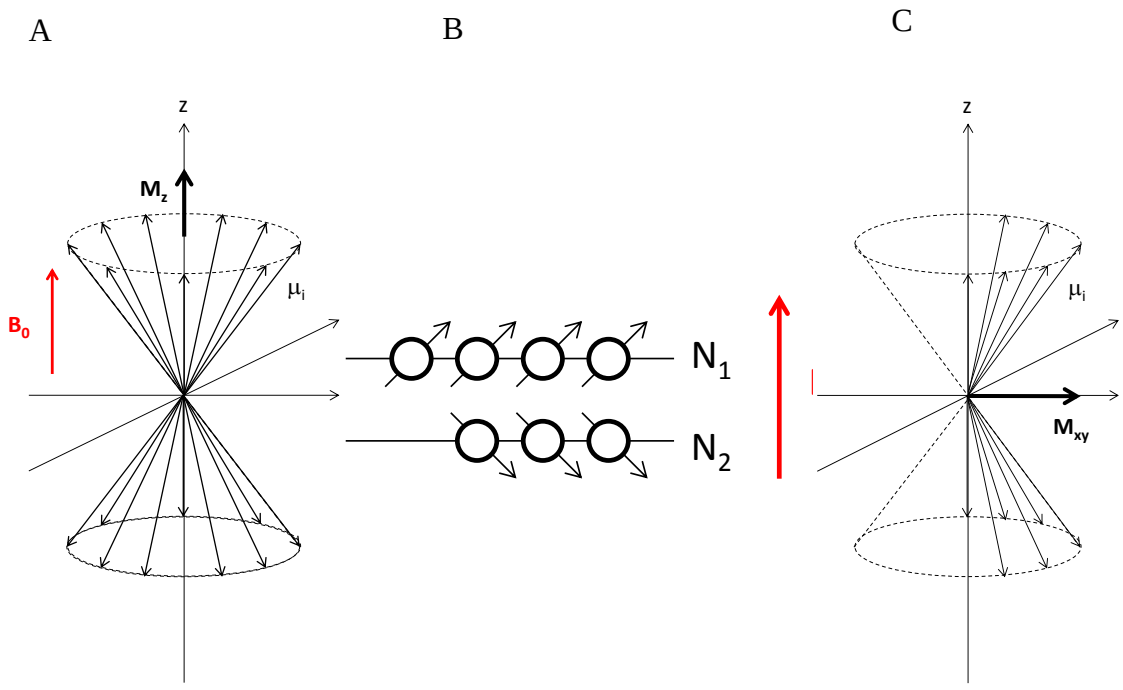

Figure 3.7: (a) Vectorial representation of magnetic moments of I= 1/2 nuclei, following a precess around the z axis (conventionally all vectors have a common origin) with overall magnetization M_z, no magnetization on xy plane M_{xy}. **(b)** Excess of nuclei with magnetic moment aligned with B_0. **(c)** Spin system in phase coherence, $M_{xy} \neq 0$.

3.1.2 The NMR experiments

During an NMR experiment, the sample is subjected to a highly homogeneous static magnetic field B_0. To produce a phase coherence within spins, a rotating magnetic field (B_1) is applied perpendicular to B_0 by a tuned spire allowing the generation M_{xy} magnetization component with a ω_0 precession frequency (resonance frequency) (*Fig. 3.8*). When B_1 is removed, a *relaxation* process causes the loss of phase coherency to the initial equilibrium situation with $M_{xy}=0$. The relaxation process consists in an exponential decay of M_{xy} with a time constant T_2 (*transversal relaxation time* or *spin-spin*). The results of the relaxation is a transient signal, captured by a sensor on *x* axes, with ω_0 frequency and decay speed of $1/T_2$ called Free Induction Decay (*FID*) (*Fig. 3.9a*) [**4**].

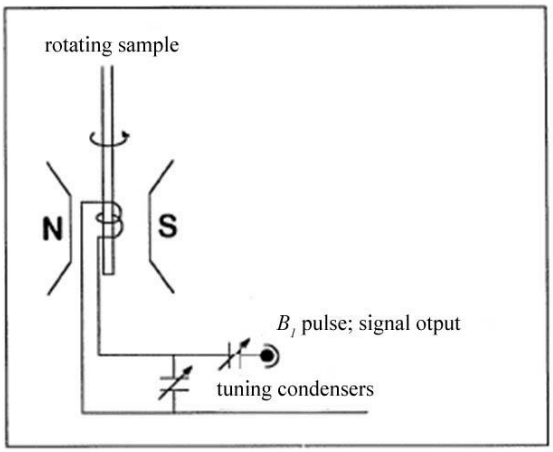

Figure 3.8: Schematic representation of the NMR spectroscope. The sample is positioned within the magnetic field B_0 generated by a magnet (N-S) and surrounded by a spire, tuned on the resonance frequency, that produce the B_1 pulse.

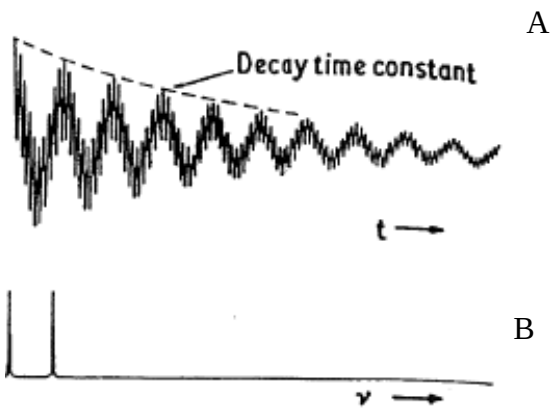

Figure 3.9:
(a) FID of two NMR signal. **(b)** the spectrum obtained applying the Fourier transform to the FID.

The NMR spectral signals are produced by the small displacement of resonance frequency ω_0 in the nuclei population under analysis caused by the physic-chemical environment. When different ω_0 and, as consequence different $1/T_2$ are present, the resulting *FID* is a superimposition of all signals. The complex *FID* originated by multiple signals can be resolved using a mathematical processing known as Fourier Transformation (*FT*) that changes the transient signal in a normal spectrum (*Fig. 3.9b*). Whereas NMR spectrum is a diagram where intensity is a function of frequency, in *FID*, the intensity is a function of time. The time domain and frequency domain is linked by the Fourier Transformation [**4**].

At this stage, it is important the definition of the applied magnetic field pulse B_1 in terms of angle. Similar to the precession in the B_0 field, the precession concept can be extended to B_1 using the expedient of a rotating reference system so B_1 became static. When B_1 is applied, it occurs the situation in *figure 3.10a* where B_1 is aligned to the rotating axes *x* and the equilibrium magnetization M_0, aligned to *z*, precess around B_1. The precession frequency of M_0 is:

$$\boldsymbol{\omega_1 = \gamma B_1} \tag{3.16}$$

ω_1 is an angular frequency (radius sec^{-1}). The M_0 rotation angle is:

$$\theta = \gamma B_1 t_p \tag{3.17}$$

Where t_p is the B_1 pulse application time and γB_1 is the pulse amplitude or power. After a pulse at 90° (or $\pi/2$ in radius), $M_{xy}=M_0$ (*Fig. 3.10b*), while after 180° pulse (or π in radius) $M_z=-M_0$ and $M_{xy}=0$ (*Fig. 3.10c*).

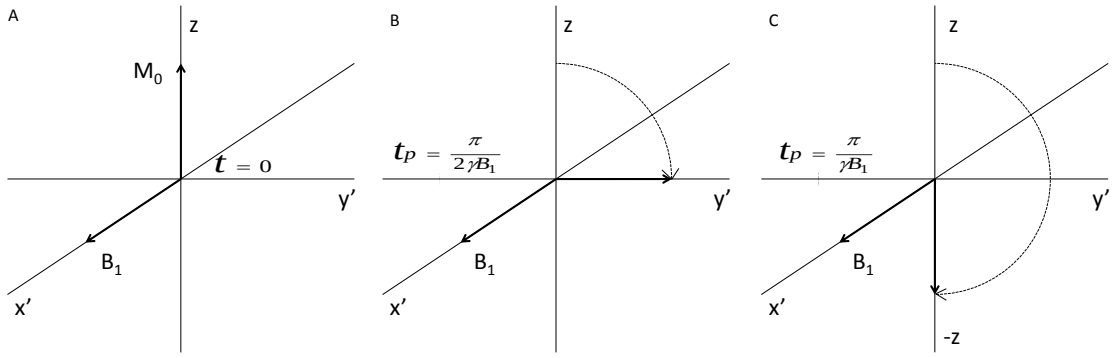

Figure 3.10: effect of the rotating magnetic field B_1 application on the magnetization M_0 (x' and y' belong to a reference system rotating with the same frequency of B_1. **(a)** Time zero; **(b)** after a 90° pulse; **(c)** after 180° pulse.

To evaluate the effect of a radiofrequency pulse on the nuclear levels populations, let's consider a system of two state levels α and β containing *N* nuclei that could be in one state or in the other. For degenerate levels, there should be *N*/2 nuclei in each state but, because the α magnetic moment is oriented parallel to the B_0 field, α has a lower energy compared to β (antiparallel magnetic moment). This energy difference causes a small excess of nuclei in the α state and, defining δ as the excess of nuclei, the number of nuclei in each population can be written as $(N+\delta)/2$ or $(N-\delta)/2$ respectively for α and for β (*Fig. 3.11*).

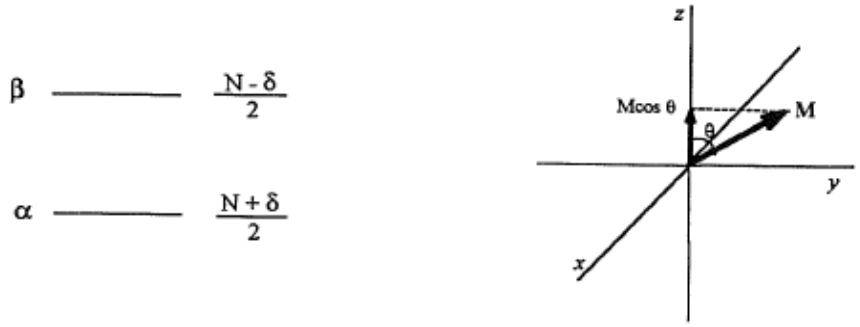

Figure 3.11: on the left, initial number of nuclei in α and β energetic levels population. On the right, the effect on a pulse that rotate the magnetization of an angle θ.

In order to understand what happens to the nuclei populations when the macroscopic magnetization is deflected by an angle θ due to a radiofrequency pulse it is better focusing the attention to the M_z component. On the contrary considering the whole α and β nuclei population, it is better considering the deviation from $N/2$ defined as $P_\alpha = +\delta/2$ and $P_\beta = -\delta/2$.

In every moment, M_z is proportional to the difference within levels:

$$M_z \propto P_\alpha - P_\beta \tag{3.18}$$

Or, it is possible to say that $M_o \propto \delta$. Moreover, it is known that:

$$P_\alpha + P_\beta = 0 \tag{3.19}$$

After the radiofrequency pulse, the M_z magnetization component becomes

$$M_z = M_o \cos\theta \tag{3.20}$$

And, consequently

$$P_\alpha - P_\beta = \delta \cos\theta \tag{3.21}$$

That, combined with equation (3.19), allows to calculate the new population:

$$P_\alpha = \frac{\delta \cos\theta}{2} \tag{3.22}$$

$$P_\beta = \frac{-\delta \cos\theta}{2} \tag{3.23}$$

These equations allow correlating the change occurring to the magnetization for a $\pi/2$ and π pulse. For $\theta = \pi/2$, $\cos\theta = 0$ and no nuclei excess is present in any state and the radiofrequency pulse equals the populations. For $\theta = \pi$, $\cos\theta = -1$ and the populations are inverted [**4**].

Practically, a short, strong and repeated radiofrequency pulse is applied to the nuclei system allowing the simultaneous excitation of nuclei with a Larmor precession v_0 in an interval Δv (*Fig. 3.12*).

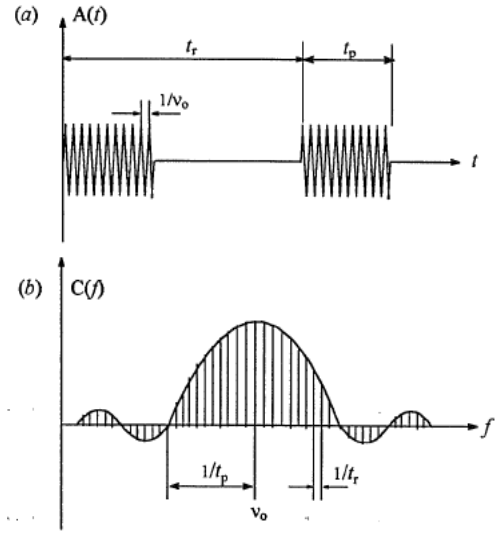

Figure 3.12: (*a*) RF pulse sequence of v_0, duration length t_p, and repetition time t_r. **(*b*)** the correspondent frequency component.

Equation (3.17) relates the deflection angle θ caused by the pulse with the pulse amplitude (or intensity) γB_1 and the pulse time t_p. Both can be modified in order to obtain the desired deflection angle. One of the most important is θ=90° (or $\pi/2$) where all the magnetization is on the *xy* plane and the signal has the maximum intensity (*Fig. 3.10b*). Another is θ=180° (or π). In this case the magnetization is inverted and becomes antiparallel to the *z* axis (*Fig. 3.10c*). Summarizing, the *RF* pulse deflects the vector M_z (same direction of B_0) with a certain angle θ generating the M_{xy} magnetization component. M_{xy} exponentially decay with the time constant T_2 emitting a signal that was detected as an alternate voltage on a receiving spire on the *x* axis. The signal collected is called free induction decay (*FID*). *Figure 3.13* illustrates in details the change of the magnetization during a pulsed NMR experiment in a rotating coordinate system. At the beginning the net magnetization M_o is aligned to the magnetic field B_0 (*Fig. 3.13a*). After application of an *RF* pulse that rotates the magnetization of $\pi/2$ (90°), magnetization vector moves (*Fig. 3.13b*) and, for a pulse of sufficient duration, reaches the final position on the *x'y'* plane, generating the M_{xy} magnetization component (*Fig. 3.13c*). At the end of *RF* pulse (B_1=0), the relaxation process starts and the phase coherency is lost, causing decay of M_{xy} component (*Fig. 3.13d* and *e*). This relaxation process is called *transversal relaxation* or *spin-spin* and it

proceeds with a constant time T_2 by the energy transfer within high energy nuclei without loss of energy [**1-2**].

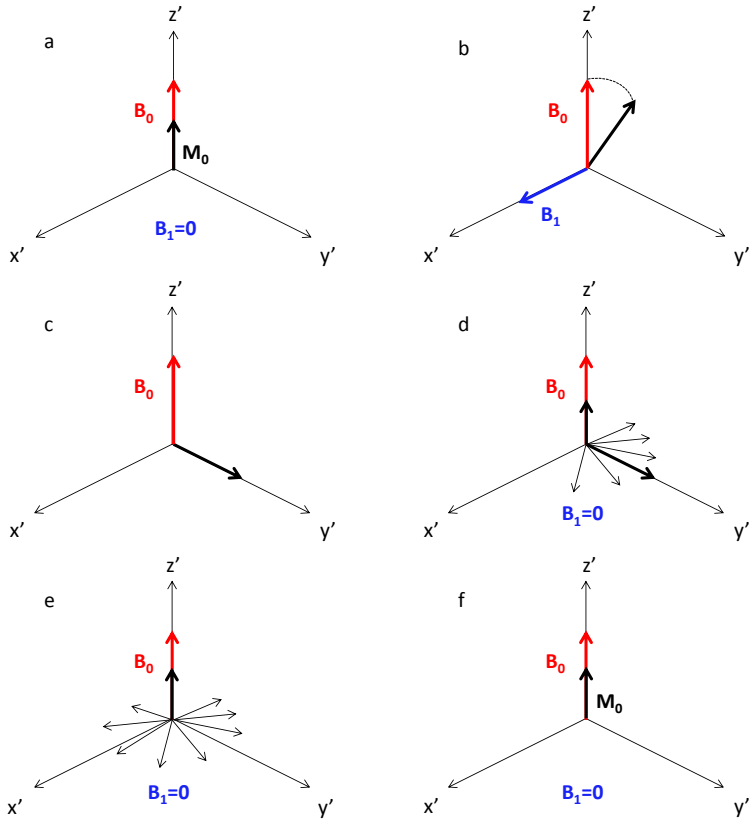

Figure 3.13:diagrams in the rotating coordinate system *x'y'z'* showing the magnetization during an NMR experiment. (***a***) The net magnetization M_0 is aligned to B_0. (***b***) and (***c***) an RF B_1 pulse is applied perpendiculat to B_0; the pulse length is sufficient to rotate the magnetization by 90°. (***d***) and (***e***) after B_1 ceasing, the spins start to relax by a spin-spin mechanism on the *x'y'* plane (time constant T_2) and by a spin-lattice mechanism on the *z'* direction (time constant T_1). (***f***) After sufficient time, the starting equilibrium magnetization M_0 is re-established.

During the transversal relaxation process, the M_{xy} component decay to 0 by the low

$$\frac{dM_{xy}}{dt} = -\frac{M_{xy}}{T_2} \tag{3.24}$$

Or

$$M_{xy} = M_0 \cdot e^{-(t/T_2)} \tag{3.25}$$

The relaxation time T_2 is related to the width of the spectral peak at middle height ($\Delta\nu_{0,5}$) by the equation

$$\Delta\nu_{0.5} = \frac{1}{\pi T_2} \tag{3.26}$$

At the same time, it is possible to observe also the longitudinal component of magnetization M_z that, during relaxation, comes back to the initial equilibrium magnetization M_o (*Fig. 3.13d*, *e* and *f*). This type of relaxation process is known as *longitudinal relaxation* or *spin-lattice* and proceed with a time constant T_1.

$$\frac{dM_z}{dt} = \frac{M_o - M_z}{T_1} \tag{3.27}$$

$$M_z = M_0 \cdot (1 - e^{t/T_1}) \tag{3.28}$$

3.1.3 Low Field NMR

3.1.3.1 Introduction to the Low field NMR

As T_2 and T_1 depend also on the chemical and physical environment embedding the particular nucleus, low field NMR can provide information on the structure of the matter. The technique can be easily applied to solid samples, liquid samples, suspension, gel systems or emulsion as it is not destructive and independent from the color or the surface on the sample. The field of application is between 10 and 65 MHz (corresponding to a magnetic field within 0.23 and 1.53 *T*) and a temperature varying within -10 and +70 °C [**5**].

The shape and amplitude of the resonance signal are related to the physical environment of the nucleus under examination. In particular, the amplitude is function of the nucleolus degrees of freedom movement in the specific physical environment, an useful information in polymer chemistry and solid state physics. From the qualitative side, the transversal relaxation time T_2 depends on the nucleus mobility. In the solids there is a reduced mobility so that T_2 is low (1-100 ms). In case of intermediate mobility, such as gel systems, the T_2 is medium (200-800 ms) and finally, into liquids, nuclei mobility is higher and the T_2 is slower (800-2500 ms).

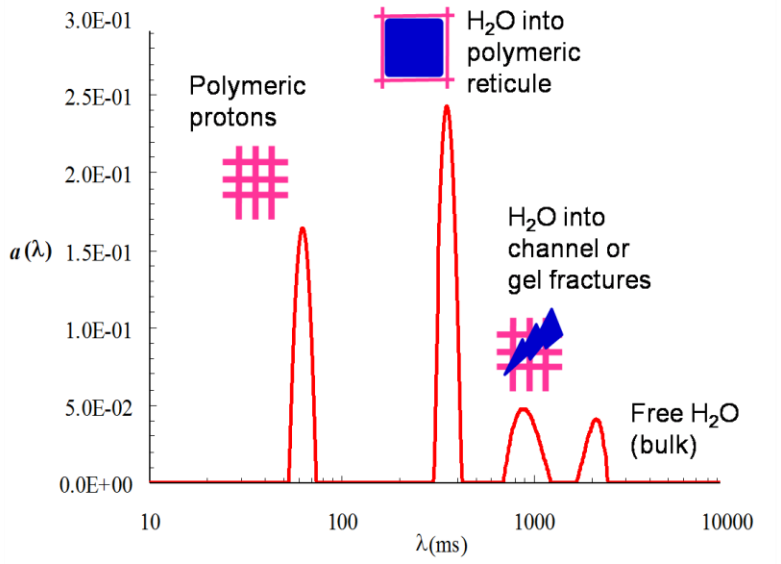

Figure 3.14: Typical example of ^{1}H relaxation spectrum of a not homogeneous hydrogel.

The low field NMR finds applications in many different areas: food science and technology, industrial analysis, pharmaceutics and cosmetics for a fast and non destructive analysis of protonic content in oil and fat, moisture and water content determination in different type of materials. One of the most recent applications is the quantitative analysis of a particular isotope by the integration of peak area under the absorbance signal. For hydrogels analysis, the time domain NMR spectrum (a mathematical elaboration of the NMR data also called relaxation spectrum) of the ^{1}H proton allows to distinguish different sample phases such as the polymers protons, the water entrapped into the polymeric network and the water in small channel or fracture and the free water (*Fig. 3.14*) [**5**]**.**

3.1.3.2 T_2 measurements and analysis in low field NMR

A typical instruments for low field NMR is a Bruker minispec mq20™, that operates at a frequency of 20 MHz (corresponding to ~0.47 *T*; in NMR, the B_0 field applied by the instruments is commonly expressed as the correspondent ^{1}H proton Larmor frequency) in controlled temperature conditions (*Fig. 3.15).*

Figure 3.15: the low field NMR spectrometer Bruker minispec mq20™.

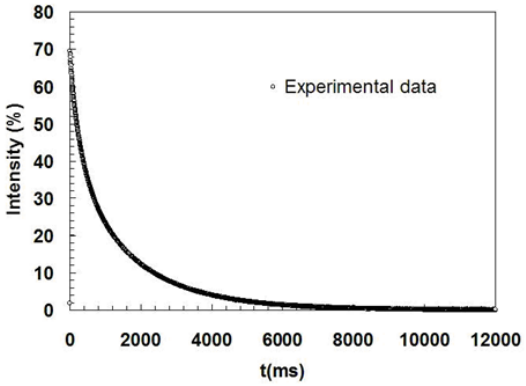

Figure 3.16: Exponential curve of the transversal relaxation time T_2.

The typical sequence adopted is the Carr-Purcell-Meiboom-Gill sequence (CPMG):

90° - τ - {[180° - 2τ -]M 180° - τ - measurement - τ}N

The sequence consists in the application of a first 90° pulse followed by a time interval τ. Then, a series of *M* 180° pulse applied at 2τ intervals are forwarded by the last 180° pulse after a τ interval. The sequence is repeated 8 times every 5 seconds.

The exponential T_2 relaxations curve obtained during the measurements (*Fig. 3.16*) can be represented by a sum of exponential decays [**6**]:

$$\frac{M_{xy}(t>0)}{M_{xy}(t=0)} = I(t) = \sum_{\mathrm{i}=1}^{\mathrm{m}} A_{\mathrm{i}} e^{-t/T_{2\mathrm{i}}} \tag{3.29}$$

Where t is the time, and A_i are the pre-exponential factors (dimensionless) proportional to the number of protons relaxing with the relaxation time T_{2i}. Obviously, eq. (3.29) holds also in the case of a mixture composed by n different liquids each one characterized by its own T_{2i}. The determination of A_i, T_{2i} and m is achieved by fitting eq. (3.29) to experimental *I(t)* values. The statistically most probable value of m is that minimizing the product $\chi^2*(2m)$, where $\chi 2$ is the sum of the squared errors and $2m$ represents the number of fitting parameters of eq. (3.29) [**7**]. The m (A_i– T_{2i}) couples represent the so called discrete relaxation times spectrum. In order to get the continuum relaxation time spectrum (m $\rightarrow\infty$), eq.(3.29) has to be written in integral form:

$$I(t) = \int_{T_2^{\min}}^{T_2^{\max}} a(T_2) e^{(-t/T_2)} \mathrm{d}T_2 \tag{3.30}$$

Where T_2^{min} - T_2^{max} indicates the range of the T_2 distribution and $a(T_2)$ is the unknown amplitude of the spectral component at relaxation time T_2. $a(T_2)$ determination requires eq.(3.30) fitting to the experimental *I(t)* values. At this purpose, eq. (3.30) can be discretized according to the criterion of Whittal and MacKay [**8**]:

$$I(t) = \int_{T_2^{\min}}^{T_2^{\max}} a(T_2) e^{(-t/T_2)} \mathrm{d}T_2 \approx \sum_{i=1}^{N} a_{\mathrm{i}}\left(T_2^{\mathrm{i}}\right) e^{(-t/T_{2\mathrm{i}})} \left(T_2^{\mathrm{i}+1} - T_2^{\mathrm{i}}\right) = \sum_{i=1}^{N} A_{\mathrm{i}}\left(T_2^{\mathrm{i}}\right) e^{(-t/T_{2\mathrm{i}})} \tag{3.31}$$

Where the range of the T_2 distribution (T_2^{min} - T_2^{max}) is logarithmically subdivided into N parts (≈ 200). Because of the noise disturbing the *I(t)*experimental data, fitting procedure must not minimize the $\chi 2$ statistic, but a smoothed version (χ_s^2):

$$\chi_{\mathrm{s}}^2 = \sum_{i=1}^{N} \left(\frac{I_s(t_{\mathrm{i}}) - I(t_{\mathrm{i}})}{\sigma_{\mathrm{i}}} \right)^2 + \mu \sum_{i=1}^{N-2} \left| A_{\mathrm{i}+2} - 2A_{\mathrm{i}+1} + A_{\mathrm{i}} \right|^2 \tag{3.32}$$

Where σ_i is i^{th} datum standard deviation, μ is the smoothing term weight (second summation in eq. (3.32)) proposed by Provencher [**9**]. Although different criteria can be followed for the μ determination, the strategy adopted by Wang [**10**] can be considered. According to this approach, eq. (3.32) has to be repeatedly fitted to experimental data assuming increasing μ values. As the function $Ln(\chi_s)$ vs $Ln(\mu)$ is linearly increasing up to a clear slope increase (curve heel), Wang suggests to take as optimal μ value that occurring just after the heel. Alternatively, Whittal [**8**] suggests, lacking further information, to choose the μ value ensuring that $\chi^2 \approx N$, where χ^2 is expressed by eq. (3.32) with $\mu = 0$. Indeed, in this case, each datum is misfit by about one standard deviation.

3.1.3.3 Relation between the relaxation time and mesh diameter

As anticipated in the previous paragraph, the interactions with the polymeric chains surface render the relaxation time of protons belonging to water molecules near the polymeric surface faster than that of bulk water protons [**11**]. Accordingly, in heterogeneous systems, the average relaxation time of protons will depend on the ratio between system volume and system solid surface, as demonstrated by Brownstein and Tarr [**12**] in the case of solid porous systems. These authors studied the problem assuming that the time (t) evolution of the magnetization density, $\rho(t)$, can be described by the following diffusion equation:

$$\frac{\partial \rho}{\partial t} = D\nabla^2\rho - \theta\rho \qquad\qquad M(t) = \int_V \rho(\boldsymbol{r}, t) \tag{3.33}$$

Where D is the self-diffusion coefficient of water molecules, θ is a parameter accounting for losses in magnetization density occurring in the bulk, M is the total magnetization of the sample (proportional to the NMR signal), r is the position vector, and V is the system volume. Eq.(3.33) is solved assuming that, initially the magnetization density $\rho(r,0)$ is uniform and equal to $M(0)/V$ and, on the solid surfaces of the system (pores wall), the following boundary condition holds:

$$\left(D\,\boldsymbol{n}\bullet\nabla\rho + \mathcal{M}\rho\right)\Big|_S = 0 \tag{3.34}$$

Where ***n*** is the surface normal vector, S is the solid surface (pores wall) and *M* (length/time) is an empirical parameter (relaxivity) accounting for the effect of surface on proton relaxations. Chui [**11**] adapted this theoretical approach for gels, building up the so called "Fiber – Cell" model (*Figure 3.17*).

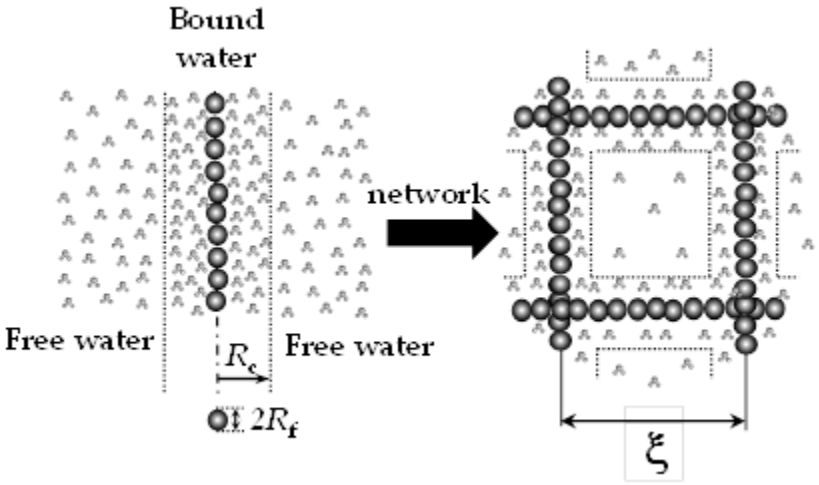

Figure 3.17:*Fiber – Cell* model. The relaxation time of protons belonging to water molecules (light gray ensembles) near the polymeric chain surface (bound water) is lower than that competing to free water protons. *Rf* is the polymeric chain radius (dark gray spheres indicate rigid chain segments), ξ is mesh size while *Rc* indicates the radial position where the magnetization gradient zeroes.

In this theory, the polymeric network is considered as a unique long fiber, of radius *Rf*, surrounded by an annular region (defined the "pore", in the terminology of Brownstein and Tarr [**12**]) of internal radius *Rf* and external radius *Rc*.

Rc is defined as the distance from the fiber symmetry axis to the cylindrical surface where the gradient of the magnetization density zeroes ($\nabla\rho = 0$) (the cylinder of radius R_c is termed "Cell"). Accordingly, eq.(3.33) is solved applying the condition $\nabla\rho = 0$ in *Rc* and the condition expressed by eq.(3.34) on the fiber (polymer chain) surface, i.e., in R_f. As polymer gels are diluted systems (polymer volume fraction $\phi \leq 0.1$), it is supposed that the fiber content in the "Cell" coincides with ϕ. Accordingly, R_c can be expressed by:

$$\phi = \frac{\pi R_f^2 L}{\pi R_c^2 L} = \left(\frac{R_f}{R_c}\right)^2 \Rightarrow \frac{R_c}{R_f} = \frac{1}{\sqrt{\phi}} \qquad (3.35)$$

Where *L* is the total fiber (= polymer chains) length. On the basis of this frame, the pore hydraulic radius (R_h) can be deduced:

$$R_h = \frac{2V_p}{S} = 2\frac{\pi\left(R_c^2 - R_f^2\right)L}{L2\pi R_f} = R_f\left(\frac{1-\phi}{\phi}\right) \tag{3.36}$$

Where V_p is pore volume. The relation between R_h and the polymeric network mesh size (ξ) can be found recalling the Scherer theory [**13**]. This author assumed that the polymeric network can be represented by as an ensemble of cylinders of radius R_f (i.e. polymeric chains) intersecting in a regular, cubic, array. Accordingly, he demonstrated that the hydraulic radius of the cubic cell depends on ξ according to the following relation:

$$R_h = \frac{2V_p}{S} = 2\frac{(1-\phi)}{\left(6\pi - 24\sqrt{2}(R_f/\xi)\right)(R_f/\xi)^2}R_f \tag{3.37}$$

Where $(R_f/\xi) \leq 0.5$. Starting from eq.(3.37) it is possible deriving two simple expressions relating R_h to R_f and ξ to R_f. Indeed, defining ξ the ratio R_f/ξ, according to Sherer, we have:

$$\phi = 3\pi x^2 - 8\sqrt{2}x^3 \tag{3.38}$$

$$R_h = 2\frac{(1-\phi)}{\left(6\pi x^2 - 24\sqrt{2}x^3\right)}R_f \tag{3.39}$$

In the limit $x \to 0$ (i.e $\phi \to 0$), it is easy to see that the denominator appearing in eq.(3.39) can be approximated by 2ϕ:

$$\psi = 6\pi x^2 - 24\sqrt{2}x^3 = 6\pi x^2 - 16\sqrt{2}x^3 - 8\sqrt{2}x^3 \tag{3.40}$$

$$\psi \approx 6\pi x^2 - 16\sqrt{2}x^3 = 2\phi \tag{3.41}$$

Figure 3.18 shows the comparison between ψ and ϕ for different x values. It can be seen that for $x \leq 0.1$, the error involved in the substitution of ψ by 2ϕ is lower than 8%. It can also be noted that $x \leq 0.1$ corresponds to $\phi \leq 0.16$.

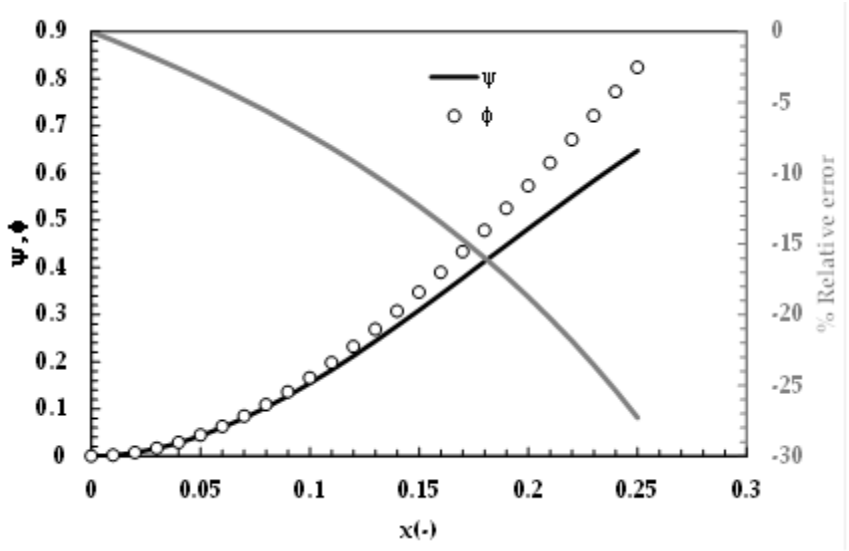

Figure 3.18: Comparison between functions ψ (solid black line, eq.(3.40)) and 2ϕ (open circles, eq.(3.38)). Gray solid line indicates the % relative error between ψ and ϕ (see right hand vertical axis).

Thus, eq.(3.37) can be approximated by:

$$R_h \approx \frac{(1-\phi)}{\phi} R_f \tag{3.42}$$

Now let's focus the attention on the simplified relation between ξ and R_f. Assuming z = 1/x and y = R_f/R_h, eq.(3.37) can be re-arranged to give:

$$R_h \left\{ z^3 \left(2y^2\right) - z 6\pi \left(y^2 + y\right) + 8\sqrt{2}\, y (3 + 2y) \right\} = 0 \tag{3.43}$$

In the limit y →0, the cubic equation contained in eq.(3.43) can be approximated by:

$$z\left\{ z^2 \left(2y^2\right) - 6\pi (y) \right\} = 0 \tag{3.44}$$

Apart from the trivial and un-physical solution z = 0, the only admissible solution of eq.(3.44) is:

$$z = \sqrt{\frac{3\pi}{y}} \tag{3.45}$$

Figure 3.19 makes clear that eq. (3.45) is a good approximation of the only physically admissible solution of eq.(3.43) in the entire ϕ range explored.

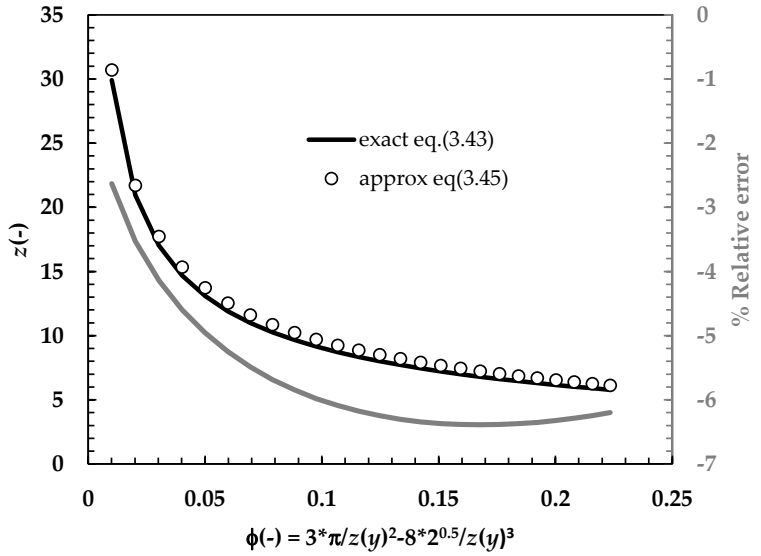

Figure 3.19: Comparison between the exact solution of eq.(3.43) (solid black line) and the solution of eq.(3.44) (open circles, eq.(3.45)). Solid gray line indicates the % relative error between the two solutions (right hand vertical axis).

Figure 3.19 is built by fixing y in the range 0.01 – 0.25, solving both eq.(3.43) and eq.(3.44) and calculating ϕ according to eq.(3.38). Thus, eq. (3.37) can be approximated by:

$$\xi \overset{\text{eq.(3.45)}}{\approx} R_f \sqrt{\frac{3\pi}{y}} \overset{\text{eq.(3.42)}}{\approx} R_f \sqrt{3\pi \frac{(1-\phi)}{\phi}} \tag{3.46}$$

The error involved in adopting this simplified expression in place of the exact one (eq.(3.37) or eq.(3.43)) is lower than 2.25% in the ϕ range considered $0 \leq \phi \leq 0.23$.

Eq.(3.42) and eq.(3.46) are fundamental for the practical application of the "Fiber-Cell" model. Indeed, Chui [**11**] demonstrated that when the mobility of the water molecules, identifiable with *D*, is high compared to the rate of magnetization loss (identifiable with MR_c; fast-diffusion regime: $MR_c/D << 1$), the following relation holds:

$$\left\langle \frac{1}{T_2} \right\rangle = \frac{1}{T_{2H_2O}} + 2\left\langle \frac{\mathcal{M}}{R_h} \right\rangle = \frac{1}{T_{2H_2O}} + 2\frac{\langle \mathcal{M} \rangle}{R_h} \tag{3.47}$$

where <1/T2> is the average value of the inverse of the relaxation time of the protons belonging to the water molecules trapped within the polymeric network of the gel, T_{2H2O}

is the relaxation time of the protons of the bulk water (i.e. protons of the free water, whose relaxation is not affected by the presence of the polymeric chains) and $\langle \mathcal{M} \rangle$ is the *M* value averaged on the whole gel volume. In the case of a real polymeric network made up by cubic cells (polymeric mesh) of different dimensions (ξ_i), i.e. of different hydraulic radius Rhi, eq. (3.47) becomes:

$$\frac{1}{T_{2i}} = \frac{1}{T_{2H_2O}} + 2\frac{\mathcal{M}_i}{R_{hi}} = \frac{1}{T_{2H_2O}} + 2\frac{\langle \mathcal{M} \rangle}{R_{hi}} \tag{3.48}$$

where T_{2i} and M_i are, respectively, the relaxation time and the *M* value of the water molecules protons trapped in cubic cells (polymeric mesh) of size ξ_i (or, hydraulic radius Rhi). Eq.(3.48) is based on the assumption that M_i does not depend on mesh size ξ_i and $M_i = \langle \mathcal{M} \rangle$ for every "i". Thus, knowing R_h (eq.(3.42)), $\langle 1/T_2 \rangle$ (determinable by eq.(3.30) or (3.31) data fitting)) and T_{2H2O}, eq.(3.47) allows the determination of $\langle \mathcal{M} \rangle$. In addition, knowing $\langle \mathcal{M} \rangle$ and T_{2i} (see eq.(3.30)), together with eq. (3.48), it is possible evaluating ξ_i for each class of cubic cells. Finally, relying on $\langle \mathcal{M} \rangle$ and $a(T_2)$ (eq.(3.31)) knowledge, it is possible determining the continuous ξ distribution $a(\xi)$. Indeed, the combination of eqs. (3.47) and (3.48) allows finding the relation between $d\xi$ and dT_2:

$$\xi = \frac{2\langle \mathcal{M} \rangle}{\sqrt{\frac{1-\phi}{\phi 3\pi}}} \Bigg/ \left(\frac{1}{T_2} - \frac{1}{T_{2H_2O}} \right) \mathrm{d}\xi = \frac{2\langle \mathcal{M} \rangle}{\sqrt{\frac{1-\phi}{\phi 3\pi}}} \left(\frac{T_{2H_2O}}{T_{2H_2O} - T_2} \right)^2 \mathrm{d}T_2 \tag{3.49}$$

Consequently, $a(\xi)$ will be:

$$a(\xi) = \frac{dT_2}{d\xi} a(T_2) = \frac{\sqrt{\frac{1-\phi}{\phi 3\pi}}}{2\langle \mathcal{M} \rangle} \left(\frac{T_{2H_2O} - T_2}{T_{2H_2O}} \right)^2 a(T_2) \tag{3.50}$$

Thus, the probability $P(\xi)$ of finding a mesh of size ξ inside the polymeric network, is:

$$P(\xi) = \frac{a(\xi)d\xi}{\int_{\xi_{min}}^{\xi_{max}} a(\xi)d\xi} \tag{3.51}.$$

3.1.3.4 Water self diffusion coefficient D_G measurement

The nuclear magnetic resonance is a very powerful non-invasive technique that can determine the water self diffusion coefficient of a protoaned liquid. [**14**].

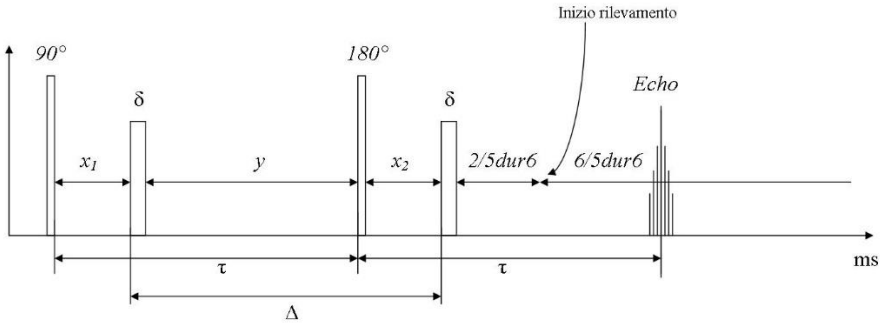

Figure 3.20: PGSE sequence. It is a Hahn Spin-echo sequence where two magnetic field gradients have been added. δ is the gradients duration while Δ is the lag time between the two gradients.

The measurable values of the self-diffusion coefficient span, approximately, between $10^{-7}m^2s^{-2}$ and $10^{-14}m^2s^{-2}$ [**14**]. In order to perform the measurement of the self-diffusion coefficient the sequence PGSE "Pulsed Gradient Spin Echo" is used. This sequence was developed by Stejskal and Tanner [**15**] and, as it can be seen in *Figure 3.20*, it comprehends two the magnetic field gradients of duration δ, spaced by a time length Δ. The gradients allow to generate a space-dependent magnetization that "label" the molecules of the protonated liquid. The observation of the magnetization and its evolution over time allows calculating the liquid molecules self-diffusion coefficient (as well as the generation of images in the medical field). As intensity of a magnetic field intensity is expressed in Tesla (*T*), the gradient of the magnetic field is expressed in Tesla on meter (*T*/m). The magnetization has no spatial dependence and can be considered only dependent on z (see *Figure 3.21 A*).

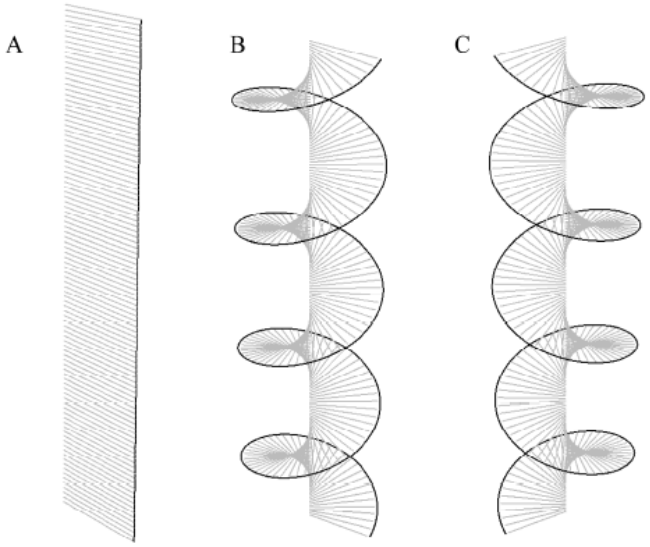

Figure 3.21: (A) Magnetization after a pulse of 90 ° **(B)** A spatial variation in the magnetization is impressed by the application of the gradient **(C)** The impulse to 180 ° reverses the pitch of the propeller.

The gradient operates around the *z* axis, therefore its application imparts a specific rotation to signals that are on the *xy* plane. Three signals that just before the gradient share the same angle with respect to the *y* axis, but that occupy different positions within the sample, will experience a gradient of varying intensity that will rotate them of a different amount as shown in *Figure 3.22*. Consequently, the magnetization will change as depicted in Figure *3.21 B*. The application of the 180° pulse will rotate the signals and it reverses the magnetization helix pitch as shown in *Figure 3.23* and *Figure 3.21 C*.

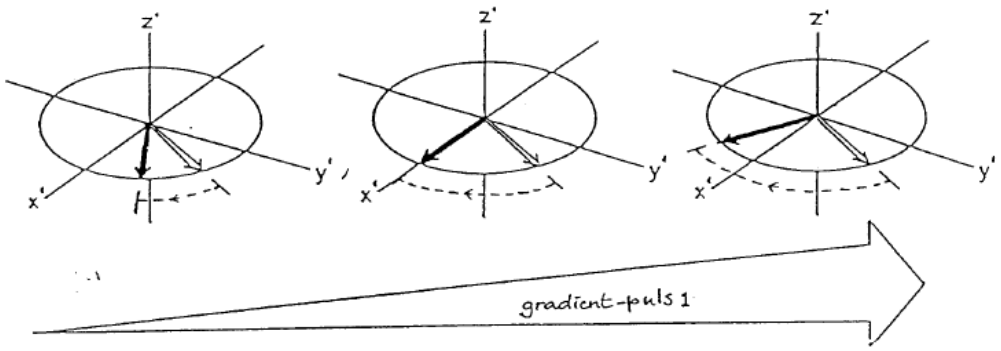

Figure 3.22: Rotation of signals around *z* axis depends on signals position in the sample

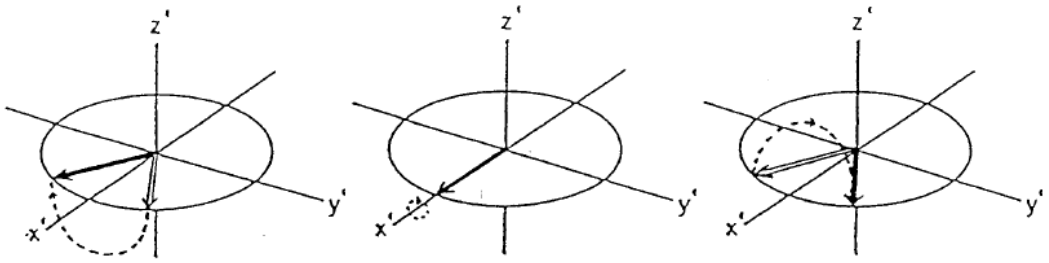

Figure 3.23: Application of a pulse to 180°

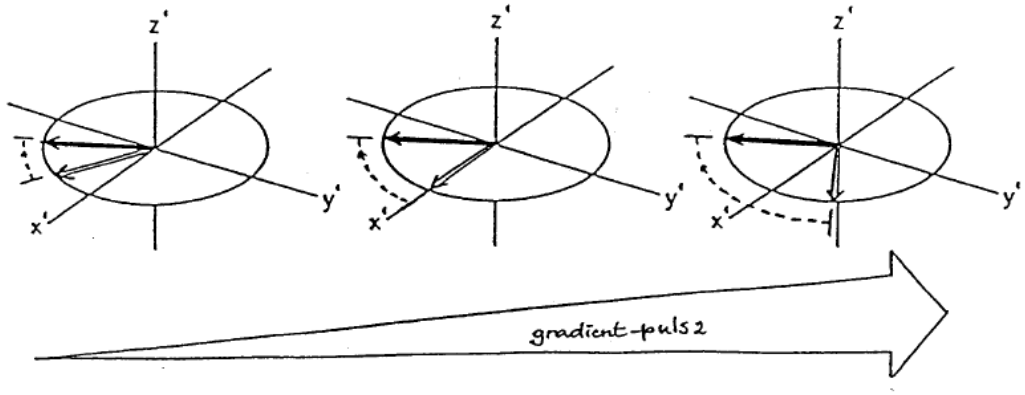

Figure 3.24: Application of the second gradient and re-alignment of the signals.

The second gradient will reduce the helix pitch and it rotates the signals of the same amount imposed by the first gradient. Consequently, all signals will be re-aligned with the same angle from the axis *y* as if the gradients had not been applied and how it was applied only the impulse to 180 ° (*Figure 3.24*). Once aligned, the signals will close and will generate a signal as it happens in the Hahn Spin-echo sequence. This would be the fate of signals in the case of molecules that cannot move inside the sample. On the contrary, in the case of moving (diffusing) molecules, the situation will be different. In the time length Δ occurring between the two gradients, molecules will move and, consequently, the signals re-alignment is no longer possible. Accordingly, the final echo will be attenuated. The knowledge of the attenuation of the echo between a sequence without gradients (Hahn Spin-Echo) and the one with the gradients allow to calculate the self-diffusion coefficient according to the following relation [**16**]:

$$\ln \frac{A_{G(t)}}{A_{G(0)}} = -\gamma^2 \cdot D \cdot \delta^2 \cdot \left(t_d\right) \cdot G^2 \qquad (3.52)$$

where $A_{G(t)}$ is the signal amplitude of the echo with the gradient applied and $A_{G(0)}$ is the signal amplitude of the echo without the application of gradients, γ is the gyromagnetic ratio of the atom studied, t_d is the diffusion time defined as $\Delta - 1/3\delta$ and G is the intensity of the gradient expressed in Tesla (*T*) on the meter. Since then all known parameters except *D*, it will be possible to obtain the value of the self-diffusion coefficient.

3.1.3.5 Diffusion in confined systems

So far it has been assumed that the molecules could freely diffuse within the sample. However, it is not always the case. For example, in the case of a porous matrix swollen by water (or another protonated liquid), as far as the diffusion time $t_d << a^2/D_0$ (where *a* is the pore dimension and D_0 is the self-diffusion coefficient of the free water), the measurement of *D* will coincide with D_0. When, on the contrary, $t_d \approx a^2/D_0$, part of the water molecules will begin to suffer the effect (constraint) of the pore walls and the self-diffusion coefficient will be reduced according to [**14**]:

$$D_{app}(t_d) = D_0\left(1 - \frac{4}{9\sqrt{\pi}}\frac{S}{V}(D_0 t_d)^{1/2}\right) \tag{3.53}$$

where $D_{app}(t_d)$ is the apparent self-diffusion coefficient and S/V is the ratio of surface to volume reported to the pore size. If the diffusion time t_d increases up to $t_d >> a^2/D_0$, the maximum distance that molecules will travel by diffusion will be limited by the geometric boundaries of the system and the validity of equation 3.53 will decay. In this situation, the measured value of the diffusion coefficient will be t_d independent and it attains a constant value $D_{app\infty}$ [**17**] equal to D_0/α where α is the tortuosity of the pores network [**14**]. Interestingly, when pores are not interconnected, $D_{app\infty}$ approaches zero (this condition corresponds to an infinite tortuosity).

3.1.3.1 Relation between T_2, *D* and the pores size distribution

In the case of spherical pores, eq.(3.53) becomes [**18**]:

$$D_{app}(t_d) \approx 1 - \frac{8}{3\sqrt{\pi}} D^{1.5}\sqrt{t_d}\frac{1}{\xi} \tag{3.54}$$

Indeed, in this case, $S/V = 6/\xi$. Eq.(3.54) allows determining the mean pores diameter (ξ) once $D_{app}(t_d)$ has been experimentally determined according to PGSE experiments. In order to get the (discrete) pores size distribution, it is necessary recalling the theory of

Brownstein and Tarr [**12**], suitable for mono-dispersed spherical pores, generalized for poly-dispersed spherical pores by Chui [**11**]. This approach leads to the conclusion that the signal intensity $I(t)$, related to the decay of the transverse component of the magnetization vector (M_{xy}), is given by:

$$I(t) = \sum_{i=1}^{m} A_i \sum_{j=1}^{\infty} I_{ij} e^{-t/T_{2ij}} \tag{3.55}$$

where t is time, A_i are the pre-exponential factors (dimensionless) proportional to the number of protons whose relaxation is ruled by the sum of exponentials of intensities I_{ij} and relaxation times T_{2ij}. Eq.(3.55) states that the relaxation of the protons belonging to the molecules of the liquid trapped in the pores of radius R_i is, in principle, described by an infinite number of relaxation times (T_{2ij}). I_{ij} and T_{2ij} are expressed, respectively, by:

$$T_{2ij} = \frac{R_i^2}{D_G X_{ij}} \qquad I_{ij} = \frac{12\left(\sin\left(X_{ij}\right) - X_{ij}\cos\left(X_{ij}\right)\right)^2}{X_{ij}^3\left(2X_{ij} - \sin\left(2X_{ij}\right)\right)} \tag{3.56}$$

where X_{ij} are the positive roots of the following equation:

$$1 - X_{ij}\cot\left(X_{ij}\right) = \frac{\mathcal{M} R_i}{D_G} \tag{3.57}$$

where $\mathcal{M}$ (length/time) is an empirical parameter (relaxation sink strength), independent on pore radius and accounting for the effect of the polymeric surface on proton relaxations. Eq.(3.57) solution needs a numerical approach such as the Newton method (tolerance to 10^{-6}). As T_{2ij} are not independent from each other (on the basis of eq.(3.56) it follows $T_{2ij} = T_{2i1}\left(X_{i1}/X_{ij}\right)^2$), model unknown parameters are T_{2i1}, A_i and MRD_i ($=\mathcal{M}R_i/D_G$) for a total of $3m$ parameters. Recalling eq.(3.47), in this case, it follows:

$$\left\langle \frac{1}{T_{2i}} \right\rangle = \sum_{j=1}^{\infty} \frac{I_{ij}}{T_{2ij}} = \frac{6\mathcal{M}}{\xi_i} + \frac{1}{T_{2H2O}} \tag{3.58}$$

where T_{2H2O} is the free water relaxation time (3694 ms at 37°C [**19**]), ξ is the average pores diameter and $\langle 1/T_2 \rangle$ is the average of the inverse of the relaxation time of all protons. While eq.(3.58) holds on average for all pores, similar expressions can be written for pores of different size ($\xi_i = 2R_i$):

$$\left\langle \frac{1}{T_{2i}} \right\rangle = \sum_{j=1}^{\infty} \frac{I_{ij}}{T_{2ij}} = \frac{6\mathcal{M}}{\xi_i} + \frac{1}{T_{2H2O}} \tag{3.59}$$

where $\langle 1/T_{2i} \rangle$ is the average of the inverse of the relaxation time of protons entrapped in pores of diameter ξ_i. As $\langle 1/T_2 \rangle$ can be calculated on the basis of eq.(3.55) fitting to relaxation data and T_{2H2O} and ξ are known, eq.(3.58) allows the determination of $\mathcal{M}$. Furthermore, by knowing $\mathcal{M}$ and T_{2i} (eq.(3.55) fitting to relaxation data), eq.(3.59) makes it possible the evaluation of ξ_i for each class of polymeric network meshes. The volumetric fraction of pores characterized by diameter ξ_i is given by A_i.

3.1.3.2 Release Tests

This approach relies on the reduced mobility of a probe molecule inside a polymeric network due to the hindering effect exerted by the chains [**20**]. Indeed, in the case of negligible convection, network swelling, erosion and probe molecule interaction with polymeric chains [**21**], probe molecule diffusion is essentially ruled by the chains presence. In particular, in the case of a polymeric network, mesh diameter plays the key role in ruling probe movements. Probe mobility is represented by its diffusion coefficient D_p (dimensionally an aerial velocity) that is sometimes referred to as Fickian diffusion coefficient as it is related to movements induced by the presence of a probe concentration gradient [**22**]. On the contrary, the tracer diffusion coefficient refers to the mobility of a probe molecule in an environment where no concentration gradient exists, i.e. probe movements are dictated only by Brownian motion. Indeed, if the probe molecule is present in traces, its concentration is almost vanishing as well as its concentration gradient. The tracer diffusion coefficient is also called self-diffusion coefficient as the absence of concentration gradient takes also place in a pure liquid where molecules movements are, again, due to only Brownian motion. In the case of diluted solution, the difference between the Fickian and the tracer diffusion coefficient becomes negligible [**22**].The relation between D_p and the mean mesh diameter ξ is given by the Peppas and Merryl model [**23**]:

$$\frac{D_p}{D_0} = \left(1 - \frac{2r_s}{\xi}\right) \exp\left(-y_p \frac{\phi}{1-\phi}\right) \tag{3.60}$$

Which combines the free volume theory [**24**] with the assumption that the probability of a solute of radius r passing through an opening of diameter eps is linearly dependent on

the ratio $2r_s/\xi$. In eq.(3.60) D_0 indicates the probe (Fickian) diffusion coefficient in the pure solvent, ϕ is the polymer volume fraction in the gel and y_p represents the ratio of the critical volume required for a successful translational movement of the probe molecule and the average free volume per molecule of the swelling medium. Although y_p depends on many factors, the authors suggest that, when r_s is expected to be much smaller than ξ, it can be approximately assumed as equal to one. Thus, known D_0, r_s and ϕ, the experimental measurement of D_p allows the determination of ξ according to eq.(3.60). Although D_p can be measured by different methods such as the high field NMR [**4**], the most common way of proceeding is to experimentally record the release of a probe molecule from a gel matrix [**21**]. The release curve is then fitted by a mathematical model relying on Fick'law [**21**]:

$$\frac{\partial C}{\partial t} = \nabla\left(D_p \nabla C\right) \tag{3.61}$$

$$V_r C_r(t) = VC_0 - \iiint_V C(X,Y,Z,t)dV \tag{3.62}$$

where t is time, C is probe concentration in the generic position (X, Y, Z) of the releasing gel matrix of volume V, V_r and C_r are, respectively, the volume and the probe concentration of the release environment, ∇ is the nabla operator and C_0 is the initial, uniform, probe concentration in the gel matrix. While eq.(3.61) expresses a mass balance on the probe at the micro-scale, eq.(3.48) represents a mass balance on the probe at the macro-scale. Indeed, it states that at each time, the amount of probe in the release environment (V_rC_r) is equal to the difference between the initial amount of probe in the gel matrix (VC_0) less the amount still present in the gel matrix. Eq.(3.61) has to be solved with the following initial and boundary conditions:

initial conditions

$$C(\mathrm{X}, \mathrm{Y}, \mathrm{Z})=0 \tag{3.63}$$

boundary conditions

$$C(\text{gel surface}) = k_p C_r \tag{3.64}$$

where k_p is the probe partition coefficient between the gel and the environmental release fluid. Eq.(3.63) sets a uniform concentration in the gel at the beginning (t = 0) while eq.(3.64) assumes that at the gel-release environment interface, the equilibrium condition for what concerns probe concentration holds. In order to determine D_p, eq.(3.63) and

(3.64) have to be simultaneously solved (according to a numerical method [**25**]) and fitted to the experimental C_r trend, usually assuming $k_p = 1$.

3.2 Rheological Characterization

Rheology is the science field dealing with the relation between stress (τ) and deformation (γ). In other words, its aim is to study, theoretically and experimentally, the effect (deformation state) of a stress imposed on a material (and vice versa).

In this work the rheological characterizations is performed by a rotational rheometer HAAKE Rheostress RS-150™ (controlled stress) equipped with a set of different geometry sensors able to stress the samples with a shear strain.

The rheometer applies on the sample, a torque T (generated by a magnetic field) registering the displacement of the mobile portion of the measuring probe. The probes used are basically constituted by two parallel plates and the sample is placed in between filling all the volume that separate the two plates.

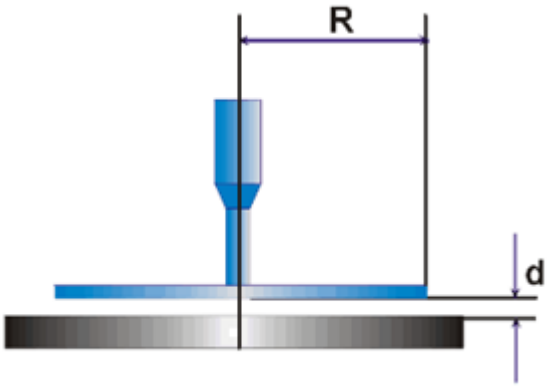

Figure 3.25: Schematic representation of the parallel plates sensor: R is the plates radius and d, the gap between plates.

3.2.1 The parallel plates measuring system geometry

The parallel plates measuring geometry (*Fig. 3.25*) is widely used for measuring the non-Newtonian fluids properties and for the characterization of viscoelastic materials. The reasons reside in some advantages: the easier sample loading, the possibility to modify the shear rate independently from the rotational speed Ω by simply changing the gap d between the plates. On the other side, the torque measuring systems, need a particular attention in order to avoid (or limit) systematic errors during the operative phase. The most common sources of errors are listed below.

- *Inertial effects*: especially at high shear rate, toroidal secondary fluxes generated in the sample leads to an overestimation of the viscous properties and, as consequence, the torque moment results higher of that related only to the rheological properties.
- *Geometrical effects*: if the fluid is loaded in excess, the free surface is not spherical and edge effects are generated; others error can be generated by wrong assets that results in acentricity, not alignment and vertical oscillations.
- *Instability effects*: the materials does not preserve its shape in all the conditions so, at high speed, the sample separates in two parts and finally it is pulled out by the centrifugal forces (splitting).
- *Shear heating*: due to energy dissipation, a not uniform temperature field can take place inside the gap.

In particular, during this studies, was used the parallel plate sensor PP35 Ti96010 witch have diameter of 35 mm and milled surface in order to minimize the slippage phenomena (*Fig.3.26*). In order to ensure more consistent environmental conditions and to limit the evaporation, a glass bell (solvent trap) was used to cover the measuring device in all the experiments (*Fig. 3.27*).

Figure 3.26: the parallel plates sensor PP25 Ti96010.

Figure 3.27: the PP25 Ti96010 sensor isolated by a solvent trap in order to limit the water evaporation from the systems.

3.2.2 Stress sweep tests

The stress sweep test (SS), serve for the identification of the linear viscoelastic region. Within the linear viscoelastic limits, the storage modulus *G'* (also called *elastic modulus*) and the loss modulus *G"* (also called *viscous modulus*), are independent from the applied deformation and remain constant up the limit deformation γ_0 (called *critical deformation*). For higher deformation, *G'* and *G"* rapidly decrease. *G'* give information related to the elastic energy accumulated by the materials during a deformation while, *G"* is related to the energy dissipated. The SS test is based on the sample solicitation by a sinusoidal stress of constant *frequency f* (1 Hz) and increasing amplitude.

For a stress (or deformation) lower than the linear viscoelastic limit, the value of *G'* and *G"* are independent from the applied stress and the system conditions, can be considered as equilibrium state because the material structure does not undergo significant alterations or disruption. Above the critical deformation γ_0, the material structure collapses and both modulus values change, normally with a decreasing. Deformation γ, deformation speed $\dot{\gamma}_0$ and stress τ, are related by the following equations:

$$\gamma = \gamma_0 \sin(\omega t) \tag{3.65}$$

$$\dot{\gamma} = \gamma_0 \omega \cos(\omega t) = \dot{\gamma}_0 \cos(\omega t) \tag{3.66}$$

$$\tau = \tau_0 \sin(\omega t + \delta) = \tau_0 \cos\delta \cdot \sin(\omega t) + \tau_0 \sin\delta \cdot \cos(\omega t) \tag{3.67}$$

where, $\dot{\gamma}_0$ is the *critical deformation speed*, ω the *angular frequency* or pulsation (ω=2πf) and δ the *loss angle* between stress and deformation.

The first term of the equation (3.67), $\tau_0 \cos\delta \cdot \sin(\omega t)$, is related to the elastic component while, the second, $\tau_0 \sin\delta \cdot \cos(\omega t)$, is related to the viscous component. In the two limiting cases of δ=0 or δ=π/2, the material behavior is totally elastic or totally viscous, respectively. Equation (3.67) can be also written as:

$$\tau = G'\gamma_0 \cdot \sin(\omega t) + G''\gamma_0 \cdot \cos(\omega t) \tag{3.68}$$

Where, the storage modulus *G'* is related to the component in phase with the applied deformation while, the dissipative loss modulus *G"*, is in square phase with it.

The complex modulus *G** is represented by the ratio within maximum stress and maximum applied deformation:

$$|G^*| = \sqrt{(G') + (G'')^2} = \sqrt{\left(\frac{\tau_0 \cos\delta}{\gamma_0}\right)^2 + \left(\frac{\tau_0 \sin\delta}{\gamma_0}\right)^2} = \frac{\tau_0}{\gamma_0} \tag{3.69}$$

The loss angle δ is defined as:

$$tg\delta = \frac{G''}{G'} \tag{3.70}$$

3.2.3 Gap determination: short stress sweep tests

The determination of the best sensor gap is a crucial point in the experimental procedure because the errors caused by inaccurate settings can be relevant due to possible wall slippage. The method used to determine the optimal gap and samples compression, consists in the applications of a series of short stress sweep test gradually reducing the plates gap. In order to avoid irreversible effects on the systems, the short SS were performed inside the linear viscoelastic field (shear stress τ around 1 Pa). Fixed the initial gap, the short SS was performed registering the *G'* at 1 Hz. The test continues with others short SS reducing each time the plates gap till the detection of a plateau in the *G'* trend (or a maximum value). The distance so determinate was identified as the optimal gap in order to minimize wall slippage effects and was applied in all the following rheological tests (*Fig. 3.28 and 3.29*) [**26**].

The advantages of this methodology consist in the capability to reproduce the same G' characteristics without preparing the gel in situ within the rheometer plates and the possibility to perform the experiments without knowing the exact thickness of the gel system.

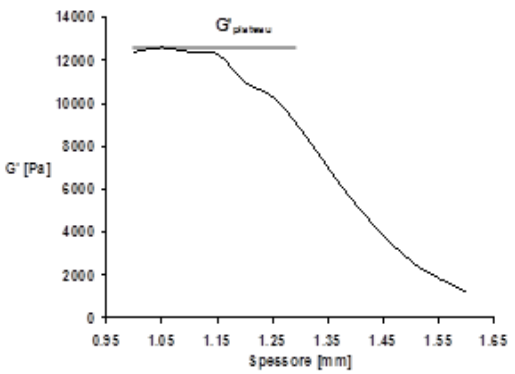

Figure 3.28: example of G' trend as function of the plates gap during a short SS test; the gap applied when G' reaches the plateau (1,15 mm) was considered the optimal plates distance for the sample.

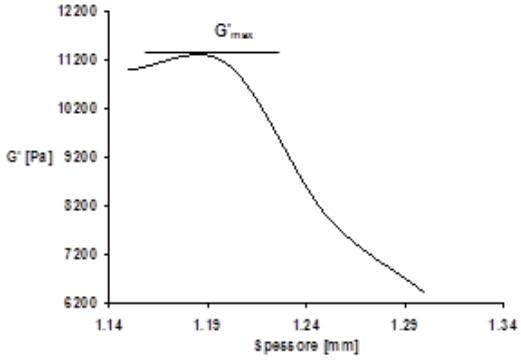

Figure 3.29: another example of G' trend as function of the pleats gap during a short SS test; the gap applied when G' reaches a maximum (1,2 mm) was considered the optimal plates distance for the sample.

3.2.4 Frequency sweep tests

The frequency sweep test (FS) is performed in order to obtain the89 mechanical spectrum of a material; this allows the characterization of structural properties under equilibrium. The test consists in the application of asinusoidal stress of constant amplitude but varying *frequency f* ($\omega=2\pi f$), usually in the range 0,01-100 Hz. Stress amplitude must belong to the linear viscoelastic field. An important parameter for the materials behavior classification, is the *number of Deborah (De).* This parameter, is the ratio within the characteristic *relaxation time* (λ) (referred to the mechanical prope8rties, not related to the relaxation time T_2 in NMR spectroscopy) and the characteristic deformation process time Λ applied to the material:

$$De = \lambda / \Lambda \tag{3.71}$$

as

$$\Lambda \propto 1/\omega \tag{3.72}$$

we have

$$De \propto \lambda\omega \tag{3.73}$$

Elastic behavior implies De=∞, while liquid behavior implies De=0. A viscoelastic behavior happens for 0<De<∞ (typical De≈1 or 10).

3.2.5 Correlation Models

Among the different models that can be used for the interpretation of FS test, Maxwell model is one of the most popular. According to this model, the mechanical properties are represented by a dashpot and a spring in series (*Fig. 3.30a*). The equation describing the mechanical behavior of the Maxwell model is:

$$\tau + \frac{\eta}{g}\frac{\partial \tau}{\partial t} = -\eta\dot{\gamma} \tag{3.74}$$

where τ is stress, γ is deformation, t is time, η is the dashpot viscosity, g is the spring constant and $\lambda = \eta/g$ is the relaxation time. The relaxation time λ represents the time necessary to the structure to relax the strain after the application of a constant deformation. In the frequency sweep tests, low values of *De*, correspond to a deformation applied in longer time than the material relaxation time therefore, the time frame for the material is enough to relax from the strain and respond as a viscous-like system. Opposite, for high values of *De*, the deformation is applied in a short time and the system does not relax completely; the behavior assumes the typical elastic response.

The solution of equation (3.74), in the case of a sinusoidal deformation $\gamma=\gamma_0 sen(\omega t)$, leads to

$$\tau = \gamma_0 G' sen(\omega t) + \gamma_0 G'' \cos(\omega t) \tag{3.75}$$

where

$$G'(\omega) = \frac{g(\lambda\omega)^2}{1+(\lambda\omega)^2} \tag{3.76}$$

$$G''(\omega) = \frac{g\omega\lambda}{1+(\lambda\omega)^2} \tag{3.77}$$

These equations of *G'(ω)* and *G''(ω)* can be plotted into a bi-logarithmic chart. The interception point represent $\omega=1/\lambda$ corresponding to a *G''* maximum and *De*=1. In general Maxwell model is not enough for a good description of properties. At this purpose it is

possible to combine in parallel n Maxwell elements (*Fig. 3.30b*). In this case equation (3.74) solution leads to:

$$G'(\omega) = \sum_{k=1}^{n} \frac{g_k (\lambda_k \omega)^2}{1 + (\lambda_k \omega)^2} \tag{3.78}$$

$$G''(\omega) = \sum_{k=1}^{n} \frac{g_k \omega \lambda}{1 + (\lambda_k \omega)^2} \tag{3.79}$$

where n is the number of Maxwell elements considered while G_i, η_i and λ_I represent, respectively, the spring constant, the dashpot viscosity and the relaxation time of the ith Maxwell element. The simultaneous fitting of Equation (3.78) and (3.79) to experimental *G'* and *G''* data was performed assuming that relaxation times (λ_i) were scaled by a factor 10. Hence, the parameters of the model are 1 + *n* (i.e. λ_1 plus G_i). Based on a statistical procedure, n was selected in order to minimize the product $\chi^2(1+n)$, where χ^2 is the sum of the squared errors. *G'* and *G''*data represent the average of three experiments. Flory's theory enables the determination of polymeric network crosslink density ρ_x (defined as the moles of junctions between different polymeric chains per hydrogel unit volume):

$$\rho_x = G/RT \tag{3.80}$$

where *R* is the universal gas constant, *T* is the temperature and *G* (shear modulus) can be computed as the sum of the elastic contributions (G_i) pertaining to each element of the generalized Maxwell model describing the hydrogel mechanical spectrum. Finally, the equivalent network theory allows evaluating the average network mesh size ξ :

$$\xi = \sqrt[3]{6/\pi \rho_x N_A} \tag{3.81}$$

where N_A is the Avogadro number.

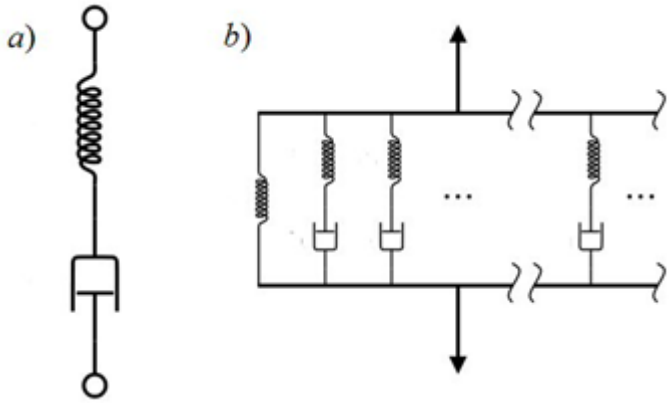

Figure 3.30: a) schematic representation of a viscoelastic element in the Maxwell model constituted by a spring in series with a dashpot that represents the elastic and viscous component respectively. **b)** The generalized Maxwell model constituted by several viscoelastic elements in parallel (the spring on the left represent the pure elastic element).

3.3 Cryoporosimetry

3.3.1 An introduction

Porous materials have many, different, important role in several industrial field such as chemicals and petrochemicals, papers, textile, constructions, leathers, etc. The extensive need for different characteristics stimulated intensive researches on porous materials.

The porimetric techniques can be classified in *direct methods* and *indirect methods*.

- *Direct methods* are based on the direct observation by the electronic microscopes, X ray diffraction crystallography techniques and others. Unfortunately, these methods, though allowing the direct observations, are not suitable for the mesoporosus materials study where the porus radius is between 2 and 50 nm.
- *Indirect methods* are based on the analysis of the capillarity phenomena. The most used are the mercury porosimetry (for big pores) and the Gas porosimetry (for small pores). Substantially, the phase transitions of a substance filling a porous material, allows the internal structure characterization.

Cryoporometry is a calorimetric methods that recently emerged among indirect methods for pores size determination [**27**]. Cryoporosimetry is based on the solid-liquid transition of a substance inside porous structure. Many authors observed that the melting temperature of a pure disperse substance depends on the curvature radius of the solid-liquid interface. Inside a pore, the radius strictly depends on the pore dimension.

Therefore, the solidification/melting temperature vary for each pores of the material as function of the pore diameters [**28**]. In particular the smaller the curvature radius, the lower the melting temperature is. This means that a DSC analysis of a liquid filled porous material can provide its pore size distribution.

For its biological, water is usually the election liquid in cryoporometric studies [**29**]. In addition, due to its high specific melting heat (Δh=334 J/gr, one order of magnitude higher than most of others organic solvents) DSC is increased. Main disadvantage of this method consists in the possibility of network corruption due to the liquid solidification. Cryoporosimetry is not a common methods, not diffused as nitrogen porimetry or mercury porimetry but, can be adopted for the pore size determinations when we know [**30**]:

- liquid probe surface tension and heat of fusion
- contact angle within sample material and liquid probe
- liquid probe density
- heat capacity dependence on temperature

3.3.2 Cryoporosimetry Principles

Cryoporosimetry relies on the triple point dependence on the dimension of the solid phase (ice crystal), as theoretically demonstrated by Brun and co-workers [**31**]. Brun theory assumes different mathematical forms depending on the ice crystals shape (dictated by the polymeric mesh geometry where water solidification takes place) and boundary conditions (water in excess with respect to nano-pores volume or not), as shown in *Figure 3.31*:

cylindrical mesh with water excess, spherical mesh:

$$\int_{T_0}^{T_R} \frac{\Delta h_R}{T} \mathrm{d}T = -\frac{2}{R_{sl}} \frac{\gamma_{sl}}{\rho_s} \tag{3.82}$$

cylindrical mesh with no water excess:

$$\int_{T_0}^{T_R} \frac{\Delta h_R}{T} \mathrm{d}T = -\frac{2}{R_{sl}} \left(\frac{\gamma_{sl}}{\rho_s} - \gamma_{lv} \left(\frac{1}{\rho_s} - \frac{1}{\rho_l} \right) \right) \tag{3.83}$$

where T_0 represents the melting temperature of an infinitely large ice crystal (0°C), T_R and Δh_R are, respectively, ice melting temperature and specific melting enthalpy for a

crystal characterized by a solid-liquid interface of curvature radius equal to R_{sl}; γ_{sl} and γ_{lv} are, the ice-water and water-vapor interface tensions while ρ_s and ρ_l are ice and water density, respectively.

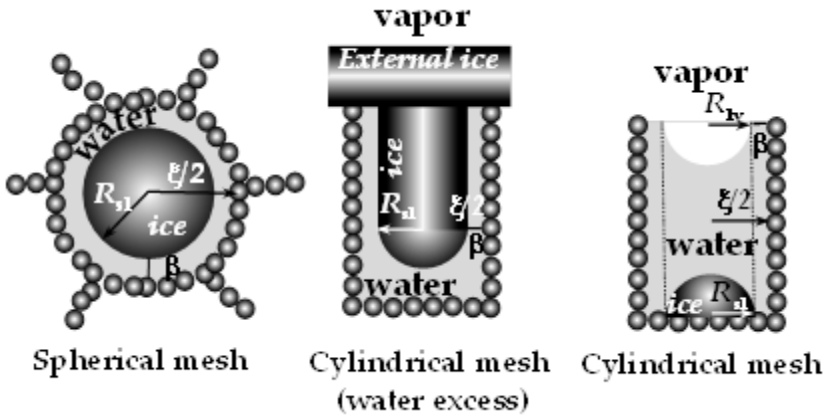

Figure 3.31: Ice crystals shape in relation to different polymeric mesh geometries (gray spheres indicate rigid chain segments). R_{sl} and R_{lv} indicate, respectively, the solid (ice) – liquid (water) and the liquid (water) – vapor interface radius of curvature, ξ is mesh size and β is the constant thickness of the not-freezable water layer adsorbed on the mesh wall.

In order to simultaneously take into account both situations, Eqs. (3.82) - (3.83) can be rewritten as:

$$\int_{T_0}^{T_R} \frac{\Delta h_R}{T} \mathrm{d}T = -\left(X \frac{2}{R_{sl}} \frac{\gamma_{sl}}{\rho_s} + (1-X) \frac{2}{R_{sl}} \left(\frac{\gamma_{sl}}{\rho_s} - \gamma_{lv} \left(\frac{1}{\rho_s} - \frac{1}{\rho_l} \right) \right) \right) \tag{3.84}$$

Although empirical, this choice of weighing the contribute of eq.(3.82) and eq.(3.83) is coherent with a common approach adopted for the characterization of meshes that are neither spherical nor cylindrical [**32**]. Indeed, identifying the mesh shape factor, Z, as the power expressing the mesh volume dependence on mesh radius (3 for spherical meshes and 2 for cylindrical meshes), it is possible connecting Z to our weigh X according to the relation Z = 2*(1-X) + 3*X. For X = 1 and 0, spherical (Z = 3) and cylindrical (Z = 2) meshes can be found, respectively. For 0 < X < 1, Z varies between 2 and 3 and it represents meshes with geometrical characteristics in between those of cylinders and spheres. It is also important to point out that, due to the similar values of ice and water density (whatever temperature), the right hand side terms of Eq.(3.82) and (3.83) do not differ too much each other. The numerical solution of Eq. (3.84) requires the knowledge

of the Δh_R dependence on melting temperature and curvature radius. For this purpose, a classical thermodynamic relation can be used [**33**]:

$$\Delta h_{\mathrm{R}} = \Delta h \; - \frac{3}{R_{\mathrm{sl}}}\left(\frac{\gamma_{\mathrm{sv}}}{\rho_{\mathrm{s}}} - \frac{\gamma_{\mathrm{lv}}}{\rho_{\mathrm{l}}}\right) - \int_{T_{\mathrm{R}}}^{T_0}\left(c_{\mathrm{ps}} - c_{\mathrm{pl}}\right)\mathrm{d}T \tag{3.85}$$

where Δh is the specific ice melting enthalpy for an infinitely large crystal (the corresponding solid-liquid interface is flat; $R_{sl} \approx \infty$; T_R = 0°C), while c_{ps} and c_{pl} are, respectively, the ice and water specific heat capacities. The ρ_s,ρ_l, c_{ps} and c_{pl} temperature dependence can be expressed by:

$$\rho_s(\mathrm{g/cm3}) = 0.917*(1.032\text{-}1.170*\mathrm{T(K)}*10\text{-}4) \tag{3.86}$$

$$\rho_l(\mathrm{g/cm^3}) = -7.1114+0.0882*T(\mathrm{K})-3.1959*\mathrm{T^2(K)}*10^{-4}+3.8649*T^3(\mathrm{K})*10^{-7} \tag{3.87}$$

$$c_{ps}(\mathrm{J/g°C}) = 2.114*(1+373.7*\mathrm{T(°C)}*10\text{-}5) \tag{3.88}$$

$$c_{pl}(\mathrm{J/g°C}) = 4.222*(1\text{-}54*\mathrm{T(°C)}*10\text{-}5) \tag{3.89}$$

The γ_{sl}, γ_{lv} and γ_{sv} dependence on R_{sl} can be described according to the Tolman approach [**33**]:

$$\frac{\gamma}{\gamma_\infty} = \left(1+\frac{2\delta}{r}\right)^{-1} \tag{3.90}$$

where $\gamma\infty$ and γ are, respectively, the surface tension competing to a flat surface (infinite curvature radius) and a surface of curvature radius r (now identifiable with R_{sl}), while δ is the Tolmann length whose order of magnitude corresponds to the effective water molecule diameter [**34**] dm and it is usually assumed [**35**] to be dm/3 (in the case of water, $\delta \approx 0.0681$ nm). The numerical solution [**35**] of eqs. (3.84)-(3.90) allows determining the Δh_R dependence on T_R as well as the T_R derivative with respect to R_{sl} ($\mathrm{d}T_R/\mathrm{d}R_{sl}$), fundamental functions for the determination of the mesh size distribution [*22*] dV_m/dR_m:

$$\frac{\mathrm{d}V_{\mathrm{m}}}{\mathrm{d}R_{\mathrm{m}}} = \frac{\mathrm{d}V_{\mathrm{s}}}{\mathrm{d}R_{\mathrm{m}}}\left(\frac{R_{\mathrm{m}}}{R_{\mathrm{m}}-\beta}\right)^Z = \frac{\mathrm{d}T_{\mathrm{R}}}{\mathrm{d}R_{\mathrm{sl}}}\frac{\dot{\mathrm{Q}}}{v\Delta h_R \rho_s}\left(\frac{R_{\mathrm{m}}}{R_{\mathrm{m}}-\beta}\right)^Z \tag{3.91}$$

where V_m is the meshes volume, R_m is the mesh radius (= ξ/2), V_s is the volume of the ice nano-crystals trapped inside the meshes, β is the constant thickness of the not-freezable water layer adsorbed on the mesh wall [**37**], v is the differential scanning calorimeter (DSC) heating speed, Q° is the DSC signal (W) and Z is the mesh shape factor. It is important to underline that the presence of a layer of not-freezable water adhering to the

mesh walls makes the mesh volume (V_m) greater than the nanocrystals volume (V_s) and, at the same time, it makes the mesh radius (R_m) equal to the crystal radius (R_{sl}) plus the thickness β (being β radius independent, $dR_{sl} = dR_m$). On the basis of Eq. (3.91), it is possible determining the probability *P* of finding a mesh of diameter $2*R_m$:

$$P = \mathrm{d}V_\mathrm{m} \Big/ \int_{2R_\mathrm{min}}^{2R_\mathrm{max}} \left(\frac{\mathrm{d}V_\mathrm{m}}{\mathrm{d}(2R_\mathrm{m})} \right) \mathrm{d}(2R_\mathrm{m}) \tag{3.92}$$

where R_{min} and R_{max} are, respectively, the minimum and maximum values for R_m (= ξ/2) (they indicate the distribution wideness).

The determination of *β*, essential for the *P* estimation, requires an iterative procedure [**37**, **32**]. This procedure relies on the evidence that the total amount of water constituting the hydrogel (W_t) is given by the sum of the water amount that can freeze inside the hydrogel (W_f), the amount that cannot freeze inside the hydrogel due to the interaction with mesh wall (W_{nf}) and the amount of water that is out of the polymeric network (bulk or excess water, W_e). While W_t can be estimated knowing the hydrogel mass and polymer concentration, W_f can be evaluated by measuring the amount of water melting below 0°C:

$$W_\mathrm{f} = \int_{T_R}^{0°C} \frac{\overset{\circ}{Q}}{v\Delta h_\mathrm{R}} \mathrm{d}T \tag{3.93}$$

In addition, we can be evaluated measuring the amount of water melting for T ≥ 0°C:

$$W_\mathrm{e} = \int_{0°C}^{T>0°C} \frac{\overset{\circ}{Q}}{v\Delta h_\mathrm{R}} \mathrm{d}T \tag{3.94}$$

Thus, the amount of non-freezable water (W_{nf}) can be calculated as:

$$W_\mathrm{nf} = W_\mathrm{t} - W_\mathrm{f} - W_\mathrm{e} \tag{3.95}$$

Consequently, mesh volume (V_m) can be calculated as the sum of freezable (V_f) and not-freezable (V_{nf}) water:

$$V_\mathrm{m} = \frac{W_\mathrm{nf}}{\rho_\mathrm{s}(0°\mathrm{C})} + V_\mathrm{f} \qquad \text{where} \qquad V_\mathrm{f} = \int_{T_R}^{0°C} \frac{\overset{\circ}{Q}}{v\Delta h_\mathrm{R}\rho_\mathrm{s}(T)} \mathrm{d}T \tag{3.96}$$

Now, an iterative procedure is started assuming β = 0 and calculating the mesh volume V_{mc} as follows:

$$V_\mathrm{mc} = \int_{\mathrm{R_{min}}(T_R<0°C)}^{\mathrm{R_{max}}(T=0°C)} \frac{\mathrm{d}T_\mathrm{R}}{\mathrm{d}R_\mathrm{sl}} \frac{\overset{\circ}{Q}}{v\Delta h_R\rho_s} \left(\frac{R_\mathrm{m}}{R_\mathrm{m} - \beta} \right)^Z \mathrm{d}R_\mathrm{sl} \tag{3.97}$$

When the relative difference $\Delta V = |V_{mc} - V_m|/V_m$ is lower than a fixed tolerance ε, the assumed value for β is correct. Hence, the procedure is repeated increasing β of Δβ up to convergence. As β is usually bigger than 0.5 nm [**32**], a prudential choice guaranteeing the convergence of the procedure consists in setting Δβ = 0.01 nm [**37**]. This setting is usually compatible with the choice of $\varepsilon = 10^{-5}$.

3.4 Scanning Electron Microscopy

A scanning Electron Microscope (SEM) is a powerful magnification tool that utilizes focused beams of electron to obtain topographical, morphological and compositional information. In addition, a Scanning Electron Microscope can detect and analyze surface fractures, provide information in microstructures, examine surface contaminations, reveal spatial variations in chemical compositions, provide qualitative chemical analyses and identify crystalline structures. SEMs can be as essential research tool in fields such as life science, biology, gemology, medical and forensic science, metallurgy. In addition, SEMs have practical industrial and technological applications such as semiconductor inspection, production line of miniscule products and assembly of microchips for computers [**38**].

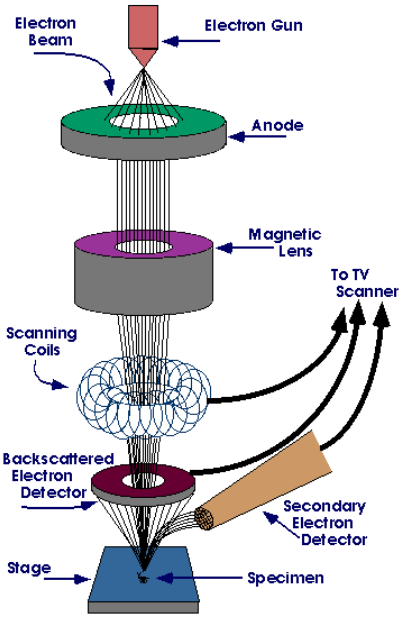

Figure 3.32: Structure of SEM machine.

A scanning electron microscope consist of the following components:

- Electron Source
- Thermionic Gun
- Field Emission Gun
- Electromagnetic and/or Electrostatic Lenses
- Vacuum Chamber
- Sample chamber and stage
- Computer
- Detectors (one or more)
- Secondary Electron Detector (SED)
- Backscatter Detector
- Diffracted Backscatter Detector (EBSD)
- X-ray Detector (EDS)

In addition, SEMs require a stable power supply, vacuum and cooling system, vibration - free space and need to be housed in an area that isolates the instrument from ambient magnetic and electric fields. A SEM provides details surface information by tracing a sample in a raster pattern with an electron beam. The process begins with an electron gun generating a beam of energetic electrons down the column and onto a series of electromagnetic lenses. These lenses are tubes, wrapped in coil and referred to as solenoids. The coils are adjusted to focus the incident electron beam onto the sample; these adjustments cause fluctuations in the voltage, increasing/decreasing the speed in which the electrons come in contact with the specimen surface. Controlled via computer, the SEM operator can adjust the beam to control magnification as well as determine the surface area to be scanned. The beam is focused onto the stage, where a solid sample is placed. Most samples require some preparation before being placed in the vacuum chamber. Of the variety of different preparation processes, the two most commonly used prior to SEM analysis are sputter coating for non-conductive samples and dehydration of most biological specimens. In addition, all samples need to be able to handle the low pressure inside the vacuum chamber. The interaction between the incident electrons and the surface of the sample is determined by the acceleration rate of incident electrons, which carry significant amounts of kinetic energy before focused onto the sample. When the incident electrons come in contact with the sample, energetic electrons are released

from the surface of the sample. The scatter patterns made by the interaction yields information on size, shape, texture and composition of the sample. A variety of detectors are used to attract different types of scattered electrons, including secondary and backscattered electrons as well as X-rays. Backscatter electrons are incidental electrons reflected backwards; images provide composition data related to element and compound detection. Although topographic information can be obtained using a backscatter detector, it is not as accurate as an SED. Diffracted backscatter electrons determine crystalline structures as well as the orientation of minerals and micro-fabrics.X-rays, emitted from beneath the sample surface, can provide element and mineral information. Image magnification can be up to 10 nanometers and, although it is not as powerful as its TEM counterpart, the intense interactions that take place on the surface of the specimen provide a greater depth of view, higher-resolution and, ultimately, a more detailed surface picture. Advantages of a Scanning Electron Microscope include its wide-array of applications, the detailed three-dimensional and topographical imaging and the versatile information garnered from different detectors. SEMs are also easy to operate with the proper training and advances in computer technology and associated software make operation user-friendly.This instrument works fast, often completing SEI, BSE and EDS analyses in less than five minutes. In addition, the technological advances in modern SEMs allow for the generation of data in digital form [**38**]. The disadvantages of a Scanning Electron Microscope start with the size and cost.SEMs are expensive, large and must be housed in an area free of any possible electric, magnetic or vibration interference. Maintenance involves keeping a steady voltage, currents to electromagnetic coils and circulation of cool water. Special training is required to operate an SEM as well as prepare samples. In addition, SEMs are limited to solid, inorganic samples small enough to fit inside the vacuum chamber that can handle moderate vacuum pressure. Finally, SEMs carry a small risk of radiation exposure associated with the electrons that scatter from beneath the sample surface. The sample chamber is designed to prevent any electrical and magnetic interference, which should eliminate the chance of radiation escaping the chamber. Even though the risk is minimal, SEM operators and researchers are advised to observe safety precautions.

A high-resolution SEM image can show detail down to 25 Angstroms, or better. When used in conjunction with the closely-related technique of energy-dispersive X-ray

microanalysis (EDX, EDS, EDAX), the composition of individual crystals or features can be determined. A development of the normal high-vacuum scanning electron microscope is the ESEM, or Environmental SEM. The ESEM can operate with air in the specimen chamber - the pressure is lower than atmospheric pressure but higher that the high-vacuum of a normal SEM. This has the advantage that wet specimens can be examined without them dehydrating and is especially useful for biological specimens and other specimens containing water, such as freshly-mixed cement paste.

3.5 Micro Computed Tomography

Feldkamp et al. pioneered micro-CT when they developed an X-ray-based microtomographic system to analyze trabecular samples at a spatial resolution of 50 mm [**39**, **40**]. Since then, micro-CT had been used extensively in the study of trabecular architecture [**41**] and there are increasing applications of it in other areas. Its popularity can be attributed to its ability to provide precise quantitative and qualitative information on the 3D morphology of the specimen. The interior of the specimen can be studied in great detail without resorting to physical sectioning and using toxic chemicals. Moreover, after scanning, the intact samples can be subjected to other tests, therefore resolving the problem of sample scarcity. As researchers began to recognize the potential of this radiographic technique, various biomedical applications are being explored which would include the assessment of scaffolds structure, tissue regeneration [**42**] and vasculature networks [**43-45**]. In micro-CT scanning, the specimen is computed as a series of 2D slices which are irradiated from the edges with X-rays. Upon transversing through the slice, the X-rays are attenuated and the emergent X-rays with reduced intensities are captured by the detector array. From the detector measurements, the X-ray paths are calculated and the attenuation coefficients are derived. A 2D pixel map is created from these computations and each pixel is denoted by a threshold value which corresponds to the attenuation coefficient measured at a similar location within the specimen. As the attenuation coefficient correlates to the material density, the resultant 2D maps reveal the material phases within the specimen. The quality of the 2D maps is dependent on the scanning resolution which ranges from 1 to 50 mm [**39**, **46**]. At high resolutions, intricate details are imaged, however more time is required for high resolution scanning and the resultant large data set poses a challenge for data storage and processing. 3D modelling programs such as Image Pro Plus (Media Cybernetics) stacks the 2D maps to create 3D models. As computation is inherent in this technique, the selection of software and hardware facilities would influence the efficiency and effectiveness of this radiographical assessment. The recent use of μ-CT in scaffold research enabled morphological studies to be carried out, yielding comprehensive data sets. From the scan data, measurements of the scaffold material volume, surface area, trabecular width and pore sizes were taken.

Using threshold inversion, the pore network was visualized and the pore interconnectivity was studied [**40]**

Mechanical tests are conducted so as to ascertain the mechanical properties of the scaffold, however most of these tests are destructive; hence, a non-destructive method is sought. Researchers have considered finite element modelling (FEM) as an alternative to mechanical testing as simulations can be carried out via computations. FEM requires the input of precise 3D structural and architectural information of scaffolds, which can be obtained from μ-CT scans [**47**]. Similarly, diffusion patterns in scaffolds can also be investigated through fluid flow studies which are simulated via FEM. Scaffolds with intricate interior structures can be scrutinized using μ-CT, as any spatial location of the architecture can be digitally isolated out. This is crucial for scaffolds that exhibit different geometric layouts at different spatial locations. Micro Computed Tomography possesses this key advantage over other techniques such as mercury and flow porosimetry.

Within the digitally excised scaffold cube, scaffold material volume and surface area are measured, thus allowing the calculation of porosity and surface area to volume ratio. Three-dimensional imaging allows a close up view of any specific location, thus the observation of pore shape and the measurement of pore size and trabecular thickness can be conducted in these close ups. Scaffold anisotropy is evaluated via algorithms [**48**] and the cross-sectional area can be measured from the 2D slice images. By inverting the threshold, a negative image is created which captures only the scaffold pores. By measuring the total and the interconnected pore volumes, interconnectivity is derived [**39**]. In studying scaffold permeability, a suitable visualization program needs to be selected. As μ-CT employs penetrative X-rays, closed pores can be imaged. The flexibility of micro CT analysis allows the evaluation of foams, textiles and nanofiber scaffolds. There are associated concerns despite of the numerous advantages of using μ-CT. Image thresholding is a crucial step that has to be executed prior to 3D modelling and it affects the subsequent analysis and visualization [**48**, **49**]. In the conventional approach, the thresholding range is selected via histographics and visual estimation and the problem arises when the scaffold composes of multiple materials whose thresholding ranges overlap and this renders the digital separation of these materials a difficult task. Moreover, as polychromatic X-ray beams are used in micro CT, the lower energy rays would be readily attenuated by the sample resulting in a high exposure at the centre of the scaffold.

This effect is known as beam hardening and as a result thresholding is no longer dependent solely on radio-density but also on the specimen size [**42**]. Micro CT analysis is not suitable for scaffolds containing metals as X-rays are heavily attenuated by these metals. The presence of metals results in dark and bright grainy artifacts which obscure important details in the scan images [**40**]. As μ-CT is a relatively new technology, improved algorithms and setups are anticipated, thus resolving such imaging errors.

References:

1. Gunter, H., NMR Spectroscopy: Basic principles, Concepts, and Applications in Chemistry 2nd ed. 1995: Wiley.
2. Rahman, A.U., Nuclear Magnetic Resonance: Basic Principles 1986, Berlin: Springer
3. Gambaro, S., Risonanza Magnetica Nucleare: Appunti di Lezione 2008, Stan's Library
4. Rahman, A.u and M.I. Choudhary, Solving Problems with NMR Spectroscopy 1996 Accademic Press
5. Vanhamme, L., et al., MR spectroscopy quantitation: a review of time-domain methods NMR in Biomedicine, 2001. 14(4): p. 233-46.
6. . Press, W.H., et al., Numerical recepies in FORTRAN. 2nd ed. 1992, Cambridge USA: University Press.
7. Brun, M., Lallemand, A., Quinson, J.-F., Eyraud, C.(1977). A new method for the simulataneous determination of the size and the shape of pores: the thermoporometry. Thermochim. Acta, 21, pp. 59-88.
8. Whittal, K. P., MacKay, A. L. (1989). Quantitative interpretation of NMR relaxation data. J. Magnetic Resonance, 84, pp. 134-152.
9. Provencher, S. W. (1982). A constrained regularization method for inverting data represented by linear algebraic or integral equations. Comput. Phys. Comm., 27, pp. 213-227.
10. Wang, X., Ni, Q. J. (2003). Determination of of cortical bone porosity and pore size distribution using low field pulsed NMR approach. J. Orthopaedic Research, 21, pp. 312-319.
11. Chui, M. M., Phillips, R. J., McCarthy, M. J. (1995). Measurement of the porous microstructure of hydrogels by nuclear magnetic resonance. J. Coll. Inter. Sci., 174, pp. 336-344.
12. Brownstein, K. R., Tarr, C. E. (1979). Importance of classical diffusion in NMR studies of water in biological cells. Phys. Rew. A, 19, 2446-2453.
13. Scherer, G. W. (1994). Hydraulic radius and mesh size of gels. J. Sol-Gel Sci. Technol., 1, pp. 285-291.

14. Tim Stait-Gardner, Scott A. Willis, Nirbhay N. Yadav, Gang Zheng, and William S Price, "NMR Diffusion Measurements of Complex Systems", diffusion-fundamentals.org 11 (2009) 15:, 1-22.

15. Stejskal EO, Tanner JE. "Spin Diffusion Measurements: Spin Echoes in the Presence of a Time-Dependent Field Gradient", J Chem Phys 42 (1965): 288-292.

16. "Mq Series Manuals", Bruker Optik GmbH, Version 1, (2001).

17. Latour L.L. et al., "Time dependent diffusion coefficient of fluids in porous media as probe of surface to volume rato", J. Magnetic Resonance A, (1993), 101(3), 342-346

18. Mitra P.P., Sen P.N., and Schwartz L.M., "Short-time Behavior of the Diffusion Coefficient as a Geometrical Probe of Porous Media", Physical Review B Volume 47, Number 14 (1993) 8565-8574.

19. Coviello T., Matricardi P., Alhaique F., Farra R., Tesei G., Fiorentino S., Asaro F., Milcovich G., Grassi M. Guar gum/borax hydrogel: rheological, low field NMR and release characterizations Express Polymer Letters, 2013 7(9), 733-746.

20. Amsden, B. (1998). Solute Diffusion within Hydrogels. Mechanisms and Models. Macromolecules, 31, pp. 8382-8395.

21. Grassi, M., Grassi G., Lapasin R., Colombo, I. (2007) Understanding Drug Release and Absorption Mechanisms: a physical and mathematical approach. (CRC Press, Boca Raton, USA).

22. Fierro, D., Scharnagl, N., Emmler, T., Boschetti-de-Fierro, A., Abetz, V. (2011). Experimental determination of self-diffusivities through a polymer network for single components in a mixture. J. Membr. Sci., 384, 63-71.

23. Peppas, N. A., Merrill, E. W. (1977). Crosslinked poly(vinyl alcohol) hydrogels as swollen elastic networks, J. Appl. Polym. Sci., 21, pp. 1763-1770.

24. Vrentas, J. S., Duda, J. L., Ju, S. T., Liu, H. T. (1982). Prediction of diffusion coefficients for polymer-solvent systems. AIChe J., 28, pp. 279-285.

25. Patankar, S. V. (1990). Numerical heat transfer and fluid flow. (Hemisphere Publishing, New York, USA).

26. Meyvis, T.K.L., S.C. De Smedt, and J. Demeester, Rheological monitoring of long-termdegrading polymer hydrogels. J Rheol, 1999. 43(4): p. 933-40.

27. Brun, M., et al., A new method for the simultaneous determination of the size and shape of pores: the thermoporometry. Thermochim Acta, 1977. 21(1): p. 59-88.

28. Zhang, M., et al., Size-dependent melting point depression ofnanostructures: Nanocalorimetric measurements. Physical Review B, 2000. 62: p. 10548–10557.

29. Yamamoto, T., et al., Evaluation of porous structure of resorcinol-formaldehyde hydrogelsby thermoporometry Thermochim Acta, 2005. 439(1-2): p. 74-9.

30. Landry, M.R., Thermoporometry by differential scanning calorimetry: experimentalconsiderations and applications Thermochim Acta, 2005. 433(1-2): p. 27-50.

31. Brun, M., Lallemand, A., Quinson, J.F., Eyraud, C. (1973). Changement d'etat liquide-solide dans les milieux poreux. J. De Chimie Physique, 70, pp. 979-989.

32. Ishikiriyama, K., Todoki, M., Motomura, K. (1995). Pore size distribution (PSD) measurements of silica gels by means ofdifferential scanning calorimtery. J. Colloid Interface Sci., 171, pp. 92-102.

33. Tolman, R. C. (1949). The effect of droplet size on surface tension. J. Chem. Phys., 17, pp. 333-337.

34. Samsonov, V. M., Sdobnyakov, N. Y., Bazulev, A. N. (2004). Size deoendence of the surface tension and the problem of Gibbs thermodynamics extension to nanosystems. Colloids Surf. A, 239, pp. 113-117.

35. Rowlinson, J. S., Widom, B. (2003). Molecular Theory of Capillarity (Clarendon Press, Oxford, GB).

36. Pescosolido, L., Feruglio, L., Farra, R., Fiorentino, S. M., Colombo, I., Coviello, T., Matricardi, P., Hennink, W. E., Tina Vermonden, T., Grassi, M. (2012). Mesh size distribution determination of interpenetrating polymer network hydrogels. Soft Matter, 8, pp. 7708-7715.

37. Ishikiriyama, K., Sakamoto, A., Todoki, M., Tayama, T., Tanaka, K., Kobayashi, T. (1995). Pore size distribution measurements of polymer hydrogel membranes for artificial kidney using differential scanning calorimetry. Thermochim. Acta, 267, pp. 169-180.

38. http://www.purdue.edu/ehps/rem/rs/sem.htm

39. Feldkamp, L.A., Goldstein, S.A., Parfitt, A.M., Jesion, G., and Kleerekoper, M. (1989). The direct examination of three dimensional bone architecture in vitro by computed tomography. J Bone Miner. Res. 4, 3-11.

40. Ho, S.T., and Hutmacher, D.W. (2006). A comparison of micro CT with other techniques used in the characterization of scaffolds. Biomaterials 27, 1362-1376.

41. Ruegsegger, P., Koller, B., and Muller, R. (1996). A microtomographic system for the nondestructive evaluation of bone architecture. Calcif. Tissue Int. 58, 24-29.

42. Verna, C., Dalstra, M., Wikesjo, U.M., and Trombelli, L. (2002). Healing patterns in calvarial bone defects following guided bone regeneration in rats. A micro CT scan analysis. J Clin. Periodontol. 29, 865-870.

43. Bentley, M.D., Ortiz, M.C., Ritman, E.L., and Romero, J.C. (2002). The use of microcomputed tomography to study microvasculature in small rodents. Am J Physiol Regul. Integr. Comp Physiol 282, R1267-R1279.

44. Jogensen, S.M., Demirkaya, O., and Ritman, E.L. (1998). Three dimensional imaging of vasculature and parenchyma in intact rodent organs with X-ray micro-CT. Am J physiol 275, H1103-H1114.

45. Ortiz, M.C., Garcia-Sanz. A., Bentley, M.D., Fortepiani, L.A., Garcia-Estan, J., Ritman, E.L., Romero, J.C., and Juncos, L.A. (2000). Microcomputed tomography of kidneys following chronic bile duct ligation. Kydney Int. 58, 1632-1640.

46. Weiss, P., Obadia, L., Magne, D., Bourges, X., Rau, C., Weikamp, T., Khairoun, I., Bouler, J.M., Chappard, D., Gauthier, O., and Daculsi, G. (2003). Synchrotron X-ray microtomography (on a micron scale) provides three dimensional imaging representation of bone ingrowth in calcium phosphate biomaterials. Biomaterials 24, 4591-4601.

47. Jaecques, S.V., Van, O.H., Muraru, L., Van, C.T., De, S.E., Wevers, M., Naert, I., and Vander, S.J. (2004). Individualised, micro-CT based finite element modeling as a tool for biomechanical analysis related to tissue engineering of bone. Biomaterials 25, 1683-1696.

48. Meinel, L., Karageorgiou, V., Fajardo, R., Snyder, B., Shinde-Patil, V., Zichner, L., Kaplam, D., Langer, R., and Vunjalk-Novakovic, G. (2004). Bone tissue

engineering using human mesenchymal stem cells: effects of scaffold material and medium flow. Ann. Biomed. Eng.32, 11-122.

49. Duvall, C.L., Taylor, W.R., Weiss, D., and Guldberg, R.E., (2004). Quantitative microcomputed tomography analysis of collateral vessel development after ischemic injury. Am J Physiol Heart Circ. Physiol 287, H302-H310.

4 Homogeneous Gels

In this chapter, two different types of homogeneous gels are considered. The first one is represented by *guar gum* (GG) and *guar gum borax* (GGb), while the second is represented by *alginate* and *pluronic F127*. Both hydrogels types are characterized by means of rheology and low field nuclear magnetic resonance. In addition, while release tests are performed in the case of GGb hydrogels, TEM characterization is adopted for the *alginate*/*pluronic F127* hydrogels. Basically, all these characterizations serve to estimate the mesh size (ξ) of the polymeric network.

4.1 Guar Gum and Guar Gum borax Hydrogels

4.1.1 Introduction

Guar gum (GG) is a neutral galactomannan, extracted from the seeds of *Cyamopsis tetragonoloba*. It consists of a linear backbone of $\beta(1\rightarrow4)$-linked D-mannopyranose units (Man) and with the presence of randomly attached $\alpha(1\rightarrow6)$-linked galactopyranose units (Gal) as side chains [**1**]. Due to the presence of these galactose units, the polymer is soluble in water [**2**]. The ratio of mannose to galactose units (M/G) depends on climate variations and ranges from 1.5:1 to 1.8:1. Because of its low cost and its ability to produce a highly viscous solution even at low concentrations, GG finds important applications in food [**3**], in oil recovery [**4**] and in personal care industries [**5**]. Other industrial applications of guar gum include the textile industry where guar gum's excellent thickening properties are used for textile sizing, finishing and printing. In the paper industry, guar is used as an additive as it gives denser surface to the paper used in printing. In the food, pharmaceutical and cosmetics industry guar gum is used as an effective binder, stabilizer, and thickener. In cosmetics, especially shampoos and toothpastes, guar gum is used primarily as a thickener and suspending agent. In beverages, it is used as stabilizer for preparing chocolate drinks and juices.

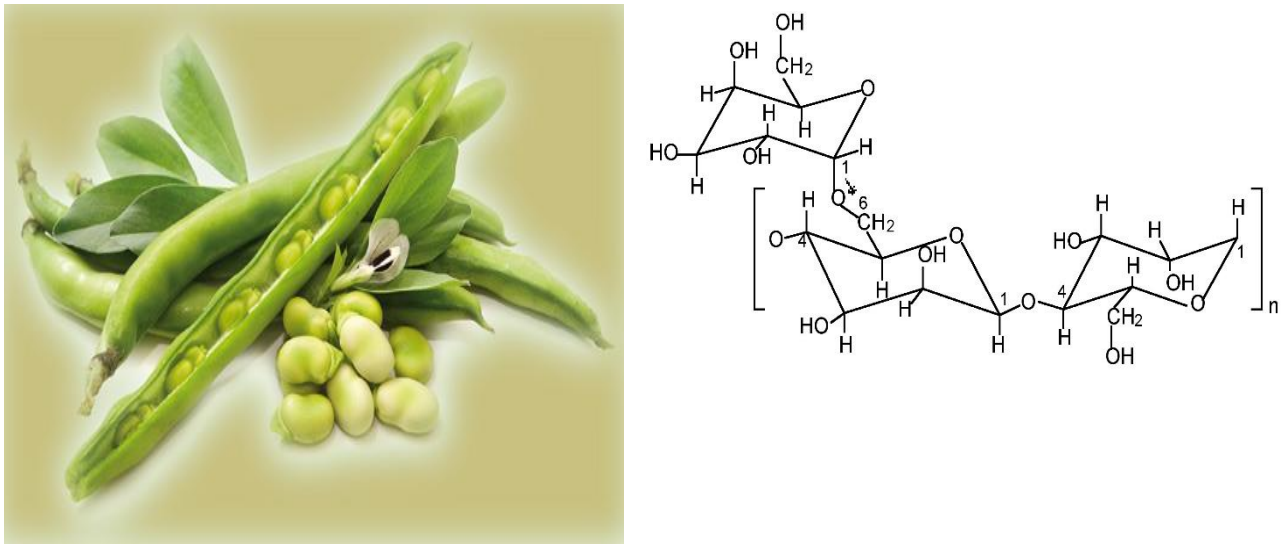

Figure 4.1: Left: the Cyamopsis tetragonoloba. **Right**: the chemical structure of the guar gum.

The high viscosity of GG solutions arises from the high molecular weight of GG (up to 2 million and further) [**6**] and from the presence of extensive intermolecular associations (entanglements) by means of hydrogen bonds.

In aqueous solution GG assumes a flexible coil conformation as evidenced by the Mark-Houwink-Sakurada exponent and by the relatively low value of its characteristic ratio and its persistence length [**7**]. GG, crosslinked with glutaraldehyde, was proposed for colon delivery [**8**], and it was also tested as a matrix for oral solid dosage forms [**9**].

Scleroglucan (SCLG), a water soluble polysaccharide produced by fungi of the genus Sclerotium, consists of a main chain of (1–3)-linked β-D-glucopyranosyl units bearing, every third unit, a single β-D-glucopyranosyl unit linked (1–6). It is known that SCLG assumes a triple-stranded helical conformation in aqueous solution and a single coiled disordered conformation in methylsulphoxide or at high pH values (NaOH >0.2 M) [**10-11**]. Due to its peculiar properties, SCLG was extensively used for various commercial applications (secondary oil recovery, ceramic glazes, food, paints, cosmetics, etc.) [**12**] and it was also investigated for modified/sustained release formulations and ophthalmic preparations [**13**].

Actually, it is well known that borax is an efficient crosslinker for polymers bearing hydroxyl groups but the type of formed linkages is still debated and so far, two main models have been proposed. The most popular one implies the existence of pure chemical crosslinks between the polymeric chains and borax [**14**], and it was proposed for the

GG/borax interactions. According to the other model, the borax ions hold together the polymeric chains by means of mixed physical/chemical linkages. This model was firstly proposed for poly-(vinyl-alcohol) [**15**] and it was recently suggested also for SCLG [**16**, **17**]. The considerable effort devoted to the study of polymer-ion complexes is due to the wide range of application of these systems. In particular, the complex between GG and borate was previously studied by several authors [**18**, **19**] that investigated the effect of polymer and borate concentration, temperature, environmental pH conditions and GG molecular weight on the peculiar rheological properties detected by the frequency dependence of relaxation spectra.

It is interesting to note that both, GG and SCLG, interact with borax leading to a three-dimensional network that, besides the intrinsic differences between the two polymers, (see below), shows a peculiar anisotropic elongation during swelling, when tablets of these two systems are prepared. In particular, GG and SCLG show important different characteristics: (a) GG dissolves in water as a random coil while SCLG exhibits a triple helix conformation in aqueous solution with a persistence length of about 200 nm [**10**, **20**]; (b) borax promotes a rapid gelation of GG [**21**] by means of crosslinks characterized by a lifetime of the order of seconds [**22**], leading to self-healing properties of the network. On the other side, SCLG requires several hours for gelation in the presence of borax and no self-healing occurs. Nevertheless, both, GG and SCLG, in the presence of borax, are capable to give self-sustaining gels [**23**]. Furthermore, also the interaction with borax takes place in a different way. In the case of SCLG the borax promotes mixed (chemical and physical) interactions between triplexes; on the other side, in the case of GG, the borax forms chemical bridges between chains by means of reversible linkages. In addition, molecular dynamics simulation and AFM images indicate that the borax groups increase the stiffness of GG making such system more similar to SCLG-borax. Upon swelling, the labile nature of the borax cross-links in the GG makes the inter-chains interactions able to undergo the needed rearrangement, similar to that of SCLG where full chemical bridges are not present. These similarities explain the quite unexpected parallel swelling behavior of GG and SCLG, in the presence of borax [**16**, **23**]. However, in all these previous research works, no attention was specifically focused on the estimation of the mesh sizes of the networks, a very important parameter affecting the possible industrial and bio-pharmaceutical applications that these hydrogels may have.

4.1.2 Experimental Section

4.1.2.1 Materials

Guar Gum (GG) was provided by CarboMer (San Diego, USA). The ratio between mannose and galactose was estimated by means of ^{1}H NMR (carried out at 70 °C with a Brucker AVANCE AQS 600 spectrometer, operating at 600.13 MHz) and an M/G value of ≈1.5 was found. The molecular weight ($1.2 \bullet 10^6$) was estimated by means of viscosimetric measurements carried out at 25 °C. Scleroglucan (SCLG) was provided by Degussa (Germany). The molecular weight ($1.1 \bullet 10^6$) was estimated by means of viscosimetric measurements carried out at 25 °C in 0.01 M NaOH. For the viscosity measurements, an automatic viscometer (Instrument Schott AVS 370, Lauda, Germany) with a water bath (Lauda 0.15 T) allowing the temperature control to 0.1 °C was used. An Ubbelohde capillary viscometer (Type No 531 01, with a capillary diameter = 0.54 mm, Schott-Geräte) for dilution sequences was used. The GG solutions were prepared in distilled water while the SCLG solutions were prepared in 0.01 N NaOH (in order to break possible aggregates). Before measurements, the samples were filtered twice with 1.2 μ Millipore filters. From the flux time of solvent and solutions the intrinsic viscosity, [η] (cm^3/g), was estimated for each polymer. According to the Mark-Houwink-Sakurada equation, the intrinsic viscosity is related to the molar mass of the sample: $[\eta] = KM_w^a$, where K and *a* are constants for each polymer-solvent system at a given temperature. From the value of K and *a* found in the literature for the GG [**11**] and for the SCLG [**7**] samples, the molecular weight of the two polymers were evaluated.

Theophylline (TPH, molecular weight 198, radius of van der Waals = 3.7 Å) and borax were Carlo Erba products (Italy), Vitamin B_{12} (Vit B_{12}, molecular weight 13,500) was purchased from Fluka (Germany). All other products and reagents were of analytical grade. Distilled water was always used.

4.1.2.2 Purification Polymer

A given amount of polymer (GG and SCLG) was dissolved in distilled water (polymer concentration, cp = 0.5% w/v). GG samples were kept under magnetic and mechanical stirring at 60° C for 24 h and then at room temperature for 24 additional hours [**24**]. SCLG samples were kept under magnetic and mechanical stirring for 24 h at room temperature.

The resulting solutions were exhaustively dialyzed at 7 °C against distilled water with dialysis membranes of a cut-off 12,000 – 14,000 and then freeze dried. The lyophilized products were stored in a desiccator until use.

4.1.2.3 Hydrogels preparation

A given amount of GG or SCLG (200 mg for the release experiments and 35 mg for the rheological analysis and for NMR measurements; cp = 0.7% w/v) was dissolved in water for 24 h. GG and SCLG crosslinking was carried out by addition of 0.1 M borax solution to the homogeneous polymer system in order to get a unitary value of the ratio between borax moles and moles of the repeating GG or SCLG units (r = 1). The resulting mixture was magnetically stirred for 5 min and then left for 2 days at 7 °C for gel setting. For the release experiments, a known amount of model drug was first dissolved in water before the addition of the polymer.

4.1.2.4 Rheological characterization

The rheological characterization, carried out at 25 and 37 °C, was performed by means of a controlled stress rheometer, Haake Rheo-Stress RS300 model, with a Thermo Haake DC50 water bath. Two geometries were used: a cone–plate device (C60/1 Ti with a cone diameter of 60 mm and a cone angle of 1° and a MP60 steel 8/800 plate with a diameter of 60 mm, Haake) for the GG and SCLG samples and a grained plate-plate device (Haake PP35/S: diameter = 35mm; gap between plates = 1mm) was used for the SCLGb and GGb samples in order to prevent wall slippage phenomena [**25**]. To perform the measurements on SCLGb and GGb, the hydrogels, obtained with a thickness of 1.0–3.0 mm, were removed with the aid of a small spatula from the beaker in which they had settled, and they were laid with care on the lower plate of the rheometer. The upper plate was then lowered until it reached the hydrogel surface. Gap-setting optimizations were undertaken according to a procedure described elsewhere [**26**]. When GG or SCLG were tested, an appropriate amount of the samples was spread onto the plate geometry to obtain a sample of the appropriate height. To avoid gel shrinking due to a possible solvent evaporation, the equipment was kept inside a glass bell with a constant moisture level. Rheological properties were studied by means of oscillatory tests. In particular, the hydrogel linear viscoelastic regions were assessed, at 1 Hz, by stress sweep experiments. Frequency

sweep tests were carried out in the frequency (f) range 0.01–100 Hz at constant deformations γ = 0.01 (well inside the linear viscoelastic range for all the studied hydrogels). Each test was carried out in duplicate.

4.1.2.5 LF-NMR characterization

Low Field NMR (LF - NMR) characterization was performed, at 25 and 37 °C, by means of a Bruker Minispec mq20 (0.47 T, 20 MHz). Transverse relaxation time (T_2) measurements were carried out according to the (Carr-Purcell-Meiboom-Gill; CPMG) sequence (number of scans = 4; delay = 5 s). In order to study water mobility inside the hydrogel network, Pulsed Gradient Spin Echo (PGSE) measurements were performed. The applied sequence consists in the classical echo sequence with two equal gradient pulses (of length δ = 0.5 ms) occurring at x_1 = 0.1 ms and x_2 = 0.1 ms after the 90° and 180° pulses, respectively. The time separation, indicated by Δ ($\approx \tau$-x_1-δ+x_2), is related to the diffusion time, t_d, according to $t_d = (\Delta - \delta/3)$. After an appropriate calibration procedure, based on the knowledge of the free water self-diffusion coefficient (D_{H2O}), it is possible measuring the average water self-diffusion coefficient inside the hydrogel (D). The details of this calibration procedure can be found in the Bruker Manual, mq Gradient Unit Users Guide, version 1, January 2000, and it essentially replicates the standard procedures for the D determination used in high field NMR [**27**]. In the case of T_2 measurements, data are the average of 27 experiments (9 repetitions for three different samples), while in the case of PGSE measurements, data are the average of 15 experiments (5 repetitions for three different samples).

The combination of the information coming from the relaxation and PGSE experiments were used for the estimation of the mesh size distribution of our polymeric hydrogels.

4.1.2.6 Release

The hydrogels, freshly prepared in a beaker (thus in their swollen form), assumed the cylindrical shape of the vessel (height = 1.0 cm, diameter = 2.2 cm) and they were tested for the release of the two model drugs TPH and Vit B_{12}, at 37 °C. The gels were immersed in 200 ml (V_r) of distilled water (pH = 5.4), and they were kept at a certain height from the bottom of the container by a thin web. The medium was gently magnetically stirred and 3ml samples were withdrawn from the solution at appropriate time intervals and replaced with the same amount of fresh solvent (thus, experimental concentration data were corrected for dilution). The amount of the released model drug was spectrophotometrically detected (TPH at 272 nm, Vit. B_{12} at 361 nm), by means of a Perkin-Elmer (lambda 3a, UV–Vis) spectrometer using quartz cells with path-lengths of 1.0 or 0.1 cm. All experiments were carried out in triplicate. The possible erosion of the gel, in terms of polymer dissolution in the medium during the release experiments, was quantitatively determined by a colorimetric method [**28**] using phenol in the presence of sulphuric acid. Obtained results indicate that such erosion, in the first 8 h, is almost negligible ($\leq 4\%$).

4.1.3 Results and Discussion

Stress sweep tests, carried out at 25 and 37 °C, indicated that for all studied systems (GG, GGb, SCLG and SCLGb), the critical deformation γ_c is always much higher than the constant one ($\gamma = 0.01$) applied in frequency sweep tests. *Figure 4.2* and *4.3* show the mechanical spectra referring to the four systems, studied at 25 and 37 °C, respectively. It can be noticed (see *Figure 2a*) that, at 25 °C, SCLG exhibits a gel behavior as the elastic modulus (*G'*) is always bigger than the viscous one (*G''*) and both are, almost, pulsation (ω) independent. On the other side, GG shows the typical solution behavior as *G''* prevails on *G'* and both moduli depend on ω. Five and four Maxwell elements are, respectively, necessary for a statistically good description (see F test values in *Figure 4.2a* caption) of the GG and SCLG mechanical spectra (see fitting parameters values in *Table 4.1*).

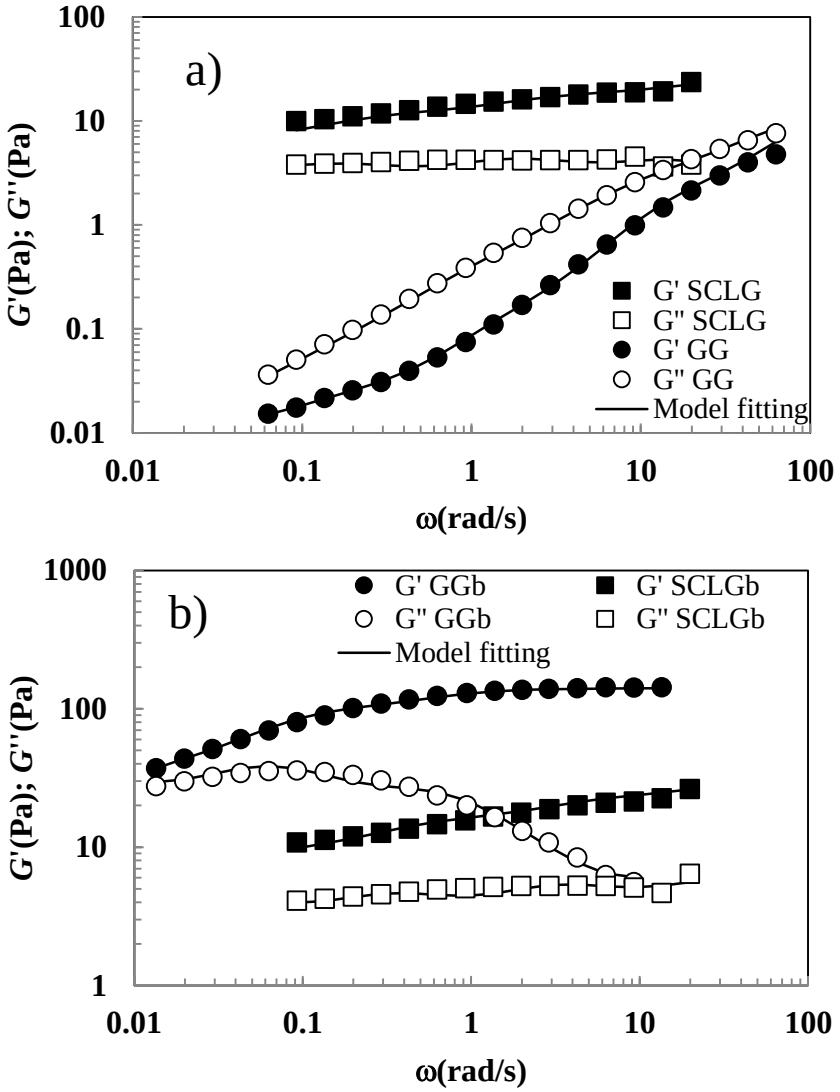

Figure 4.2: a) mechanical spectra (*G*' elastic modulus, *G*'' viscous modulus) referring to the Guar gum (GG) and Scleroglucan (SCLG) systems at 25 °C. Solid lines indicate the best fitting of the generalized Maxwell Model (*F* test always positive: $F_{GG}(5,32,0.95) < 150$, $F_{SCLG}(4,25,0.95) < 374$). **b)** mechanical spectra (*G*' elastic modulus, *G*'' viscous modulus) referring to the Guar gum/borax (GGb) and Scleroglucan/borax (SCLGb) systems at 25 °C. Solid lines indicate the best fitting of the generalized Maxwell Model (eqs.(1), (2)) (*F* test always positive: $F_{GGb}(4,32,0.95) < 103.5$, $F_{SCLGb}(5,24,0.95) < 251$).

Figure 4.2b clearly shows the different effect of borax addition to the GG and SCLG systems. In fact, while borax presence plays a marginal role in the case of SCLG (only a very small increase of the moduli can be noticed), for the GG system a relevant change occurs in the mechanical properties.

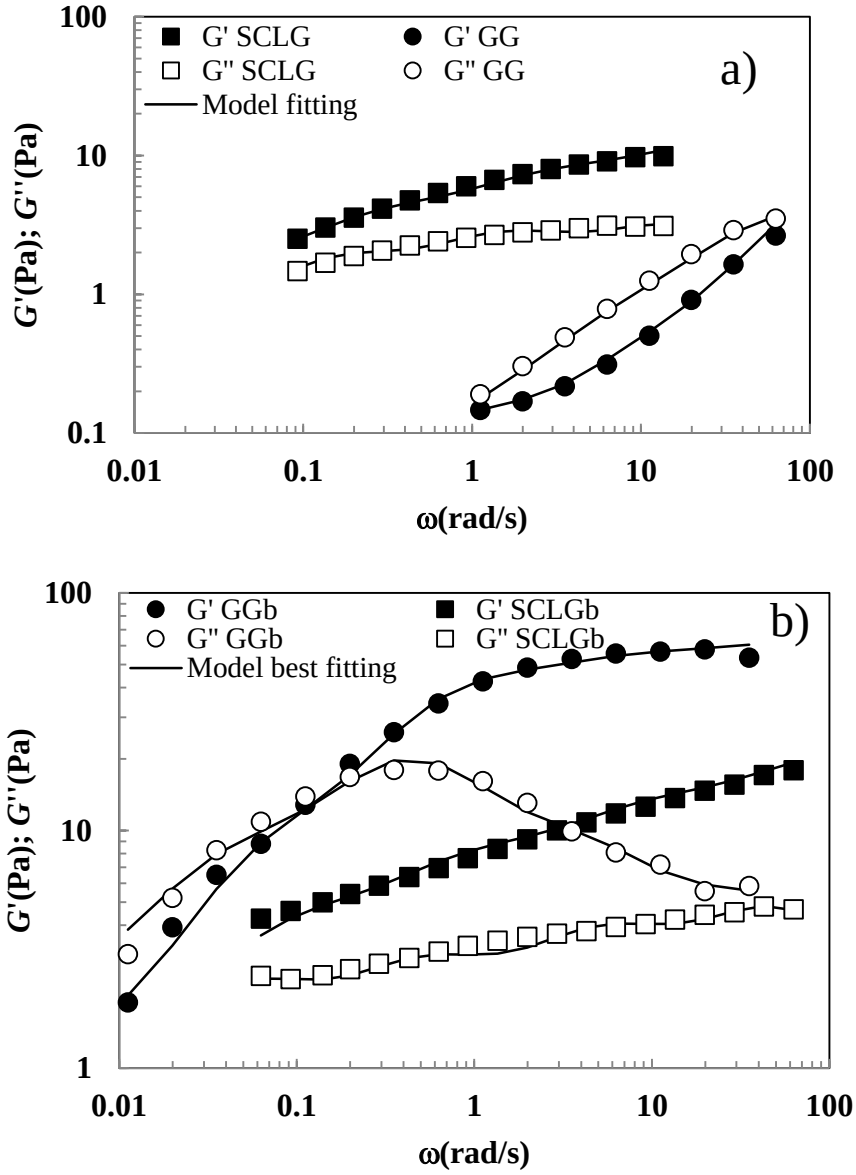

Figure 4.3: a) mechanical spectra (G' elastic modulus, G'' viscous modulus) referring to the Guar gum (GG) and Scleroglucan (SCLG) systems at 37 °C. Solid lines indicate the best fitting of the generalized Maxwell Model (F test always positive: $F_{GG}(5,10,0.95) < 38.1$, $F_{SCLG}(5,22,0.95) < 504.5$). **b)** mechanical spectra (*G*' elastic modulus, *G*'' viscous modulus) referring to the Guar gum/borax (GGb) and Scleroglucan/borax (SCLGb) systems at 37 °C. Solid lines indicate the best fitting of the generalized Maxwell Model (*F* test always positive: $F_{GGb}(5,24,0.95) < 55.4$, $F_{SCLGb}(5,32,0.95) < 2076$).

Now, *G'* prevails over G'' in the whole experimental frequency window and the crossing point is around ω = 0.01 rad/s. The ω dependence of *G'* and *G''* witnesses the weak nature of the formed hydrogel. Also in this case, the generalized Maxwell model provides a statistically good fitting (see F test values in *Figure 4.2b* caption) adopting, respectively, four and five elements for the GGb and SCLGb systems.

Temperature increase to 37 °C does not modify the gel and the solution nature of the SCLG and GG systems. Nevertheless *G'* and *G''*, for both systems, are reduced (see *Figure 4.3a*). Again, borax addition (*Figure 4.3b*) implies a moderate increase of the SCLGb moduli and a considerable modification of the GG characteristics.

25 °C	**GG**	**SCLG**	**GGb**	**SCLGb**
λ_1 (s)	$(7.7 \pm 3)\cdot10^{-3}$	$(81.7 \pm 11)\cdot10^{-3}$	$(15.7 \pm 4)\cdot10^{-3}$	$(30.0 \pm 5)\cdot10^{-3}$
G_1 (Pa)	20.3 ±4.4	7.0 ± 0.4	21.8 ± 6.1	9.7 ± 0.84
G_2 (Pa)	2.3 ± 1.1	6.2 ± 0.36	0	7.4 ± 0.5
G_3 (Pa)	0.12 ± 0.07	5.0 ± 0.37	36.5 ± 8.4	6.4 ± 0.5
G_4 (Pa)	0.014 ± 0.007	7.4 ± 0.53	61.6 ± 9.8	6.1 ± 0.76
G_5 (Pa)	0.012 ± 0.004	-	42.0 ± 13	4.0 ± 0.9
G (Pa)	22.9 ± 4.5	25.6 ± 0.8	162 ± 19	33.6 ± 1.6
ρ_x (mol/cm^3)	-	$(1.0 \pm 0.03)\cdot10^{-8}$	$(6.5 \pm 0.79)\cdot10^{-8}$	$(1.4 \pm 0.06)\cdot10^{-8}$
ξ (nm)	-	67.4 ± 0.8	36.5 ± 1.4	61.6 ± 1.0
37 °C	**GG**	**SCLG**	**GGb**	**SCLGb**
λ_1 (s)	$(11.6 \pm 2)\cdot10^{-3}$	$(62.5 \pm 6.6)\cdot10^{-3}$	$(22.7 \pm 6.4)\cdot10^{-3}$	$(18.9 \pm 2)\cdot10^{-3}$
G_1 (Pa)	7.6 ± 1.1	5.4 ± 0.23	7.9 ± 2.5	8.3 ± 0.32
G_2 (Pa)	0.40 ± 0.22	4.1 ± 0.16	10.0 ± 3.8	5.5 ± 0.27
G_3 (Pa)	0.049 ± 0.045	2.9 ± 0.15	36.1 ± 3.8	4.0 ± 0.2
G_4 (Pa)	0.04 ± 0.038	0	9.8 ± 2.9	3.5 ± 0.24
G_5 (Pa)	0.069 ± 0.043	1.8 ± 0.5	1.6 ± 0.6	1.5 ± 0.3
G (Pa)	8.2 ± 1.1	14.2 ± 0.75	65.5 ± 6.6	22.9 ± 0.6
ρ_x (mol/cm^3)	-	$(5.5 \pm 0.3)\cdot10^{-9}$	$(2.5 \pm 0.25)\cdot10^{-8}$	$(8.9 \pm 0.2)\cdot10^{-9}$
ξ (nm)	-	83.2 ± 1.5	49.9 ± 1.7	71.0 ± 0.6

Table 4.1: Generalized Maxwell model (Equations (3.78), (3.79)) parameters (± standard deviation) deriving from the fitting of data shown in *Figures 4.2* and *4.3*. λ_1 is the first relaxation time, G_i represents the spring constant of the ith Maxwell element, G is the shear modulus (sum of all G_i), ρ_x is the crosslink density calculated according to Equation (3.80), while ξ is the average network mesh size calculated according to Equation (3.81).

Indeed, not only *G'* and *G''* are clearly increased (about one order of magnitude) but also the system behavior shifts from that of a solution (GG) to that of an incipient weak gel (GGb) as testified by the presence of the crossover point (detectable at ω ≈ 0.2 rad/s)

where system elastic and viscous characteristics are equal. This means that the system is moving from a sol to a gel condition, i.e, it lies in a sort of transition zone. Generalized Maxwell model gives a statistically good fitting of data shown in *Figure 4.3a* and *4.3b* (see F test values in the captions to this figures) assuming four or five Maxwell elements (see *Table 4.1*). In conclusion, rheological characterization evidences the marked effect of borax addition to the GG system and the weak effect exerted on the SCLG system at both temperatures. While SCLG always exhibits gel properties, GG system becomes a weak gel (or incipient weak gel) only in the presence of borax. On the basis of the crosslink density (ρ_x) evaluation (see Equation (3.80)), equivalent network theory (see Equation (3.81)) allows to estimate, for the gel systems, the average network mesh size ξ. *Table 4.1* shows that ξ spans from 36.5 nm (GGb, 25 °C) to 83.2 nm (SCLG, 37 °C). The high ξ values witness the low connectivity of all tested gels.

***T* (°C)**		***T*$_{21}$ (ms)**	***A*$_1$%**	***T*$_{22}$ (ms)**	***A*$_2$%**
25	**GG**	2032 ± 92	100		
	GGb	1527 ± 46	100		
	SCLG	1359 ± 23	100		
	SCLGb	343 ± 84	84.5 ± 23.5	173 ± 77	15.5 ± 7.8
	water	3007 ± 20	100		
37	**GG**	2466 ± 80	100		
	GGb	1912 ± 94	100		
	SCLG	1321 ± 46	100		
	SCLGb	451 ± 74	100	-	-
	water	3694 ± 60	100		

Table 4.2: Relaxation times, T_{22} and T_{21} ± standard deviation, and % weight, A_1% and A_2% ± standard deviation, referring to GG, SCLG, GGb, SCLGb and distilled water, at 25 and 37 °C. $A_1\% = 100 * A_1/(A_1 + A_2)$.

LF NMR analysis indicates that, regardless of temperature, GG is characterized by only one relaxation time (T_{21}) (see *Table 4.2*), as expected for aqueous solutions, while the relaxation of the protons belonging to the polymeric chains are not detectable, due to their very low amount (around 0.5%) in comparison with those of water. Thus, LF NMR and rheology analysis lead to the same conclusion: the GG system is an aqueous polymer solution at both temperatures. The addition of borax to the GG system induces a significant reduction of T_{21} at both temperatures. Since the addition of borax to distilled water does not substantially modify the water relaxation time T_{2H2O} (data not shown), we

can assert that the observed reduction of T_{21}, at both temperatures, cannot directly depend on the presence of borax. Thus, the T_{21} reduction is in agreement with the formation of a new, more compact, architecture of the polymeric chains (gel network) related to the addition of borax. It is interesting to point out that, in the case of a dextran system (c_p = 0.7% w/v)), the addition of borax (r = borax moles/dextran moles = 1; data not shown) does not modify T_{21}, this being a clear indication that, in this case, the presence of borax does not lead to the formation of a polymeric network. It is also interesting to notice that the relative increase of T_{21} with temperature is similar for both GGb (25%) and GG (21%) systems (see *Table 4.2*). This result shows that the interactions among polymeric chains and water molecules are not so strong, as expected for a weak gel. Although the SCLG system shows, as GG, only one relaxation time at 25 °C and 37 °C, it cannot be considered a solution, because T_{21} is, essentially, temperature independent and this behavior should not occur in a polymeric solution at such low concentration (c_p = 0.7% v/w). In addition, also the relatively small T_{21} value (recorded at both temperatures) with respect to that of water, T_{2H2O}, is not compatible with such a low c_p. Finally, *Table 4.2* shows that the addition of borax to the SCLG system implies a drastic reduction of the average relaxation time $\langle T_2 \rangle$ at 25 °C (317 ms) and 37 °C (451 ms). Again, the essential $\langle T_2 \rangle$ independence on temperature and its high reduction in comparison with water, (T_{2H2O}), indicates the gel nature of the SCLGb system. The fact that, for this last system, two relaxation times were detected at 25 °C and only one at 37 °C can be explained by the formation, at 37 °C, of a more homogeneous polymeric network due to a higher mobility of borax ions in the initial polymer solution. In conclusion, as far as the macroscopic behavior is concerned, the relaxation analysis shows the same findings obtained from the rheological characterization of our polymeric systems. On the other side, some differences arose in the estimation of ξ. Indeed, knowing that $\phi = 4.35 \cdot 10^{-3}$ and $R_f \approx 2.15$ nm for both GG and SCLG systems [**29**], the application of Equation (3.81) leads to ξ = 99.8 nm. The comparison between the values reported in *Table 4.1* (25°C and 37°C) and *Table 4.3* shows that the ξ values from rheological approach are about 40% for GGb and about 75% for SCLG and SCLGb of those obtained by LF NMR theory. Nevertheless, taking into account the simplifications adopted in both approaches, we believe that these cannot be considered as significant differences. In order to estimate the continuous mesh size distribution of GGb, SCLG and SCLGb systems, Equation (3.47) was used for the

determination of parameter $\langle \mathcal{M} \rangle$ whose values are reported in *Table 4.3*. It can be seen that $\langle \mathcal{M} \rangle$ values, regardless of temperature, increase going from GGb to SCLG and SCLGb systems. This indicates a stronger and stronger effect of polymer chain surfaces on the relaxation of protons. The diffusion coefficient, *D*, was practically constant with the diffusion time t_d for all studied systems (see, for example, *Figure 4.4*), and therefore the check on the fast diffusion conditions (evaluation of the dimensionless parameter $\frac{\langle \mathcal{M} \rangle R_c}{D}$) was carried out taking into account the *D* value averaged on the measurements performed at all t_d.

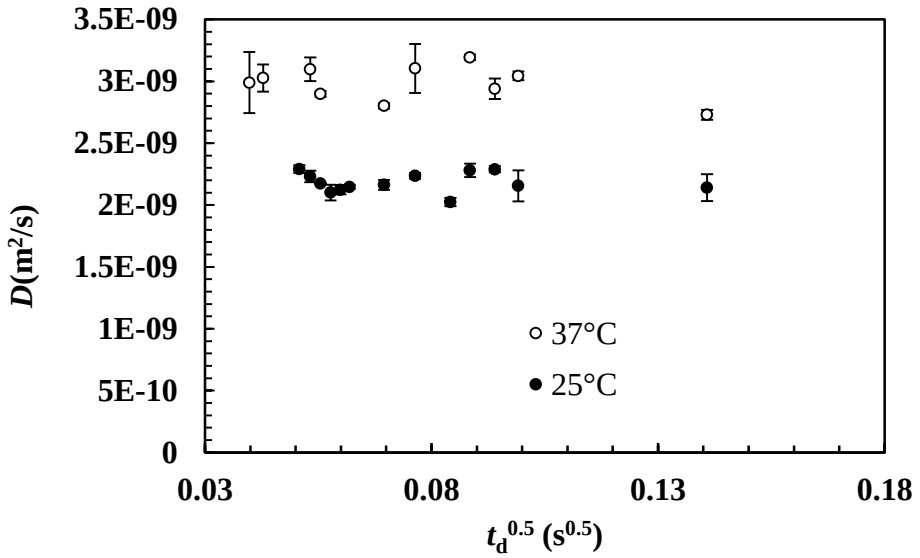

Figure 4.4: Experimental self diffusion coefficient of water (*D*) at 25 °C and 37 °C in GGb hydrogel. Vertical bars indicate datum standard error.

Table 4.3 clearly shows that in all gel systems, $\frac{\langle \mathcal{M} \rangle R_c}{D}$ was much less than 1, i.e. fast diffusion conditions always apply. Accordingly, Equation (3.50) and (.51) can be used for the estimation of $a(T_2)$, $a(\xi)$ and, finally of $P(\xi)$, as shown in *Figure 4.5* (37 °C).

Figure 4.5 shows that, for GGb, the mesh size distribution spans, approximately, from 10 nm to 300 nm while it is slightly less wide for SCLG and SCLGb. As the ξ values estimated by means of rheology experiments fall inside these distributions and they are not too far from the distribution peaks, we may conclude that the two approaches do not lead to very different results (see *Table 4.1*).

T (°C)		T_{2a} (ms)	ξ (nm)	$D*10^9$ (m^2/s)	$\langle \mathcal{M} \rangle *10^3$ (nm/ms)	$\frac{\langle \mathcal{M} \rangle R_c}{D} *10^6$
25 °C	**GGb**	1527 ± 46	99.8	2.2 ± 0.1	62 ± 6	1.2
	SCLG	1359 ± 23	99.8	2.2 ± 0.1	99 ± 3	1.5
	SCLGb	317 ± 23	109 ± 16 (84.5%) 31 ± 9 (15.5%)	2.3 ± 0.1	693 ± 263	10.0
37 °C	**GGb**	1912 ± 94	99.8	2.9 ± 0.2	79 ± 5	0.7
	SCLG	1321 ± 46	99.8	2.8 ± 0.2	119 ± 6	1.4
	SCLGb	451 ± 74	99.8	2.9 ± 0.2	477 ± 89	5.4

Table 4.3: Average relaxation time $\langle T_2 \rangle$ ± standard deviation, water self-diffusion coefficient D ± standard deviation, average effect of surface on protons relaxation $\langle \mathcal{M} \rangle$ ± standard deviation, R_c = 32.6 nm (see Equation (3.35)) and mesh diameter ξ, referring to SCLG, GGb and SCLGb systems at 25 and 37 °C. Proton relaxation times (T_2H_2O) at 25 °C is 3007 ± 20 ms while at 37 °C it is 3694 ± 60 ms.

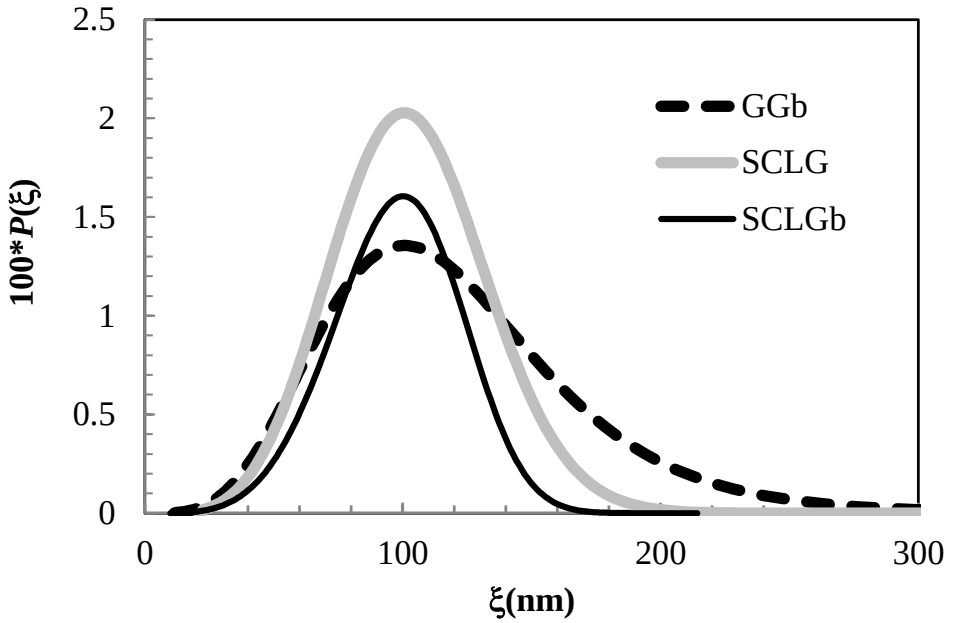

Figure 4.5: Mesh size distribution, $P(\xi)$, of GGb (Guar gum/borax), SCLG (Scleroglucan) and SCLGb (Scleroglucan/borax) hydrogels at 37 °C.

Another approach to acquire some insight about polymeric network characteristics is the determination of model molecule diffusion coefficients. For this purpose, two model drugs, TPH and Vit B_{12}, were considered. *Figure 4.6* reports TPH and Vit B_{12} release from GGb at 37 °C. These two release kinetics are fitted by means of Equation (3.61) knowing that the release volume V_r = 200 cm^3 and the initial drug concentration C_0 in the gel is equal to 5.2 mg/cm^3 for the two drugs. In both cases, the fitting is statistically good as proved by the F test ($F_{TPH}(1, 10, 0.95) < 75$; $F_{Vit\ B12}(1, 10, 0.95) < 30627$). In the case of TPH we have that the diffusion coefficient $D_d = D_{di} = (2.7 \pm 0.5)\cdot 10^{-10}$ m^2/s while, for Vit B_{12}, model fitting yields to $D_d = (2.3 \pm 0.1)\ 10^{-10}$ m^2/s and $D_{di} = (3.0 \pm 0.1)\ 10^{-11}$ m^2/s (D_{di} is the interfacial diffusion coefficient that can be different from the bulk one, D_d. D_{di} accounts for possible interfacial mass transfer resistances).

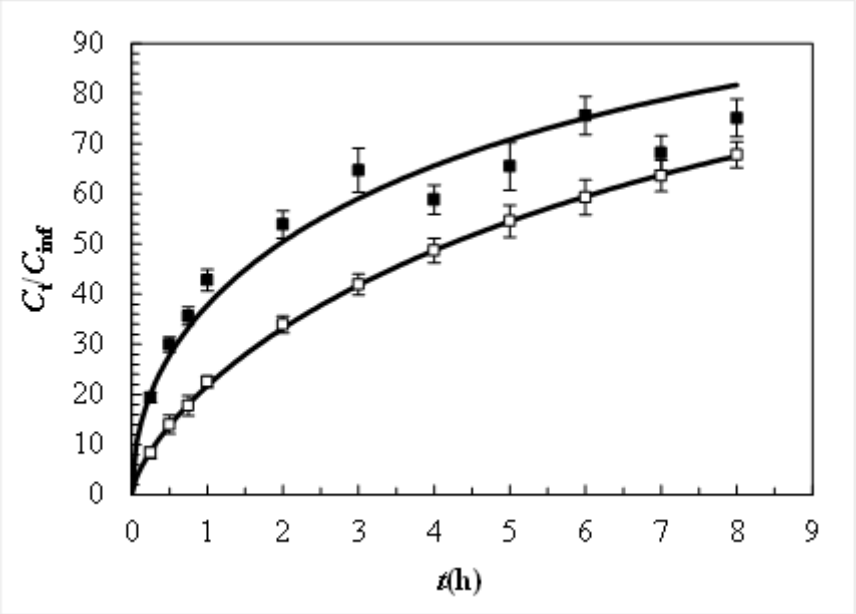

Figure 4.6: Theophylline (TPH; filled squares) and Vit B_{12} release (open squares) from GGb hydrogel at 37 °C (vertical bars indicate standard error). C_t and C_{inf} are, respectively, drug concentration at time t and after an infinite time. Solid lines indicate model best fitting (Equation (3.61)).

These results indicate that the resistance due to the thin web, suspending the gel in the release environment, is negligible for TPH while it plays a significant role in the case of Vit B_{12}. This seems reasonable if we consider the different model drug dimensions (TPH van der Waals radius r = 3.7 Å; Vit B_{12} van der Waals radius r = 8.5 Å) [**30**]. On the basis of the diffusion coefficients in water at 37 °C of TPH ($D_{d0} = 8.2\cdot 10^{-10}$ m^2/s) and of Vit B_{12} ($D_{d0} = 3.8\cdot 10^{-10}$ m^2/s) [**45**], Equation (3.81) allows estimating the polymeric network

mesh size (ξ) knowing that polymer volume fraction (φ) in GGb hydrogel is equal to $4.35 \cdot 10^{-3}$. It turns out that ξ = (1.1 ± 0.1) and (4.3 ± 0.06) nm in the case of TPH and Vit B_{12}, respectively. These values are much smaller than those estimated by means of rheology and LF NMR (49.9 nm, see *Table 4.1*, and 99.8 nm, see *Table 4.3*). Due to the low polymer concentration and crosslink density of GGb hydrogel, the ξ values estimated according to Equation (3.81) seem too small. The motivation for the Equation (3.81) failure should rely on the fact that GGb system, at 37 °C, represents an incipient hydrogel condition (as previously discussed, see also *Figure 4.3b*). Here, drug diffusion is not only affected by the presence of the structured polymeric network but also by the chains that, although bound to the network to one end, can freely fluctuate among meshes. These chains are elastically inactive but can hinder drug diffusion through a viscous drag, favored by weak van der Walls interactions with drug molecules. Tomic and co-workers [**31**] found that also very weak van der Waals interactions are sufficient to hinder drug molecule movements in the presence of a polymeric network with mesh size much larger than the drug molecular size. In addition, the rheological analysis suggests that the number of elastically inactive chains is high, as proved by the importance of the viscous contribution to the GGb mechanical behavior (see *Figure 4.3b*). On the contrary, in the case of a true hydrogel, such as SCLGb (where the viscous contribution is low), we found a good agreement between the estimation of ξ according to the rheological approach and Equation (3.81) was found [**32**].

4.2 Alginate Pluronic F127 Hydrogels

4.2.1 Introduction

Alginates family includes a broad variety of anionic polysaccharides of natural origin with an increasing numbers of applications in the biotechnological field. Since many years, these compounds were successfully used in the food industry as thickening agents, gelling agents and colloidal stabilizer for food and beverage. Their particular characteristics are ideal for the development of hydrogels matrices intended for controlled release or immobilization of biological agents such as living cells, proteins or active molecules in general. Indeed, alginate hydrogels have a relatively inert aqueous environment inside the matrix and the encapsulation processes can occur at room

temperature without the use of organic solvent allowing the prevention of activity loosing of biological agents. Moreover, the hydrogels structure can be easily modulated and the systems is biodegradable in the physiologic conditions [**33**].

Alginates commercially available mainly derive from three species of brown seaweeds: *Laminaria hyperborea*, *Ascophyllum nodosum* and *Macrocystis pyrifera*. Other minor sources include the species *Laminaria japonica*, *Eclonia maxima*, *Lessonia nigrescens* and the species of the genus *Sargassum* (*Fig. 4.7*). In all these species, the alginate is the principle polysaccharides in the seaweed matrix (up to 40% by weight of dry seaweed) [**33-34**].

Figure 4.7: seaweed used for alginates extraction. From left to right*: Laminaria hyperborea*, *Ascophyllum nodosum*, *Macrocystis pyrifera* and the genus *Sargassum*.

The alginate chains are unbranched linear copolymers consisting of (1-4) linked β-D-mannuronic acid (M) and α-D-guluronic acid (G) that are organized in different sequences or blocks. The monomers can appear in homopolymeric blocks of consecutive G-residues (G-blocks), consecutive M-residues (M-blocks), heteropolymeric blocks of regularly alternated M- and G-residues (MG-block), or randomly organized blocks (*Fig. 4.8*). The polymer characteristics are strongly influenced by the blocks sequences belonging to the polymeric chain. The alginates family have a high sequence variability that depends on the source organism, tissue, season and growth conditions [**33-34**].

High content of G are generally found in alginate prepared from old L. hyperborea plants whereas, alginate prepared from A. nodosum and M. pyrifera, are characterized by low G content and low gel strength. Recently, particular preparation of alginate with very high

content of G or M (up to 100%) can be obtained from culturing of bacteria (Azotobacter vinalandii and the genus Pseudomonas are some natural producer), from particular algae tissue (outer cortex), or by enzymatic modification using mannuronan C-5 epimerase that converts M-units in G-units [**34**]. The units links difference in G-blocks and M-blocks, reflect a different conformations belong the polymeric chain: while the M-blocks are substantially linear and flat, the G-blocks assuming a buckled conformations (*Fig. 4.8*).

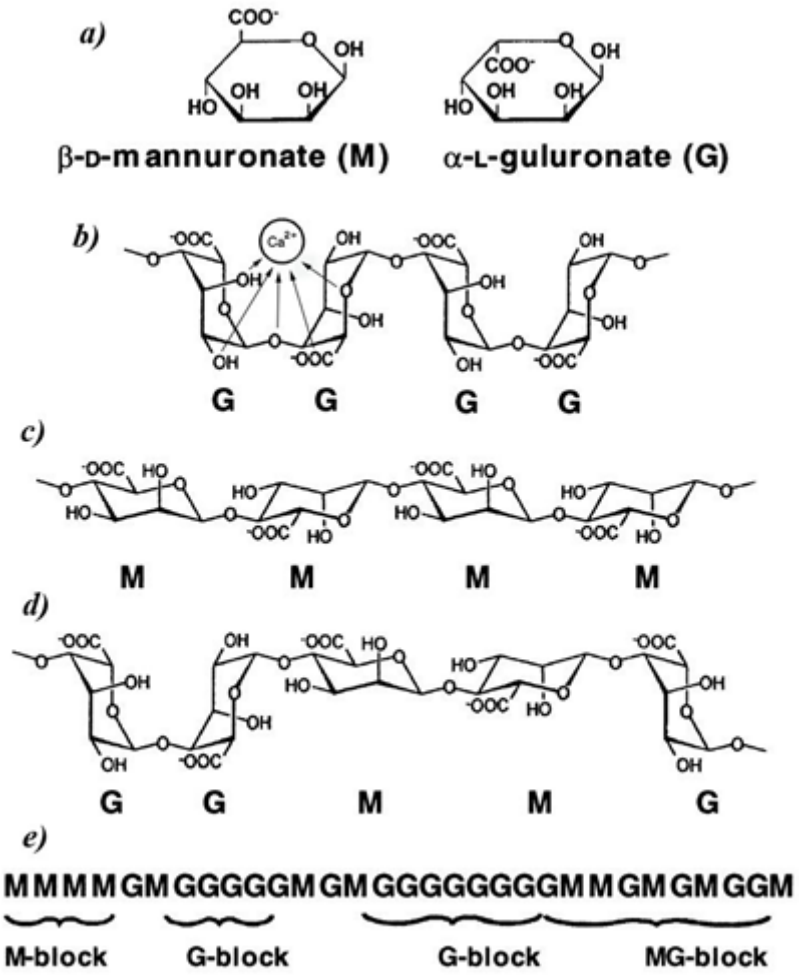

Figure 4.8: alginate structure and monomers. **a)** structure of β-D-mannuronic acid (M) and α-D-guluronic acid (G). **b)** G-blocks region, the coordination with a Ca^{2+} ion is also showed **c)** M-blocks region **d)** MG-blocks region. **e)** examples of blocks distributions inside polymer chain.

This difference influences chain flexibility. Indeed, M-blocks regions are more flexible than G-blocks regions because the carboxylic steric effect. In other words, the higher the mannuronic content the higher the M-blocks regions and more flexible is the alginate chain in solution [**35**]. The most important consequence of the monomers arrangement

consists in the capability of the alginates (especially of the sodium alginate) to form hydrogels in water solutions in presence of bivalent cations. The gelation is consequence of the ions exchange between the Na^+ of the G monomers, with the bivalent cations. Contrarily to the monovalent cations, bivalent cations promoting the physical interaction between G-blocks regions belonging to different chains in a characteristic structure called *egg-box*. Each chain is able to interact with many other originating the gel networking (*Fig. 4.9*).

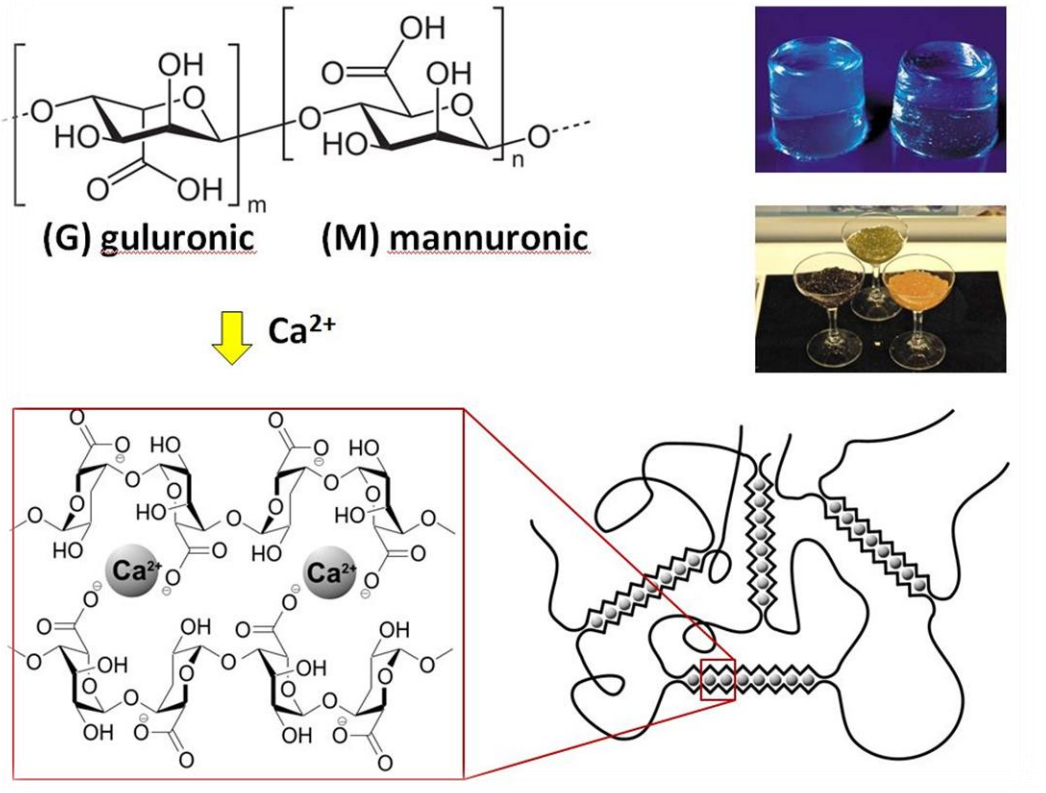

Figure 4.9: Schematic rapresentation of the egg box structure in the alginate in presence of divalatent cations.

The most used cation is the Ca^{2+} but also Ba^{2+} and Sr^{2+} are used because of their ability to produce stronger gelation than calcium. Pb^{2+}, Cu^{2+}, Cd^{2+}, Co^{2+}, Ni^{2+}, Zn^{2+} and Mn^{2+} also results in a gelation but their use is limited because of potential toxicity problems. Mg^{2+} does not produce gelation. Alginates with a G contents equal or higher than 70% in weight and G-blocks longer than 15 units allow the production of hydrogels characterized by a low shrinkage, high mechanical resistance and high stability. These systems can be also distinguished for their rigidity and fragility while, in hydrogels with higher content of M, the elastic characters are prevalent [**33**].

Gel preparation can be realized by two methodologies: the *diffusional setting* and the *internal setting*. In the first case, alginate solution is placed in contact with solution of bivalent cations that diffuse across the polymeric matrix and trigger gelation. On the contrary, in the internal setting technique, the bivalent cations are released into the polymeric solution exploiting a combination of alginate, bivalent ions source (normally a salt) and a chelating agent. The chelating agent sequesters the bivalent cations preventing the gelation during components mixing and formation. Cations release from the chelator agent is triggered by environment change such as temperature, pH or solubility and results in a uniform gelation of all the alginate solution. It is clear how the internal setting is particularly useful in the production of bulk gel, fibers or large objects. However, due to the limited amount of divalent cations that can be carried by the chelator agent, hydrogels prepared by internal settings results to be softer than those prepared by diffusional setting. For pharmaceutical applications, the biological agent can be incorporated in the preparation by simple mixing with the polymeric solution before gelation. The different structures resulting from gelation and the flexibility of the M-blocks and MG-blocks not interested by the physical interactions represent an important parameter for the diffusion control of the incorporated molecules. Molecules diffusion into the hydrogels matrix can be caused by two mechanisms: diffusion through the network meshes or the structure breakup. The electronic microscope analysis of the calcium alginate gels shows mesh variability in the range of 5 and 200 nm. A wide number of different compounds can be included in the alginate matrix: ionic or neutral, big or small (proteins, glucose, ethanol etc.). Possible molecules interactions with the polymeric network must be evaluated. High rigidity alginates (high content of G) produce an open and static structures and therefore are more permeable while, the presence of long, flexible M-blocks causes structure collapsing in an entanglements configuration [**36**]. Moreover, in general the diffusion inside the gels decreases with increasing of the alginate concentrations. The mesh of these systems can be significantly reduced by dehydrating the swollen materials. Depending on the starting hydrogel composition, different results can be achieved: a high G alginate, after dehydration, can be only partially re-swollen resulting in a more concentrated system at lower mesh [**33**]. Regarding the structural stability, because of the reversibility of the physical chain links, alginate hydrogels are affected by degradation processes. Alginates hydrogel dissolutions is promoted by the bivalent ions subtraction from a chelating agent

that destabilize the chains interactions causing the entrapped materials release and the polysaccharides dissolution. The same phenomena occurs when the system is exposed to high concentration of monovalent cations or Mg^{2+} that compete with the bivalent cations for the polymers interaction. In order to prevent the hydrogel dissolutions, it is possible to store the system in a bivalent cations containing environment (i.e. a Ca^{2+} solution) or complexing the alginate with polycations (i.e. chitosan), polypeptides (i.e. poly(L-lysine)) or synthetic polymers (i.e. poly(ethylenimine)). The complex stabilize the hydrogels, reduce the mesh size and it does not dissolve in presence of a chelator [**33**]. Alginate hydrogels are not toxic and immunologically inert hydrogel with a high level of biocompatibility and biodegradability. They can easily undergo gelation with divalent cations under the very mild condition suitable for incorporation of biomacromolecules and living cells, thus alginate and its hydrogels have been popularized for pharmaceutical applications like wound dressings, dental impression materials, in vitro cell culture and tissue engineering applications. Important applications of alginate hydrogel in tissue engineering include drug delivery applications, such as microencapsulation of pancreatic islet cells, creation of a supporting matrix for cells through encapsulation techniques, and alginate-based bioreactors for large-scale manufacture of biological products.

Pluronic™ is the BASF commercial name of a class of block copolymers constituted by poly(ethylene oxide) (PEO) and poly(propylene oxide) (PPO) also known as Poloxamer. The Pluronic™ is commercialized in more than fifty different types but the detailed description of all the family members is outside the purpose of this work. Here, it will be treated only the general aspects of the Pluronic™ systems with a particular regard to the Pluronic™ F127, used in this study. Normally, the different type of blocks in a copolymer, are mutually incompatible and the polymer has an amphiphile behavior: in water solutions, associative mechanisms cause the polymeric chain aggregation in structures. The Pluronics™ are not-ionic copolymers characterized by a three blocks structures of poly(ethylene oxide)-poly(propylene oxide)- poly(ethylene oxide), usually represented also by the abbreviations PEO-PPO-PEO or (EO)n(PO)m(EO)n, where the hydrophobic block PPO is embedded between two hydrophilic blocks of PEO (*Fig. 4.10b*). The possibility to change the copolymer composition (in terms of PPO/PEO ratio) and the molecular weight (in terms of blocks length) make this class of polymers versatile for several technological applications. In the biomedical fields, in particular, these products

can find many applications in virtue of being chemically inert with respect to tissues and organic fluids, good solvents and water solubility. All these characteristics correspond to the Pluronic™ polymers and therefore, it is justified the large usage, especially in the pharmaceutical field [**37**]. Pluronics™ synthesis is a two steps process. Firstly the hydrophobic central block is created by the polymerization of propylene oxide (PO) on the two sides of propylene glycol. In the second step, the ethylene oxide (EO) is introduced on the two sides of the PPO block polymerizing in the external PEO blocks. The reaction takes place in presence of an alkaline catalyst, generally sodium or potassium hydroxide (*Fig 4.10a*). Reaction tuning allows the production of polymer with the desiderate characteristics therefore, Pluronics™ are commercialized in a wide range of variety in terms of copolymers composition and molecular weight. Their classifications is based on a precise nomenclature where, each polymer is identified by a sign composed of one letter followed by two or three numbers. The letter specifies the physical form: "L" for liquid, "P" for paste and "F" for solid. The first number (or first two numbers in case of three numbers), multiplied by 300 gives the approximated molecular weight of the hydrophobic block (PPO). The last number, multiplied by 10, indicate the weight percent of PEO. For example, Pluronic™ F127 used in this work is commercialized as solid (F), the PPO block molecular weight is approximate 3600 Da (12x300) while the PEO weight fraction is about the 70% of the total mass. The wide range of Pluronics™ formulations is justified by their use not only as hydrogels but also in the preparation of emulsions, dispersions, detergents, foams and lubricant (indeed they are surfactants) [**37**].

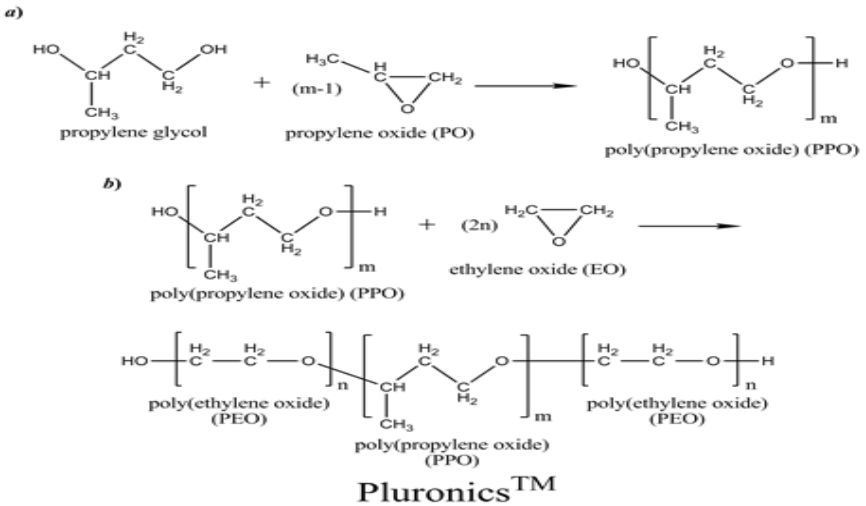

Figure 4.10: Pluronics™ synthesis. **a)** formation of the central hydrophobic PPO block followed by the addition of the hydrophilic PEO side blocks **(b)**.

At low temperatures and/or low concentrations, Pluronic™ copolymers, are present in water solution as single molecules also called unimers. As consequence of a temperature and/or concentration increase in solution, the formations of thermodynamically stable micelles occur. Therefore, Pluronics™ can be considered both thermotropic and liotropic (respectively temperature and concentration dependent) structures forming species [**38**]. Starting from the micelles solution, where micelles and unimers coexist, some copolymers of the Pluronics™ class (such as the Pluronic™ F127), are able to generate higher ordered structures that result in the formation of thermos-reversible gel systems. Several studies investigated the Pluronic™ copolymer gelation but, up till now, many aspects remain unclear. The accepted mechanism consists in a response to the temperature increase that brings to the increase of the micelles volume fraction. When this parameter, in solution, exceeds the critical values of 0.53, the micelles solution organize to form a crystalline-like structure that results in a physical networking and system gelation. In this structure, the micelles become hard spheres packed together and organized in cells that constitute the crystalline units [**37-38**]. In the case of Pluronic™ F127, by means of SANS measurements, some authors discovered that the geometry of the crystalline structural unit is a simple cubic cell. Accordingly, they excluded the formation of other geometries such as hexagonal cell, body centered cubic cell or face centered cubic cell [**39-40**].

4.2.2 Experimental section

4.2.2.1 Materials

The Alginate used in this work (molecular weight ≈ 10^6 Da), a kind gift from FMC Biopolymer LtD, UK, was characterized by a high G content (≈ 70% G and 30% M). Pluronic F127 was purchased from Sigma-Aldrich Chemie GmbH, Germany. Two model drugs were considered in this study to get information about gel structure. The first one was Theophylline (TPH), a small organic molecule (molecular weight 198 Da), purchased from Sigma-Aldrich Chemie GmbH, Germany. The second one, an oligonucleotide 51 nt long (DNA GT15H), was purchased by Eurofins MWG Operon, Ebersberg, Germany. All other chemicals were of analytical grade.

4.2.2.2 Gel preparation

Three kinds of gels were prepared: the first one contained only alginate (2% w/w; A2) the second one contained only Pluronic PF127 (18% w/w; PF18) and the third contained alginate (2%w/w) and PF127 (18% w/w) (A2PF18). The polymeric blend A2PF18 was prepared using the so-called "*cold method*" proposed by Schmolka [**41**]. Briefly, a proper amount of alginate powder was slowly added to stirred distilled water contained in a beaker maintained at 7°C. Subsequently, the desired amount of pluronic flakes were slowly added to the alginate solution. The system was stirred until complete polymer dissolution and then kept at 4°C for 12 h before use. A proper amount of polymeric solution was then poured into a bottom flat beaker to get a film of thickness approximately equal to 1 mm (7°C). The solution was heated to 37°C to get the thermal gelation of pluronic (A2PF18 thermal gelation starts at 20°C and it is complete at 24°C) [**42**]. Subsequently, a $CaCl_2$ water solution (Ca^{+2} concentration equal to 5 g/l) was rapidly sprayed on the gel surface to get alginate crosslinking. In order to prevent from the possible lack of Ca^{+2}, the volume of the sprayed crosslinking solution was approximately equal to gel volume. After 5 minutes contact, the crosslinking solution was removed and the crosslinked film was immediately and gently cleaned by laboratory paper. The preparation of the PF18 gel was equal to that of the A2PF18 gel except for the addition of the alginate and the crosslinking solution (PF18 thermal gelation starts at 22°C and it is complete at 26°C) [**42**]. The preparation of the A2 gel was equal to that of the A2PF18 gel except for the addition of pluronic PF127. The preparation of gels containing the model drug (theophylline or oligonucleotide) and devoted to the high field NMR analysis, implied polymers dissolution in a D_2O solution containing the model drug at the desired concentration (10 mg/cm^3 for theophylline and 1 mg/cm^3 for oligonucleotide). Indeed, D_2O presence was necessary to silence the water protons that would have otherwise hidden the presence of the model drug.

4.2.2.3 Rheological characterization

The rheological characterization, carried out at 37 °C, was performed by means of a controlled stress rheometer, Haake Rheo-Stress RS150 model equipped with a Thermo Haake C25 water bath and mounting a grained plate-plate device (Haake PP35Ti: diameter = 35mm). Due to the A2 and A2PF18 gels rigid nature, the gap-setting

optimization was undertaken according to a procedure described elsewhere [**43**]. In the PF18 case, on the contrary, gel softness allowed to fix the gap to 1 mm. To avoid gel shrinking due to a possible solvent evaporation, the equipment was kept inside a glass bell with a constant moisture level. Rheological properties were studied by means of oscillatory tests. In particular, the linear viscoelastic regions were assessed, at 1 Hz, by stress sweep experiments. Frequency sweep tests were carried out in the frequency (f) range 0.01–10 Hz at constant stress τ = 5 Pa (well inside the linear viscoelastic range for all the studied gels). Each test was carried out in triplicate.

4.2.2.4 LF NMR characterization

Low Field NMR (LF - NMR) characterization was performed, at 37 °C, by means of a Bruker Minispec mq20 (0.47 T, 20 MHz). Transverse relaxation time (T_2) measurements were carried out according to the (Carr-Purcell-Meiboom-Gill; CPMG) sequence (number of scans = 4; delay = 5 s) adopting a 90° - 180° pulse separation times τ of 0.25 ms.In order to study water mobility inside the gel network, Pulsed Gradient Spin Echo (PGSE) measurements were performed at 37°C. The applied sequence consisted in the classical CPMG sequence with two equal gradient pulses (of length δ = 1 ms) occurring at x1 = 1 ms and x2 = 1 ms after the 90° and 180° pulses, respectively. The time separation, indicated by Δ ($\approx \tau$-x1-δ+x2), is related to the water molecule diffusion time t_d according to $t_d = (\Delta - \delta/3)$. The determination of the water self-diffusion coefficient was led fitting the following equation to experimental data [**44**]:

$$A_t = \sum_{i=1}^{p} A_{0i} e^{-q^2 t_d D_{wi}} \qquad q = \gamma * g * \delta \qquad A_0 = \sum_{i=1}^{p} A_{0i} \qquad (4.1)$$

where A_t and A_0 are, respectively, the measured amplitude of the signal at the echo with and without gradient applied, γ is the proton gyromagnetic ratio, g is the known magnetic field gradient while A_{0i} are the fractions of water molecules characterized by a self-diffusion coefficient D_{wi}. In the case of a homogeneous system, of course, the summation limits to the first term (p = 1) as the water molecules are all characterized by the same self-diffusion coefficient. p was determined minimizing the product $\chi^2 * 2p$ where χ^2 is the sum of the squared errors and 2p represents the number of fitting parameters (A_{0i}, D_{wi}) of eq.(4.1) [**45**]. Measurements were led in triplicate.

4.2.2.5 TEM characterization

A2 and A2PF18 gels were dehydrated and embedded in Epoxy resin. Then, ultrathin sections were contrasted using $Pb_3(C_6H_5O_7)_2$. Images were recorded by means of a Philips EM 208 (100 KV) Transmission Electron Microscope.

4.2.2.6 High Field NMR

Self-diffusion NMR measurements (PGSTE) were carried out at 37 °C on a Varian 500 MHz NMR spectrometer (11.74 T) operating at 500 MHz for 1H, equipped with a model L650 Highland Technology pulsed field gradient (PFA) amplifier (10 A) and a standard 5 mm indirect detection, PFG probe. The lock was made on D2O and solvent suppression was accomplished by pre-saturation. A one-shot sequence has been employed for theophylline gels diffusion measurements [**46**, **47**], with 20 different z-gradient strengths, Gz , between 0.02 and 0.54 T/m, a pulsed gradient duration, δ, of 2 ms, and at different diffusion interval (Δ). At each gradient strength, 64 transients have been accumulated employing a spectral width of 5,5 kHz (11 ppm) over 16K data points. Oligonucleotide samples have been analyzed thanks to an excitation sculpting PGSTE experiment [**48**]. PGSTE NMR spectra were processed using MestRenova and self-diffusion coefficients were determined by means of eq.(4.1).

4.2.3 Results and discussion

Stress sweep tests revealed (data not shown) that, for all the studied gels (A2, PF18 and A2PF18), the linear viscoelastic range holds for stresses well above the constant one (τ = 5 Pa) adopted in the execution of the frequency sweep tests. *Figure 4.11* shows the comparison among the mechanical spectra referring to A2, A2PF18 and PF18 systems. *G*' (filled symbols) indicates the elastic or storage modulus while *G''* (open symbols) indicates the viscous or loss modulus. It can be seen that for all the three systems, *G*' and *G*'' are quite independent of pulsation ω (= $2\pi f$) and *G*' is always neatly prevalent on *G*", this being typical of strong gels. It is also clear that while A2 is the strongest gel, PF18 is the weakest one. Indeed, both *G*' and *G*'' decrease in the order A2, A2PF18, PF18. Thus, we have to conclude that pluronic presence hinders the alginate crosslinking process.

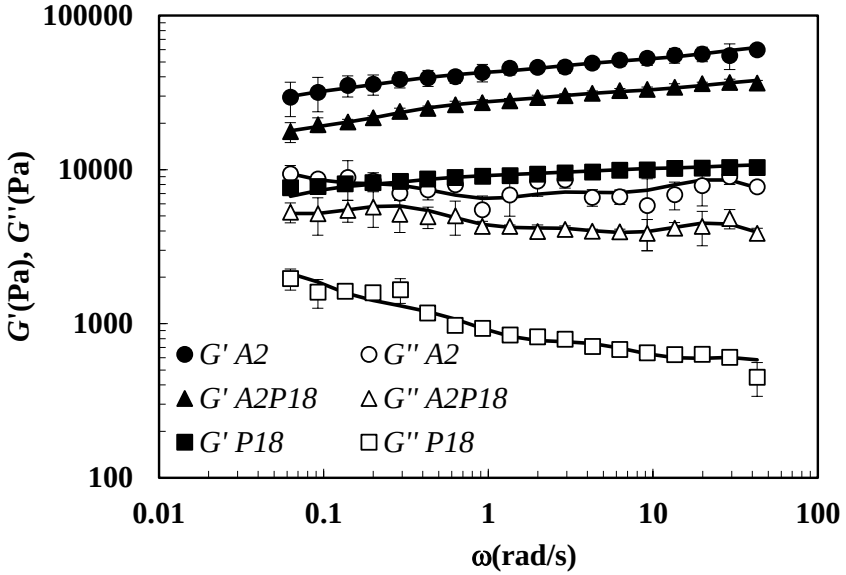

Figure 4.11: Mechanical spectra referring to alginate (A2), pluronic (PF18) and alginate-pluronic (A2PF18) gels at 37°C. Close and open symbols represent, respectively, storage (*G*') and loss (*G*'') modulus while solid lines represent the best fitting of the generalized Maxwell model composed by 5 elements (eqs.(3.78) and (3.79)). Vertical bars indicate standard error.

Five Maxwell elements (one purely elastic and four viscoelastic) are necessary for the statistically reliable fitting of the mechanical spectra reported in *Figure 4.11* (see solid lines). Best fitting parameters values are reported in *Table 4.4*.

	A2	***A2PF18***	***PF18***
λ_1**(s)**	$(2.5 \pm 0.4)10^{-2}$	$(3.6 \pm 0.1)10^{-2}$	$(2.4 \pm 0.2)10^{-2}$
G_e**(Pa) =** G_{min}**(Pa)**	17259 ± 3853	10283 ± 772	3830 ± 925
G_1**(Pa)**	13761 ± 610	7781 ± 177	947 ± 13
G_2**(Pa)**	9123± 596	4863 ± 109	944 ± 36
G_3**(Pa)**	9883 ± 589	8848 ± 277	1393 ± 87
G_4**(Pa)**	17072 ± 908	8565 ± 633	4108 ± 342
G_{max}**(Pa)**	67099 ± 4092	40341 ± 1057	11223 ± 992
ρ_x**(mol/cm^3)** $\rightarrow G_{max}$	$(18.6 \pm 1.1)10^{-7}$	$(11.1 \pm 0.3)10^{-7}$	-
ρ_x**(mol/cm^3)** $\rightarrow G_{min}$	$(4.8 \pm 1.0)10^{-7}$	$(2.8 \pm 0.2)10^{-7}$	-
ξ **(nm)** $\rightarrow G_{max}$	12 ± 0.24	14 ± 0.12	-
ξ **(nm)** $\rightarrow G_{min}$	19 ± 1.40	22 ± 0.50	-
***F*(5,30) <**	27	413	138

Table 4.4: Parameters relative to the eq.(3.78)-(3.79) best fitting to the experimental data (systems A2, A2PF18, PF18) shown in Figure 4.11. G_e, G_1, G_2, G_3 and G_4, are the spring constants of the generalized Maxwell model, λ_1 is the relaxation time of the first viscoelastic Maxwell element, G_{min} (=G_e) and G_{max} (=G_e + G_1 + G_2 + G_3 +G_4) indicate, respectively, the minimum and the maximum value of the shear modulus, ρ_x is the crosslink density, ξ is the mesh size of the polymeric network while *F*(5,30) indicate the *F*-test results about the statistical acceptability of data fitting.

Table 4.4 (see F-test) and *Figure 4.11* reveal that the three fitting are statistically good and that the mesh size of the polymeric network should be comprised between 12 and 19 nm for the A2 gel and between 14 and 22 nm for the A2PF18 gel. In the A2PF18 case, the evaluation of the mesh size according to the Flory [**49**] and Sherer [**50**] theories can be questionable as pluronic does not give origin to the network topology assumed by Flory and Scherer. Nevertheless, the ξ increase, with respect to the A2 case, is another way of quantifying the hindering action exerted by pluronic on alginate crosslinking process. Low field NMR tests revealed that, for the PF18 gel, three relaxation times are necessary to describe the relaxation of the x-y component of the magnetization vector (M_{xy}). In the A2 and A2PF18 cases, on the contrary, four relaxation times are needed as reported in *Table 4.5*. Although it is never simple associating a relaxation time to a particular protons status, in the case of PF18 we can argue that the highest relaxation time (T_{21}) essentially corresponds to "free" water protons, i.e. it corresponds to the water molecules that are weakly influenced by PF18 micelles and that pervade the micelles three-dimensional network. This hypothesis is supported by their abundance (A1% ≈ 84%, see *Table 4.5*) and by the relatively high value of the relaxation time (T_{21} = 2280, see *Table 4.5*) in comparison to that of the bulk water that, at 37°C, is approximately 3700 ms [**51**]. The last two relaxation times (T_{22}, T_{23}) could be attributed to the system made up by pluronic micelles and water molecules that are in deep contact with micelles hydrophilic tails ("bound" water) as observed by Lindmann [**52**]. This hypothesis is supported by the fact the sum of T_{22} and T_{23} abundance (16.3%) is slightly higher than that theoretically competing to pluronic protons (15.9%). In addition, the average T_{22} and T_{23} value (weighted on their relative abundance) (280 ms) is close to the relaxation time (224 ms) we measured for pluronic protons in the PF18-D_2O gel (37°C). In the A2 case, the fastest relaxation times (T_{22}, T_{23}, T_{24},) should correspond to the protons of the water trapped inside the polymeric meshes as their values are very low in comparison to free water relaxation at 37°C (3700 ms [**51**]) and they represent about 80% of the relaxing protons. The first relaxation time (T_{21}), on the contrary, is too high to be associated to water trapped in the polymeric meshes and it could be related to the water present on the film surface due to the unavoidable alginate shrinkage upon crosslinking as also found elsewhere [**53**]. Due to the low alginate concentration, the contribute of alginate protons is not detectable (≈ 0.64%). The A2PF18 gel shows a relaxation behavior similar to the

A2 one (see *Table 4.5*) the main difference occurring for the slowest relaxation time (T_{21}). Indeed, the pluronic presence in the alginate network clearly reduces T_{21} value and weight ($A_{1\%}$) that becomes approximately one/third. This last evidence further supports the hypothesis that T_{21} is associated to surface water due to network shrinkage. Indeed, in the presence of pluronic, network shrinking is considerable reduced (data not shown) and it is also reasonable that the surface water is more "bound" due to the presence of pluronic. Due to the existence of two structures (that of alginate and that of pluronic) the physical interpretation of T_{22}, T_{23} and T_{24} in the A2PF18 case is much more problematic.

A2PF18		***A2***		***PF18***	
$A_{i\%}$	T_{2i}**(ms)**	$A_{i\%}$	T_{2i}**(ms)**	$A_{i\%}$	T_{2i}**(ms)**
7.8 ± 2.5	1312 ± 300	21.4 ± 5.7	1925 ± 310	83.7 ± 0.1	2280 ± 77
13.2 ± 1.4	402 ± 92	9.1 ± 2.9	474 ± 173	9.8 ± 0.2	407 ± 8
67.6 ± 8.5	124 ± 8.5	46.8 ± 8.4	126 ± 22	6.5 ± 0.2	88 ± 5
11.4 ± 6.8	54 ± 17	22.7 ± 6.0	62 ± 14		
$\langle T_2 \rangle$ **(ms)**	$\langle 1/T_2 \rangle$ **(ms^{-1})**	$\langle T_2 \rangle$ **(ms)**	$\langle 1/T_2 \rangle$ **(ms^{-1})**	$\langle T_2 \rangle$ **(ms)**	$\langle 1/T_2 \rangle$ **(ms^{-1})**
246	$7.92*10^{-3}$	529	$7.62*10^{-3}$	1956	$1.33*10^{-3}$

Table 4.5: Relaxation times (T_{2i}) and relative weights ($A_{i\%}$) referring to the three gels considered (A2PF18, A2, PF18).The relative weights are evaluated as $A_{i\%} = 100A_i \Big/ \sum_{i=1}^{m} A_i$. The average inverse relaxation time is evaluated as $\langle 1/T_2 \rangle = 0.01 \sum_{i=1}^{m} A_{i\%}/T_{2i}$.

Anyway, their values are statistically equal to those competing to the A2 gel (see *Table 4.5*) and differences arise for what concerns their relative abundance (see *Table 4.5*). Thus, we could conclude that pluronic presence does not qualitatively modify the structures present in the A2 gel, but it implies a variation of their relative abundance. Interestingly, A2PF18 is the gel characterized by the lowest average relaxation time $\langle T_2 \rangle$ among the three gels considered. In the A2 case, the theory shown in the Low field NMR (Chapter 3) can be considered for the determination of the polymeric network mesh size distribution. Indeed, knowing that polymer volume fraction (ϕ) is 0.0114 and alginate fiber radius (R_f) is equal to 0.8 nm, eq.(3.46) returns ξ = 22.9 nm. ξ knowledge and eq.(3.47) allow to conclude that the relaxivity $\langle \mathcal{M} \rangle$ is equal to $3.24*10^{-7}$ m/s. This estimation was carried out calculating the average inverse relaxation time (= 9.6*10-3 ms-1) on the basis of the three fastest relaxation times (T_{22}, T_{23} and T_{24} in *Table 4.5*) as

the first one was not attributed to water trapped in the polymeric network. Knowing that the free water diffusion coefficient *D* at 37°C in the A2 gel (see *Figure 4.14*) is around to $3*10^{-9}$ m^2/s [**54**] and that R_c = 69.4 nm, it turns out that $\langle \mathcal{M} \rangle$ R_c/D = 8*10-7, i.e, << 1. Accordingly, fast conditions are met and eq.(3.48) can be adopted to estimate the mesh size (ξ_i) corresponding to relaxation times T_{22}, T_{23} and T_{24}: ξ_2 = 114 nm (11%), ξ_3 = 28 nm (59%) and ξ_4 = 13.6 nm (30%). It can be noticed that the ξ range, found according to rheology (12 – 19 nm; see *Table 4.5*), is not so far from the ξ_3 - ξ_4 range that represents, according to the low field NMR analysis, the 89% of the network meshes. The reasonability of both estimations is supported by the TEM image of A2 gel (*Figure 4.12*) showing the existence of few big meshes (≈ 100 nm) as well as much smaller and frequent meshes.

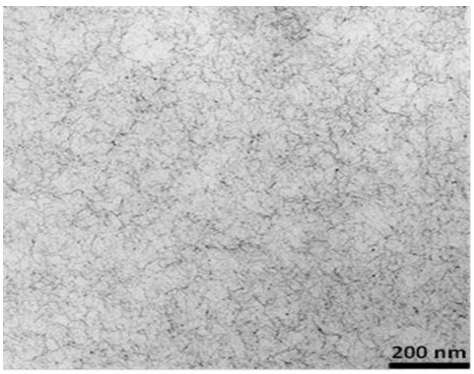

Figure 4.12: TEM image referring to the alginate (A2) gel.

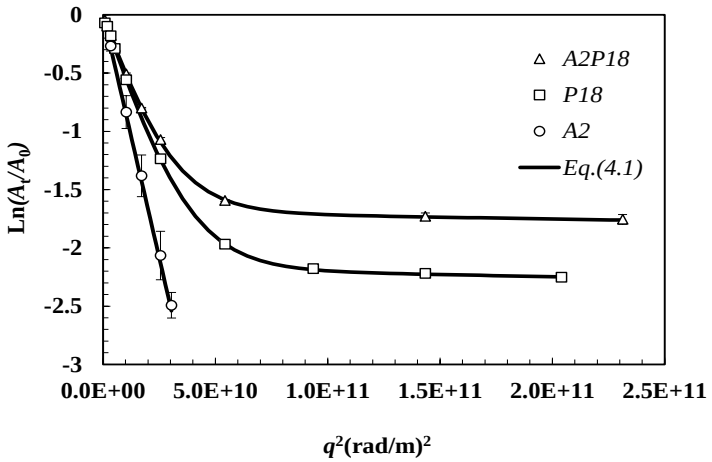

Figure 4.12: Logarithmic decrease, $L_n(A_t/A_0)$, of the ratio between the measured amplitude of the signal at the echo with (A_t) and without (A_0) gradient applied, versus q^2 ($q = \gamma * g * \delta$, see eq.(4.1)) for the three gels studied (A2, PF18, and A2PF18) assuming a diffusion time td = 29.66 ms (Δ = 30 ms) (37°C). Symbols indicate the experimental data while solid line indicate eq.4.1) best fitting. Vertical bars indicate standard error.

In order to get some more insight about the structure of the A2PF18 gel, the determination of the water self-diffusion coefficient (*D*) according to PGSE experiments can be useful. As an example, *Figure 4.13* shows the trend of $Ln(A_t/A_0)$ *versus* q^2 (see eq.(4.1)) for the three gels studied (A2, PF18, and A2PF18) and considering Δ = 30 ms (i.e. t_d = 29.66 ms). It is easy to see that in the A2 case only one of the p exponentials appearing in eq.(4.1) is necessary for a reliable data fitting.

On the contrary, for PF18 and A2PF18 gels, two exponentials are needed. This means that in the A2 gel all the water molecules diffuse in the same way (obviously, the crosslinked alginate chains cannot diffuse), while in the other two systems two distinct diffusion modes are detectable. *Figure 4.14* extends this finding for all the Δ, or t_d, considered. For the A2 gel, the water self-diffusion coefficient (D_wA2, see crosses) is independent on t_d, or its square root, this meaning that the A2 polymeric network is substantially homogeneous (interconnected mesh) as its hindering action on water molecules diffusion is the same whatever the td considered [**55**]. In addition, its hindering action is very limited as D_wA2 is very close to the bulk water self-diffusion coefficient (37°C; $3.04*10^{-9}$ m^2/s [**54**]). In the PF18 case, on the contrary, two diffusing species can be found. The first one, D_{w1} P18, should be attributed to free water (water molecules that are weakly influenced by PF18) while the second one, D_{w2} P18 should correspond to pluronic micelles and bound water. Indeed, not only D_{w1} P18 is very close to bulk water self-diffusion coefficient at 37°C, but also eq.(4.1) data fitting reveals that, regardless of the diffusion time t_d, about 80% of the protons diffuse with self-diffusion coefficient equal to D_{w1} P18 while the remaining 20% diffuses according to D_{w2} P18. This finding is absolutely in accordance with what found in relaxation experiments (see *Table 4.5*). In addition, PGSE experiments carried out on the PF18-D_2O gel, reveal that only one diffusing species can be found and its self-diffusion coefficient is, regardless of t_d, around $2.7*10^{-11}$ m^2/s, i.e. close to D_{w2} P18. In the PF18A2 gel, again, two diffusion modes can be detected: D_{w1} P18A2 and D_{w2} P18A2. Their relative abundance (80%, 20%) is equal to that of the PF18 case while D_{w2} P18A2 values are slightly smaller than those competing to D_{w2} P18 (see *Figure 4.14*). In conclusion, also PGSE experiments reveal the homogeneous nature of A2 gel and the inhomogeneous nature of the PF18A2 gel. This conclusion is also supported by the high field NMR analysis devoted to study the self-diffusion coefficient of theophylline (DTH) in our gel systems.

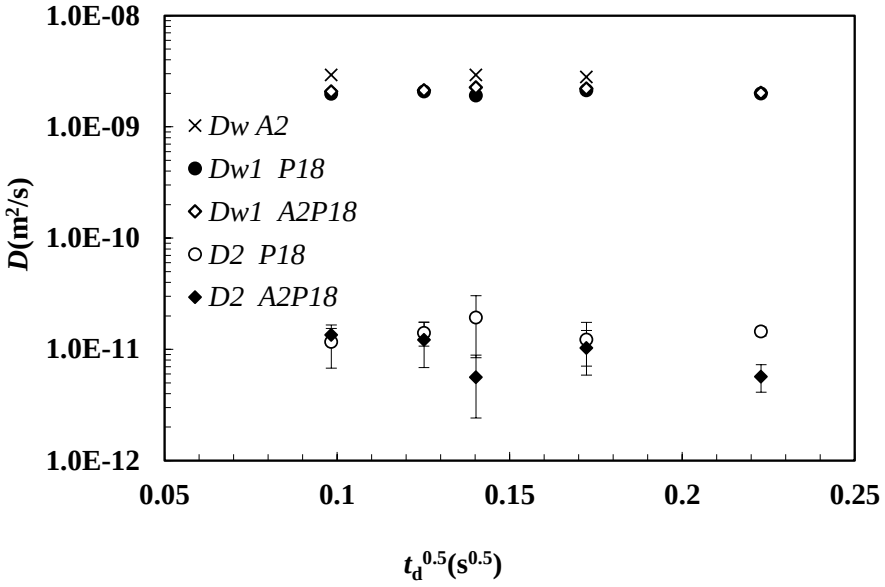

Figure 4.13: Diffusion time (t_d) dependence of the water self-diffusion coefficient in alginate (D_w A2), pluronic (D_{w1} P18, D_{w2} P18) and alginate-pluronic (D_{w1} P18A2, D_{w2} P18A2) gels (37°C). While in the A2 gel only one diffusion mode can be seen, two diffusion modes are detectable for the P18 and P18A2 gels. Vertical bars indicate standard error.

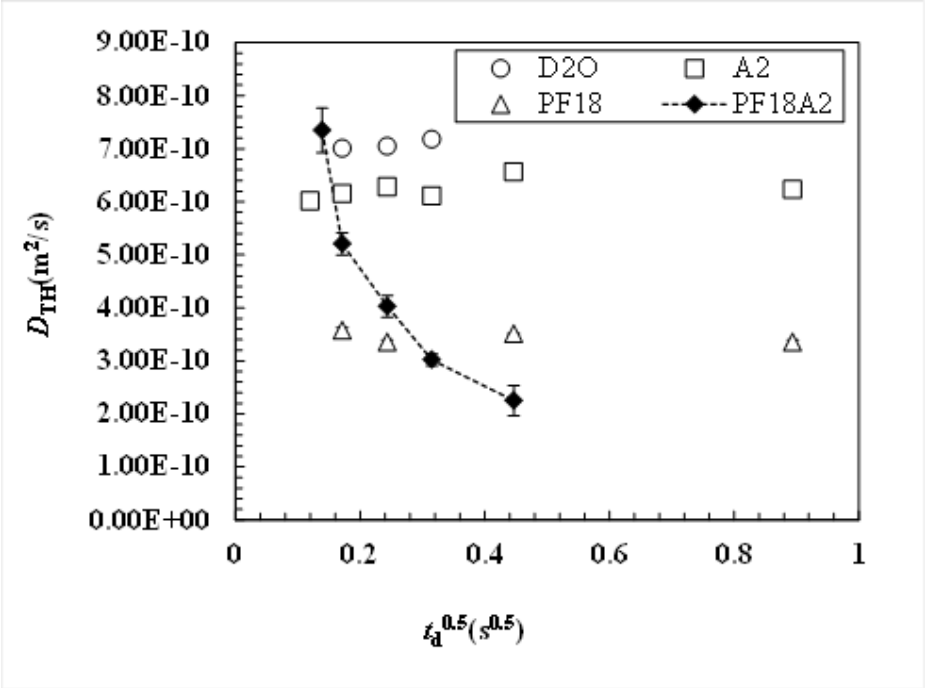

Figure 4.14: Diffusion time (t_d) dependence of the theophylline self-diffusion coefficient (DTH) in D2O (open circles), alginate (A2, open squares), pluronic (PF18, open triangles) and alginate-pluronic (PF18A2, black diamonds with dotted line) gels (37°C). Vertical bars indicate standard error.

Figure 4.15 shows the DTH dependence on the square root of the diffusion time, t_d, in a D_2O-theophylline solution (10 mg/cm^3, 37°C) and in the three gels prepared with the same D_2O-theophylline solution. It can be seen that, in the D_2O solution, D_{TH} is independent on t_d and its value is a little bit smaller than that in H_2O at the same temperature [**56**] ($8.2*10^{-10}$ m^2/s). This little difference can be explained by the higher viscosity of D_2O with respect to that of H_2O. In the A2 gel, again, D_{TH} is independent on t_d and this is a clear indication of a homogeneous network that offers the same hindering action on theophylline diffusion whatever the distance explored in the diffusion time. In addition, D_{TH} is slightly depressed by the presence of the polymeric network as its values is not so far from that in D_2O. This means that theophylline diameter (0.78 nm) [**56**] has to be small in comparison to network meshes, this being in line with the estimations performed according to rheology (12 – 19 nm) and low field NMR (114 – 13 nm). In the PF18 gel, D_{TH} is still constant but its reduction with respect to that in D_2O is now considerable. Thus, this gel is homogeneous but its architecture is completely different from that of A2. As the PF18A2 gel is characterized by a t_d dependent D_{TH}, we have to argue that this gel is not homogeneous. In other words, for small t_d, the theophylline mobility is almost un-affected by the gel structure (see *Figure 4.15*) while its mobility is considerably reduced when it is let to explore wider space portions (big t_d) where the probability of matching an obstacle is considerably increased. Interestingly, the D_{TH} value corresponding to the highest td explored (see *Figure 4.14*) is lower than that competing to the PF18 system and this seems reasonable due to the simultaneous presence of alginate and pluronic in the PF18A2 gel. A final confirmation of the not homogeneous nature of the PF18A2 gel is given in *Figure 4.16* that reports the comparison between the TEM picture of the A2 gel (that of *Figure 4.12*) and the PF18A2 gel. It is clear that the alginate chains (black traces; pluronic micelles are not visible) form wider meshes when pluronic is present (PF18A2 image in *Figure 4.16*). On the contrary, pluronic absence implies the formation of a more uniform structure characterized by smaller meshes (A2 image in *Figure 4.16*). On the basis of the results coming from the rheology, low and high filed NMR characterizations, we should conclude that structure of the PF18A2 gel is that reported in *Figure 4.17*. *Figure 4.17* was built catching the alginate chains architecture from Figure 4.15 (PF18A2) and then inserting the cubic structures formed by pluronic micelles (stars of diameter ≈ 20 nm [**57**]; stars are in scale with mesh size).

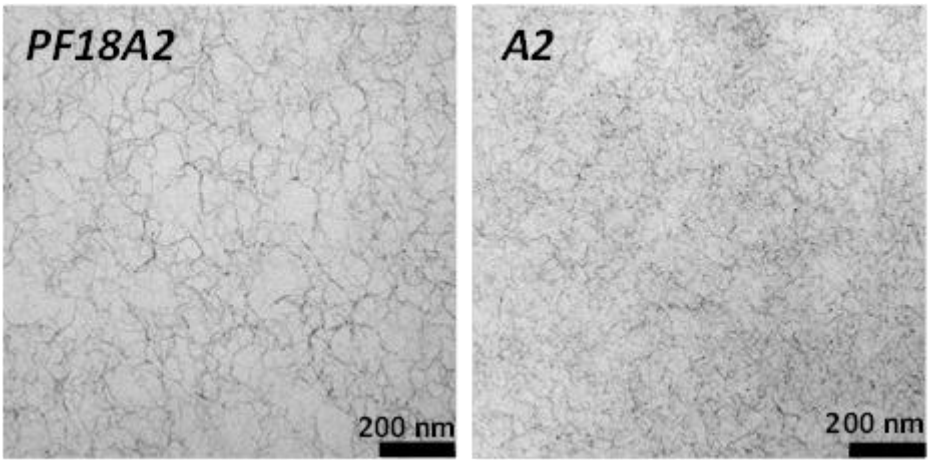

Figure 4.15: Comparison between the TEM images referring to the alginate-pluronic (PF18A2) and the alginate (A2) gels.

Depending on size, we can find meshes that can host the pluronic crystalline structure (ensemble of stars) and meshes that cannot in virtue of their small dimensions. Small meshes can host not structured micelles, or just water. Accordingly, our model drug (theophylline) can freely diffuse in smaller meshes (those without the crystalline pluronic structure) while its diffusion is hindered in large meshes where the pluronic crystalline structure can form.

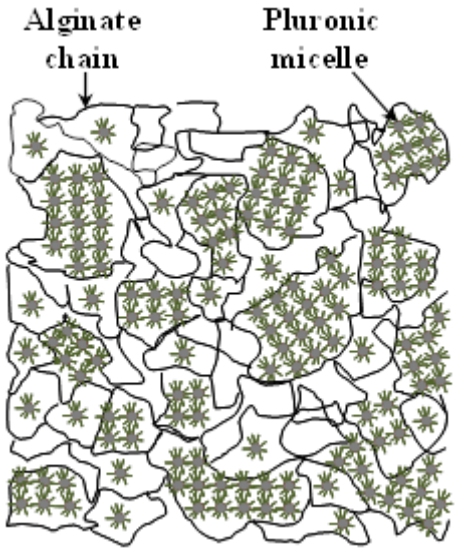

Figure 4.16: Schematic representation of the PF18A2 gel nanostructure as deduced by our characterization.

Finally, high field NMR, allowed also to estimate the self-diffusion coefficient (D_0) of our second model drug (oligonucleotide) in the PF18A2 gel. It turned out that, in the

explored diffusion time range (300 ms < t_d < 1800 ms), D_O decreases from $2*10^{-11}$ m^2/s to $3*10^{-12}$ m^2/s (37°C). Thus, for small t_d, its diffusivity is about 1/3 of that measured in pure D_2O ($6.6*10^{-11}$ m^2/s; 37°C) while this ratio falls to about 1/20 for longer t_d. Again, this behavior should be due to the inhomogeneous structure of the PF18A2 gel.

References

1. Maier H., Anderson M., Karl C., Magnuson K., Whistler R. L.: Guar, Locust bean gum, tara, and fenugreek gums. In: Industrial Gums, third ed., Chapter 8, Whistler, R. L., BeMiller J. N. editors. New York: Academic Press, p. 181–226 (1993).
2. McCleary B. V., Clark A. H., Dea I. C. M., Rees D. A.: The fine structures of carob and guar galactomannans. Carbohydrate Research, 139, 237–260 (1985). DOI: 10.1016/0008-6215(85)90024-2.
3. Fox J. E.: Seed gums. In: Thickening and gelling agents for food, Imeson, A. editor. Blackie Academic Professional, New York, p. 262-283 (1997).
4. Kucera C. H., DeMott D. N.: Drilling fluid containing crosslinked polysaccharide derivative. US patent no. 4,257,903 (1981).
5. Brode G. L., Goddard E. D., Harris W. C., Salensky G. A.: Cationic polysaccharides for cosmetics and therapeutics. In: Gebelein, C. G., Cheng, T. C., Yang, V. C. editors. Cosmetic and pharmaceutical applications of polymers. New York: Plenum Press, p. 117–128 (1991).
6. Vijayendran B. R., Bone T.: 1984. Absolute molecular weight and molecular weight distribution of guar by size exclusion chromatography and low-angle laser light scattering. Carbohydrate Polymers, 4, 299–313 (1984). DOI: 10.1016/0144-8617(84)90005-5.
7. Picout D. R., Ross-Murphy S. B.: On the Mark–Houwink parameters for galactomannans. Carbohydrate Polymers, 70, 145–148 (2007). DOI: 10.1016/j.carbpol.2007.03.010
8. Gliko-Kabir I., Yagen B., Penasi A., Rubinstein A.: 1998. Low swelling, crosslinked guar and its potential use as colon-specific drug carrier. Pharmaceutical Research, 15, 1019–1025 (1998). DOI: 10.1023/A:1011921925745
9. Coviello T., Alhaique F., Dorigo A., Matricardi P., Grassi M.: Two galactomannans and scleroglucan as matrices for drug delivery: preparation and release studies. European Journal of Pharmaceutics and Biopharmaceutics, 66, 200–209 (2007). DOI: 10.1016/j.ejpb.2006.10.024

10. Norisuye T., Yanaki T., Fujita H.: Triple helix of a Schizophyllum commune polysaccharide in aqueous solution. Journal of Polymer Science Polymer Physics, 18, 547–558 (1980). DOI: 10.1002/pol.1980.180180314.

11. Yanaki T., Norisuye T., Fujita, H.: Triple helix of Schizophyllum commune polysaccharide in dilute solution. 3. Hydrodynamic properties in water. Macromolecules, 13, 1462–1466 (1980).

12. Giavasis I., Harvey L. M., McNeil B.: Scleroglucan. In: Biopolymers, polysaccharides II (Vol. 6,), De Baets, S., Vandamme, E. J., Steinbüchel, A. editors: Weinheim Wiley-VCH, p. 37-60 (2002).

13. Rizk S., Duru C., Gaudy D., Jacob M., Ferrari F., Bertoni M., Caramella C. Physico-chemical characterization and tabletting properties of Scleroglucan. International Journal of Pharmaceutics, 112, 125-131 (1994). DOI: 10.1016/0378-5173(94)90422-7.

14. Pezron E., Leibler L., Lafuma F.: Complex formation in polymer-ion solutions. 2. Polyelectrolyte effects. Macromolecules, 22, 2656–2662 (1989). DOI: 10.1021/ma00196a021.

15. Shibayama M., Yoshizawa H., Kurokawa H., Fujiwara H., Nomura N.: Sol–gel transition of poly(vinyl alcohol)–borate complex. Polymer, 29, 2066–2071 (1988). DOI: 10.1016/0032-3861(88)90182-6.

16. Bocchinfuso G., Palleschi A., Mazzuca C., Coviello T., Alhaique F., Marletta G.: Theoretical and experimental study on a self-assembling polysaccharide forming nanochannels: static and dynamic effects induced by a soft confinement. Journal of Physical Chemistry B, 112, 6473-6483 (2008). DOI: 10.1021/jp076074f.

17. Palleschi A., Coviello T., Bocchinfuso G., Alhaique F.: Investigation of a new scleroglucan/borax hydrogel: structure and drug release. International Journal of Pharmaceutics, 322, 13-21 (2006). DOI:10.1016/j.ijpharm.2006.05.029

18. Kesavan S., Prud'homme R. K.: Rheology of guar and HPG crosslinked by borate. Macromolecules, 25, 2026–2032 (1992). DOI: 10.1021/ma00033a029.

19. Tayal A., Pai V. B., Khan, S. A.: Rheology and microstructure changes during enzymatic degradation of a guar-borax hydrogel. Macromolecules, 32, 5567–5574 (1999). DOI: 10.1021/ma990167g.

20. Bluhm L.T., Deslandes Y., Marchessault R. H., Perez S., Rinaudo M.: Solid-state and solution conformations of Scleroglucan. Carbohydrate Research, 100, 117–130 (1982). DOI: 10.1016/S0008-6215(00)81030-7.

21. Sandolo C., Matricardi P., Alhaique F., Coviello T.: Effect of temperature and cross-linking density on rheology of chemical cross-linked guar gum at the gel point. Food Hydrocolloid, 23, 210-220 (2009). DOI: /10.1016/j.foodhyd. 2008.01.001.

22. Pezron E., Ricard A., Leibler L.: Rheology of galactomannan-borax gels. Journal of Polymer Science Polymer Physics, 28, 2445–2461 (1990). DOI: 10.1002/polb.1990.090281301.

23. Bocchinfuso G., Mazzuca C., Sandolo C., Margheritelli S., Alhaique F., Coviello T., Palleschi A.: Guar Gum and Scleroglucan interactions with borax: experimental and theoretical studies of an unexpected similarity. Journal of Physical Chemistry B, 114, 13059-13068 (2010). DOI: 10.1021/jp105838t.

24. Kok M. S., Hill S. E., Mitchell J. R. Viscosity of galactomannans during high temperature processing: Influence of degradation and solubilisation. Food Hydrocolloid, 13, 535–542 (1999). DOI: 10.1016/S0268-005X(99)00040-5.

25. Lapasin R., Pricl S.: Rheology of industrial polysaccharides: Theory and applications. London: Blackie Academic & Professional (1995).

26. Kuijpers A. J., Engbers G. H. M., Feijen J., De Smedt S. C., Meyvis T. K. L., Demeester J., Krijgsveld J., Zaat S. A. J., Dankert J.: 1999. Characterization of the Network Structure of Carbodiimide Cross-Linked Gelatin Gels. Macromolecules, 32, 3325-3334 (1999). DOI: 10.1021/ma981929v.

27. Uh J., Watson A. T.: Nuclear magnetic resonance determination of surface relaxivity in permeable media. Industrial & Engineering Chemistry Research., 43, 3026-3032 (2004). DOI: 10.1021/ie030599m.

28. Dubois M., Gilles K. A., Hamilton J. K., Rebers P. A., Smith F.: Colorimetric method for determination of sugars and related substances. Analytical Chemistry, 28, 350–356 (1956). DOI: 10.1021/ac60111a017.

29. Palleschi A., Bocchinfuso G., Coviello T., Alhaique F.: Molecular dynamics investigations of the polysaccharide scleroglucan: first study on the triple helix structure. Carbohydrate Research, 340, 2154–2162 (2005).

30. Grassi M., Grassi G., Lapasin R., Colombo I.: Understanding drug release and absorption mechanisms: a physical and mathematical approach. Boca Raton (USA): CRC Press, (2007).

31. Tomic K., Veeman W. S., Boerakker M., Litvinov V. M., Dias A. A.: Lateral and rotational mobility of some drug molecules in a poly(ethylene glycol) diacrylate hydrogel and the effect of drug-cyclodextrin complexation. Journal of Pharmaceutical Sciences, 97, 3245-3256 (2008). DOI: 10.1002/jps.21251.

32. Grassi M., Lapasin R., Coviello T., Matricardi P., Di Meo C., Alhaique, F. Scleroglucan/borax/drug hydrogels: structure characterisation by means of rheological and diffusion experiments. Carbohydrate Polymers 78, 377–383 (2009). DOI: 10.1016/j.carbpol.2009.04.025.

33. Gombotz, W.R. and S.F. Wee, Protein release from alginate matrices. Adv Drug Deliv Rev, 1998. 31(3): p. 267-85.

34. Draget, K.I., O. Smidsrød, and G. Skjåk-Bræk, Alginates from algae, in Polysaccharides and polyamides in the food industries. Properties, production and patents, A. Steinbüchel and S.K. Rhee, Editors. 2005, Willey-VCH: Weinheim.

35. Amsden, B. and N. Turner, Diffusion characteristics of calcium alginate gels. Biotechnology and Bioengineering, 1999. 65(5): p. 605-610.

36. Draget, K.I., G. Skjåk-Bræk, and O. Smidsrød, Alginate based new materials. j Biol Macromol, 1997. 21: p. 47-55.

37. Alexandridis, P. and T.A. Hatton, Poly(ethylene oxide)-poly(propylene oxide)-poly(ethylene oxide) block copolymer surfactants in aqueous solutions and at interfaces: thermodynamics, structure, dynamics, and modeling. Colloids Surf A, 1995. 96: p. 1-46.

38. Lau, B.K., et al., Micellization to gelation of a triblock copolymer in water: Thermoreversibility and scaling. J. Polym. Sci. Part B, 2004. 42: p. 2014-25.

39. Wanka, G., H. Hoffmann, and W. Ulbricht, The aggregation behavior of poly-(oxyethylene)-poly-(oxypropylene)-poly-(oxyethylene)-block-copolymers in aqueous solution. Colloid Polym Sci, 1990. 268: p. 101-17.

40. Yu, G.E., et al., Micellisation and gelation of triblock copoly(oxyethylene/oxypropylene/oxyethylene), F127. J Chem Soc, Faraday Trans, 1992. 88: p. 2537 - 2544.

41. Schmolka, I. R. "A review of block polymer surfactants"J. Am. Oil Chem. Soc. 1977, 54, 110-116.

42. Grassi, G.; Farra, R.; Noro, E.; Voinovich, D.; Lapasin, R.; Dapas, B.; Alpar, O.;4, Zennaro, C.; Carraro, M.; Giansante, C.; Guarnieri, G.; Pascotto, A.; Rehimers, B.; Grassi, M. J. Drug. Del. Sci. Tech. 2007, 17, 325-331.

43. Kuijpers, A. J.; Engbers, G. H. M.; Feijen, J.; De Smedt, S. C.; Meyvis T. K. L.; Demeester, J.; Krijgsveld, J.; Zaat, S. A. J.; Dankert, J. Macromolecules 1999, 32, 3325-3334.

44. Grassi, M.; Fiorentino, S.; Farra, R.; Dapas, B.; Grassi, G. In Polysaccharide hydrogels: characterization and biomedical applications. Pan Stanford publishing, Singapore in press (2013).

45. Draper, N. R.; Smith, H. Applied Regression Analysis. John Wiley & Sons, Inc., New York, 1966.

46. Pelta, Michelle D.; Morris, Gareth A.; Stchedroff, Marc J.; Hammond, Stephen J. A one-shot sequence for high-resolution diffusion-ordered spectroscopy. Magnetic Resonance in Chemistry. 2002; 40: S147-S152.

47. Johnson Jr C. S.,"Progress in Nuclear Magnetic Resonance Spettroscopy" Progr. Nucl. Magn. Reson. Spettrosc., 1999, 34, 203-256

48. Hwang T. L., Shaka A.J.,"Water suppression that works- excitation sculpting using arbitrary wave-fors and pulsed-field gradients" J. Magn. Reson. Ser.A, 1995, 112, 275-279;

49. Flory, P. J. Principles of polymer chemistry. Cornell University Press, Ithaca (USA), 1953.

50. Scherer, G. W.: Hydraulic radius and mesh size of gels. J. Sol-Gel Sci. Technol. 1994, 1, 285-291.

51. Coviello, T.; Matricardi, P.; Alhaique, F.; Farra, R.; Tesei, G.; Fiorentino, S.; Asaro, F.; G. Milcovich, G.; Grassi, M. Express Polymer Letters 2013, in press.

52. Malmsten, M.; Lindman, B. Macromolecules 1992, 25, 5446-5450.

53. Turco, G.; Donati, I.; Grassi, M.; Marchioli, G.; Lapasin, R.; Paoletti, S. Biomacromolecules 2011, 12, 1272–1282.

54. (35) Holz, M.; Heil, S. R.; Sacco, A. Phys. Chem. Chem. Phys. 2000, 2, 4740-4742.

55. Stait-Gardner, T.; Willis, S. A.; Yadav, N. N.; Zheng, G.; Price, W. S. Diffusion Fundamentals 2009, 11, 1-22.

56. Grassi, M.; Grassi, G; Lapasin, R.; Colombo, I. Understanding drug release and absorption mechanisms: a physical and mathematical approach. CRC Press, Boca Raton (USA), 2007, 1-627.

57. Alexandridis, P.; Hatton, T. A. Colloids Surf. 1995, 96, 1-46.

5 Porous Systems

In this section, four different kinds of porous systems will be presented. The first one is constituted by *spherical glass beads* immersed in water, while the second one consists of *green coffee seeds*, kindly donated by Illycaffè (Trieste). Finally, the third and the fourth systems are represented by *styrene-butadiene rubbers* and by *bacterial cellulose / acrylic acid hydrogels*. In all these systems, Low Field NMR was adopted for the estimation of the pores size distribution. The main difference between these systems and those discussed in Chapter 4 consists in the dimension of the "pores". Indeed, while in Chapter 4 the systems were characterized by nano-sized pores (called, more properly, mesh), in this chapter the attention is focused on micro-pores systems. Accordingly, a different characterization strategy is needed.

5.1 Spherical glass beads

5.1.1 Experimental section

5.1.1.1 Materials and Methods

Laboratory glass beads with different diameter have been considered:

- Glass beads with a medium diameter of 50 μm (Sample A)
- Glass beads with a medium diameter of 100 μm (Sample B)
- Glass beads with a medium diameter of 150 μm (Sample C)
- Glass beads with a medium diameter of 3 mm (Sample D).

A		B		C	
Diameter (µm)	**Cumulate %**	**Diameter (µm)**	**Cumulate %**	**Diameter (µm)**	**Cumulate %**
22.44	0.00	44.77	0.00	112.47	0.00
25.18	0.06	50.24	0.11	126.19	0.08
28.25	0.63	56.37	0.71	141.59	0.58
31.70	2.58	63.25	3.35	158.87	3.44
35.57	7.96	70.96	8.96	178.25	9.31
39.91	16.64	79.62	18.77	200.00	20.47
44.77	30.36	89.34	33.49	224.40	36.83
50.24	47.20	100.24	50.53	251.79	55.31
56.37	64.27	112.47	67.68	282.51	73.06
63.25	79.36	126.19	82.08	316.98	86.80
70.96	90.01	141.59	91.24	355.66	94.41
79.62	95.95	158.87	97.08	399.05	98.76
89.34	99.09	178.25	99.28	447.74	99.82
100.24	99.85	200.00	99.93	502.38	100.00
-	-	224.40	100.00		

Table 5.1: Glass beads diameters (cumulate dates).

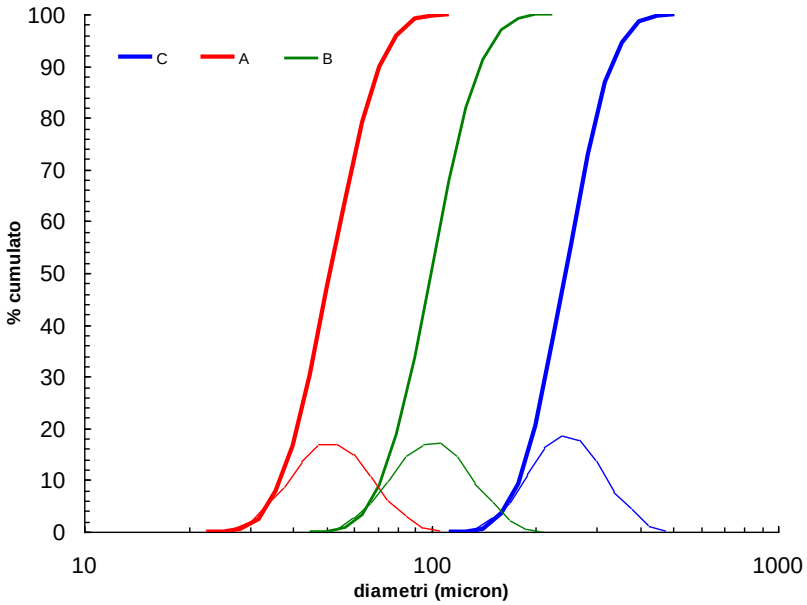

Figure 5.1: Cumulative distributions (thick lines) and differential distributions (thin lines) of the sample A, B and C.

In the first three samples, the diameters size distribution was determined by means of a laser (Malvern Mastersizer 2000E equipped by al Malvern Hydro 2000ME). *Table 5.1* and *Figure 5.1* show the cumulative and differential distributions relative to our spheres.

For each sample (A, B, C and D) a known beads amount was placed in the NMR tube. Subsequently, distilled water was added up to the top of the beads ensemble. Knowing the dry and wet weight of the glass beads, it was possible to have a preliminary date of porosity [density ρ_{glass} = 2.2g / cm^3; ρ_{H2O} (25 °C) = 0.99707g / cm^3]. The samples were then left to rest for 72 hours in order to give enough time to the glass beads to reach the maximum packing.

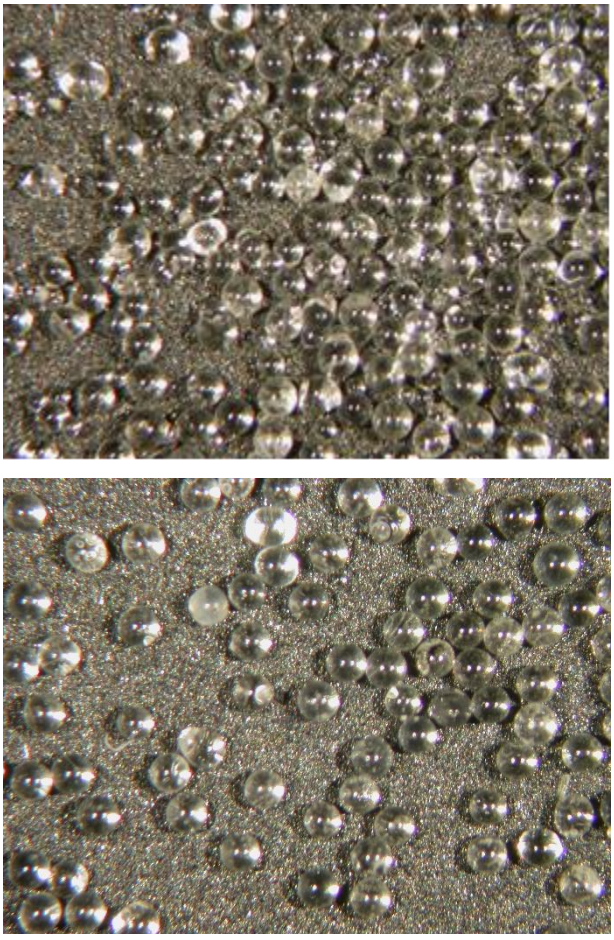

Figure 5.2: Microscopy pictures of the glass beads (A and B).

5.1.1.2 LF-NMR characterization

Low Field NMR (LF-NMR) characterization was performed, at 37 °C, by means of a Bruker Minispec mq20 (0.47 T, 20 MHz). Transverse relaxation time (T_2) measurements were carried out according to the (Carr-Purcell-Meiboom-Gill; CPMG) sequence (number of scans = 4; delay = 5 s). In order to study water mobility inside the glass beads, Pulsed Gradient Spin Echo (PGSE) measurements were performed. After an appropriate

calibration procedure, based on the knowledge of the free water self-diffusion coefficient (D_{H2O}), it is possible measuring the average water self-diffusion coefficient inside the glass beads structure (D).

5.1.2 Results and discussion

5.1.2.1 Relaxation Time T_2 measurement

After a time of about 30 minutes, needed for the stabilization of the temperature, 9 tests were performed. $\tau = 0.5$ ms was chosen for sample A, B and C while $\tau = 1$ ms for set for sample D. *Figure 5.3* shows the average intensity trend recorded for the different samples.

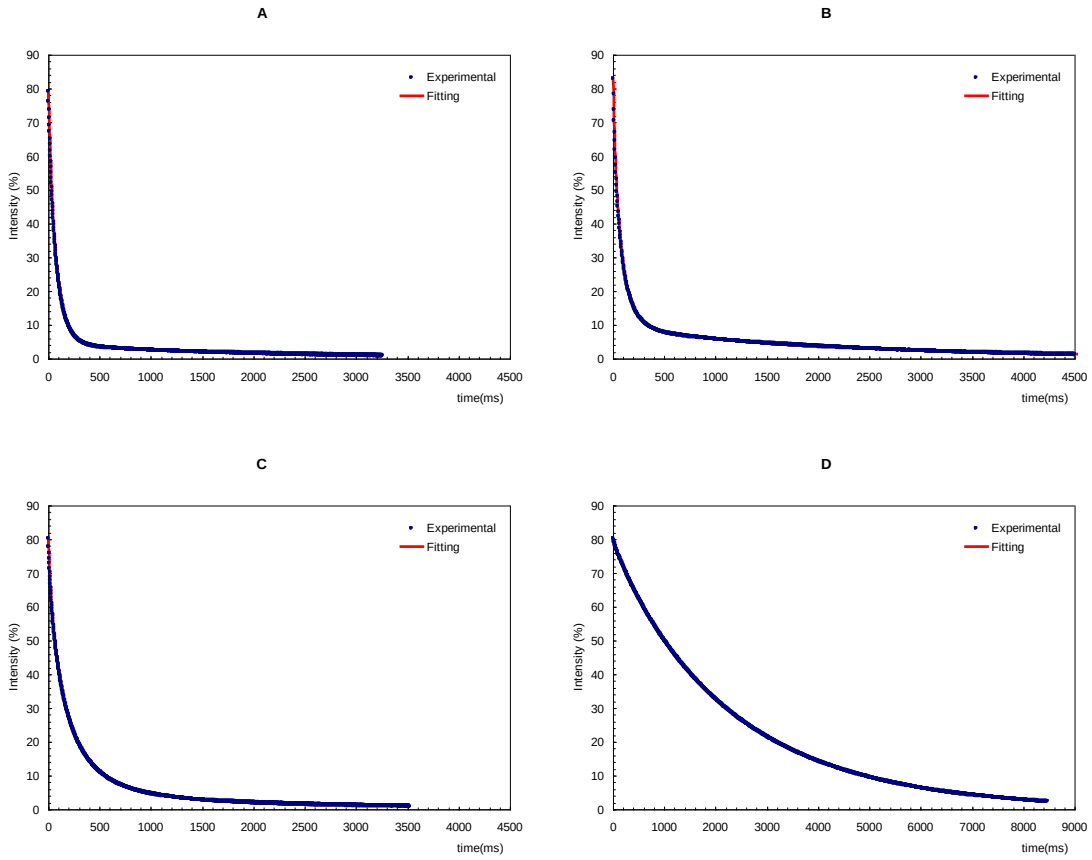

Figure 5.3: Relaxation Times T_2 trends of the samples A, B, C and D.

Tables 5.2 – 5.5 report the data obtained from the LF-NMR experiments.

$T_{21}(ms) =$	2363 ± 136	$A_1(\%) =$	8.1 ± 2.8
$T_{22}(ms) =$	226 ± 143	$A_2(\%) =$	9.0 ± 5.9
$T_{23}(ms) =$	80 ± 10	$A_3(\%) =$	73.1 ± 2.8
$T_{24}(ms) =$	19 ± 6	$A_4(\%) =$	9.8 ± 2.0

Table 5.2: Relaxation Times T_2 of the sample A (T= 25°C)

$T_{21}(ms) =$	2244 ± 111	$A_1(\%) =$	6.3 ± 3.1
$T_{22}(ms) =$	415 ± 236	$A_2(\%) =$	8.2 ± 11.7
$T_{23}(ms) =$	96 ± 18	$A_3(\%) =$	49.4 ± 1.4
$T_{24}(ms) =$	36 ± 11	$A_4(\%) =$	26.6 ± 8.3
$T_{25}(ms) =$	7.2 ± 2.2	$A_5(\%) =$	10.0 ± 1.6

Table 5.3: Relaxation Times T_2 of the sample B (T=25 °C)

$T_{21}(ms) =$	2207 ± 76	$A_1(\%) =$	7.0 ± 1.4
$T_{22}(ms) =$	399 ± 12	$A_2(\%) =$	23.0 ± 3.5
$T_{23}(ms) =$	169 ± 9	$A_3(\%) =$	43.2 ± 1.7
$T_{24}(ms) =$	54 ± 3	$A_4(\%) =$	19.2 ± 0.5
$T_{25}(ms) =$	9.2 ± 0.4	$A_5(\%) =$	7.6 ± 0.3

Table 5.4: Relaxation Times T_2 of the sample C (T= 25 °C)

$T_{21}(ms) =$	2516 ± 22	$A_1(\%) =$	90.1 ± 0.3
$T_{22}(ms) =$	891 ± 21	$A_2(\%) =$	9.9 ± 0.3

Table 5.5: Relaxation Times T_2 of the sample D (T= 25°C)

5.1.2.1.1 Measurement of the diffusion coefficient *D* and the average pores diameter ξ

The test parameters were as follows: $x_1 = x_2 = 1$ ms and $\delta = 1$ms. The self-diffusion coefficients measured are shown in *Figure 5.4* and in *Tables 5.6-5.9.*

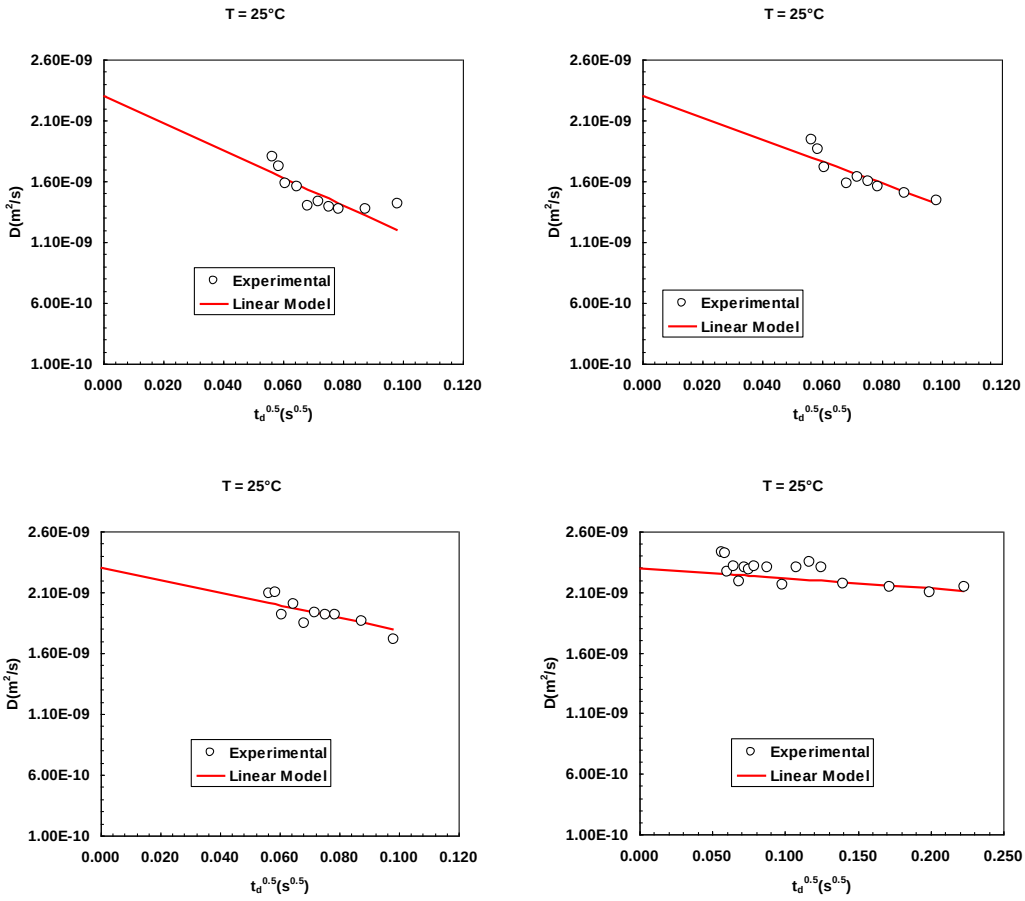

Figure 5.4: water self- diffusion coefficient *D* relative to samples A, B, C and D.

Δ(ms)	***(td(s))0.5***	***D(m²/s)***	***σi***
3.5	0.056	1.80E-09	1.04E-11
3.75	0.058	1.72E-09	1.31E-11
4	0.061	1.58E-09	3.63E-11
4.5	0.065	1.56E-09	2.32E-11
5	0.068	1.40E-09	1.10E-11
5.5	0.072	1.43E-09	1.24E-11
6	0.075	1.39E-09	1.21E-11
6.5	0.079	1.37E-09	1.56E-11
8	0.088	1.37E-09	1.08E-11
10	0.098	1.41E-09	2.88E-11

Table 5.6: water self-diffusion coefficient *D* relative to sample A (*T*= 25 °C, 15 repetitions).

7

Δ(ms)	$(t_d(s))^{0.5}$	$D(m^2/s)$	σ_i
3.5	0.056	1.94E-09	1.06E-11
3.75	0.058	1.87E-09	4.86E-11
4	0.061	1.71E-09	2.72E-11
4.5	0.065	3.83E-09	4.71E-09
5	0.068	1.58E-09	2.01E-11
5.5	0.072	1.63E-09	1.50E-11
6	0.075	1.60E-09	1.31E-11
6.5	0.079	1.56E-09	1.06E-11
8	0.088	1.50E-09	1.43E-11
10	0.098	1.44E-09	4.05E-11

Table 5.7: water self-diffusion coefficient *D* relative to sample B (*T*=25 °C, 15 repetitions).

Δ(ms)	$(t_d(s))^{0.5}$	$D(m^2/s)$	σ_i
3.5	0.056	2.09E-09	1.72E-11
3.75	0.058	2.10E-09	5.45E-11
4	0.061	1.91E-09	5.91E-11
4.5	0.065	2.00E-09	1.91E-11
5	0.068	1.84E-09	9.87E-12
5.5	0.072	1.93E-09	1.68E-11
6	0.075	1.92E-09	1.26E-11
6.5	0.079	1.92E-09	1.87E-11
8	0.088	1.86E-09	3.74E-12
10	0.098	1.71E-09	1.01E-11
12	0.108	1.79E-09	1.03E-11
14	0.117	1.80E-09	6.58E-11
16	0.125	1.78E-09	3.96E-11
18	0.133	1.64E-09	3.55E-11

Table 5.8: water self-diffusion coefficient *D* relative to sample C (*T*= 25 °C, 15 repetitions).

$\Delta(ms)$	$(t_d(s))^{0.5}$	$D(m^2/s)$	σ_i
3.5	0.056	2.43E-09	1.44E-11
3.75	0.058	2.42E-09	4.36E-11
4	0.061	2.27E-09	8.09E-11
4.5	0.065	2.32E-09	1.85E-11
5	0.068	2.19E-09	1.75E-11
5.5	0.072	2.30E-09	2.32E-11
6	0.075	2.29E-09	1.24E-11
6.5	0.079	2.31E-09	2.01E-11
8	0.088	2.30E-09	1.92E-11
10	0.098	2.16E-09	1.37E-11
12	0.108	2.30E-09	1.39E-11
14	0.117	2.35E-09	5.60E-11
16	0.125	2.30E-09	1.06E-11
20	0.140	2.17E-09	3.93E-12
30	0.172	2.15E-09	5.56E-12
40	0.199	2.09E-09	8.51E-12
50	0.223	2.14E-09	2.85E-11

Table 5.9: water self-diffusion coefficient *D* relative tosample D (*T*= 25° C, 15 repetitions).

Eq. 3.54 fitting to the above shown data yields to the following values of the average pores diameter ξ (pores generated by beads packing):

Sample	ξ (μm)
A	14.8 ± 0.2
B	18.5 ± 0.3
C	32.4 ± 0.3
D	196 ± 8

Table 5.10: Average diameter ξ of samples A, B, C and D.

On the basis of the average values of ξ and the relaxation times presented in *tables 5.2-5.5*, eqs. 3.55-3.59 allow the evaluation of the distribution of the pores diameter formed by the beads packing in the case of the systems A, B, C and D:

$\xi_1(\mu m)$ =	993 ± 588	$A_1(\%)$ =	8.1 ± 2.8
$\xi_2(\mu m)$ =	12 ± 9	$A_2(\%)$ =	9.0 ± 5.9
$\xi_3(\mu m)$ =	4.1 ± 1.4	$A_3(\%)$ =	73.1 ± 2.8
$\xi_4(\mu m)$ =	1.0 ± 0.4	$A_4(\%)$ =	9.8 ± 2.0

Table 5.11: Sample A, pore size distribution

$\xi_1(\mu m)$ =	1085 ± 533	$A_1(\%)$ =	6.3 ± 3.1
$\xi_2(\mu m)$ =	39 ± 30	$A_2(\%)$ =	8.2 ± 11.7
$\xi_3(\mu m)$ =	7.8 ± 3.4	$A_3(\%)$ =	49.4 ± 1.4
$\xi_4(\mu m)$ =	2.9 ± 1.4	$A_4(\%)$ =	26.6 ± 8.3
$\xi_5(\mu m)$ =	0.6 ± 0.3	$A_5(\%)$ =	10.0 ± 1.6

Table 5.12: Sample B, pore size distribution

$\xi_1(\mu m)$ =	1075 ± 248	$A_1(\%)$ =	7.0 ± 1.4
$\xi_2(\mu m)$ =	40 ± 5	$A_2(\%)$ =	23.0 ± 3.5
$\xi_3(\mu m)$ =	15 ± 2	$A_3(\%)$ =	43.2 ± 1.7
$\xi_4(\mu m)$ =	4.7 ± 0.6	$A_4(\%)$ =	19.2 ± 0.5
$\xi_5(\mu m)$ =	0.8 ± 0.1	$A_5(\%)$ =	7.6 ± 0.3

Table 5.13: Sample C, pore size distribution

$\xi_1(\mu m)$ =	416 ± 105	$A_1(\%)$ =	90.1 ± 0.3
$\xi_2(\mu m)$ =	13 ± 2	$A_2(\%)$ =	9.9 ± 0.3

Table 5.14: Sample D, pore size distribution

In order to evaluate the reliability of the above results, an alternative approach was undertaken to evaluate the pores dimension competing to the beads packing considered. In particular, the attention was focused on the theory proposed by Mayer and Stowe [**1**]. According to this theory, the packing of glass beads can range between two extremes: the first, which has the highest porosity, occurs when the spheres are packed vertically (cubic cell, *Fig. 5.5a*), the second, which has the lowest porosity, occurs when the glass beads are in conditions of maximum packing (*Fig. 5.5b*). The porosity ε varies from a maximum of 47.64% to a minimum of 25.95%.

As can be seen in *Figure 5.5*, the packing of the spheres can be described only by the angle σ, and the porosity of the packing described can be calculated by the following equation:

$$\varepsilon = 1 - \frac{\pi}{6}\left(1 - 3\cos^2\sigma + 2\cos^2\sigma\right)^{-\frac{1}{2}} \qquad (5.1)$$

Knowing the porosity of the samples (evaluated on the basis of the water volume needed to fill the voids of the beads packing), equation 5.1 allows the determination of σ. Known σ, it is possible to derive the minimum, maximum, and average diameter (*Fig. 5.5c*) of the empty space of the pores by means of the following equations:

$$\xi_{\min} = \phi_{sfera} \cdot \left(2sen\left(\frac{\sigma}{2}\right) - 1 \right) \tag{5.2}$$

$$\xi_{\max} = \phi_{sfera} \cdot \left(2\cos\left(\frac{\sigma}{2}\right) - 1 \right) \tag{5.3}$$

$$\xi = \frac{\xi_{\max} + \xi_{\min}}{2} \tag{5.4}$$

where σ is in radians and ϕ_{sphere} is the bead diameter. The results deriving from this theoretical approach are shown in *Table 5.15.*

	Glass Bead A	**Glass Bead B**	**Glass Bead C**	**Glass Bead D**
ξ_{min}(μm)	7.4 ± 2.5	13 ± 3	31 ± 6	851 ± 67
ξ_{max}(μm)	34 ±1.7	67 ± 2	164 ± 4	1601 ± 56
ξ (μm)	21 ± 1	40 ± 1	97 ± 1	1226 ± 5

Table 5.15: Pores diameters of the glass beads derived by theory.

It can be observed that the NMR estimations underestimate the average theoretical data of the samples A, B and C, even if they remain in the range $\xi_{min} - \xi_{max}$ range. This is no longer true for the glass beads D. This is probably due to the edge effects that in this case (D) should be considerable as beads diameter is about one half of the NMR tube diameter (*Figure 5.6*). Accordingly, a not homogeneous beads arrangement can be realized inside the NMR tube.

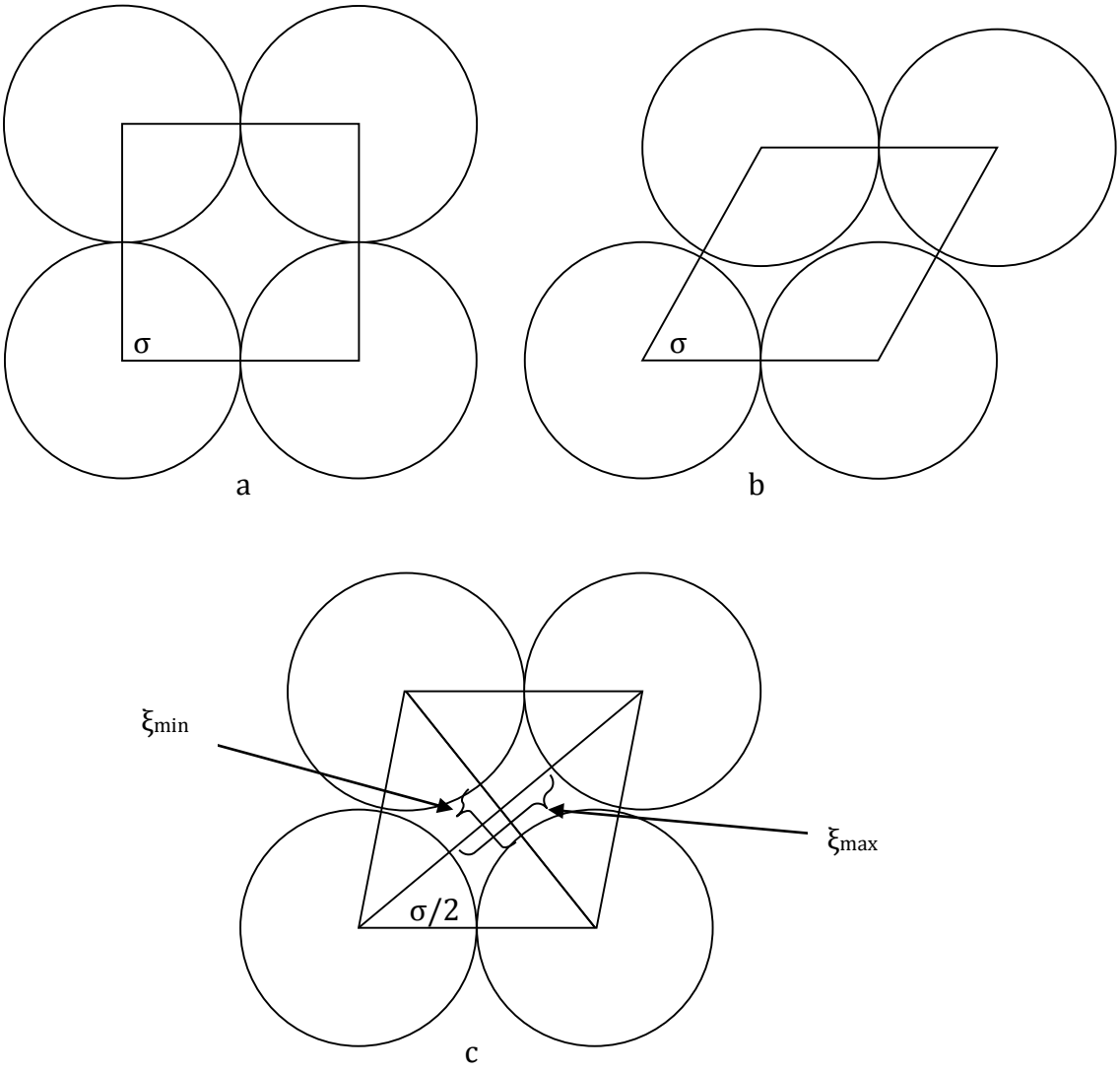

Figure 5.5: a. Condition of minimum packing (ε = 47.64%, σ = 90°) **b**. Condition of maximum packing (ε = 25.95%, σ = 60°), **c**. minimum and maximum diameter.

Figure 5.6: Sample D in the NMR tube.

For samples A, B and C, the results obtained by means of LF-NMR are encouraging, because we must not forget that the theoretical measurements are based on mono-disperse beads. Accordingly, it seems correct that the LF-NMR gives values below the theoretical average and close to ξ_{min}. The fact that the best results compete to sample A (the smallest), could be explained looking at beads size distribution. Indeed, sample A is that characterized by the narrowest size distribution (see *Figure 5.4*; note that a logarithmic scale is used).

M

5.2 Coffee beads

5.2.1 Introduction

Coffee is one of the most popular beverages in the world. Coffee plants are mainly grown in tropical and subtropical regions of central and South America, Africa and South East Asia, in temperate and humid climates at altitude between 600 and 2500 m. The genus coffee belongs to the botanical family of Rubiaceae and comprises more than 90 species. However, only C. Arabica, C. Canephora and C. Liberica are of commercial importance [**2-3**].

Figure 5.7: Coffee plant on the left and green coffee beans on the right.

It is well known that coffee cannot be considered a "food" consumed for its nutritional values, but it represents a pleasure, a socio – cultural moment, an excuse to meet friends, a way to be ready and active for the daily jobs, and the quality must be the main requisite because it is directly related to positive moments in our lives. A good quality cup of coffee depends on many factors, such as the quality of green beans, the roasting conditions, the time since the bean are roasted and the type of water used for brewing [**4**]. The quality of green coffee represents the main condition for the production of a good end product at a

cup level. The overall quality and chemical composition of green coffee beans are affected by many factors, such as the composition of the soil and its fertilization, the altitude and weather of the plantation, the cultivation and the drying methods used for the beans. The knowledge of water content in green coffee is of great importance to produce a quality cup, especially when dealing with *espresso* coffee. Some undesired effects, such as mold growth, fermentation, development of mycotoxins and off-flavors, are found to be closely related to the water moisture level present in the raw beans. Generally, a water content ranging from 8% to 2.5% is considered adequate to avoid the issues mentioned above during transportation and storage. To estimate the water content in green coffee samples, a few ISO reference methods are available. Among them, those known as oven-based methods are commonly used for commercial reasons, even though they generally suffer from common drawbacks, and the water content measured is influenced by the particular procedure adopted [**5-6**]. The reasons for the protocol dependence of the water/moisture is, on the one hand, that additional water can be produced as a result of the drying process, due to the decomposition of the material or due to chemical reactions, such as the Maillard reaction. On the other hand, the large variety of bonding states of water in a given raw bean may result in a not exhaustive dehydration. Moreover, volatile substances may contribute to the mass loss upon heating. In general, it is well known that the availability of water is governed by its interaction with the macromolecules nearby. Thus, a deep understanding of the distribution of water molecules and their interactions with the macromolecules of the solid green bean matrix could explain the inaccuracies of the standard methods of quantification and would help to build clear cut models to improve quality control. More works in literature deal with the role of water in roasted coffee bean, rather than in the native green beans [**7-8**].

5.2.2 Experimental section

5.2.2.1 Materials

Green coffee beans, from Brasil, was a kind gift by Illy Coffee, Trieste, Italy. All other reagents were of analytical grade. Distillate water was always used.

5.2.2.2 Samples preparation

Coffee Arabica of the same commercial lot (Brasil) was used.

In order to allow the hydration of the green coffee beans, a wetting procedure consisting in the direct addition of the desired amounts of distillate water on the surface of dried bean was performed. The hydration of samples treated in these conditions was monitored as a function of time. At the end of the hydration stage, a single coffee bean was accurately weighted and immediately transferred to LF-NMR tube just before the measurement. A hydration time of 24 h was found to be sufficient.

5.2.2.3 LF-NMR characterization

Low Field NMR (LF-NMR) characterization was performed, at 37 °C, by means of a Bruker Minispec mq20 (0.47 T, 20 MHz). Transverse relaxation time (T_2) measurements were carried out according to the (Carr-Purcell-Meiboom-Gill; CPMG) sequence (number of scans = 4; delay = 5 s). In order to study water mobility inside the green coffee beans, Pulsed Gradient Spin Echo (PGSE) measurements were performed. After an appropriate calibration procedure, based on the knowledge of the free water self-diffusion coefficient (D_{H2O}), it is possible measuring the average water self-diffusion coefficient inside the green coffee beans structure (D). In the case of T_2 measurements, data were the average of 27 experiments (9 repetitions for three different samples), while in the case of PGSE measurements, data are the average of 15 experiments (5 repetitions for three different samples). Pulsed Gradient Spin Echo (PGSE) measurements were performed in triplicate.

5.2.2.4 SEM characterization

Coffee beads structure was analyzed using a Quanta250 SEM, FEI, Oregon, USA.The coffee beads were hydrated at room temperature for 48 hours and then visualized by electron microscope.

5.2.3 Results and discussions

After about 30 minutes after tube insertion into the magnetic field (time needed for temperature stabilization) 9 tests were performed and recorded for data processing. The chosen τ was equal to 0.25 ms. Relaxation curve are shown in *Figure 5.8*. The relaxation

times, reported in *Table 5.16*, were obtained by equation 3.55 fitting to experimental data of Figure 5.8. The number of relaxation times is chosen in order to minimize the product of the sum of squared errors, χ^2, and the number of fitting parameters that is equal to twice the exponentials used in equation 3.55.

T_{21}(ms) =	347	A_1(%) =	7
T_{22}(ms) =	102	A_2(%) =	12
T_{23}(ms) =	29	A_3(%) =	43
T_{23} (ms) =	10	A_4 (%)=	37

Table 5.16: Relaxation times T_2 of coffee beads.

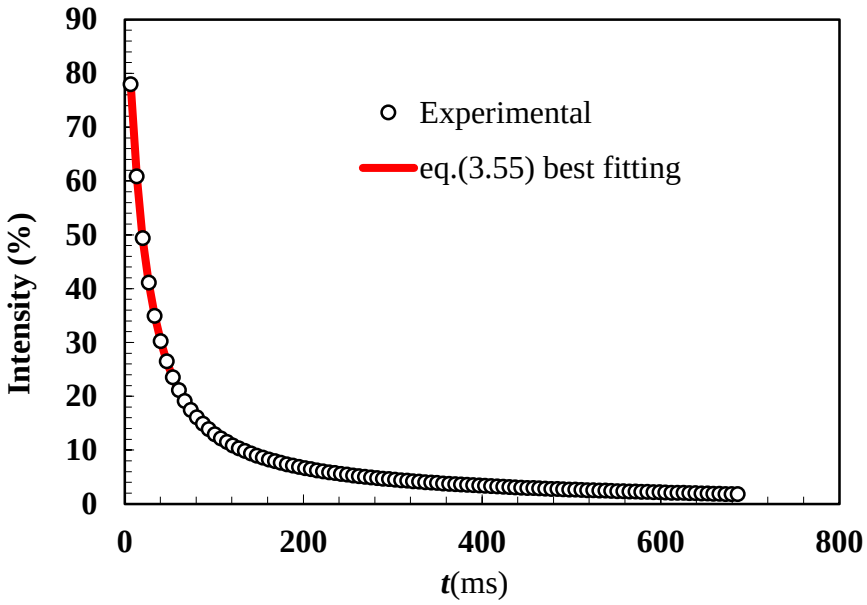

Figure 5.8: Relaxation curve relative to coffee beads

The teory shown in chapter 3 can be considered for the determination of the polymeric network mesh size distribution. In particular, the average pores diameter ξ_a is determined by eq.(3.54) fitting to the first nine data (linear portion) shown in the *Table 5.17* and *Figure 5.9*. Fitting is statistically sound ($F(1, 9, 0.95) < 181$) and it leads to $\xi_a = 9.5 \pm 0.03$.

$\Delta(ms)$	$(t_d(s))^{0.5}$	$D(m^2/s)$	σ_i
2	0,042	1.99E-9	8.17E-11
2.25	0,045	1.89E-9	8.58E-11
2.5	0,048	1.74E-9	2.66E-12
2.75	0,050	1.70E-9	8.58E-11
3	0,053	1.57E-9	1.33E-11
3.25	0,055	1.59E-9	8.58E-11
3.5	0,057	1.41E-9	9.53E-11
3.75	0,059	1.52E-9	8.58E-11
4	0,061	1.41E-9	1.30E-11
10	0,099	1.39E-9	9.17E-11
20	0,140	1.26E-9	7.26E-11
30	0,172	1.27E-9	6.15E-11
40	0,199	1.31E-9	8.00E-11
50	0,223	1.46E-9	8.58E-11

Table 5.17: Self diffusion coefficient *D* relative to coffee seeds.

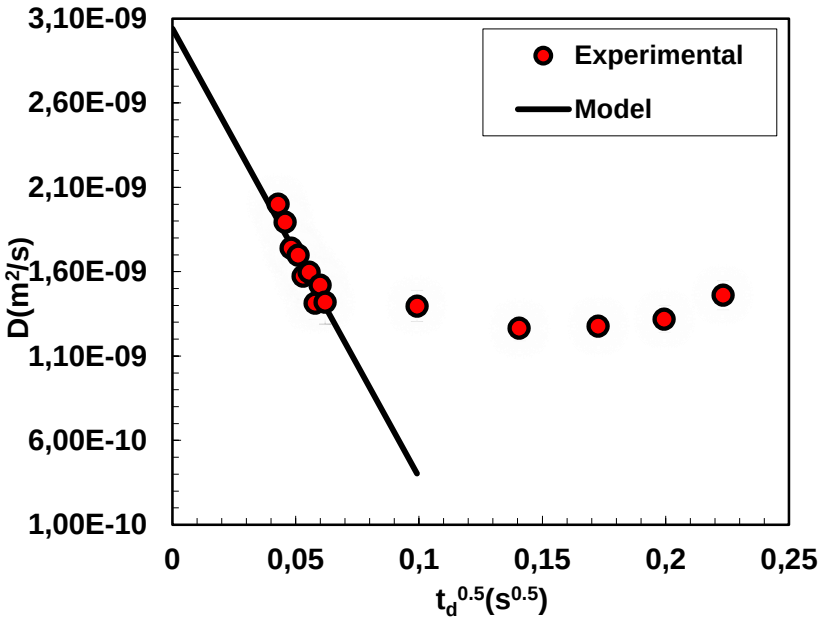

Figure 5.9: Water self diffusion coefficient *D* and model fitting (eq.(3.54) black line) referring to coffee seeds. Vertical bars indicate datum standard error.

It is interesting to underline that for the longest diffusion times, the water self diffusion coefficient (*D*) is almost constant. This indicates that coffee pores are interconnected.

Indeed, if it were not the case, we would have observed a continuous (linear) decreasing trend of D versus $t_d^{0.5}$. Knowing the average relaxation times (see *Table 5.16*) and the average pore diameter (9.5 μm), eqs. 3.55-3.59 allow the conversion of relaxation times into pore size distribution (*Table 5.18*).

$\xi_1(\mu m) =$	196	$A_1(\%) =$	6
$\xi_2(\mu m) =$	52	$A_2(\%) =$	11
$\xi_3(\mu m) =$	19	$A_3(\%) =$	26
$\xi_4(\mu m) =$	9	$A_4(\%) =$	42
$\xi_5(\mu m) =$	3	$A_5(\%) =$	13

Table 5.18: Pore size distribution referring to coffee seeds.

Table 5.18 tells us that 6% of the pores have a diameter of 196 μm, 11 % of the pores have a diameter of 52 μm, 26% have a diameter of 19 μm, 42% have a diameter of 9 μm and 13% have a diameter of 3 μm.

As described in the section 5.2.2.4, the coffee beads after hydration for 48 hours were observed by electron microscope. This technique allows to find a wide variety of pores spanning from about 100 μm to 10 μm (see *Figure 5.10*).

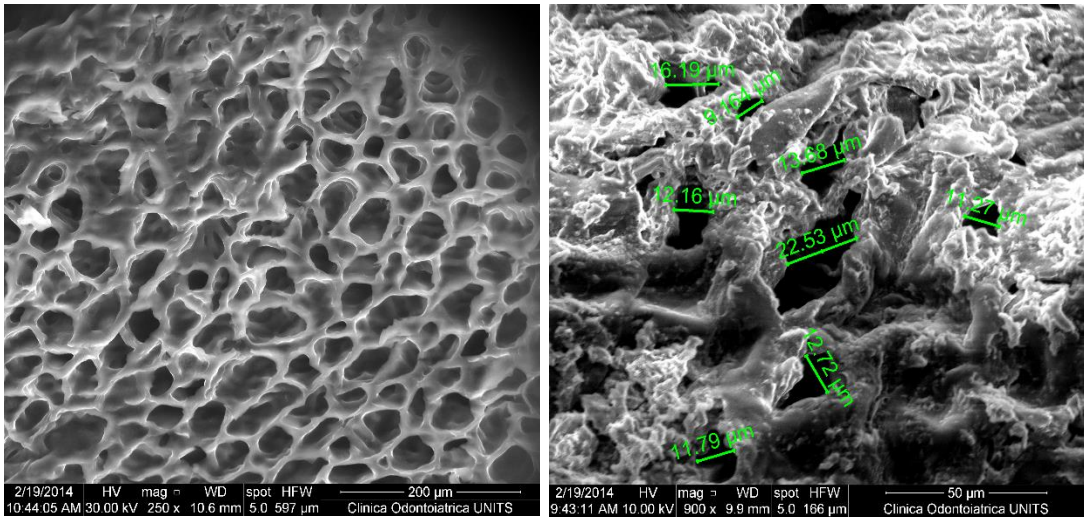

Figure 5.10: Structure of coffee beads by electron miscoscope

The comparison between LF-NMR results and SEM picture tells us the LF-NMR results are reasonable even if the bigger estimated pores (around 200 μm) seem to be attributable to water on the rough surface of coffee seeds (open pores). Indeed, SEM pictures do not

show so big pores. However, it has to be reminded that while LF-NMR considers all the seeds, SEM can focus the attention only on a small portion of just one seed. Accordingly numerous SEM picture, led on different seeds and in different positions, should be considered for a difficult statistical analysis.

5.3 Styrene butadiene rubber

5.3.1 Introduction

Rubber can be found in nature and harvested as a latex (milky liquid) from several types of trees. Natural rubber coming from tree latex is essentially a polymer made from isoprene units with a small percentage of impurities in it. Synthetic rubber is artificial rubber, made from raw materials such as butadiene, styrene, isoprene, chloroprene, ethylene and propylene. More than half of the world synthetic rubber is styrene – butadiene rubber (SBR) made from styrene and butadiene monomers which are abundant in petroleum. Three quarters of all SBR made goes into tires production. The rest goes into products such as footwear, sponge and foamed products, waterproofed materials and adhesives. Styrene butadiene rubber resembles natura rubber in processing characteristics as well as finished products. It possesses high abrasion – resistance, high loadbearing capacity and resilience. On the other hand, it gets readily oxidized, especially in presence of traces of ozone present in the atmosphere.

5.3.2 Experimental section

5.3.2.1 Materials

The styrene butadiene rubber samples were provided by ENI. In total, three samples were analyzed:

- 5570
- 5577
- 2430

Some physical characteristics of the samples are listed in the *table 5.19*:

LATTICE	5570	5577	2430
Solid %	65.5-67.5	65.5-67.5	66.5-68.5
pH	10.0-11.2	10.0-11.2	10-11.2
Viscosity (cPs)	400-800	500-900	1400max
Bound styrene (%)	24-28	29-32	34-37

Table 5.19: Physical characteristics of styrene – butadiene rubber.

The meaning of the identification codes is not known as they are related to confidential data of the manufacturer (ENI).

5.3.2.2 Samples preparation

The sample preparation implies the following procedure [**9**]: at the concentrated latex (68% solids) a vulcanizing base (mixture of sulfur) was added. The viscosity of the mixture was corrected by the addition of a rheology modifier (usually polymers polyacrylates). In the next step the liquid foam was created: the latex is stirred in order to incorporate air inside. Subsequently, sodium hexafluorosilicate (Na_2SiF_6) was added. The mixture was poured into a mold and put in infrared heater at a temperature of 160-180 ° C for about a minute. Later on, the sample was transferred in an oven at 140 ° C for 20 minutes to ensure complete drying of the product. The samples (*Figure 5.11*) looked all as flat disks, indistinguishable to the naked eye from each other. For the LF-NMR characterization, the samples were cut into strips of about 1mm x 1mm x 20 mm which were left to swell in distillate water for 72 hours at 37 ° C prior to the analysis. All tests were performed at 37°C.

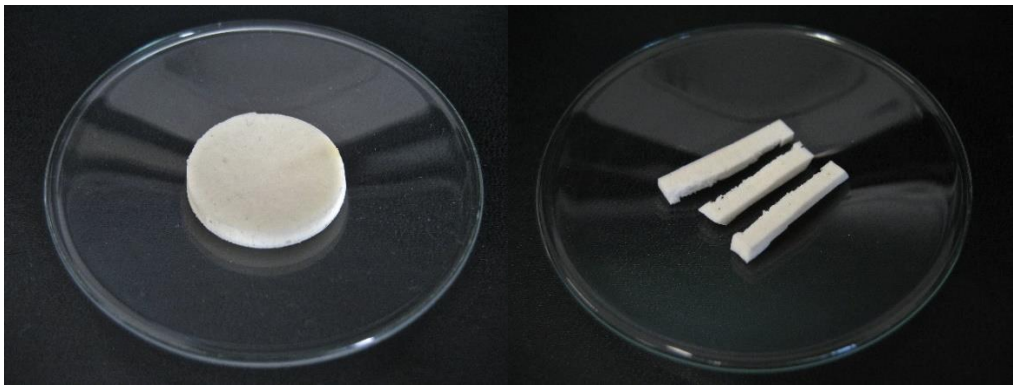

Figure 5.11: Styrene butadiene rubber before and after cutting for the LF-NMR characterization.

5.3.3 Results and discussion

5.3.3.1 Sample SBR 5570

5.3.3.1.1 Relaxation Time T_2 measurement

About 30 minutes after tube insertion into the magnetic field (time needed for temperature stabilization) 9 tests were performed and recorded for data processing. The chosen τ was equal to 0.5 ms. Relaxation curve are shown in *Figure 5.12*. The relaxation times, reported in *Table 5.20*, were obtained by equation 3.55 fitting to experimental data of *Figure 5.12*. The number of relaxation times is chosen in order to minimize the product of the sum of squared errors, χ^2, and the number of fitting parameters that is equal to twice the exponentials used in equation 3.55.

T_{21}**(ms) =**	1506 ± 2	A_1**(%) =**	66.2 ± 0.3
T_{22}**(ms) =**	657 ± 8	A_2**(%) =**	21.5 ± 0.2
T_{23}**(ms) =**	133 ± 2	A_3**(%) =**	12.3 ± 0.1

Table 5.20: Relaxation times T_2 relative to SBR 5570 sample (37°C).

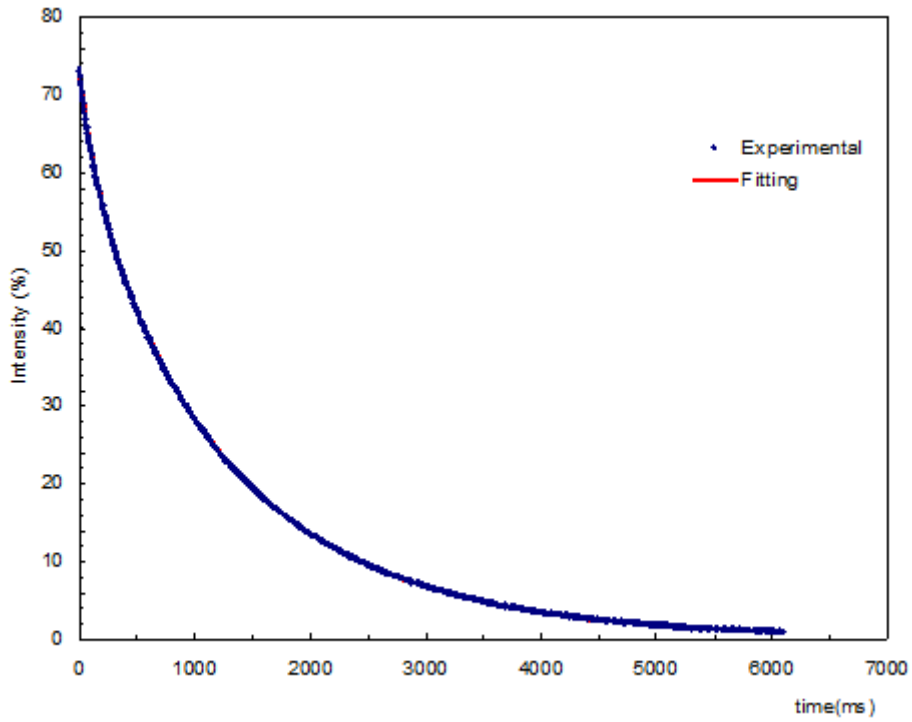

Figure 5.12: Relaxation curve relative to the SBR 5570 sample.

5.3.3.1.2 Measerement of the diffusion coefficient D and of the average pore diameter ξ.

The teory shown in chapter 3 can be considered for the determination of pores size distribution. The trend of the water self diffusion coefficient (*D)* versus the sqare root of the diffusion time t_d is shown in the *Table 5.21*.

Δ(ms)	*$(t_d(s))^{0.5}$*	*D(m²/s)*	*σ_i*
2	0.043	2.51E-09	2.07E-11
8	0.089	2.38E-09	1.09E-11
11	0.104	2.23E-09	9.79E-12
14	0.118	2.08E-09	2.19E-11
17	0.130	2.15E-09	2.25E-11
20	0.141	2.02E-09	3.30E-11
23	0.151	2.03E-09	7.60E-11
26	0.161	1.95E-09	1.98E-11

Table 5.21: Self- diffusion coefficient *D* relative to SBR 5570 sample (*T*=37°C and 5 repetitions).

For each diffusion time (t_d=*Δ-δ/3*), 5 repetitions were performed and the average was considered. The tests were performed assuming x_1=x_2=0.1 ms e δ=0.5 ms. Equation 3.53 fitting to experimental data leads to ξ = 34 ± 0.4 μm [F test, F (1,8,0.95)<26].

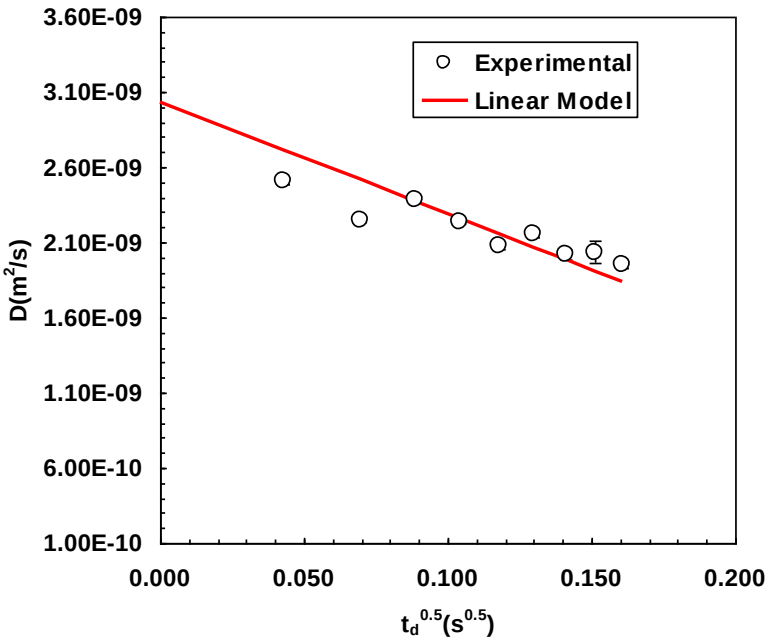

Figure 5.13: water self diffusion coefficient (*D*) and model fitting (red line) referring to sample 5570.

Knowing the average relaxation times (see *Table 5.20*) and the average pore diameter (34 μm), the equation 3.55-3.59 allow to conversion of the relaxation times into pore size distribution (*Table 5.22*).

$\xi_1(\mu m)$ =	52.4 ± 1.1	$A_1(\%)$ =	66.2 ± 0.3
$\xi_2(\mu m)$ =	15.7 ± 0.4	$A_2(\%)$ =	21.5 ± 0.2
$\xi_3(\mu m)$ =	2.7 ± 0.1	$A_3(\%)$ =	12.3 ± 0.1

Table 5.22: Pores size distribution referring to SBR 5570 sample.

Table 5.22 tells us that 66.2% of the pores have a diameter of 52.4 μm, 21.5 % of the pores have a diameter of 15.7 μm and 12.4% have a diameter of 2.7 μm.

5.3.3.2 Sample SBR 5577

5.3.3.2.1 Relaxation Time T_2 measurement

The methods of the tests are quite similar to those described in section 5.3.3.1.1. Eq.(3.55) fitting to the experimental relaxation curve, shown in Figure 5.14, shows (see Table 5.23) the presence of three main relaxation times. The number of the relaxation times is chosen in order to minimize the product of the sum off squared errors, χ^2, and the number of fitting parameters of eq. 3.55.

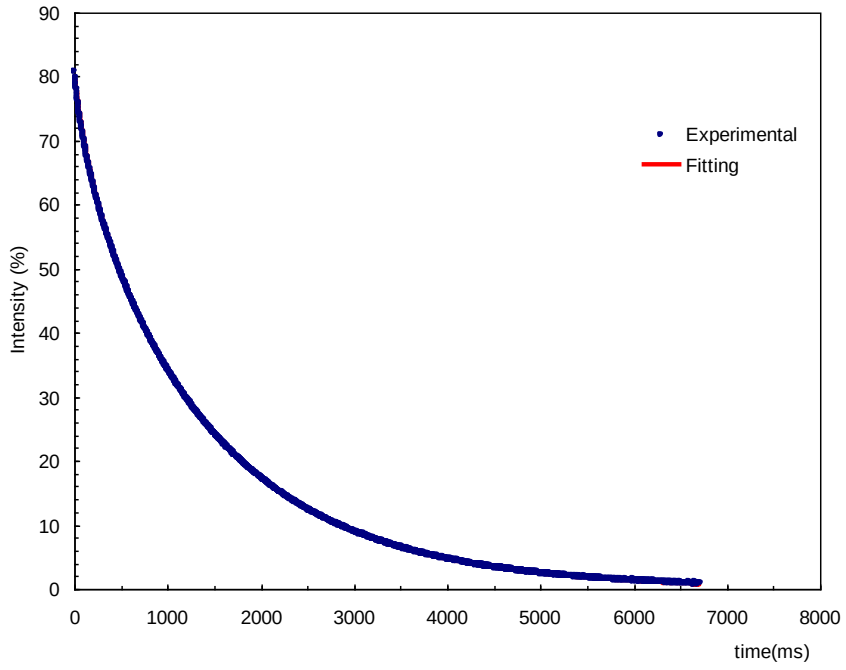

Figure 5.14: Relaxation time curve relative to the SBR 5577sample**.**

The relaxation times obtained are reported in the *Table 5.23.*

$T_{21}(ms) =$	1572 ± 2	$A_1(\%) =$	74.5 ± 0.3
$T_{22}(ms) =$	693 ± 14	$A_2(\%) =$	14.0 ± 0.2
$T_{23}(ms) =$	143 ± 3	$A_3(\%) =$	11.5 ± 0.1

Table 5.23: Relaxation times relative to the SBR 5577 sample (T= 37°C).

5.3.3.2.2 Measurement of the diffusion coefficient *D* and the average pores diameter ξ

The theory shown in chapter 3 can be considered for the determination pores size distribution. The trend of the water self-diffusion coefficient (*D*) versus the square root of the diffusion time td is shown in Table 5.24.

$\Delta(ms)$	$(t_d(s))^{0.5}$	$D(m^2/s)$	σ_i
8	0.089	2.47E-09	3.10E-11
11	0.104	2.33E-09	3.58E-11
14	0.118	2.27E-09	4.08E-11
17	0.130	2.33E-09	1.97E-11
20	0.141	2.18E-09	2.21E-11
23	0.151	2.19E-09	4.20E-11
26	0.161	2.16E-09	7.25E-12
30	0.173	2.07E-09	2.15E-11
34	0.184	2.04E-09	4.95E-11
38	0.195	2.09E-09	2.77E-11
42	0.205	2.02E-09	2.78E-11
46	0.214	1.97E-09	3.08E-11
50	0.223	2.01E-09	4.34E-11

Table 5.24: Self diffusion coefficient *D* relative to the SBR 5577 sample (T=37°C and 5 repetitions).

Eq.3.54 fitting to the experimental data reported in *Table 5.24* and *Figure 5.15* leads to $\xi = 47 \pm 0.3\ \mu m$ [*F* test, $F(1,13,0.95)<30$].

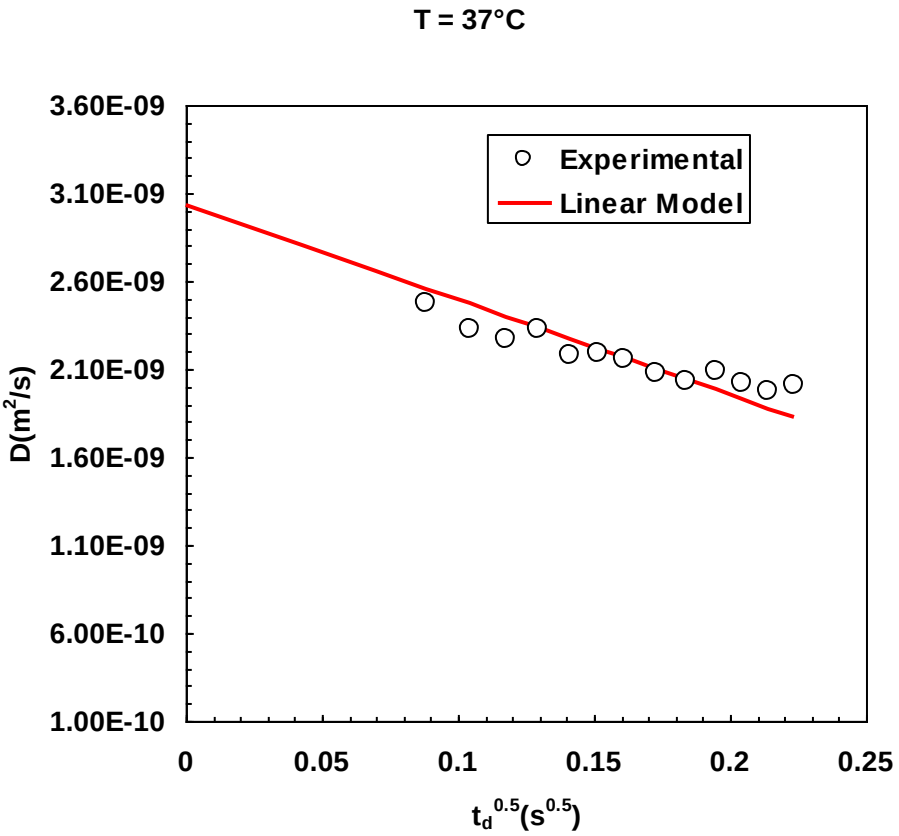

Figure 5.15: Self diffusion coefficient *D* and fitting (eq. 3.53) referring to SBR 5577 sample.

Knowing the average relaxation times (see *Table 5.23*) and the average pores diameter (47 μm), the eqs. 3.55 - 3.59 allow the conversion of the relaxation times (*Table 5.23)* into pore size distribution.

$\xi_1(\mu m)$ =	66.1 ± 1.2	$A_1(\%)$ =	74.5 ± 0.3
$\xi_2(\mu m)$ =	19.6 ± 0.6	$A_2(\%)$ =	14.0 ± 0.2
$\xi_3(\mu m)$ =	3.3 ± 0.1	$A_3(\%)$ =	11.5 ± 0.1

Table 5.25: Pores size distribution referring to the SBR 5577sample.

5.3.3.3 Sample SBR 2430

5.3.3.3.1 Relaxation Time T_2 measurements

The methods of tests are those described in section 5.3.3.1.1. Eq(3.55) fitting to the experimental relaxation curve, shown in Figure 5.16, shows (see table 5.26) the presence of three main relaxation times. The number of relaxation times is chosen in order to minimize the product of the sum of squared errors, χ^2, and the number of fitting parameters of eqs. 3.55.

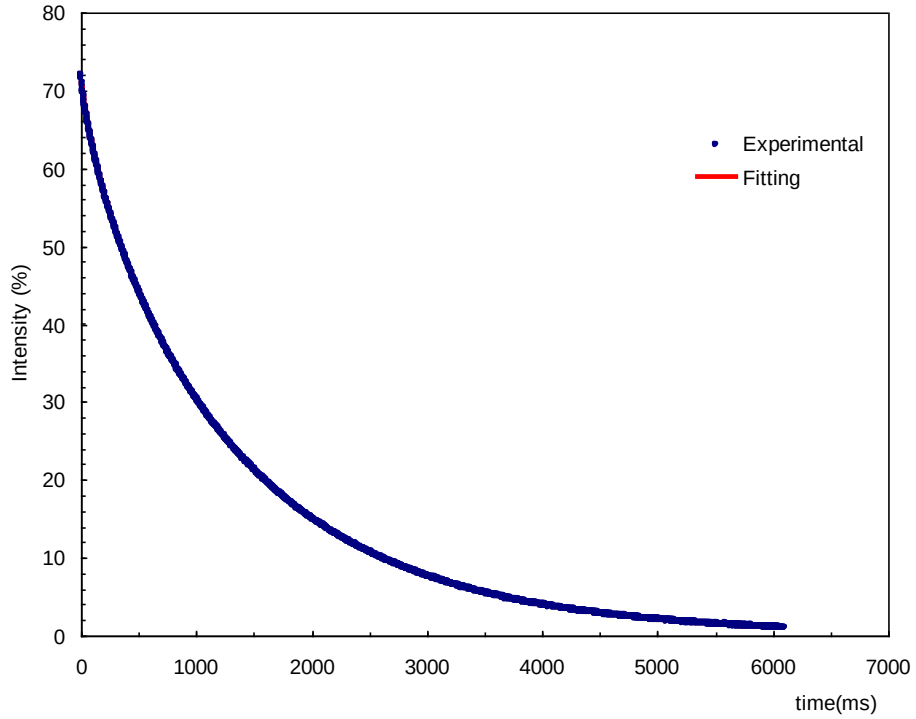

Figure 5.16: Relaxation curve relative to the SBR 2430 sample.

The relaxation times obtained are reported in the *Table 5.26.*

T_{21}(ms) =	1543 ± 2	A_1(%) =	74.2 ± 0.3
T_{22}(ms) =	662 ± 10	A_2(%) =	17.5 ± 0.2
T_{23}(ms) =	132 ± 3	A_3(%) =	8.3 ± 0.1

Table 5.26: Relaxation times relative to the SBR 2430 sample.

5.3.3.3.2 Measurement of the diffusion coefficient *D* and average pores diameter ξ

The theory shown in chapter 3 can be considered for the determination of the pores mesh size distribution. The trend of the water self – diffusion coefficient (*D*) versus the square root of the diffusion time t_d is shown in *Table 5.27*.

Δ(ms)	$(t_d(s))^{0.5}$	$D(m^2/s)$	σ_i
2	0.043	2.74E-09	4.01E-11
8	0.089	2.64E-09	1.60E-11
11	0.104	2.52E-09	1.65E-11
14	0.118	2.45E-09	4.62E-12
17	0.130	2.51E-09	1.17E-11
20	0.141	2.38E-09	7.75E-12
23	0.151	2.39E-09	5.93E-11
26	0.161	2.38E-09	3.48E-11
30	0.173	2.35E-09	4.99E-11
34	0.184	2.29E-09	4.20E-11

Table 5.27: Self diffusion coefficient *D* relative to the SBR 2430 sample (T= 37 °C and 5 repetitions).

Eq. 3.54 fitting to the experimental data reported in *Table 5.27* and *Figure 5.17* leads to $\xi = 53 \pm 0.4\ \mu m$ [*F* test, $F(1,10,0.95)<21$].

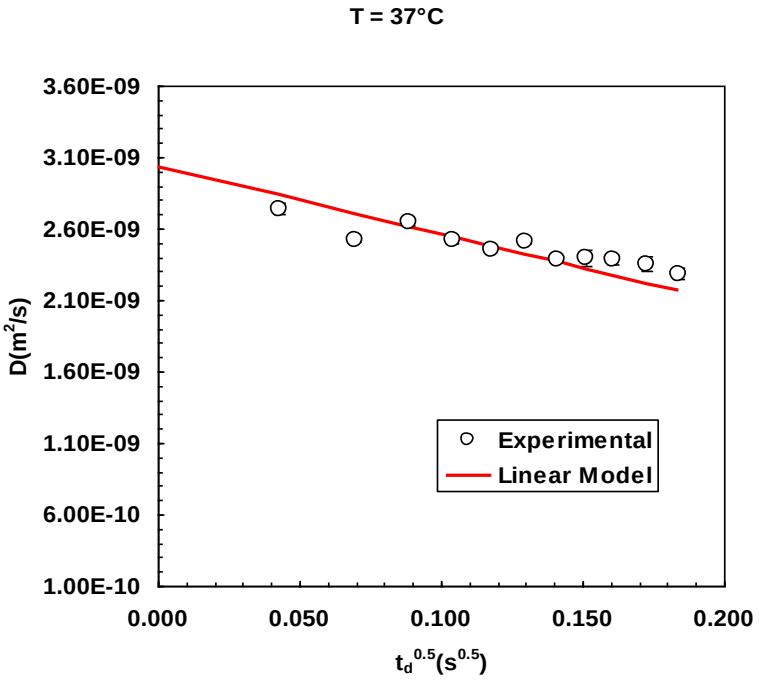

Figure 5.17: Self diffusion coefficient *D* and fitting (eq. 3.54) referring to SBR 2430 sample.

Knowing the average relaxation time T_2 (see *Table 5.26*) and the average pores diameter (53 μm), eqs. 3.55 – 3.59 allow the conversion of the relaxation times (*Table 5.26)* into pore size distribution as shown in *Table 5.28.*

$\xi_1(\mu m) =$	73.8 ± 1.4	$A_1(\%) =$	74.2 ± 0.3
$\xi_2(\mu m) =$	21.3 ± 0.5	$A_2(\%) =$	17.5 ± 0.2
$\xi_3(\mu m) =$	3.6 ± 0.1	$A_3(\%) =$	8.3 ± 0.1

Table 5.28: Pores size distribution referring to the SBR 2430 sample.

The results obtained on the latex samples SBR were really encouraging. Indeed, for all three samples, the evaluation of the pore size distribution is compatible with that determined by SEM as shown in the following pictures.

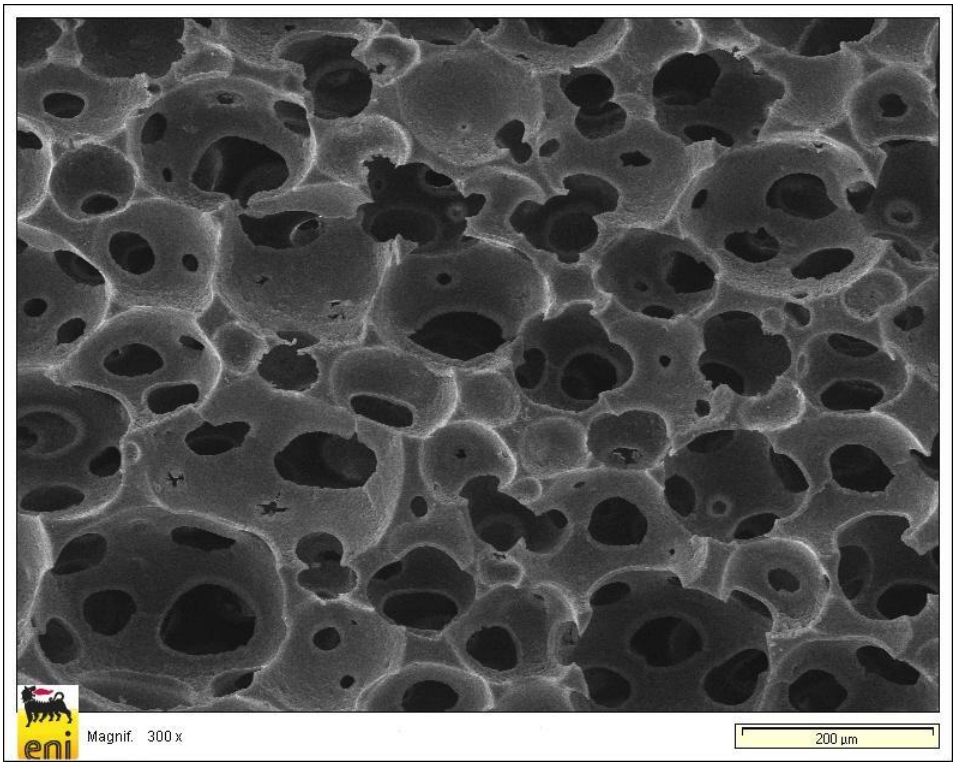

Figure 5.18: sample 2430

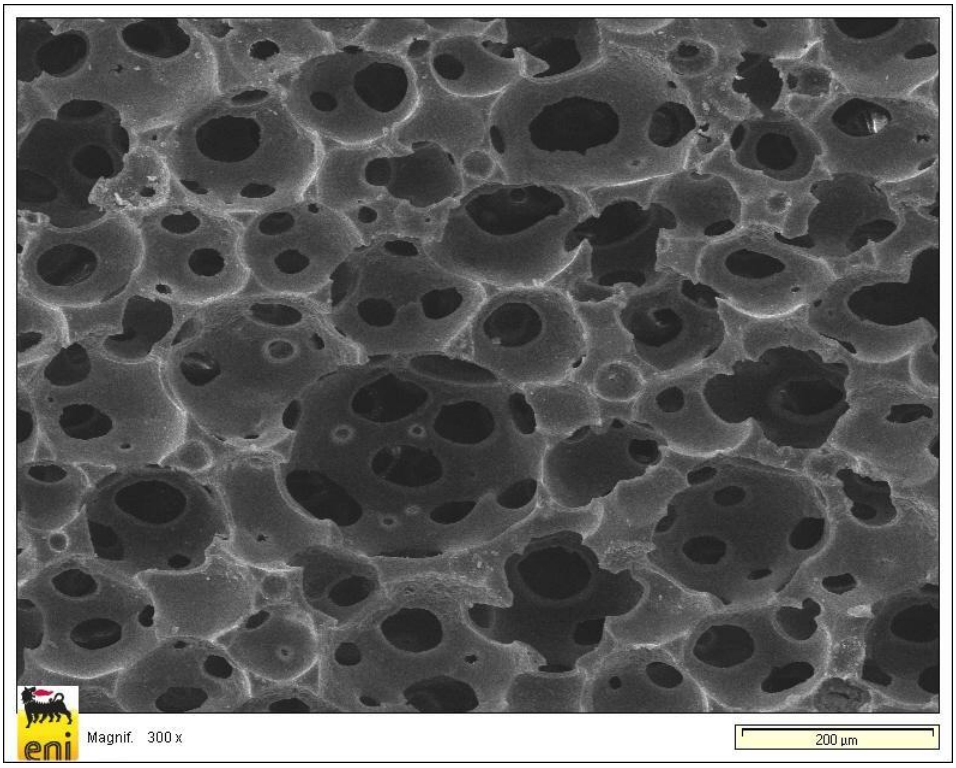

Figure 5.19: sample 5570

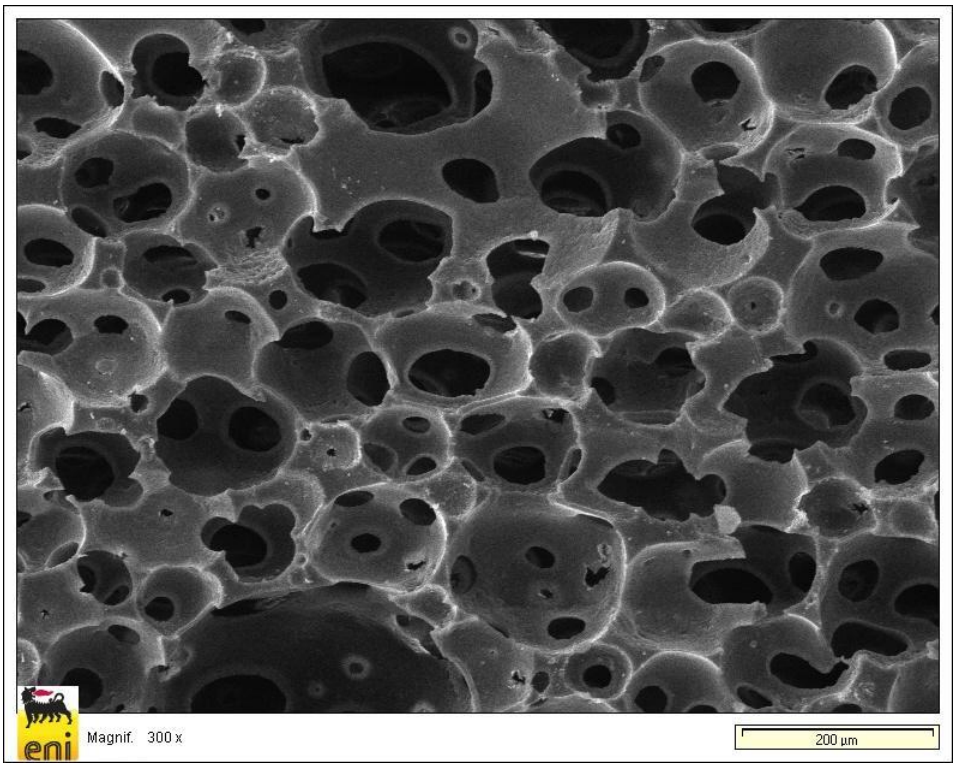

Figure 5.20: sample 5577

5.4 Bacterial cellulose/acrylic acid gels

5.4.1 Introduction

The use of synthetic fibers for the fabrication of polymer composites is decreasing due to various factors including the expensive cost of materials, the non-biodegradable nature of the synthetic fibers and the environment pollution connected to their synthesis. To minimize the above problems, scientists and engineers are focusing their attention on the use of natural fibers. In this regard, cellulose is very attractive as it is the most abundant and renewable biopolymer in nature. It is the main constituent of plant cell walls, fungi and some algae. Additionally, several bacteria have the ability to produce extra-cellular cellulose as their metabolites. Cellulose is typically obtained from higher plants where it resides as skeletal substance. In particular, cellulose is found in the plant xylem tissues where it is present as cellulosic microfibrils embedded in a matrix of amorphous non-cellulosic polysaccharides (hemicelluloses) and lignin [**10**]. To obtain pure cellulose, solvent extraction is an important method to remove the extractable fraction from cellulosic fibers. However, this procedure may cause fiber damaging due to changes in the chemical composition of the fibers and the rearrangement or transformation of the crystalline structure which determines the switch from cellulose type I to cellulose type II [**11**]. This cellulose structural change affects the thermal degradation characteristic of the fiber. Due to this problem, cellulose obtained from bacteria is more convenient. Bacterial cellulose is produced by Acetobacter xylinum which utilizes a wide range of carbon and nitrogen in liquid medium and transforms them into cellulose in the form of floating pellicles [**12**]. The cellulose produced by this organism is of exceptionally high purity and resembles the same features of plants and algae cellulose in terms of crystalline unit structure and average microfibrillar width [**13**]. Therefore, pure cellulose can be easily obtained from this source without having the difficulties associated with the extraction from plants. The cellulose produced by bacteria aggregates to form sub-fibrils which have the width of approximately 1.5 nm thus representing the thinnest natural occurring fibers. Bacterial cellulose sub-fibrils are, then, crystallized into bundles and subsequently into ribbons [**14**]. The molecular configuration of cellulose fibrils, which are highly insoluble and inelastic, makes the tensile strength of cellulose comparable to that of steel thus providing mechanical support to the tissues where it resides [**15**]. Since

cellulose fibrils are natural polymers, the biocompatibility and bio-degradability are key features which are at the base of the vast applications of this amazing material. Cellulose macro- and nano-fibers are used as reinforcing materials which could enhance mechanical, thermal, and biodegradation properties of the composites. Cellulose, commonly fabricated into matrices, became particularly popular biomaterials for controlled-release dosage forms and extended release dosage forms [**16-18**]. Formulations are relatively flexible, and a well-designed system usually gives reproducible release profiles. The large surface area and the negative charge of cellulose nano-fibers are suggested to govern the binding of large amounts of drugs to the surface of this material also ensuring optimal loading and dosing. In addition, the abundance of hydroxyl groups on the outer part of the crystalline nano-cellulose fibers enables surface modification of the material with a range of chemical groups. The surface modification is used to modulate the loading and release of drugs, such as non-ionized and hydrophobic drugs [**19**]. This versatility may potentially allow in the future the development of delivery strategies devoted to different administration routes [**20**] and clinical applications such as drug delivery to the vessel [**21**] and to the liver [**22**, **23**].

Hydrogels, that can expand and have great water absorption capacity and elasticity, demonstrate high capability to cater the release program needed in controlled release therapy [**24**]. However, in the hydrated state, hydrogels exhibit a remarkable poor mechanical strength. Previous studies have demonstrated that the incorporation of nano-cellulose has great impact in improving mechanical properties of hydrogels. For example Millon and Wan [**25**] reported that nano-cellulose fibers of an average diameter of 50 nm are used in combination with polyvinyl alcohol (PVA) to form biocompatible nano-composites which result in increased mechanical properties similar to that of cardiovascular tissues, such as aorta and heart valve leaflets. In addition, Cai and Kim [**26**] set up three different methods to prepare nano-cellulose / poly(ethylene glycol) (PEG) composite that can be used for soft tissue replacement devices. Since the favorable properties of hydrogels lie mainly in their hydrophilicity, the characterization of their water-sorption capabilities is very important [**27**]. In addition, also the hydrogel nano- and micro structure is of paramount importance for biomedical applications. In this section are reported the results of a rheological, low field Nuclear Magnetic Resonance (LF NMR), Environmental Scan Electron Microscopy (ESEM) and release study aimed

at understanding the macro-, micro- and nanoscopic characteristics of a hydrogel constituted by a mixture of bacterial cellulose and acrylic acid. Indeed, the joint use of these approaches can give important insight about the topology of this hydrogel that is made up by two interpenetrated continuous phases: the primary "pores phase" (PP) containing only water and the secondary "polymeric network phase" (PNP) constituted by the polymeric network swollen by the water. This complex topology can provide an important chance/challenge for the designing of controlled release systems. Indeed, for example, the presence of pores (or channels) can greatly improve the swelling process as solvent uptake can take place by convection (through pores) instead of by diffusion (through polymeric network meshes) as it takes place in homogeneous gels [**28**]. Consequently, pores presence reflects into a more rapid gel swelling that, in turn, implies faster drug release kinetics. In addition, it is well known that the average diffusion coefficient of a solute in a mixed structure (PNP plus PP), the so called effective diffusion coefficient [**29**], depends on both solute mobility in the PP and in the PNP [**30**]. Thus, depending on the dimension of the solute molecule, a careful tuning of the characteristics of PP (pores size distribution, pores connectivity, strictly related to structure tortuosity) and of PNP can yield to very different release kinetics. Consequently, this great potentiality requires the definition of proper strategies aimed at the characterization of the gel topological properties. This aspect becomes even more important when it is needed to evaluate the effect of different preparation parameters on the gel final structural characteristics.

5.4.2 Experimental section

5.4.2.1 Materials and methods

Acrylic acid (ACC) and theophylline (TPH) were purchased from Sigma Aldrich Chemie GmbH Germany, while bacterial cellulose (extracted from Nata de coco – Dayawan Trading (M) Sdn. Bhd.) was purified according to the British Pharmacopoeia. All other reagents were purchased from R & M Chemical (Essex, UK) and were of analytical grade. Distilled water was always used.

5.4.2.2 Gel preparation

The purified cellulose was dried and ground to obtain a powder composed of particles with sizes between 20 µm and 200 µm. The powder was dispersed in distilled water at a concentration of 1% (w/v). The acrylic acid was, then, added to the dispersion in a ratio 20:80 (w/w) compared to cellulose. The mixture was poured into a plastic container (size 12 X 12 X 1 cm) and then irradiated in air with an electron beam of 35 kGy intensity (5 kGy per pass, EPS 3000, Japan).

5.4.2.3 ESEM

The freshly prepared gel was dried and then left to swell at 37°C in distilled water for 48 h to reach the equilibrium swelling degree S_d (absorbed water weight/dry matrix weight; = 4.3 ± 0.4). A portion of the swollen gel (0.5 X 0.5 X 0.5 cm) was collected and analyzed (ESEM) for no longer than 30 s at 5°C to prevent drying due to electron bombardment. The images of the surface and the cross sections were obtained by Quanta200F SEM (FEI, USA).

5.4.2.4 Image processing and analysis

The ESEM images were processed using the software ImageJ [**31**]. The procedure used here comprised: i) a calibration step required to correlate the image dimensions in pixel to physical dimensions; ii) highlight the pores; and iii) analysis of the pore areas. From the pores' area and assuming the pores as spherical, was then possible to derive pores diameter and volume.

5.4.2.5 Rheological characterization

The rheological characterization was carried out at 37 °C by means of a Haake RS-150 controlled stress rheometer mounting a parallel plate device with serrated surfaces (HPP20: diameter = 20mm) and equipped with a thermostat Haake F6/8. Due to the rigid nature of the gel, the gap setting (1~2 mm) was optimized as described elsewhere [**32**]. The measuring device was kept inside a glass bell at saturated humidity conditions to avoid evaporation effects. The rheological tests were performed under small amplitude oscillatory shear conditions. In particular, the linear viscoelastic region was assessed, at 1 Hz, through stress sweep experiments. Frequency sweep tests were carried out in the

frequency (f) range 0.01–10 Hz at constant stress τ = 30 Pa (well within the linear viscoelastic range for the studied gel). All tests were performed in triplicate.

5.4.2.6 Low field nuclear magnetic resonance

Low Field NMR (LFNMR) characterization was performed by means of a Bruker Minispec mq20 (0.47 T, 20 MHz). In order to study the hydrogel structure, two kinds of experimental tests were performed: a) determination of the water diffusion coefficient inside the hydrogel polymeric structure (D_G; also called water self-diffusion coefficient [**33**]; water is the only mobile species as polymeric chains cannot diffuse) b) determination of the water protons transverse relaxation time inside the hydrogel (T_2).
D_G determination implied the execution of Pulsed Gradient Spin Echo (PGSE) measurements (performed in triplicate at 37°C). The measurements of the transverse relaxation time (T_2) were carried out in triplicate at 20°C and 37°C according to the Carr-Purcell-Meiboom-Gill sequence (number of scans = 4; delay = 5 s) adopting a 90° - 180° pulse separation time τ of 0.25 ms.

5.4.2.7 Release experiments

Cylindrical gels were obtained by cutting the initial, wider, parallelepiped gel. The cylindrical shape was adopted in order to reduce the three-dimension release problem to a simpler two-dimension one. These experiments, led in triplicate, consisted in placing in the release environment (distilled water of volume V_r = 150 cm^3, 37°C) a gel cylinder (diameter 2.1 cm, thickness 0.3 cm) that was in advanced swollen for 48 h in a theophylline aqueous solution to ensure a final concentration in the gel of 1400 ± 100 $\mu g/cm^3$. A magnetic stirrer guaranteed proper solution mixing. In order to prevent the contact with the magnetic stirrer, the gel was suspended in the release environment by a thin web. Theophylline concentration in the release environment was measured by an optical fiber apparatus (HELLMA, Italy) connected to a spectrophotometer (ZEISS, Germany, wavelength 272 nm). The employment of the optical fiber prevented any perturbation of the release environment. As gel weight, shape and dimensions did not change at the end of the release test, we could conclude that the gel underwent neither erosion nor swelling. The proposed (see eq.(3.61)) model is characterized by only one fitting parameter (theophylline effective diffusion coefficient D_{TPH}) as a partition

coefficient between the gel and the release environment, k_p, was set equal to 1. Indeed, all the TPH contained in the gel was released at the end of the release test (see Results and Discussion section). The numerical solution was computed with the control volume method [**34**]. In order to ensure the reliability of the numerical solution, the computational domain was subdivided into 100 control volumes in the radial direction and 30 in the axial direction (for a total of $3*10^3$ control volumes) while integration time step was set equal to 15 s.

It is worth noting that the knowledge of D_{TPH} allows evaluating an important characteristic of the gel pore phase (PP), i.e. its tortuosity. Indeed, assuming a unitary partition coefficient between the PP and the PNP (polymer network phase) phases (release tests proved this assumption) and excluding the possibility of a hindered diffusion (this happens when the radius of the diffusing probe molecule, TPH in our case, is comparable to pores radius and this was not our case) [**30**], the following relation holds:

$$D_{TPH} = \frac{D_{PNP}\,\varepsilon_{PNP}}{To_{PNP}} + \frac{D_{PP}\,\varepsilon_{PP}}{To_{PP}} \tag{5.5}$$

where D_{PNP} is the TPH diffusion coefficient in the polymer network phase, D_{PP} is the TPH diffusion coefficient in the pore phase (i.e the TPH diffusion coefficient in water at 37°C, $8.2*10^{-10}$ m^2/s [**35**]), To_{PNP} and To_{PP} are, respectively, the tortuosity of the polymer network phase and the pore phase while ε_{PNP} and ε_{PP} are, respectively, the volume fraction of the polymer network phase and the pore phase. In the light of the Carman theory [**36**], To_{PNP} can be expressed by:

$$To_{PNP} = \sqrt{\frac{D_{PP}}{D_{PNP}}} \tag{5.6}$$

Inserting eq.(5.6) into eq.(5.5) and rearranging, we have:

$$To_{PP} = \frac{D_{PP}^{3/2}\varepsilon_{PP}}{D_{PP}^{1/2}D_{TPH} - D_{PNP}^{3/2}\varepsilon_{PNP}} \approx \frac{D_{PP}\varepsilon_{PP}}{D_{TPH}} \tag{5.7}$$

The approximation introduced in eq.(5.7) holds when D_{PP} and D_{TPH} are of the same order of magnitude and D_{PNP} is, at least, one order of magnitude smaller as it occurs in our case (see Results and discussion).

5.4.3 Results and discussion

ESEM shows the complex structure of the hydrogel (*Figure 5.21*). Effectively, while its surface is characterized by small pores (mean diameter 2.9 μm, from image analysis) (*Figure 5.21 A*), its cross section (*Figure 5.21 B*) shows the existence of bigger pores whose diameter spans from about 10 to 100 μm. More precisely, the image analysis exhibits that the pores characterized by a diameter smaller than 30 μm represent the 4% of the whole pores volume, those with a diameter comprised between 30 and 80 μm are the 29% while the remaining 67% are pores characterized by a diameter spanning between 80 and 120 μm.

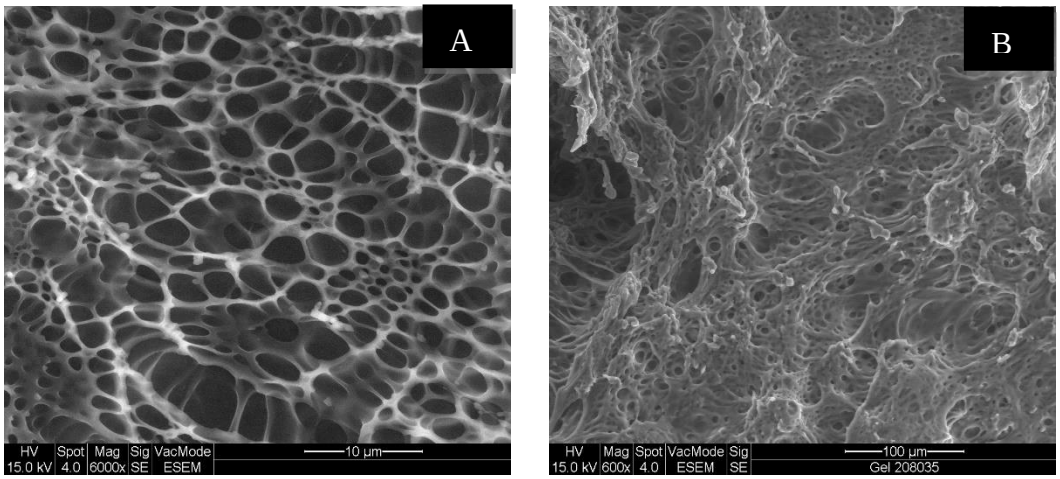

Figure 5.21: ESEM picture of surface hydrogel (**A**) and cross section (**B**).

In order to get more information about pore dimensions and its relative abundance, the hydrogel was studied according to the low field Nuclear Magnetic Resonance Pulsed Gradient Spin Echo (NMR-PGSE) experiments (as described in the section 5.4.2.6). *Figure 5.22* reveals that the water self-diffusion coefficient in the hydrogel (D_G) reduces with increasing $t_d^{0.5}$ up to approximately 0.066 $s^{0.5}$ (4.3 ms). Then, it remains substantially constant with $t_d^{0.5}$. Eq.(3.54) best fitting, led on the first 6 data (0.066 $s^{0.5}$) and knowing that the free water self diffusion coefficient at 37°C is equal to $3.04*10^{-9}$ m^2/s [**33**], confirms the linear D_G decrease with $t_d^{0.5}$ ($F(1,5,0.95) < 20.3$) and it yields to a mean pores diameter $\xi = (14.7 \pm 0.1)$ μm. As ξ results bigger than the diameter of surface pores and smaller than that of bulk pores, this estimation seems reasonable in the light of the ξ "average" nature. In addition, the D_G constancy with $t_d^{0.5}$ for higher diffusion times

indicates that hydrogel pores are interconnected. Indeed, if it were not the case, D_G would show a continuous decreasing trend with $t_d^{0.5}$ [**37**].

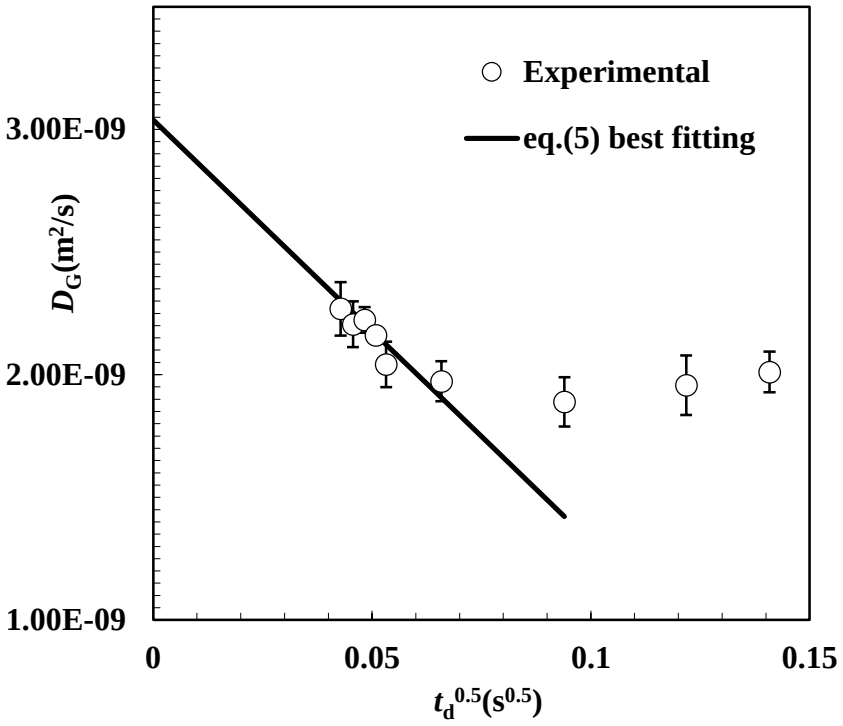

Figure 5.22: Dependence of the water self-diffusion coefficient in the hydrogel (D_G) on the square root of the diffusion time t_d (37°C). Open circles indicate experimental data while solid line indicates eq.(3.54) best fitting on the first six experimental data. Vertical bars indicate standard error.

Once the average pores diameter has been determined, further information (pores size distribution) can be found by eq.(3.55) fitting to relaxation data at 20°C and 37°C as reported in *Figure 5.23*. It can be seen that the fitting is always statistically very good ($F_{20°C}(12,45,0.95) < 8*10^6$; $F_{37°C}(12,53,0.95) < 5*10^5$) adopting four elements in the first eq.(3.55) summation ($m = 4$). *Figure 5.23* correctly shows that temperature increase (from 20°C to 37°C) implies a slower relaxation even if this phenomenon is not so marked. Indeed, as shown in *Table 5.29*, A_i are almost temperature insensitive while a small general increase of all T_{2i1} occurs when temperature is increased from 20°C to 37°C.

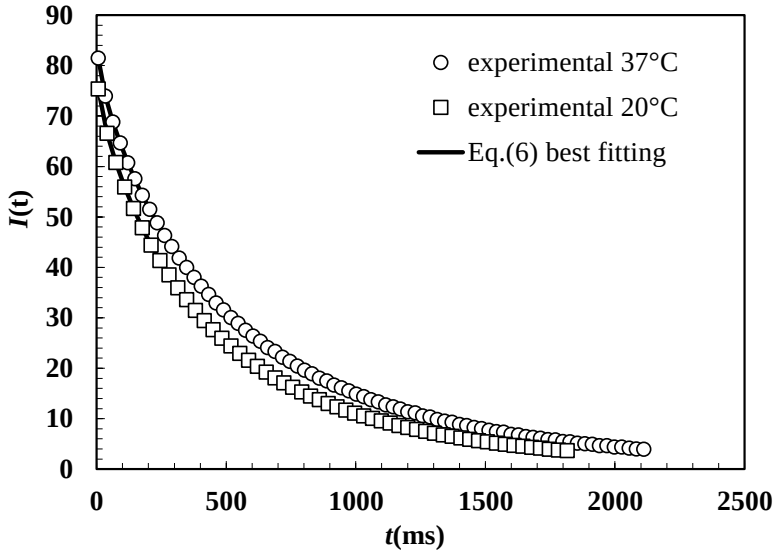

Figure 5.23: Decay of the normalized intensity, $I(t)$, of the transverse component of the magnetization vector (M_{xy}) versus time t. Circles and squares indicate, respectively, the $I(t)$ experimental trend at 37°C and 20°C while solid lines represent eq.(3.55) best fitting. Data standard error, not reported for the sake of clarity, is always lower than 1.5% of the measured value.

37°C					
i	A_i**(-)%**	I_{i1}**(-)**	T_{2i1}**(ms)**	MRD_i**(-)**	$\langle 1/T_{2i} \rangle$ (ms^{-1})
1	38 ± 3.0	99.954	973 ± 29	(17 ± 1.2)*10^{-2}	(1.06 ± 0.03)*10^{-3}
2	47 ± 3.0	99.994	410 ± 11	(6.2 ± 0.35)*10^{-2}	(2.47 ± 0.06)*10^{-3}
3	9 ± 0.5	99.999	128 ± 0.5	(1.8 ± 0.15)*10^{-2}	(7.83 ± 0.03)*10^{-3}
4	6 ± 0.3	100.000	20 ± 0.8	(0.3 ± 0.02)*10^{-2}	(51 ± 2)*10^{-3}
20°C					
i	A_i**(-)%**	I_{i1}**(-)**	T_{2i1}**(ms)**	MRD_i**(-)**	-
1	37 ± 1.5	99.901	856 ± 20	(23 ± 1.6)*10^{-2}	-
2	51 ± 1.7	99.988	340 ± 6	(7.7 ± 0.6)*10^{-2}	-
3	7 ± 0.2	99.999	90 ± 4.5	(2 ± 0.3)*10^{-2}	-
4	5 ± 0.3	100.000	14 ± 0.5	(0.3 ± 0.02)*10^{-2}	-

Table 5.29: Eq.(3.55) fitting parameters (A_i, T_{2i1}, MRD_i) ± standard deviation relative to the protons relaxation in the gel at 20°C and 37°C. I_{i1} is the first intensity appearing in the second summation of eq.(3.55) while $\langle 1/T_{2i} \rangle$ is defined in eq.(10). The small MRD_i values indicate that we are in fast diffusion conditions [**39, 40**].

In addition, *Table 5.29* makes clear that the first relaxation term (I_{i1}) in the second summation of eq.(3.55) is the most important one as it represents more than 99% for every *i* (1 - 4) whatever the temperature. Although, theoretically, polymer protons represent about 11% of all the hydrogel protons, due to the relatively high values of the smallest relaxation time, T_{241}, at both temperatures (see *Table 5.29*), we can conclude that all the relaxation times T_{2i1} have to be referred to water protons. This conclusion is also supported by the fact that in the case of the gel realized by deuterated water (D_2O) (37°C), any possible relaxation phenomenon (polymer protons relaxation) was too fast to be detected. In order to better understand the effect of temperature, it is useful calculating the % of the variation (ΔT_{2i1}) of each T_{2i1} with respect to the variation, ΔT_w, of the relaxation time of free water protons in the same range (37°C – 20°C; ΔT_w = 687 ms [**38**]). ΔT_{2i1} results equal to 17%, 10%, 5.5% and 0.84% for *i* = 1, 2, 3 and 4 respectively. The small values of all ΔT_{2i1} indicate that we are dealing with bound water, i.e. water inside the polymeric structure and not on its surface. In addition, the decrease of the ΔT_{2i1} values implies the existence of a more and more bound water as it occurs in smaller and smaller pores [**39, 40**]. Interestingly, while the ratio $\Delta T_{2i1}/\Delta T_{2(i+1)1}$ is almost constant for i = 1 and 2 (i = 1, $\Delta T_{211}/\Delta T_{221}$ = 1.7; i = 2 $\Delta T_{221}/\Delta T_{231}$ 1.8) it considerably increases for i = 3 ($\Delta T_{231}/\Delta T_{241}$ = 6.5). This means that the last relaxation time (T_{241}) corresponds to water protons that are strongly bound to the polymer phase.

On the basis of eq.(3.55) fitting to the relaxation data, it is possible to evaluate the average value of the inverse of the relaxation time $\langle 1/T_2 \rangle$ = (5.2 ± 0.25 s^{-1}) (see eq.(3.58)).

i	A_i**(-)%**	ξ_i**(μm)**
1	38 ± 3.0	91 ± 3
2	47 ± 3.0	33 ± 1
3	9 ± 0.5	9.6 ± 0.5
4	6 ± 0.3	1.4 ± 0.02

Table 5.30: Pores size (ξ_i) distribution of the studied hydrogel (37°C).

Then, the knowledge of the mean pores diameter ξ (see PGSE experiment) allows the determination of $\mathcal{M}$ value resorting to eq.(3.58) ($\mathcal{M}$ = (1.21 ± 0.07)*10^{-5} m/s). As $\mathcal{M}$ does not only depend on the solid surface chemistry but it is also a function of the temperature,

the fluid and the magnetic field strength [**41**], the comparison of $\mathcal{M}$ values coming from different studies has to be carefully evaluated. For example, at room temperature and at 20 MHz, Munn and co-workers [**42**] found that $\mathcal{M}$ order of magnitude ranges between 10^{-6} -10^{-5} m/s for inorganic materials (alumina, silica and sand stones). Chui and co-workers [**40**], working with homogeneous hydrogels made up by agar, agarose and polyacrylamide (polymer concentration ranging between 1% and 5% w/w), determined 10^{-10} m/s < $\mathcal{M}$ < 10^{-8} m/s at 40°C and 10 MHz. Brownstein and Tarr [**39**] determined, in physiological conditions for rat gastrocnemius muscle, $\mathcal{M}$ = 8*10^{-4} m/s. In low concentration scleroglucan-borax and guar gum-borax hydrogels (0.7% w/v), we found 10^{-7} m/s < $\mathcal{M}$ < 10^{-6} m/s at 37°C and 20 MHz [**38**]. Finally, in a poly-L-lactic acid (*PLLA*) porous scaffold (25°C, 20 MHz) we found an $\mathcal{M}$ value (2.4*10^{-5} m/s) close to that found in this work. Thus, the $\mathcal{M}$ value here determined seems physically sound. Once $\mathcal{M}$ and $\langle 1/T_{2i} \rangle$ (see *Table 5.29*) are known, eq.(3.59) allows to convert the relaxation times into pores diameter ξ_i as shown in *Table 5.30*. Interestingly, these results are, substantially, in agreement with the image analysis (Figure 5.21, right) according to which the majority of the pores (96%) are characterized by a diameter spanning between 30 and 120 μm. The image analysis results and those shown in *Table 5.29* become also closer if we assume that the pores belonging to the fourth class (i = 4, ξ = 1.4 μm, T_{241} = 20 ms,) have not to be associated to water trapped in small pores but to water trapped in the polymeric meshes. Indeed, the inspection of *Figure 5.21* would suggest that so small pores do not exist. In the light of this interpretation, only 6% (= A_4) of the water volume present in the gel would fill the polymeric network while the remaining 94% (A_1 + A_2 + A_3) would fill the pores. This would lead to a swelling degree of the polymeric meshes equal to 0.26 which is absolutely compatible with that of pure cellulose that can range between 0.17 and 0.36 [**43**]. Thus, our interpretation of the forth relaxation seems reliable. Interestingly, the physical meaning attributed to the forth relaxation time (water inside the polymeric meshes) allows the estimation of the hydrogel porosity ε_{PP} (i.e. the pores phase PP volume fraction). Indeed, knowing that the mean polymer density (ρ_p) is 1370 kg/m^3, that the water density at 37°C (ρ_{H2O}) is 992.98 kg/m^3 and that system swelling degree S_d (= absorbed water weight/dry matrix weight) is equal to (4.3 ± 0.4), ε_{PP} turns out to be:

$$\varepsilon_{PP} = \frac{0.01\left(A_1 + A_2 + A_3\right)}{1 + \rho_{H2O} / \left(\rho_p S_d\right)} \approx 0.81 \tag{5.8}$$

Consequently, the water filled polymeric network phase PNP occupies the remaining 0.19 of the total volume ($\varepsilon_{PNP} = 1-\varepsilon_{PP}$). Interestingly, this ε_{pp} value is close to what found, by means of another approach, by Karakutuz and Okay [**44**] who worked on porous organogels. In order to get further insights about hydrogel structure, a rheological characterization was performed.

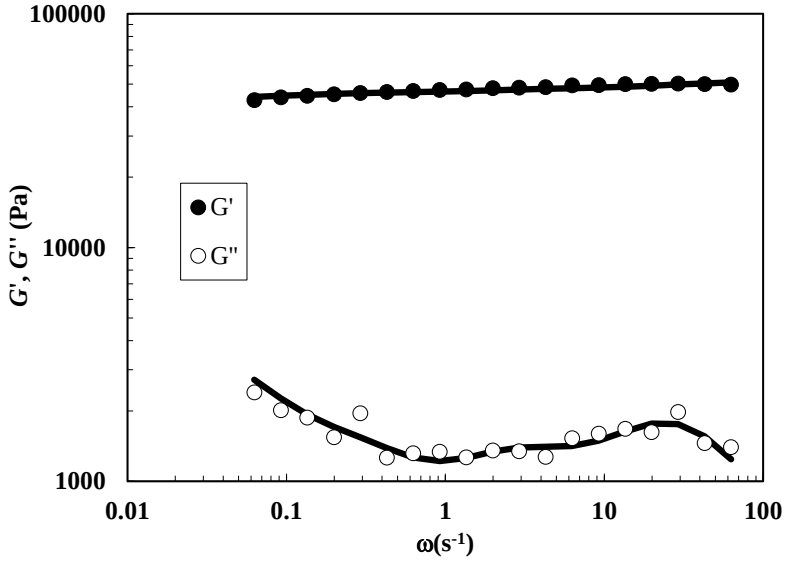

Figure 5.24: Hydrogel mechanical spectra. *G*'(filled circles) represents the elastic modulus, *G*'' (open circles) is the viscous, or loss, modulus while ω is the pulsation (ω = 2π*f*). Solid lines indicates the best fitting of the generalized Maxwell model (eqs.(3.78) and (3.79)). Data standard error, not reported for the sake of clarity, is always lower than 15% of the measured value.

Stress sweep test revealed that the linear viscoelasticity regime is very broad extending up to a critical stress of about 400 Pa. Accordingly, the shear stress value (30 Pa) used in the frequency sweep test is well within the linear viscoelastic range. *Figure 5.24* shows that our system behaves as a typical strong gel as the elastic modulus (*G*') is more than ten times of the loss modulus (*G*'') and both of them are substantially independent from pulsation ω [**45**]. In addition, the high *G*' and G_e values collocate our hydrogel in the family of mainly elastic materials. For a statistically good data fitting ($F(13,5,0.95) < 199$), the use of one purely elastic Maxwell element (G_e) plus other four viscoelastic Maxwell elements is required (see *Table 5.31*)

λ_1(s)	$(3.6 \pm 0.6)*10^{-2}$
G_e(Pa)	38548 ± 1889
G_1(Pa)	3158 ± 264
G_2(Pa)	1738 ± 264
G_3(Pa)	1458 ± 414
G_4(Pa)	6422 ± 1304
G(Pa)	51326 ± 2363
ρ_x(mol/cm^3)	$(1.8 \pm 0.1)10^{-5}$

Table 5.31: Parameters relative to the eq.(3.78)-(3.79) best fitting to the experimental data shown in *Figure 5.21*. G_e, G_1, G_2, G_3 and G_4, are the elastic moduli of the generalized Maxwell model, λ_1 is the relaxation time of the first viscoelastic Maxwell element (lowest relaxation time), G ($= G_e + \sum_{i=1}^{4} G_i$) indicates the shear modulus and ρ_x is the crosslink density.

The knowledge of the hydrogel shear modulus G allows the determination of the mean crosslink density ρx (see *Table 5.31*) according to eq.(3.80). On the basis of the discussion performed in the last part of section 5.4.3, the crosslink density of the polymer network phase (PNP) is given by $\rho_{xr} = \rho_x/\varepsilon_{PNP} = (9.3 \pm 0.5)*10^{-5}$ mol/cm^3. This implies (see eq.(3.81)) an average mesh diameter $\xi_a = (3.2 \pm 0.05)$ nm, typical of highly cross-linked network [**46**].

Finally, release tests allowed to complete the topological description of our hydrogel. *Figure 5.25*, reporting the theophylline (TPH) release kinetics (circles), shows that the model fitting (eq.(3.61) –(3.64), solid line) is good ($F(1,122,0.95) < 3121$). In addition, the only model fitting parameter, the effective TPH diffusion coefficient DTPH, turns out to be $(2.8 \pm 0.1)*10^{-10}$ m^2/s. As all the TPH was released at the end of the experiment, its partition coefficient must be equal to 1. The D_{TPH} and ε_{PP} (0.81) knowledge allows the determination of the tortuosity T_{oPP} of the pores phase. The simplified form of eq.(5.7) leads to the conclusion that $T_{oPP} = 2.3$, this indicating a considerably tortuous architecture.

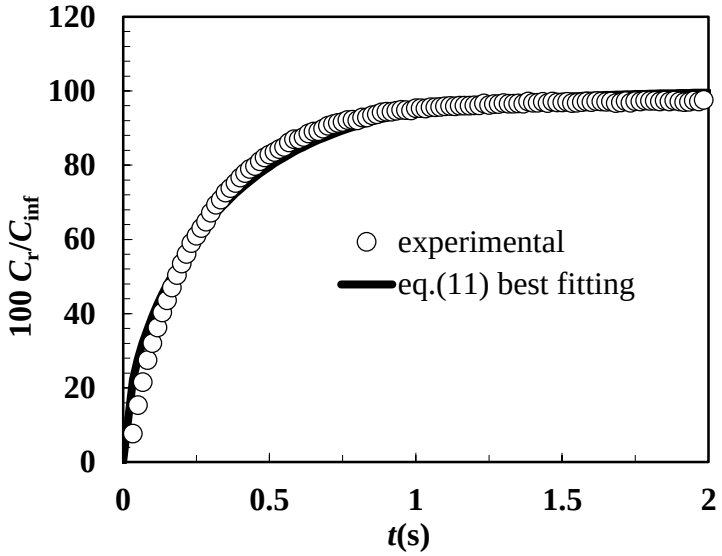

Figure 5.25: Theophylline (TPH) release kinetics (37°C). C_r is the time (t) dependent TPH concentration while C_{inf} is TPH concentration after an infinite time (equilibrium). Data standard error, not reported for the sake of clarity, is always lower than 5% of the measured value.

This suggests that big pores are not directly connected to each other, but their connection is realized by a series of interconnected small pores that render the drug path tortuous (*Figure 5.21*, right, seems compatible with this interpretation) as shown in *Figure 5.26*. The use of the simplified version of eq.(5.7) is allowed by the small TPH diffusion coefficient in the polymeric network phase (PNP). Indeed, in the light of our hypothesis about the volume fraction competing to the PP and PNP phases, the polymer volume fraction (φ_p) in the PNP phase is high:

$$\varphi_p = \left(1 + 0.01\frac{S_d A_4 \rho_p}{\rho_{H2O}}\right)^{-1} \approx 0.73 \qquad (5.9)$$

In the presence of a so high a polymer volume fraction, all the molecular theories, devoted to the determination of the drug diffusion coefficient in a polymeric network, predict values around one tenth (or less) of the drug diffusion coefficient in pure water at the same temperature [**47**].

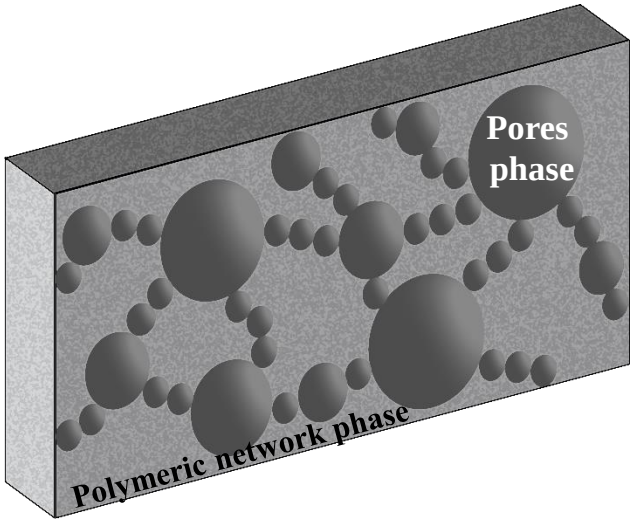

Figure 5.26: Sketch of the hydrogel micro and nano- topology.

Thus, D_{PNP} has to be negligible in comparison to D_{PP} and D_{TPH} that, in this case, are of the same order of magnitude.

References

1. Mayer P.R., and Stowe R.A., "Mercury Porosimetry-Breakthrough Pressure for Penetration between Packed Spheres", *Journal of Colloid Science* 20 (1965) 893-911.
2. M.N. Clifford, Chemical and physical aspects of green coffee and coffee products. In: M.N. Clifford, K.C. Willson (eds), Coffee: botany, biochemistry and production of beans and beverage, 305-374. Avi Publishing Company, Westport, Connecticut, USA. (1985).
3. R.J. Clarke, R. Macrae, Coffee volume 1: Chemistry, (Cap. 6, P. Folstar Lipids), Elsevier Applied Science, (1985).
4. A. Illy, R. Viani, Espresso coffee: the chemistry of quality, Academic Press (1995)
5. P. Pittia, G. Sacchetti, Food Chem. 106, 1417–1427 (2008).
6. J. Diaz Santanilla, S. Gomez, G. Felsner, G. Fritsch, Colloque Intern. Chim. Cafés Verts Torréfiés Derivés, 6, 172–177 (1974).
7. J. Avelino, B. Barboza, J. C. Araya, C. Fonseca, F. Davrieux, B. Guyot, C. Cilas, J. Sci. Food Agric., 85, 1869–1876 (2005).
8. Mateus M.L., Champion D., Liardon R., Voilley A., Characterization of water mobility in dry and wetted roasted coffee using low field proton nuclear magnetic resonance, (2007) Journal of Food Engineering 572-579.
9. Del Negro E., "Caratterizzazione di Lattici SBR per la produzione industriale", *Tesi di Laurea, Univ.Trieste* (2010)
10. Dammström, S., Salmén, L., Gatenholm, P. 2005. The effect of moisture on the dynamic properties of bacterial cellulose/glucuronoxylan nanocomposites. Polymer 46, 10364-10371.
11. Ouajai, S., Shanks, R.A. 2005. Composition, structure and thermal degradation of hemp cellulose after chemical treatments. Polym. Degrad. Stabil. 89, 327-335.
12. Oikawa, T., Morino, T., Ameyama, M. 1995. Production of Cellulose from D Arabitol by Acetobacter xylinum KU-1. Biosci. Biotechnol. Biochem. 59, 1564-1565.

13. Ross, P., Mayer, R., Benziman M. 1991. Cellulose Biosynthesis and Function in Bacteria. Microbiological Rev. 55, 35-58.

14. Jonas, R., Farah, L. F. 1998. Production and application of microbial cellulose. Polym. Degrad. Stabil. 59, 101-106.

15. Yamanaka, S., Watanabe, K., Kitamura, N., Iguchi, M., Mitsuhashi, S., Nishi, Y., Uryu, M. 1989. The structure and mechanical properties of sheets prepared from bacterial cellulose. J. Mater. Sci. 24, 3141-3145.

16. Alderman, D. A. 1984. A review of cellulose ethers in hydrophilic matrices for oral controlled-release dosage forms. Int. J. Pharm. Technol. Prod. Manufact. 5, 1–9.

17. Heller, J. 1987. Use of polymers in controlled release of active agents in controlled drug delivery, in: Fundamentals and Applications, Robinson, J. R., Lee, V. H. L (Eds.), Marcel Dekker, New York, NY, USA, 2nd edition, pp. 210–180.

18. Longer, M. A., Robinson, J. R. 1990. Sustained-release drug delivery systems, in: Remington's Pharmaceutical Sciences, Remington, J. P. (Ed.), Mack Publishing, Easton, Pa, USA, 18th edition, pp. 1676–1693.

19. Lonnberg, H., Fogelstrom, L., Samir, M. A. S. A, Berglund, L., Malmstrom, E., Hult, A. 2008. Surface grafting of microfibrillated cellulose with poly(ε-caprolactone)—synthesis and characterization. *Europ. Polym. J.* 44, 2991–2997.

20. Grassi M., Lamberti, G., Cascone, S., Grassi, G. Mathematical modeling of simultaneous drug release and in vivo absorption. 2011. Int. J. Pharm. 418, 130–141.

21. Zanetti, M, Stocca, A, Dapas, B, Farra, R, Uxa, L, Bosutti, A, Barazzoni, R, Bossi, F, Giansante, C, Tedesco, F, Cattin L, Guarnieri G, Grassi G. 2008. Inhibitory effects of fenofibrate on apoptosis and cell proliferation in human endothelial cells in high glucose. J. Mol. Med. (Berl). 86:185-195.

22. **B**aiz, D., Dapas, B., Farra, R., Scaggiante, B., Pozzato, G., Zanconati, F., Fiotti, N., Consoloni, L., Chiaretti, S., Grassi, G. 2014. Bortezomib effect on E2F and cyclin family members in human hepatocellular carcinoma cell lines. *World J. Gastroenterol*. 20,795-803.

23. Scaggiante, B., Kazemi, M., Pozzato, G., Dapas, B., Farra, R., Grassi, M., Zanconati, F., Grassi, G. 2014. Novel hepatocellular carcinoma molecules with prognostic and therapeutic potentials. *World J. Gastroenterolgy* 20,1268-1288.

24. Losi, E., Bettini, R., Santi, P., Sonvico, F., Colombo, G., Lofthus, K., Colombo, P., Peppas, N. A. 2006. Assemblage of novel release modules for the development of adaptable drug delivery systems. *J. Contr. Rel.* 111, 212–218.

25. Millon, L. E., Wan, W. K. 2006. The polyvinyl alcohol-bacterial cellulose system as a new nanocomposite for biomedical applications. *J. Biomed. Mater. Res. B* 79, 245–253.

26. Cai, Z., Kim, J. 2010. Bacterial cellulose/poly(ethylene glycol) composite: characterization and first evaluation of biocompatibility. *Cellulose*, 17, 83–91.

27. Lin, C. C., Metters, A.T. 2006. Hydrogels in controlled release formulations: Network design and mathematical modelling. *Adv. Drug Del. Rev*. 58, 1379–1408.

28. Chern, J.M., Lee, W.F., Hsieh, M.Y., 2004. Preparation and Swelling Characterization of Poly(n-isopropylacrylamide)-Based Porous Hydrogels. J. Appl. Polym. Sci. 92, 3651–3658Peppas, N. A. 1984. *Mathematical models for controlled release kinetics*. In: Langer, R. S., Wise, D. L. (Eds.), *Medical Application of Controlled Release*, vol. I. CRC Press, Boca Raton.

29. Narasimhan, B. 2000. *Accurate models in controlled drug delivery systems*. In: Wise, L. D. (Ed.), *Handbook of Pharmaceutical Controlled Release Technology*, Marcell Dekker, 2000.

30. Abramoff, M.D., Magalhaes, P.J., Ram, S.J. 2004. Image Processing with ImageJ. *Biophotonics Int.*, 11, 36-42.

31. Kuijpers, A. J., Engbers, G. H. M, Feijen, J., De Smedt, S. C., Meyvis, T. K. L., Demeester, J., Krijgsveld, J., Zaat, S. A. J., Dankert, J. 1999. Characterization of the Network Structure of Carbodiimide Cross-Linked Gelatin Gels. *Macromolecules* 32, 3325-3334.

32. Holz, M., Heil, S. R., Sacco, A. 2000. Temperature-dependent self-diffusion coefficient of water and six selected molecular liquids for calibration in accurate H NMR PFG measurements. *Phys. Chem. Chem. Phys*. 2, 4740-4742.

33. Patankar, S. V. 1990. *Numerical heat transfer and fluid flow*. Hemisphere Publishing, New York.

34. Grassi, M., Grassi, G., Lapasin, R., Colombo, I. 2007. Understanding drug release and absorption mechanisms: a physical and mathematical approach. CRC Press, Boca Raton, FL, USA.

35. Carman, P. C. 1956. Flow of Gases Through Porous Media, Butterworths, London, pp. 45–50.

36. Stait-Gardner, T., Willis, S. A., Yadav, N. N., Zheng, G., Price, W. S. 2009. NMR Diffusion measurements of complex systems. *Diffusion-fundamentals* 15, 1-22.

37. Coviello, T., Matricardi, P., Alhaique, F., Farra, R., Tesei, G., Fiorentino, S., Asaro, F., Milcovich, G., Grassi, M. 2013. *Express Polym. Lett*. 7, 733–746.

38. Brownstein, K. R., Tarr, C. E. 1979. Importance of classical diffusion in NMR studies of water in biological cells. *Phy. Rev. A* 19, 2446-2453.

39. Chui, M. M., Phillips, R. J., McCarthy, M. J. 1995. Measurement of the porous microstructure of hydrogels by nuclear magnetic resonance. *J. Coll. Inter. Sci*. 174, 336-344.

40. Gallegos, D. P., Munn, K., Smith, D.M., Stermer, D. L. 1987. A NMR technique for the analysis of pore structure: application to materials with well-defined pore structure. *J. Colloid Interface Sci*., 119, 127-139.

41. Munn, K., Smith, D. M. 1987. A NMR technique for the analysis of pore structure: Numerical inversion of relaxation measurements *J. Colloid Interface Sci*.119, 117-126.

42. Stana-Kleinschek, K., Kreze, T., Ribitsch, V., Strand, S. 2001. Reactivity and electrokinetical properties of different types of regenerated cellulose fibres. *Coll. Surf. A*., 195, 275–284.

43. Karakutuz, I., Okay, O. 2010. Macroporous rubber gels as reusable sorbents for the removal of oil from surface waters. *React. & Funct. Polym*. 70, 585 – 595.

44. Lapasin, R., Pricl, S. 1995. *Rheology of industrial polysaccharides: Theory and applications*. Blackie Academic & Professional, London.

45. Cappelli, A., Galeazzi, S., Giuliani, G., Anzini, M., Grassi, M., Lapasin, R., Grassi, G., Farra, R., Dapas, B., Aggravi, M., Donati, A., Zetta, L., Boccia, A. C., Bertini, F., Samperi, F., Vomero, S. 2009. Synthesis and Spontaneous

Polymerization of Oligo(ethyleneglycol)-Conjugated Benzofulvene Macromonomers. A Polymer Brush Forming a Physical Hydrogel. *Macromolecules* 42, 2368-2378.

46. Amsden, B. 1998. Solute Diffusion within Hydrogels. Mechanisms and Models. *Macromolecules* 31, 8382-8395.

6 Polymeric scaffolds

In this chapter, two different polymeric scaffolds will considered. The first is composed by *alginate hydroxyapatite*, while the second is made up by *Poly Left lactide Acid* (PLLA). Both of them will be characterized by ESEM and LF-NMR. In addition, the viability of MG-63 osteosarcoma human cell line and NIH-3T3 mouse embryonic fibroblast will be assessed on alginate hydroxyapatite, PLLA, PLLA/Collagen and PLLA/Collagen/glycosamminoglycans by means of MTS assay.

6.1 Alginate Hydroxyapatite scaffolds

6.1.1 Introduction

These scaffolds are constituted by a polymer of natural origin, *alginate*, and a support material, such as *hydroxyapatite*. Alginate (Alg), extensively described in the chapter 4.1, is a naturally derived polysaccharide that is abundant in cell walls of brown algae. As for agarose, it shows a high solubility in water. It is a polyanion composed of two repeating monomer units: β-D- mannuronate (M) and α-L-guluronate (G). Physical and mechanical properties of alginate are highly related to the guluronate block, in terms of chain length and proportions inside the polymer. Alginate as an electrolytic nature and it has the exclusive property of being able to form a gel in presence of certain divalent cations (for example calcium, barium, strontium etc.).

Hydroxyapatite (Hap) is a ceramic material essentially composed of calcium and phosphorus. It is well known to be biocompatible, bioactive, osteoconductive, not toxic, not inflammatory and not immunogenic agent. For all these reasons, Hap became an essential compound of bone implants, cements and scaffolds.

6.1.2 Experimental section

6.1.2.1 Materials

The sodium alginate isolated from Laminaria hyperborean were provided by FMC Biopolymer (Norway) (MW = 1.3 x 10^5, FG = 0.69, FGG = 0.56). Hap powder was from Fluka (USA). Dulbecco's modified Eagle's medium (DMEM), fetal bovine serum (FBS), penicillin, streptomycin, trypsin/EDTA solution, phosphate – buffered saline (PBS), glutamine, D – Glucolonic acid δ-lactone (GDL) were purchased from Sigma (USA). All other chemicals were of analytical grade.

6.1.2.2 Alginate hydroxyapatite scaffolds preparation

Alg/Hap composite scaffolds were prepared by mixing alginate 2% (w/v) and Hap 3% in water using calcium release method. Hap powder was homogenously dispersed into a stirred solution of alginate in water, followed by the addition of GDL 60 mM to release calcium ions from Hap. Aliquots of this solution were then cured in 24-well tissue culture plates for 24 h at room temperature to allow complete gelation. The hydrogels in the tissue-culture plate were then stepwise cooled by immersion in a liquid cryostat. Temperature was decreased stepwise from 20°C to -20°C by 5°C steps with 30 min intervals for equilibration. Samples were then freeze dried for 24 hours to obtain porous scaffolds.

6.1.2.3 LF-NMR characterization

Low Field Nuclear Magnetic Resonance characterization was performed by means of a Bruker Minispec mq20 (0.47 T, 20MHz). The theory presented in the chapter 3 was followed to investigate the time evolution of the scaffold's pore size distribution with and without cells. Basically, this implies the measurement of T_2 and D_G and the interpretation of these data according to the theory of Chui [**1**] that allows the determination of pores dimension and volumetric abundance.

6.1.2.4 Scanning Electron Microscope characterization

Scaffolds structure was analyzed using a Quanta250 SEM, FEI, Oregon, USA. Freeze-casted samples were sectioned at various planes and directly visualized by electron

microscopy after sputter-coting with an ultrathin layer of gold. Scaffolds seeded with cells were rinsed with 10 mM HEPES pH=7.4 cointaining 10 mM $CaCl_2$, 100 mM NaCl, 5 mM glucose and then were fixed with 10% gluteraldehyde in PBS for 1h at room temperature. Samples were then washed three times with water, dehydrated by stepwise treatment with ethanol and finally dried with a critical point dryer, sputter-coated with gold and visualized by electron microscope.

6.1.2.5 Micro – Computed Tomography Characterization

Micro-CT of saples was obtained by means of a conebeam system called TOMOLAB (www.elettra.tirieste.it/Labs/TOMOLAB). The device is equipped with a sealed micro-focus X-ray tube, which guaranteed a focal spot size of 5 microns, in an energy range from 40 kV up to 130 kV, and maximum current of 300 μA. As a detector was used a CCD digital camera with (49.9 X 33.2) mm^2 field of view and a pixel size of (12.5 X 12.5) μm^2.

6.1.2.6 Cell culture and seeding

Osteosarcoma MG-63 (ATCC® Number: CRL- 1427™) human cell line was cultured in DMEM supplemented with 10% FBS, 1% Penicillin-Streptomycin/ 1% L-glutamine at 37°C and 5% pCO_2. For cell seeding onto scaffolds, porous freeze-casted scaffolds produced under sterile conditions, were reswollen in 5 mM $CaCl_2$ for 30 min under agitation and immersed in complete cell culture medium for 24 hours in 24-wells culture plates to ensure chemical equilibration. Osteosarcoma cells, suspended in 50 μl of medium, were loaded with a micropipette over the whole upper surface of the scaffolds. After 4 hours, the scaffolds were placed into fresh, sterile 24-wells culture plates and 1mL of complete medium was added.

6.1.2.7 Cell proliferation and viability on Alg/Hap Scaffolds

The viability and growth rate of MG-63 cell line on alginate hydroxyapatite scaffolds were assessed as a function of the time using the MTS assay according to the protocol provided by the manufacter (CellTiter Acqueous One solution cell proliferation Assay kit from Promega). A suspension of $50*10^3$ cells was seeded on sterilized scaffolds, incubated at 37 °C and 5% of p_{CO2}. MTS assay was performed in quadruplicate 1, 7, 14

and 21 days from cell seeding. Briefly, after 4 hours of incubation with the MTS reagent in an incubator, the medium was collected from the scaffolds and the absorbance was measured on an ELISA plate reader at a wavelength of 490 nm. The absorbance obtained from an empty scaffold (blank) was subtracted from the samples values.

6.1.3 Results and discussion

One of the key requisites for tissue engineering scaffolds is to present a porous interconnected structure. The average pore size, the pore size distribution and the topology must be tailored to respond to specific application requirements as they strongly influence cell adhesion, proliferation and matrix deposition, as well as the formation of blood vessels within the scaffold to help tissue growth.

In order to get more information about pore dimensions and their relative abundance, the scaffolds were studied according to the low field nuclear magnetic resonance Pulsed Gradient Spin Echo (NMR-PSGE).

The analysis was peformed on two types of scaffolds:

- scaffolds with cells
- scaffolds without cells.

The experiments, led in duplicate, were carried out for twenty days. The tests were performed on scaffolds with and without seeded cells (line MG - 63) maintaining them in an incubator at appropriate conditions (37 °C and 5% p_{CO2}). Over the 20 days, different trend of the relaxation time T_2 and the water sef diffusion coefficient D_G were observed for cells seeded scaffolds and empty ones. *Figure 6.1* shows that four classes of pores can be detected in both cells free and cell seeded scaffolds (ξ_i and A_i indicate, respectively, pores dimension and abundance of pores class "i").

During the 20 days of the experiment, it is possible to observe that no substantial differences (for both the dimension, ξ, and relative abundance $A_{3,4}$) occur between cell seeded and cell free scaffolds for what concerns the dimension of small pores (classes 3 and 4). This is probably due to the small pore diameter that hinders cells entering. Accordingly, the fate of small pores is similar for cell seeded and cell free scaffolds. Conversely, the fate of larger pores (classes 1 and 2) is different for what concerns cell seeded and cell free scaffolds (for both the dimension, ξ, and relative abundance $A_{1,2}$). This seems reasonable as MG-63 cells can grow and produce extracellular matrix only in sufficiently wide pores (> 100 μm) in comparison to their diameter that is around 20 μm.

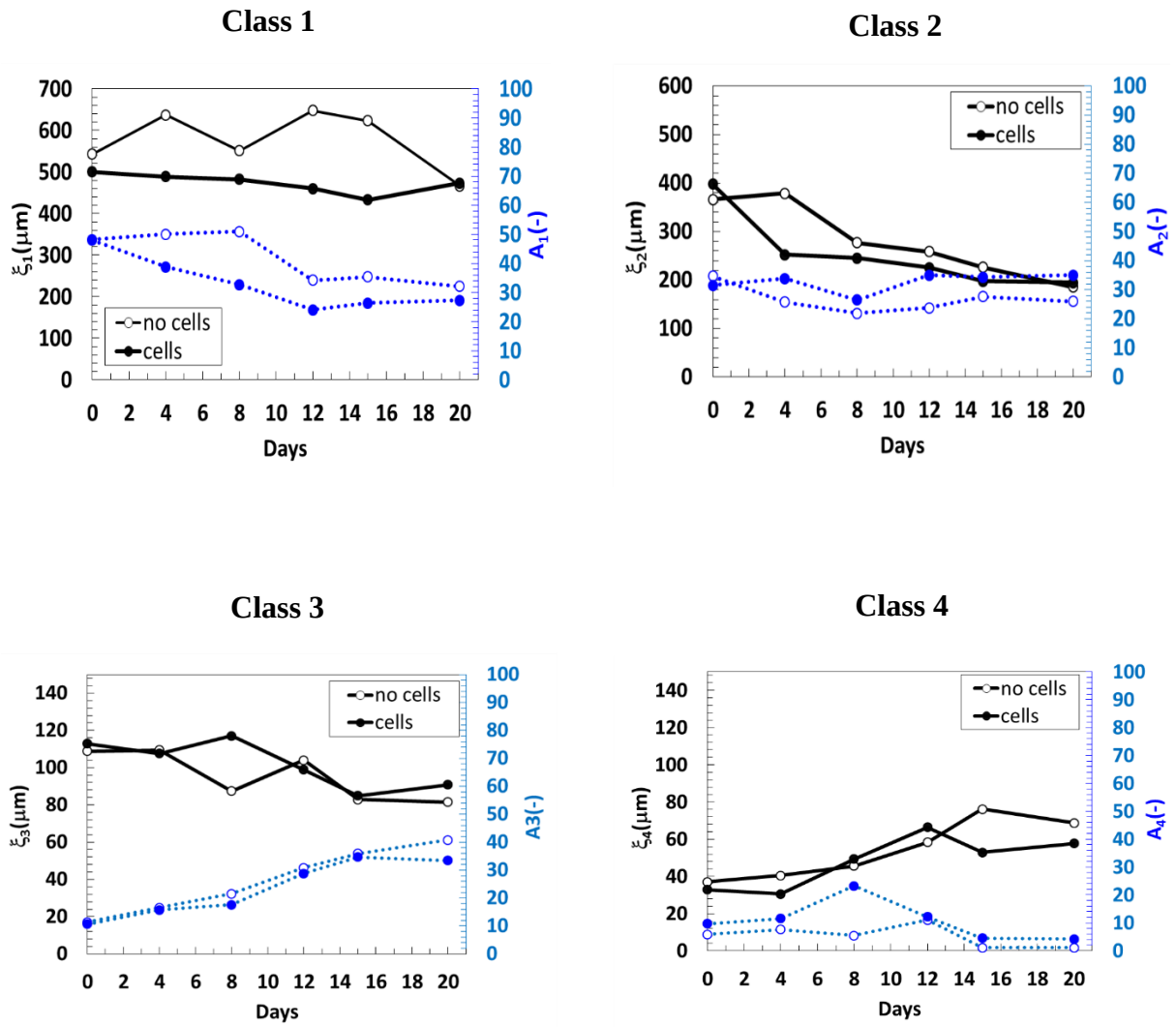

Figure 6.1: LF – NMR characterization of scaffolds with and without cells

Cell adhesion, proliferation and differentiation are the indicator of cellular compatibility towards a supporting material and they determine the suitability of the material for tissue engineering and regenerative medicine applications. The adhesion and growth of osteoblast-like cell lines on Alg/Hap scaffolds were assessed as a function of the time using a MTS assay according to the protocol tailored from the one provided by the manufacturer. Cells were seeded on the top of the scaffolds after reswelling of the structures at day 0 by means of DMEM medium. The assay was performed at days 1, 7, 14 and 21 after seeding. The cultures in Alg/Hap scaffolds were analyzed after 10 and 21 days using a scanning electron microscope (SEM). *Figure 6.2* shows SEM micrographs

of osteoblast like cells MG-63 on Alg/Hap composites after 10 and 21 days of culture (See *Figure 6.2*).

The majority of cells displayed a rounded morphology rather than a flat one and they appeared gathered together to form clusters. The cells are well adherent to the pore walls with processes and multiple filopodia, surrounded by a network of fibrillar bundles of extracellular matrix particularly abundant after 21 days of culture.

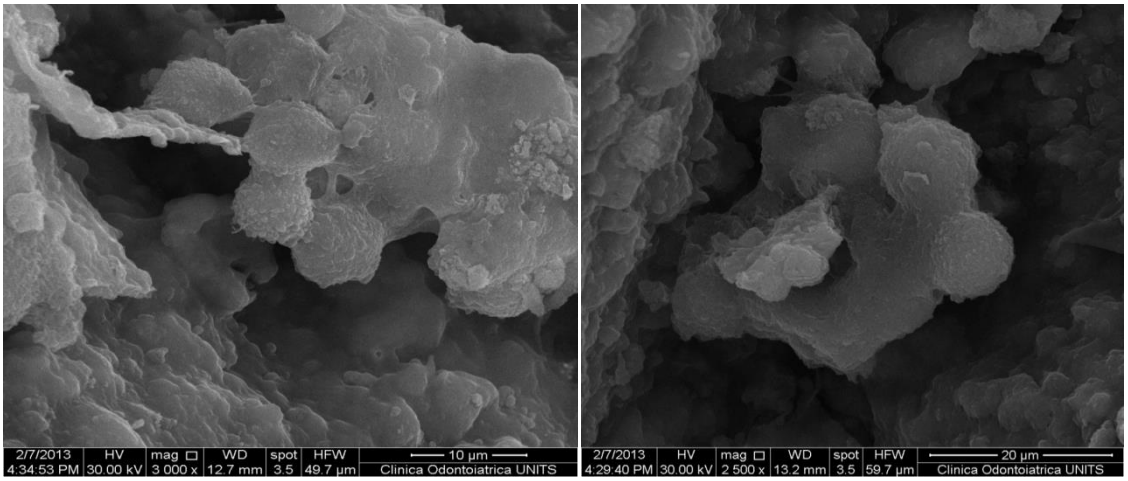

Figure 6.2: SEM micrographs of osteoblast like cells MG-63 seeded on Alg/Hap scaffolds after 10 days of culture.

It is known that the adopted freeze drying technique can yield to pores diameters spanning from 100 μm to 500 μm depending on the cooling rate speed as witnessed by *Figure 6.3*. Interestingly, this range is substantially in agreement with found by means of LF-NMR.

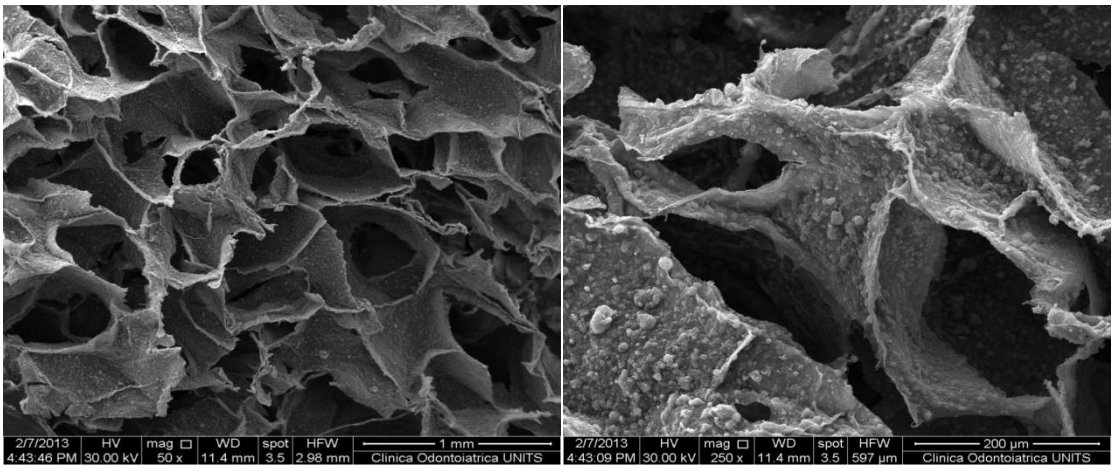

Figure 6.3: SEM micrographs showing the pore size distibution.

Micro-computed tomography is a not destructive technique that allows reconstruction of 3-D images of the developed scaffolds. A quantitative characterization of the micro-structure of the composite has been performed from a micro-CT reconstruction (*Figure 6.4*).

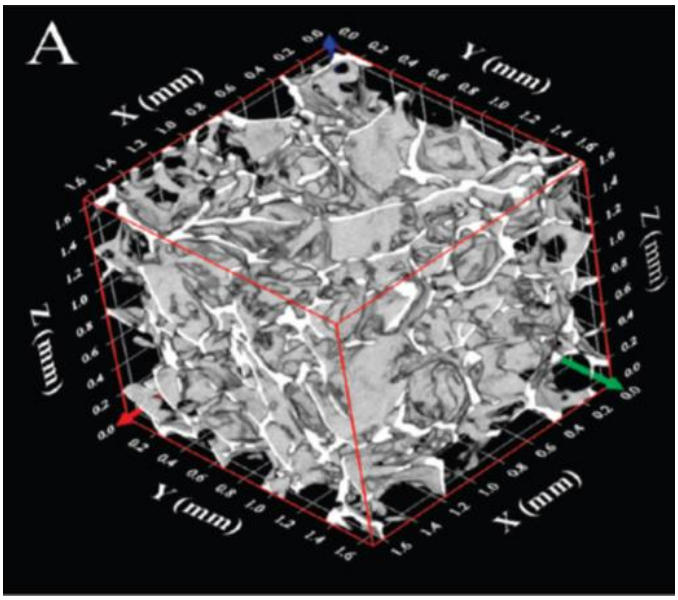

Figure 6.4: Three-dimensional reconstruction of the Alg/Hap scaffolds: from a Micro-CT segmented data of a freeze casted scaffold evidencing the porosity and the interconnection of the pores.

Quantification first requires a segmentation process, i.e the separation of voxels of the scaffold material, hereafter conventionally named as bone, from those as background. This is typically done by thresholding the grey levels of the image. Starting from a segmented image, Representative Elementary Volume (REV) needs to be extracted in order to have a small image (typically a regular cube) which is easy to handle with common computer hardware. As suggested by Bear [**2**], the REV size can be determined as the minimum value of the sub volume size- made progressively decrease- for which the calculated value of the porosity is essentially constant. The porosity can then be easily estimated by simply counting the number of pore (or background) voxels divided by the total number of REV voxels. Different methods have been proposed, especially within bone research, to get more refined parameters from micro-CT images. Micro-CT analysis revealed that the average pores dimension is around 200 μm, in substantial agreement with what found by means of LF-NMR evaluation (181 μm, see *Figure 6.1,* day zero).

6.2 Poly L-Lactide Acid Scaffolds

6.2.1 Introduction

The success of aliphatic polyesters in tissue engineering relies largely on their degradability and biocompatibility, as well as their good processability and their mechanical properties. Poly-lactic-acid (PLA) is biodegradable thermoplastic polyester that can be produced through ring-opening polymerization of lactic acid. Since lactic acid is a chiral molecule, it exists in two frms, Poly-L-Lactic acid (PLLA) and Poly-D-lactic-acid (PDLA). It is known that the properties of PLA are highly affected by the stereo-isomeric L/D ratio of the lactate units. In fact, PLLA and PDLA, consisting only of L- and D-lactate units, respectively, are highly crystalline with identical chemical and physical properties, while poly (DL-lactide) (PDLLA or simply PLA), consisting of racemic lactate units, is rather amorphous [**3**]. The involvement of D- and L- units in the sequences of PLLA and PDLA, respectively, exerts a profound effect on their thermal and mechanical crystallinity. For the aforementioned reasons, blending PLLA with PDLLA is an effective method for controlling the polymer cristallization, morphology and hydrolysis nature. PLA degrades by bulk hydrolysis and leads to the production of lactic acid. In the case of PLLA, degradation results in L (+) lactic acid, a substance that exists in the human body under natural circumstances as well, therefore PLLA is generally preferred over PDLA [**4**]. The body transports the produced L (+) lactic acid to the liver, converts it into pyruvic acid and upon entering the tricarboxylic acid cycle, secreting it as water and carbon dioxide. Despite the FDA approval of PLLA and the large number of clinical applications, a number of literature studies report inflammatory responses [**5, 6**]. During degradation, the produced lactic acid can lower the pH in the environment adjacent to the polymer. This local acidity can aversively affect cellular function and induce inflammatory response. Additionally, highly crystalline parts might stay behind which can cause an inflammatory response of the surrounding tissue. However, it was also noted that in case of relatively small material volume, no adverse biological responses occur. In addition, other literature reports that PLA does not leave significant amounts of accumulating degradation products behind in the body. The degradation of PLLA in vitro occurs in the order of years, whereas in vivo degradation takes approximately 8-10 months. Degradation of PDLLA is in the order of months. The

degradation rate of PLA scaffolds highly depends on amongst others molecular weight and polydispersity of the polymer, process parameters and scaffolds design. PLLA exhibit superior mechanical strength compared to PDLLA due to its semi-crystalline nature (10-40 % crystallinity) and higher glass transition temperature ($T_g \approx 65$ °C) with respect to that of PDLLA (Tg ≈ 54 °C).

Collagen is the most abundant structural protein found in the body. There are more than twenty genetically distinct types of collagen molecules, all of which are triple helical molecules based on polypeptide chains of amino acids. Collagen type I is the most abundant collagen found in the human body. It is found in skin, ligaments, tendons and it is the main organic substance found in bone. The scaffolds used in this work are fabricated from collagen type I.

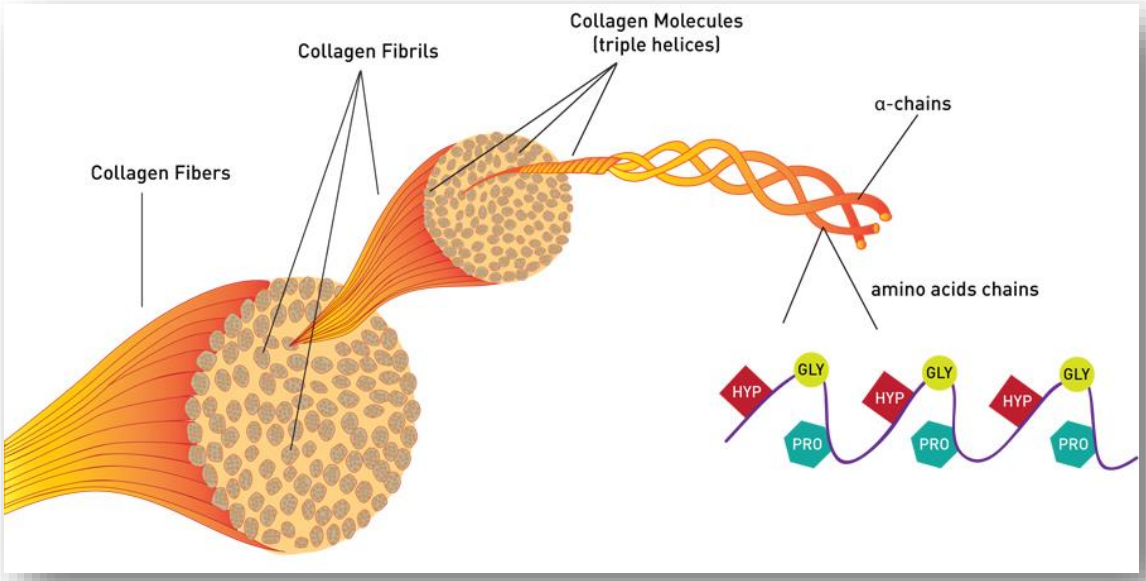

6.5: Typical collagen structure.

Collagen type I is a heterotrimer, i.e. it is a triple helix that consists of two α1 chains and one α2 chain. The α2 chain has a slightly different amino acid sequence compared to the α1 chains. Collagen type I triple helices are 300 nm long and contain approximately 3000 amino acid residues. Each of the three α-chains within the molecule forms an extended left-handed helix with a pitch of 18 aminoacids per turn [**7**]. The three chains, staggered by one residue relative to each other, are supercoiled around a central axis in a right-

handed manner to form the triple helix [**8**]. The polypeptide chains have a repeating unit $[Gly\text{-}X\text{-}Y]_n$, with a glycine residue in every third position in the polypeptide chain. The plane of each peptide bond is positioned perpendicular to the axis of the helix so that the carbonyl groups are pointed in a direction where they form strong inter chain hydrogen bonds with other chains in the molecule. The triple helix is formed such that glycine, the smallest amino acid, is positioned at the centre of the helix and the more bulky side of other amino acids occupy the outer positions. This allows a close packing along the centre of the molecule as shown in *Figure 6.6b* [**9**]. The X and Y positions are most commonly occupied by the amino acids proline and hydroxyproline, respectively.

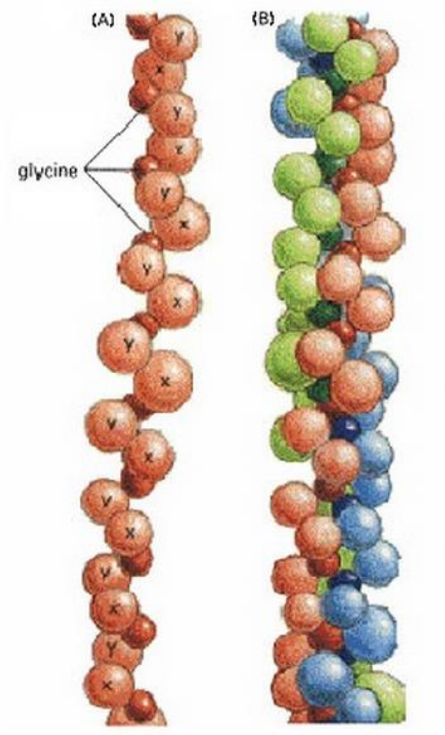

(C)

	α1	α2
3-Hydroxyproline	1.1	1.2
4-Hydroxyproline	114.0	105.0
Aspertic acid	46.0	45.0
Threonine	18.0	18.0
Serine	35.0	30.0
Glutamic acid	77.0	70.0
Proline	118.0	114.0
Glycine	330.0	331.0
Alanine	119.0	105.0
Valine	19.0	35.0
Half-cystine	ND	ND
Methionine	5.3	4.7
Isoleucine	8.2	16.0
Leucine	20.0	33.0
Tyrosine	2.1	3.2
Phenylalanine	13.0	11.0
Hydroxylysine	10.0	12.0
Lysine	27.0	20.0
Histidine	4.0	10.0
Arginine	49.0	51.0

Figure 6.6: (A) Collagen chain **(B)** Collagen molecule **(C)** Amino acid composition of type I collagen.

A breakdown of the amino acid content of type I collagen is shown in *Figure 6.6 C.* The non-helical regions at the end of the collagen molecule are called telopeptides or tropocollagens and they are involved in the intermolecular crosslinking of collagen molecules. The pro-peptides are important in the formation of the collagen molecules. Once triple helices are formed, they group together to form collagen fibrils. These fibrils have a distinctive banded appearance, which is due the quarter-staggered alignment.

Clinical applications of collagen scaffolds are highly relevant to otorhinolaryngological practice. These include the manufacture of sutures, haemostatic agents (powder, sponfe, fleece), blood vessels (extruded collagen tubes) tendons and ligaments, dermal regeneration for burn treatment and peripheral nerve regeneration (porous collagen-GAGs copolymers).

Glycosaminoglycans (**GAGs**) are linear, heterogeneous highly negatively charged, acidic polysaccharides, abundant in the extracellular matrix (ECM) and on the cell surface. GAGs are made of a basic disaccharide repeating unit composed of two, six member sugar rings, a hexosamine (D-glucosamine, GlcNAc, or D-galactosamine, GalNAc) linked to a uronic acid (D-glucuronic acid, GlcA, or L-iduronic acid, IdoA) [**10, 11**]. Both sugars of the repeat unit can be variably N- and O-sulfated, resulting in complex, chemically versatile macromolecules. Apart from their structural importance to the integrity of the ECM, GAG chains serve as fundamental modulators of a wide variety of biological processes [**12**] The high negative charge associated with GAGs facilitates their interaction with a large array of extracellular proteins [**13**], while their linear structure promotes the sliding movement of bound proteins along the chains. In this manner, GAGs facilitate molecular encounters between proteins in the assembly of multicomponent complexes, reducing the three dimensional search problem to a one dimensional search [**14**]. GAGs are classified into four main classes based on their biosynthetic pathways and chemical composition: heparan sulfate (HS) and heparin, chondroitin sulfate (CS) and dermatan sulfate (DS), keratan Sulfate (KS) and hyaluronic Acid (HA). Two classes HS/heparin, and CS/DS are linked through a common tetrasaccharide (xylose-galactosegalactose-glucuronic acid) to serine residues of a protein core forming a proteoglycan. The third class, KS, is attached to the core protein through an Nacetylglucosamine by N-linkage to asparagine or O-linkage to serine [**15**]. The fourth class, HA is produced as a free GAG (no protein attachment) and forms high molecular weight assemblies in the ECM [**14**].

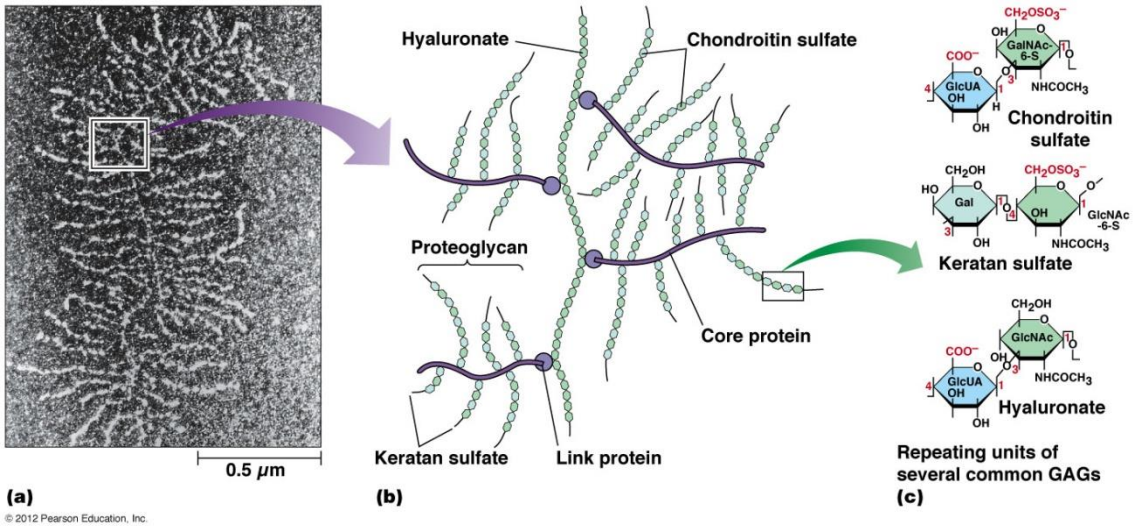

Figure 6.7: Schematic representaion of the glycosaminoglycans.

GAGs serve as key biological response modifiers by acting as stabilizers, cofactors, or co-receptors for growth factors, cytokines, and chemokines. GAGs regulate enzyme activities and signaling molecules in response to cellular damage, such as wounding, infection and tumorigenesis [**16**]. Through their properties and interactions, GAGs play important roles in intercellular communication of metazoan cells. GAGs are targets for bacterial, viral, and parasitic virulence factors for attachment, invasion, and immune system evasion. GAGs have appeared early in evolution and their prominent extracellular location have ensured their conserved roles throughout the animal kingdom.

6.2.2 Experimental section

6.2.2.1 Materials

High crystalline poly-L-lactic- acid (PLLA, Resomer^{TN} L209 S) was kindly supplied by Boehringer Ingelheim Pharma KG, 1,4 dioxane (Sigma) and double distilled water were utilized to prepare the ternary solution. Micro-fibrillary rat-tail type I collagen (BD Biosciences) and a mixture of purified GAGs from the porcine aorta and characterized for composition and structure as previously reported [**17, 18**], were used for the preparation of collagen-GAG matrix.

6.2.2.2 Poly-L-Lactic Acid scaffolds preparation

PLLA scaffolds were prepared via Thermally Induced Phase Separation (TIPS).

TIPS is a widely used technique to porous scaffolds and membranes for tissue engineering. It involves cooling a homogeneous polymeric solution to a temperature where the single phase system becomes thermodynamically unstable and spontaneously separates into a polymeric-rich and a polymeric-lean phase. The non-solvent is added to increase the free energy of mixing, thus promoting the phase separation. If one chooses the appropriate system composition, the polymer-lean phase will nucleate into a continuous polymer-rich phase. The polymer-lean phase, after solvent removal, leads to the pores (voids), whereas the polymeric-rich phase will form the "skeleton" of the porous structure.

A homogeneous ternary solution composed by PLLA, dioxane and water was prepared, with a constant dioxane to water weight ratio of 87/13. The concentration of PLLA was chosen to be 4% wt/wt. The solution, initially kept at 60 °C, was hot poured into a cylindrical polyethylene sample - holder. The temperature was then suddenly lowered to a value within the unstable region for 45 minutes, by pool immersion of the sample holder into a thermostatic water bath (25°C, 30°C and 35°C). Thereafter, a quench by immersion in an ethyl alcohol bath at a temperature of -20 °C for 15 minutes was performed, in order to freeze the obtained structure. The obtained scaffolds were removed from the sample - holder and washed in deionized water for 24 hours to eliminate the residual dioxane. Finally, the sample were dried under vacuum at 30 °C for 24 hours [**19**]. Then, the scaffolds were sterilized in ethyl alcohol under vacuum for 1 h. Smaller samples (D= 10 mm, thickness=1 mm) for the conjugation were obtained by cutting with a surgical blade the scaffold. The morphology of the foams obtained was analysed by scanning electron microscopy (SEM) using a SEM-FEI QUANTA 200F on sample cross section fractured in liquid nitrogen and gold sputtered (Sputtering Scancoat Six, Edwards) for 40s under Argon atmosphere before imaging. SEM images were exported as 24-bit image files using the tagged image file format (tiff) for further analysis.

6.2.2.3 Low Field-NMR characterization

Low Field NMR characterization was performed by means of a Bruker Minispec mq20 (0.47 T, 20 MHz). In order to study the scaffold structure, two kinds of experimental tests

were performed: (a) determination of the water protons transverse relaxation time (T_2) and (b) determination of the water diffusion coefficient (D_G) inside the scaffold. The T_2 measurement was made according to CMPG sequence with 90-180° pulse separation of $\tau = 0.25$ ms while D_G determination implied the execution of PSGE measurement. PLLA scaffolds, produced at three different temperatures (25-30-35°C) during the demixing phase, were analyzed.

6.2.2.4 Scaffolds functionalization

Three different types of scaffolds (pure PLLA, PLLA – collagene and PLLA – collagene – GAGs scaffolds) were prepared and characterized.

The PLLA scaffolds were treated with type I collagen and left at room temperature over night. Later the composites were treated with an injection of 20 μl of GAGs through an insulin syringe. The PLLA scaffolds with collagen- GAGs suspension were freeze-dried by placing them into a freeze dryer at -20°C for 60 minutes. The frozen scaffolds were then sublimated under vacuum (< 100 mTorr) for 3 hours at a temperature of 0 °C. The obtained scaffolds were dehydrothermally cross-linked in a vacuum hoven at a temperature of 105 °C for 24 hours and then sterilized in ethyl alcohol under vacuum for 30 minutes [**20**].

6.2.2.5 Cell culture and seeding

NIH-3T3 mouse embryonic fibroblast cells were cultured in standard tissue culture flasks using DMEM supplemented with 10% fetal bovine serum, 1% L-glutamine and 1% penicillin/streptomycin solution. The media was replaced every 2 days. Cells were removed from the flask using a trypsin - EDTA solution and cells number calculated using a Thoma chamber. The resulting cells solution was centrifuged for 5 minutes at 1000 rpm and re-suspended in fresh culture medium to obtain 10^6 cells/mL. Before seeding, the scaffolds were placed into wells of a 24 - well tissue culture plate and washed 3 times with PBS with Ca^{2+} and Mg^{2+}. Finally 10 μl of the cells suspension was pipetted onto the surface of the scaffold in order to have 10^4 cells per scaffold. The scaffold was then returned to the incubator for 30 minutes to allow for initial cell attachment. The wells with the seeded scaffold were then filled with 2 ml of supplemented DMEM and placed into a cell culture incubator and maintained at 37 °C with 5% CO_2.

6.2.2.6 The viability of NIH-3T3 cells

The viability and growth rate of NIH-3T3 cell line on PLLA, PLLA/collagen and PLLA/collagen/ GAGs scaffolds were assessed as a function of the time using the MTS assay according to the protocol provided by the manufacturer (Cell Counting Kit 8 from Sigma Aldrich). A suspension of 10^4 cells was seeded on sterilized scaffolds, incubated at 37 °C and 5% of p_{CO2}. MTS assay was performed in triplicate after 24 hours,3, 5 and 7 days from cell seeding. Briefly, after 2 hours of incubation with the MTS reagent in an incubator, the medium was collected from the scaffolds and the absorbance was measured on a spectrometer at a wavelength of 450 nm. The absorbance obtained from an empty scaffold (blank) was subtracted from the samples values.

6.2.3 Results and discussion

In order to get more information about pores dimensions and their relative abundance, the composite scaffolds were studied according to the low field Nuclear Magnetic Resonance Pulsed Gradient Spin Echo (NMR-PGSE) experiments. LF - NMR was led on nine types of scaffolds, plus a reference system, produced at three different temperatures (25 - 30 - 35°C) during the demixing phase:

- Reference system:30°C for 45 minutes (first production attempt)
- 25 °C for 30 minutes
- 25 °C for 45 minutes
- 25 °C for 60 minutes
- 30 °C for 30 minutes
- 30°C for 45 minutes
- 30 °C for 60 minutes
- 35 °C for 30 minutes
- 35 °C for 45 minutes
- 35 °C for 60 minutes.

The experiments, led in duplicate, have taken place on PLLA composites maintaining them under vacuum for 30 minutes in absolute alcohol in order to eliminate the air inside

the scaffold and then in distillate water to favorite the entrance of water inside the scaffold. The theory shown in chapter 3 can be considered for the determination of the relaxation times and the polymeric network mesh size distribution.

About 30 minutes after tube insertion into the magnetic field (time needed for temperature stabilization) 9 tests were performed and recorded for data processing. The chosen τ was equal to 0.25 ms. An example of relaxation curve is shown in *Figure 6.8*. The number of relaxation times is chosen in order to minimize the product of the sum of squared errors, χ^2, and the number of fitting parameters of eq. (3.55).

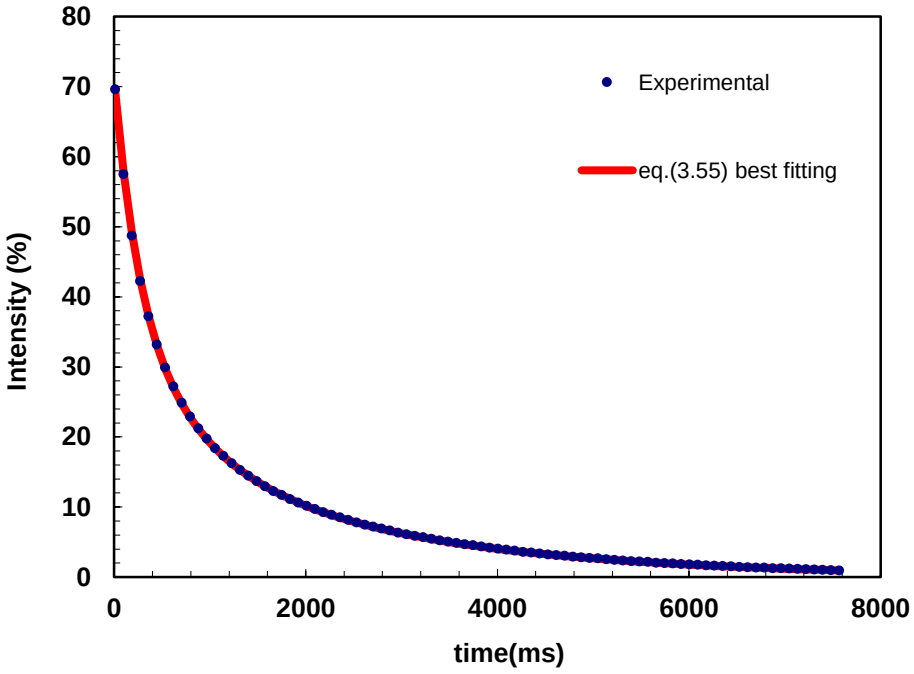

Figure 6.8: Relaxation curve relative to PLLA scaffolds (reference system)

Whatever the scaffold considered, two/three relaxation times are needed for a statistically reliable description of the relaxation time curve such as that depicted in *Figure 6.8*.

Figure 6.9 summarizes eq.(3.55) fitting results, in terms of average relaxation times (T_{2av}) and pores diameter (ξ_{2av}), for all the PLLA scaffolds studied. It can be seen that when the de-mixing phase lasts 30 or 45 minutes, an increase of the de-mixing phase temperature implies an increase of the average relaxation time. On the contrary, no significant variation of the average relaxation time occur in the case of 60 minutes. For what concerns the average pores dimension (ξ_{av}), ξ_{av} increases with the de-mixing temperature for 45 and 60 minutes while it decreases for 30 min. In any case, ξ_{av} spans between about 50

and 80 μm and these values are less than that pertaining to the reference system (Blue-red dot in *Figure 6.9*). The values of the different ξ_{av} have been deduced by eq.(3.54) fitting to the experimental data shown in *Figure 6.10 – 12*.

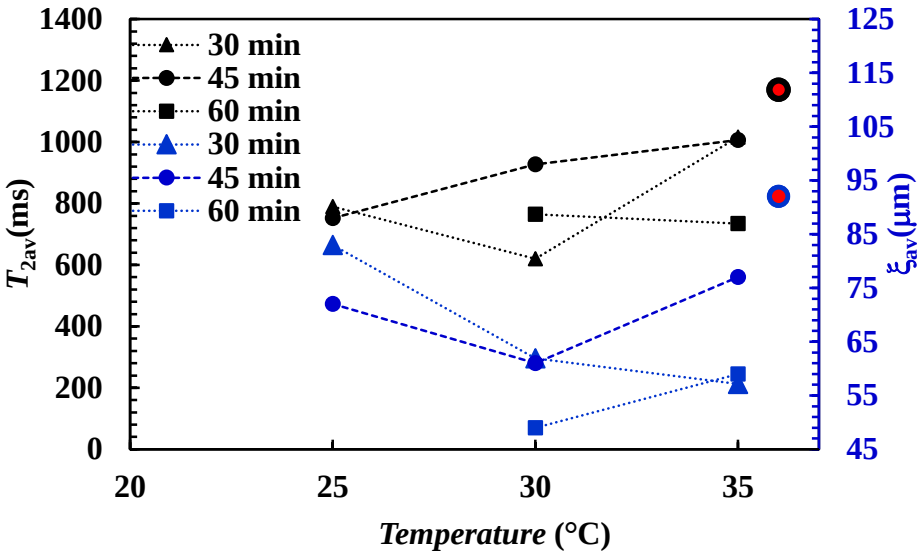

Figure 6.9: Average relaxation times T_{2av} and pores diameter ξ_{av} for the studied PLLA scaffolds. Black-red dot and Blue-red dot indicate, respectively, the average relaxation time and pore diameter of the reference scaffold. While horizontal axis reports the de-mixing phase temperature, legend reports the duration of the de-mixing step. In all cases, relaxivity $\mathcal{M}$ (the parameter accounting for the effect of surface on proton relaxations) is around 0.03 μm/ms.

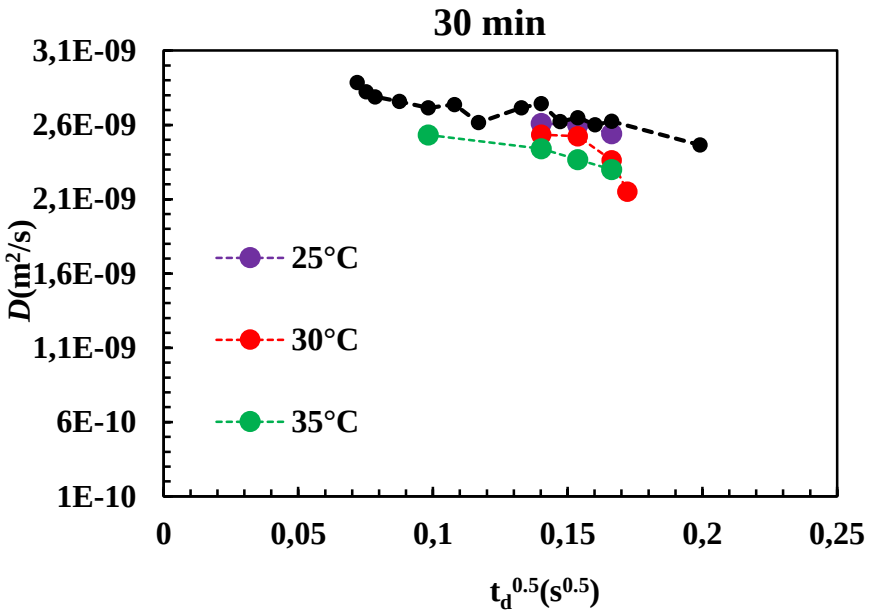

Figure 6.10: Dependence of the apparent water self-diffusion coefficient in the hydrogel (D_{app}) on the square root of the diffusion time t_d (37°C) for a de-mixing time of 30 and three different temperatures.

These figures report the dependence of the apparent water self-diffusion coefficient D_{app} on the square root of the diffusion time t_d for the different PLLA scaffold considered.

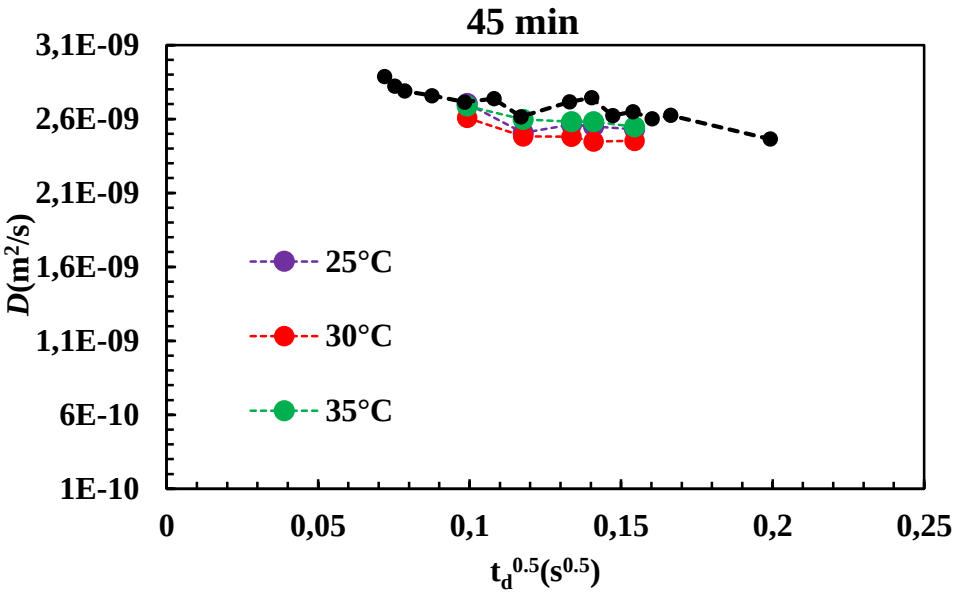

Figure 6.11: Dependence of the apparent water self-diffusion coefficient in the hydrogel (D_{app}) on the square root of the diffusion time t_d (37°C) for a de-mixing time of 45 minutes and three different temperatures.

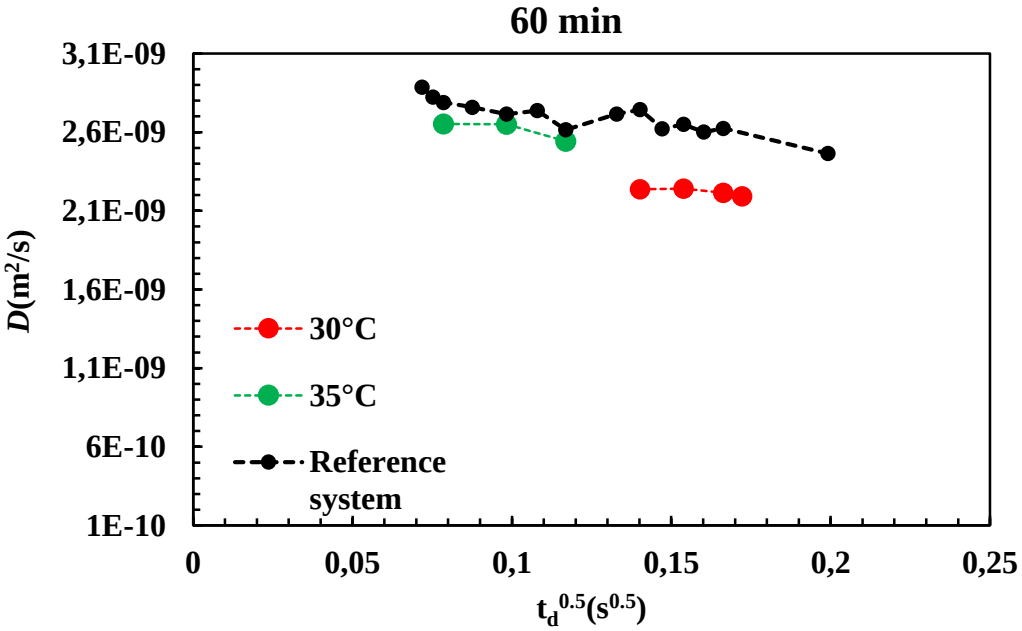

Figure 6.12: Dependence of the apparent water self-diffusion coefficient in the hydrogel (D_{app}) on the square root of the diffusion time t_d (37°C) for a de-mixing time of 60 minutes and two different temperatures.

Figures 6.10 – 6.12 make clear that the reference system is characterised by the highest values of D_{app}, this being connected with the biggest average dimension of its pores. Once the average relaxation times and the average pores diameter (see *Figure 6.9*) are known, eqs. 3.55-3.59 allow the conversion of relaxation times into pores size distribution as shown, for the different scaffolds, in *Figures 6.13 – 6.15*.

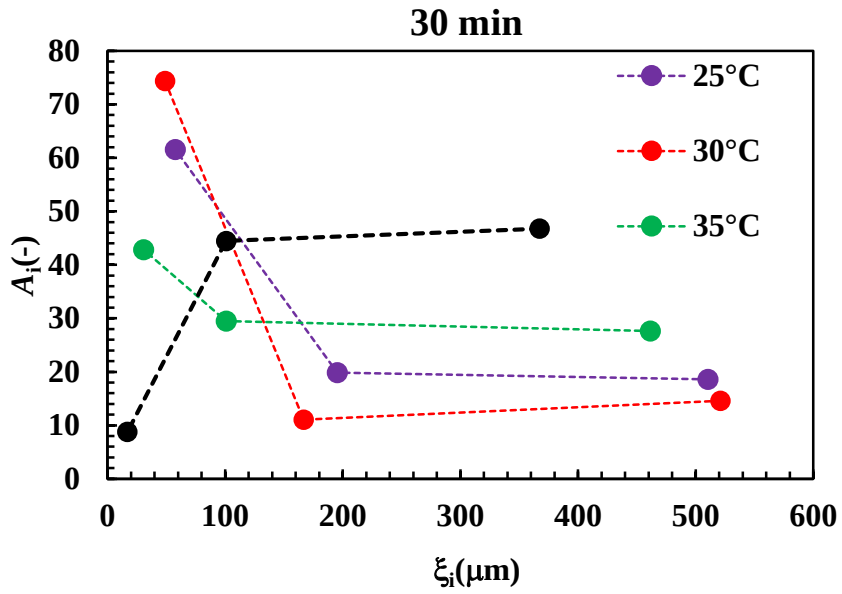

Figure 6.13: Pore size distribution referring to the scaffolds characterised by a 30 minutes de-mixing and three temperatures (25 -30 – 35 °C).

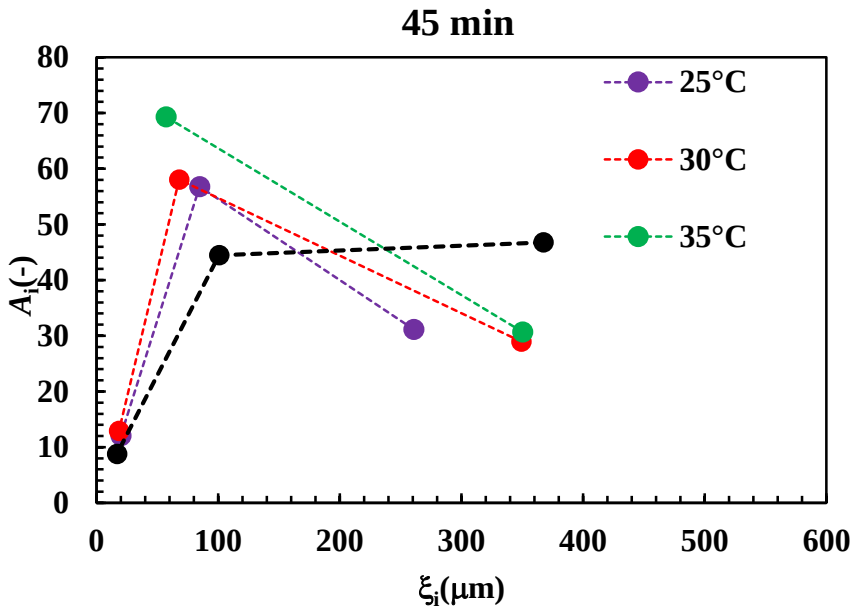

Figure 6.14: Pore size distribution referring to the scaffolds characterised by a 45 minutes de-mixing and three temperatures (25 -30 – 35 °C).

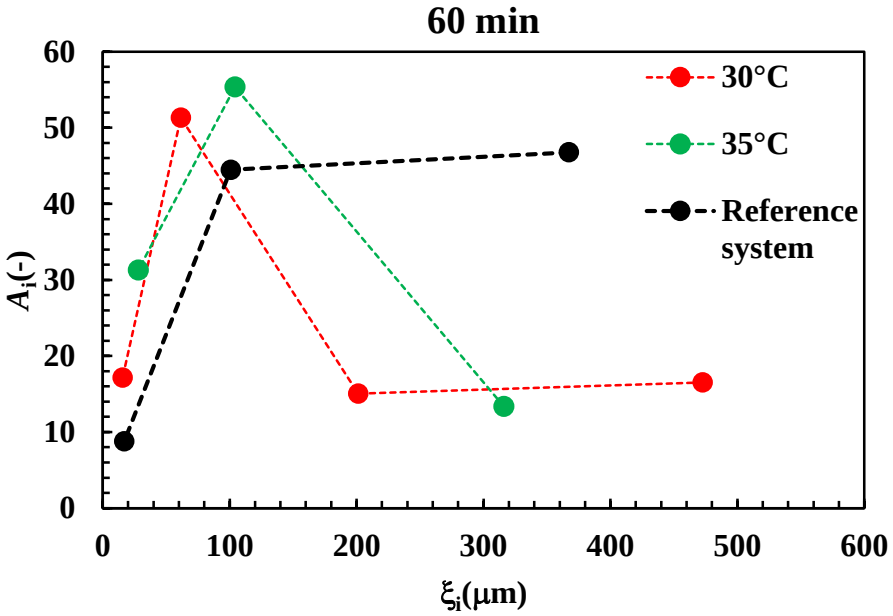

Figure 6.15: Pore size distribution referring to the scaffolds characterised by a 60 minutes de-mixing and three temperatures (25 -30 – 35 °C).

We can see that, in general, three different classes of pores are present in the studied PLLA scaffolds. It is worth to notice that, for a de-phasing step of 30 min (*Figure 6.13*), the main difference between the reference system and the systems at 25°C, 30°C and 35°C consists in a considerable increase of the smallest pores that pass from about 10% in the reference system up to 40%-75% in the other scaffolds. Consequently, the biggest pores abundance decreases from 45% (reference system) down to 20%-30% in the other scaffolds. Thus, although the average pores diameter is not so different for the reference system and the other scaffolds (see *Figure 6.9*), the pore size distribution is considerable different and this can reflect on the cells growth and proliferation. On the contrary, when the de-mixing phase lasts 45 minutes, the difference between the reference system and the other scaffolds takes place mainly on the reduction of the dimension of the biggest pores (400 μm, reference system). Indeed, the first two classes of pores (around, respectively, 20 and 90 μm) remain similar. Finally, in the case of a de-mixing phase of 60 min, the most important difference takes place for what concerns the biggest pores (around 350 μm) whose abundance goes down to about 15% when, instead, fo the reference system this class of pores represents about 45% of all pores. Again, this aspect can affect cells growth and proliferation inside the PLLA scaffold.

In order to produce a cross-linked collagen-GAGs matrix, a protocol found in literature, that allows the conjugation of the two biological molecules, was utilized. The protocol provides the combination of micro-fibrillar collagen type I solubilized in 0.02 N acetic acid and GAGs solubilized in distilled water in a volumetric ratio 90:10, followed by a process that allows to increase the number of covalent intra- and inter-molecular bonds between collagen and GAGs (cross- link). Once established the protocol for the matrix GC synthesis, a method for CG matrix formation within porous PLLA scaffolds was developed. The collagen was placed within the scaffolds by immersing them in a large volume of micro-fibrillar type I collagen, at a known concentration, solubilized in 0.02 N acetic acid for 24 hours, in order to allow the process of diffusion of the collagen into the scaffold. Then, the scaffold was freeze-dried and subjected to the process of thermal cross-link, preferred to chemical both for the absence of chemical reagents, and for the easiness of the technique. The presence of collagen within the PLLA scaffold was verified by comparing the scanning electron microscope micrographs of collagen treated and not treated scaffolds (*Figure 6.16*).

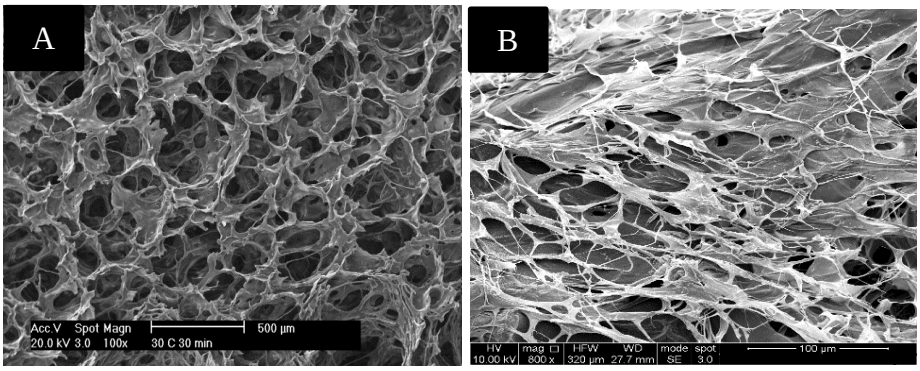

Figure 6.16: SEM micrographs of the PLLA scaffold without (**A**) and with (**B**) the collagen matrix.

Several attempts were carried out in order to identify a method that would allow a homogeneous diffusion of the GAG molecules into the scaffold and their subsequent crosslinking to the collagen matrix. The best result was attained through the injection into the scaffold of a solution of GAGs, at the same concentration of collagen, followed by a freeze-drying and a thermal cross-link. The SEM micrographs of the functionalized scaffolds in the latter way (*Figure 6.17*) show that also in this case the outer surface (A),

is completely covered forming a dense network of collagen. Also in the cross-sections (B), an abundant network formed by the matrix was detected.

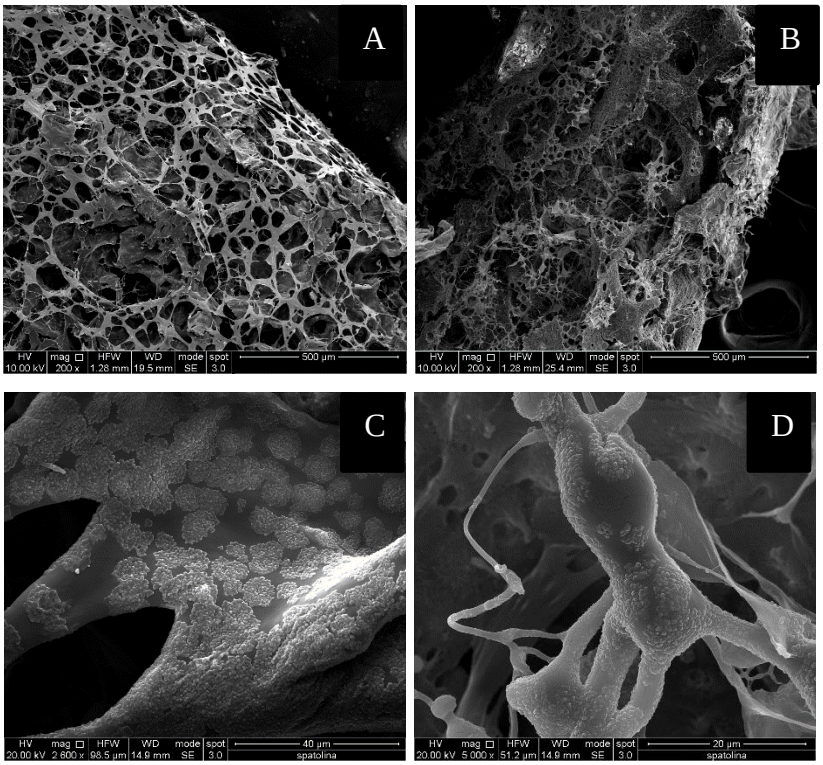

Figure 6.17: SEM micrographs of the PLLA-collagen-GAG. External surface (A); cross section (B); Collagen-GAGs matrix (C and D)

Figure 6.17C and *6.17D* show micrographs at high magnification of the micro-fibrils of the matrix embedded in the scaffold. It is possible to observe that, also in this case, the fibrils are covered by the GAGs particles, leading to suppose that the conjugation GAG-collagen occurred also within the scaffold.

In order to confirm the improvement (in terms of cellular adhesion and proliferation) of the PLLA-Collagen-GAGs scaffold, preliminary cell culture tests were carried out. The results, reported in *Figure 6.18*, confirmed a faster cell proliferation in CG scaffolds, especially in the early stages after the seeding. Specifically, the number of viable cells into the PLLA-collagen-GAG scaffold was, approximately, 1.5 that of pure PLLA and PLLA-collagen up to the third day of culture, thus indicating a better level of adhesion and consequently of the proliferation into the device.

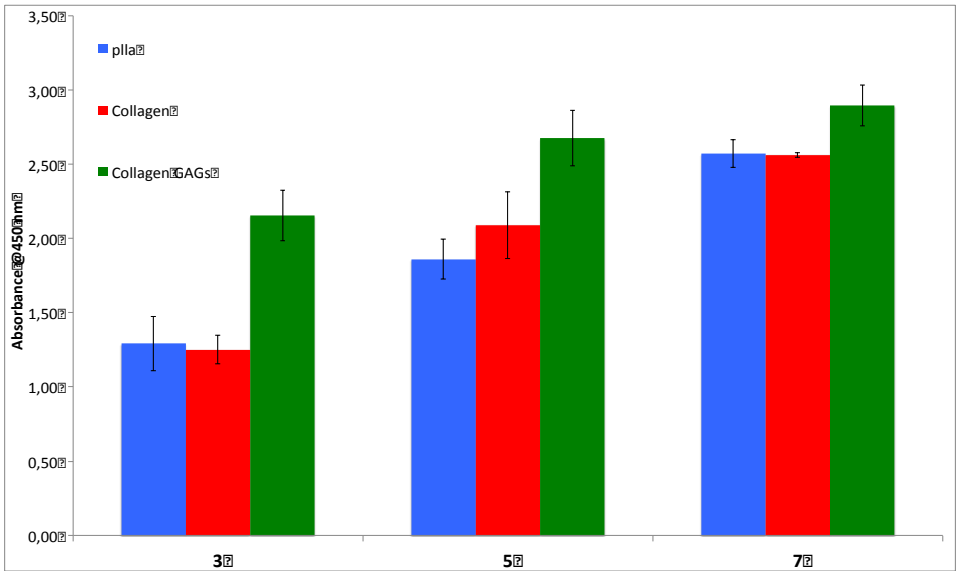

Figure 6.18: Viability and growth of mouse embryonic fibroblasts into the PLLA-collagen-GAG scaffolds. While horizontal axis reports the days elapsed from cells seeding, vertical axis report absorbance that is proportional to the number of viable cells.

References:

1. Chui, M. M., Phillips, R. J., McCarthy, M. J. (1995). Measurement of the porous microstructure of hydrogels by nuclear magnetic resonance. J. Coll. Inter. Sci., 174, pp. 336-344.
2. Bear J., Porosity and Representative Elementary Volume in dynamics of fluids in porous media pp. 19 – 22.
3. Hutmacher DW. Scaffolds in tissue engineering bone and cartilage. Biomaterials 2000;21(24):2529-2543.
4. Engelberg I, Kohn J. Physico-mechanical properties of degradable polymers used in medical applications: A comparative study. Biomaterials 1991;12(3):292-304.
5. Athanasiou KA, Niederauer GG, Agrawal CM. Sterilization, toxicity, biocompatibility and clinical applications of polylactic acid/ polyglycolic acid copolymers. Biomaterials 1996;17(2):93-102.
6. Vert M, Christel P, Chabot F, Leray J. Macromolecular Biomaterials. 1st ed. New York: CRC / Press Inc., 1984
7. Hofmann H., Fietzek P.P., Kühn K. The role of polar and hydrophobic interactions for the molecular packing of type I collagen: A three-dimensional evaluation of the amino acid sequence Journal of Molecular Biology 1978; Volume 125, Issue 2 pp.137-165
8. Fraser R.D.B., MacRae T.P., Suzuki E. Chain conformation in the collagen molecule. Journal of Molecular Biology 1979; Volume 129, Issue 3 pp.463-481
9. Gelse, K., Soeder, S., Eger, W., Diemtar, T. and Aigner, T. (2003). Osteophyte developmentmolecular characterization of differentiation stages. Osteoarthr. Cartil. 11, 141-148.
10. Ernst S, Langer R, Cooney CL & Sasisekharan R 1995a Enzymatic degradation of glycosaminoglycans. Crit.Rev.Biochem.Mol.Biol. 30 387-444.
11. Bulow HE & Hobert O 2006 The molecular diversity of glycosaminoglycans shapes animal development. Annu.Rev.Cell Dev.Biol. 22 375-407.
12. Perrimon N & Bernfield M 2001 Cellular functions of proteoglycans--an overview. Semin.Cell Dev.Biol. 12 65-67
13. Capila I & Linhardt RJ 2002 Heparin-protein interactions. Angew.Chem Int.Ed Engl. 41 391-412

14. Knudson CB & Knudson W 1993 Hyaluronan-binding proteins in development, tissue homeostasis, and disease. FASEB J 7 1233-1241

15. Funderburgh JL 2000 Keratan sulfate: structure, biosynthesis, and function. Glycobiology 10 951-958.

16. Varki A 1993 Biological roles of oligosaccharides: all of the theories are correct. Glycobiology 3 97-130.

17. Cigliano A. et al. Fine structure of glycosaminoglycans from fresh and decellularized porcine cardiac valves and pericardium. Biochem Res. Int. 2012; ISSN: 2090-2247.

18. Naso F. et al. Differential distribution of structural components and hydration in aortic and pulmonary heart valve conduits: Impact of detergent-based cell removal (2010) ACTA BIOMAT. Vol 6(12): 4675-88.

19. Mannella G., Carfì Pavia F., Conoscenti G., La Carrubba V., Brucato V. Evidence of Mechanisms Occurring in Thermally Induced Phase Separation of Polymeric Systems. Journal of Polymer Science (2014) DOI: 10.1002/polb.23518

20. Pek Y. S., Spector M., Yannas I. V., Gibson L. J. (2004) Degradation of a collagenchondroitin-6-sulfate matrix by collagenase and by chondroitinase. Biomaterials 25:473–482,(doi:10.1016/S0142-9612(03)00541-6).CrossRefMedlineWeb of Science

7 Conclusions

Tissue engineering (TE), involving the use of living cells and extracellular components from either synthetic and natural polymers, aims to regenerate tissues and restore or replace deteriorating or aging biological structures.

The present PhD project focused its attention on the determination of some important micro and nano structural characteristics of polymeric matrices intended for biomedical applications. In particular, the attention was focused on the application of the Low-Field Nuclear Magnetic Resonance (LF-NMR), a fast and non destructive technology used in food and polymeric companies to study homogeneous (i.e. not porous) and porous polymeric matrices. In particular, the first part of this work was dedicated to the characterization of *homogeneous gels* such as guar gum/ guar gum borax and alginate pluronic F127 hydrogels.

One of the most interesting homogeneous matrix studied was that composed by alginate and pluronic F127. The joint use of rheology, low and high field NMR allowed to understand the structural characteristics of this gel intended for the prevention of restenosis according to the endoluminal gel paving approach. This study revealed that pluronic micelles, organizing in cubic crystalline domains, impose, upon alginate crosslinking, the formation of meshes bigger than that occurring in the pluronic free alginate network. Nevertheless, there still exist smaller alginate meshes that can just host un-structured pluronic micelles and water. Accordingly, pluronic presence gives origin to an inhomogeneous structure formed by big meshes (filled by crystalline pluronic) where the diffusion of a solute is considerably hindered and smaller meshes where solute diffusion is faster. This aspect can be very interesting from the delivery point of view as it should roughly imply a two stages release kinetics: an initial fast stage followed by a slow one. The combination of the first stage, due to drug presence in the crystalline PF127 filled meshes (big ones), and the second, due to the drug presence in the crystalline PF127 pluronic free meshes (small ones), should guarantee an optimal balance between fast and slow release. Indeed, previous simulations indicated that the combination of a fast and a slow release stages is the desired release kinetics to get an almost constant drug concentration in the artery wall.

In the second part of the work, the attention shifted on *porous systems*, typically used as scaffolds for regenerative medicine and tissue engineering. Indeed, low field NMR provides interesting information about the size distribution of matrix pores, this being a key parameter for cells growth. It is well know that cells can grow on condition that pores are sufficiently wide (typically around 100 microns in diameters). In order to demonstrate the reliability of this technique, different systems were studied. One of the most interesting porous system studied was composed by coffee seeds. The knowledge of water content in green coffee is of great importance to produce a quality cup, especially when dealing with espresso coffee. Thus, a deep understanding of the distribution of water molecules and their interactions with the macromolecules of the solid green bean matrix could explain the inaccuracies of the standard methods of quantification. In addition, it would help to build clear protocols to improve quality control. In the case of the coffee seeds, the estimation of pores diameter according to low field NMR approach demonstrated that the coffee seeds pores are interconnected. The comparison between LF-NMR results and SEM picture tells us the LF-NMR results are reasonable even if the bigger estimated pores (around 200 μm) seem to be attributable to water on the rough surface of coffee seeds (open pores). Another porous system studied was a strong gel composed by bacterial cellulose and acrylic acid gels. This hydrogel has good muco-adhesive characteristics, an ideal requisite to deliver intestinal targeted drugs. In particular, we found that the majority of the hydrogel volume (81%) is represented by micrometric pores filled by water and only 19% of the hydrogel volume is represented by polymeric meshes swollen by water. While pores diameter spans from about 10 μm to 100 μm and the majority of pores lies between 30 and 90 μm, the mean polymer mesh size is around 3 nm. In addition, the estimation of pores phase tortuosity (~ 2.3) seems to indicate a complex architecture where big pores are not directly connected (in this case the tortuosity should be lower and not so far from 1), but communicate via a series of interconnected smaller pores.

Finally, the last part of the research activity was dedicated to explore the possibility to use LF-NMR to study *porous scaffolds*. In particular, two different types of scaffolds were considered:

- ✓ Alginate/Hydroxyapatite scaffolds
- ✓ PLLA scaffolds.

Undoubtedly, one of the most important results reached in this research activity was connected to the characterization of alginate - hydroxyapatite scaffold intended for osteocytes growth in the bone regeneration frame. Indeed, it was possible observing the temporal evolution of the pore size distribution of the scaffold without and with seeded cells. Interestingly, it was observed that while the temporal evolution of pores size, for what concerns smaller pores (< 100 μm), is similar for scaffolds hosting or not living cells, a different behavior was observed for bigger pores. Indeed, in this case, the presence of cells made the time evolution of the pores size different from what occurred in the scaffolds cells free. This seems reasonable as the effect of cell growth should be evident only in bigger pores while, in smaller pores, where cells access is more difficult, cells effect should be less evident if not negligible.

In light of the tests performed and the considerations made, it can be stated that the LF - NMR is a powerful method for the structural characterization of both porous and homogeneous polymeric matrices. In addition, LF – NMR has the considerable advantage of being used also for the monitoring of structures containing living cells as it does not damage cells. On the contrary, other widely used and powerful techniques such as ESEM or micro – CT, cannot be used to follow the time evolution of cells containing structure as they would lead to cells death.

Undoubtedly, for what concerns porous systems, the best results provided by LF – NMR can be obtained when the nature of the solid system component is clearly different from that of the swelling fluid. While this is the case of systems such as coffee seeds, it is not always true for polymeric systems characterized by wide pores.